Optoelectronic properties and photonic-based processing of printed conductive thin-film architectures

by

Luis Felipe GERLEIN REYES

MANUSCRIPT-BASED THESIS PRESENTED TO ÉCOLE DE TECHNOLOGIE SUPÉRIEURE IN PARTIAL FULFILLMENT FOR THE DEGREE OF DOCTOR OF PHILOSOPHY
Ph.D.

MONTREAL, APRIL 24th, 2024

ÉCOLE DE TECHNOLOGIE SUPÉRIEURE
UNIVERSITÉ DU QUÉBEC

BOARD OF EXAMINERS

THIS THESIS HAS BEEN EVALUATED

BY THE FOLLOWING BOARD OF EXAMINERS

Mr. Sylvain G. Cloutier, Thesis Supervisor
Département de génie électrique, École de technologie supérieure

Mr. Éric David, Chair, Board of Examiners
Département de génie mécanique, École de technologie supérieure

Mr. Vahé Nerguizian, Member of the Jury
Département de génie électrique, École de technologie supérieure

Mr. Martin Bolduc, External Examiner
Département de génie mécanique, Université du Québec à Trois-Rivières

Mrs. Claudine Allen, External Independent Examiner
Département de physique, de génie physique et d'optique, Faculté des sciences et de génie, Université Laval

THIS THESIS WAS PRESENTED AND DEFENDED

IN THE PRESENCE OF A BOARD OF EXAMINERS AND THE PUBLIC

ON APRIL 8th, 2024

AT ÉCOLE DE TECHNOLOGIE SUPÉRIEURE

ACKNOWLEDGEMENTS

There were many changes, up and downs that took place for the completion of this work. I want to humbly recognize the support, patience and constructive feedback given my supervisor and mentor Professor Sylvain G. Cloutier. I am thankful for all the opportunities given to experience, build and advance a fantastic lab. Having the chance pursue as many crazy ideas and endeavours as I wanted to, meet outstanding people as a member of the NOMAD research group and work alongside companies that made my time at ÉTS the nicest experience. Thank you Sylvain, I am forever indebted for your guidance and teachings.

I want to give thanks to my colleagues and friends in the NOMAD group for their continuous support, never-ending conversations, jokes and help whenever they were needed. To all, I wish you the best and I hope we can continue working together and sharing a nice friendship in the future. I would like to give special thanks for the support, valuable advise and discussions and specially, the relentless pushing received from my colleague and best friend Dr. Jaime Benavides in the writing of this thesis. It really helped me a lot!

I want to thank Prof. Martin Bolduc and the team at C2MI for the experience of working with state of the art printed electronics machines and expanding of my set of skills and abilities further than ever.

I want to thank all my friends outside ÉTS, whose friendship and continuous cheerful jokes always gave me a laugh. Likewise, Ultimate frisbee ETS and Les Don Qui-shots for letting me guide them and participate of this passion of mine. These team sports gave me lots of mental and physical outlets to keep going with my research.

Last but not least, I want to thank my family, my mom Clauida, my dad Eduardo Luis, my brother Eduardo Andrés and my brother Juan Camilo, whose unconditional support, sacrifices and love always pushed me to go one step ahead, even in the darkest of times. Finally, I want to thank my girlfriend Jessica, for her love, understanding and patience were instrumental to help me move in the right direction of finishing this long path. Love you all.

Propriétés optoélectroniques et traitement photonique des architectures de films minces conducteurs imprimés

Luis Felipe GERLEIN REYES

RÉSUMÉ

Le domaine en développement de l'électronique imprimée hybride promet de constituer une alternative appropriée à de nombreuses technologies traditionnelles à base de silicium en réduisant les coûts de fabrication et en augmentant la vitesse de production, tout en offrant des performances similaires. Pour concrétiser cette vision, des approches novatrices de fabrication additive et de traitement des dispositifs sont nécessaires, visant à répondre aux exigences industrielles telles que la haute conductivité électrique, la transmittance optique et la longue durée de vie des dispositifs.

Cette thèse de doctorat démontre diverses applications du traitement des nanomatériaux sur différents substrats, y compris la sintérisation directe au laser et photonique, pour la production de dispositifs optoélectroniques, avec pour objectif d'obtenir des résultats fiables et reproductibles. Pour ce faire, une revue de la littérature est présentée, où les principes du traitement photonique sont expliqués, suivis d'un aperçu des techniques de traitement et des applications de dispositifs optoélectroniques à jour. Ensuite, une description du rôle des oxydes métalliques et des nanostructures métalliques en optoélectronique est présentée, mettant l'accent sur le traitement du TiO_2 et des nanofils d'argent.

À la suite de la revue de la littérature, la cristallisation à grande échelle à la demande de films minces de TiO_2 est présentée en utilisant une source laser de 405 nm bon marché et disponible dans le commerce. Cette application du traitement laser direct démontre le processus d'optimisation pour obtenir des films uniques ou hybrides d'anatase ou de rutile TiO_2 produits dans des conditions ambiantes, sans nécessiter d'équipement supplémentaire.

Ensuite, des électrodes conductrices transparentes fabriquées à partir de nanofils d'argent sont traitées à l'aide d'un équipement de traitement de pointe par frittage photonique. Ce projet compare leurs figures de mérite optoélectroniques avec celles des films fabriqués à l'aide de méthodes thermiques traditionnelles. Une nouvelle métrique de la figure de mérite est proposée pour corréler les effets de la densité d'énergie de l'impulsion de traitement et la résistance en feuille finale des films.

Enfin, un ensemble multi-matériaux composé de nanofils d'argent et de TiO_2 est traité en utilisant deux étapes indépendantes de frittage photonique, réalisées sur un substrat souple sensible à la chaleur. Les résultats montrent comment différents matériaux peuvent être traités à l'aide de la même machine de frittage photonique en exploitant leurs qualités physiques divergentes. Les nanostructures métalliques bénéficient de conditions à densité de puissance de crête élevée et d'impulsions courtes, tandis que les oxydes métalliques photosensibles répondent à des conditions de traitement à densité de puissance de crête faible et d'impulsions

longues. Cette approche de traitement multi-matériaux est le fruit de nombreuses années d'expérience dans le domaine de l'électronique imprimée, de l'affinement des connaissances sur diverses voies de fabrication additive et d'une compréhension approfondie du traitement photonique appliqué à une grande variété de matériaux. Ces résultats seront sans aucun doute précieux pour le développement futur de dispositifs optoélectroniques flexibles et performants, contribuant ainsi à l'avancement des connaissances scientifiques dans le domaine du traitement des matériaux en électronique imprimée.

Les résultats de projets de recherche supplémentaires sont également présentés dans le cadre de cette thèse. Tout d'abord, les travaux réalisés avec des nanocristaux de plomb-soufre chalcogénides, comprenant la maîtrise de la synthèse de points quantiques de PbS pour le contrôle de la taille et la caractérisation de leurs propriétés optiques. Ces derniers ont été utilisés dans des assemblages de points quantiques en utilisant un échange de ligands pour construire des photodétecteurs et une cellule solaire sensibilisée par des points quantiques fabriquée avec du TiO_2. Le facteur de remplissage de ce dispositif a été amélioré par l'ajout de nanotubes de carbone à parois multiples facilitant l'extraction de charges. Deuxièmement, un projet industriel visant à comprendre et à optimiser la fabrication d'encres à base de graphène pour la sérigraphie, réalisées avec un graphène de qualité industrielle. Ce projet a nécessité la compréhension des propriétés des matériaux à base de graphène par une analyse approfondie de ses caractéristiques Raman, et comment le matériau réagit à différentes techniques de post-traitement pour créer des encres de sérigraphie.

Mots-clés: Nanofils d'argent, frittage photonique, frittage laser direct, films minces, substrats flexibles, points quantiques, graphène, PbS

Optoelectronic properties and photonic-based processing of printed conductive thin-film architectures

Luis Felipe GERLEIN REYES

ABSTRACT

The developing field of hybrid printed electronics promises a suitable replacement for many traditional silicon-based technologies by lowering manufacturing costs and increasing production speed, while offering similar performance. To realize this, novel approaches of additive manufacturing and processing of devices are required, aiming to meet industrial requirements such as high electrical conductivity, optical transmittance, long device lifetime.

This doctorate thesis demonstrates various applications of nanomaterials processing of atop different substrates, including direct laser and photonic sintering, to produce optoelectronic devices and aimed to obtain reliable and reproducible results. To do this, a literature review is presented where the principles of photonic processing are explained, followed by an overview of the up-to-date processing techniques and optoelectronics device applications. After, a description of the role of metal-oxides and metallic nanostructures in optoelectronics, with emphasis on processing of TiO_2 and silver nanowires.

Following the literature review, large-area, on-demand crystallization of TiO_2 thin films are presented using a low-cost, of-the-shelf 405 nm laser source. This application of direct laser processing shows the optimization process to achieve single or hybrid films of anatase or rutile TiO_2, that are produced at room conditions, without the need of additional equipment.

After, transparent conductive electrodes made of silver nanowires are processed using photonic sintering with state-of-the-art processing equipment. This project compares their optical-to-electrical figures of merit with those of films fabricated using traditional thermal methods. A new figure of merit metric is proposed to correlate the effects of the processing pulse fluence and the final sheet resistance of the films.

Lastly, a multi-material ensemble made of silver nanowires and TiO_2 is processed using two independent photonic sintering steps, done on a heat-sensitive, flexible substrate. The results show how different materials can be processed using the same photonic sintering machine by taking advantage of their divergent physical qualities. Metallic nanostructures benefit from short-pulse, high peak power density conditions and, photo-sensitive metal-oxides respond to long-pulse, low peak power density processing conditions. This multi-material processing approach is the result of years of experience working on printed electronics, refining the knowledge of various additive manufacturing avenues, and a deep understanding of photonic processing done over a wide variety of materials. These results will undoubtedly be useful in the future development of flexible, high-performance optoelectronic devices and contribute with the advancement of scientific knowledge for materials processing in printed electronics.

The results of additional research projects are also presented as part of this thesis. First, the work done with chalcogenide lead-sulfide nanocrystals, that included mastering the synthesis of PbS quantum dots for size control and characterization of their optical properties. These were utilized in QD assemblies using ligand exchange to build photodetectors and a quantum dot sensitized solar cell made with TiO_2. The fill-factor of this device was improved by the addition of multi-walled carbon nanotubes that facilitated the charge extraction. Second, an industrial project that aimed to understand and optimize the fabrication of graphene-based inks for screen printing, made with an industrial-grade graphene. This project demanded understanding the properties of graphene materials by doing in-depth analysis of its Raman characteristics, and how the material responds to different post-processing techniques to create screen-printing inks.

Keywords: TiO_2, silver nanowires, photonic sintering, direct laser sintering, thin films, flexible substrates, quantum dots, graphene, PbS

TABLE OF CONTENTS

LIST OF TABLES

LIST OF FIGURES

LIST OF ABBREVIATIONS

1D	1-Dimensional
AFM	Atomic Force Microscopy
AZO	Aluminum-doped Zinc Oxide
CVD	Chemical Vapor Deposition
CW	Continuous wave
DSSCs	Dye-Sensitized Solar Cell
ETL	Electron-Transport Layer
ETS	École de Technologie Supérieure
F_F	Fill Factor
FHE	Flexible Hybrid Electronics
FoM	Figure of Merit
FTO	Fluorine-doped Tin Oxide
GSH	L-Glutathione
HBL	Hole-Blocking Layer
HOPG	Highly Oriented Pyrolytic Graphite
ITO	Indium-doped Tin Oxide
KAPTON	Name given to a polyimide, poly (4,4'-oxydiphenylene-pyromellitimide), film for flexible printed circuits
MeCh	Metal-Chalcogenide
MO	Metal Oxide

μ-pulses	Micro-Pulses
NW	NanoWire
MWCNTs	Multi-Walled Carbon NanoTubes
NCs	Nanocrystals
OLED	Organic Light Emitting Diode
PET	Polyethylene Terephthalate
PbS	Lead Sulfide
PbSe	Lead Selenide
PV	Photovoltaic
QDs	Quantum-dots
RPM	Revolutions Per Minute
SMOs	Semiconductor Metal Oxides
TCE	Transparent Conductive Electrode
XRD	X-Ray powder Diffraction
SEM	Scanning Electron Microscopy
SL	Single Layer
TiO_2	Titanium dioxide, Titania
USD	US-Dollar
w/w	weight to weight concentration

LIST OF SYMBOLS AND UNITS OF MEASUREMENTS

Å	Angstrom
cm^{-1}	Wavenumbers
(COOH)-	Carboxyl group
°C	Degrees Celsius
EDT	1,2-Ethanedithiol
eV	Electron-volts
E_g	Band-gap energy
g	Grams
Hz	Hertz
$J.cm^{-2}$	Joules over squared centimeter, fluence, energy density
$kg.m^{-3}$	kilogram over cubic meter, volumetric density
kV	kiloVolts
mm	millimeter
$mm.min^{-1}$	millimeter per minute
mW	milliWatts
$mW.cm^{-2}$	milliwatts over centimeter squared
nm	nanometer
µm	micrometer
Ω	Ohm

Ω^{-1}	Inverse Ohm. Used in figures of merit for transparent materials
Ω/sq.	Ohm-Square
Ω/□/25μm	Industrial standard for measuring of the sheet resistance based on 25 μm film's thickness
R_{sh}	Sheet Resistance
T	optical Transmittance
$kW.cm^{-2}$	Kilowatts over centimeter squared

INTRODUCTION

0.1 Research context and problematic

This research project aims to develop optical processing avenues for various materials, and their integration in creating transparent conductive films processed atop heat-sensitive substrates. Developing these processing routes includes both single and multi-material, large-area films that can be deposited on polymeric substrates, so that in the future, they can be integrated in roll-to-roll production lines.

What motivated this investigation is the rapid growth of the printed electronics industry, showing important progress in the introduction of materials compatible with numerous printing techniques, and the development of equipment for fast processing that bring down manufacturing costs when compared to traditional industries. Indeed, this industry has been focusing in the manufacturing printed sensors, display technologies and photovoltaics that can be between 10 and 100 times cheaper than their equivalents in silicon-based industries (Markets and Markets, 2021). However, this industry currently faces limited alternatives of flexible transparent electrodes for optoelectronic devices. Expensive and slow deposition methods deliver high-performance platforms but are incompatible with the roll-to-roll approach (Baran, Corzo & Blazquez, 2020). Printing metallic particle-in-suspension inks in specific patterns that limit the interaction with the passing light may show good conductive properties, up to a certain point, and they suffer from a lack of transparency. The prevalence of flexible printed optoelectronics is increasing due to the integration of IoT smart features in various consumer products, healthcare, military, and industrial applications. Being able to produce reliable and performant multi-material, transparent conductive films that can be processed using photonic treatment equipment used in industry is crucial, particularly given the ongoing expansion of the market and the high demand for flexible platforms in both printed electronics and optoelectronics, as shown in Figures 0.1(a-c).

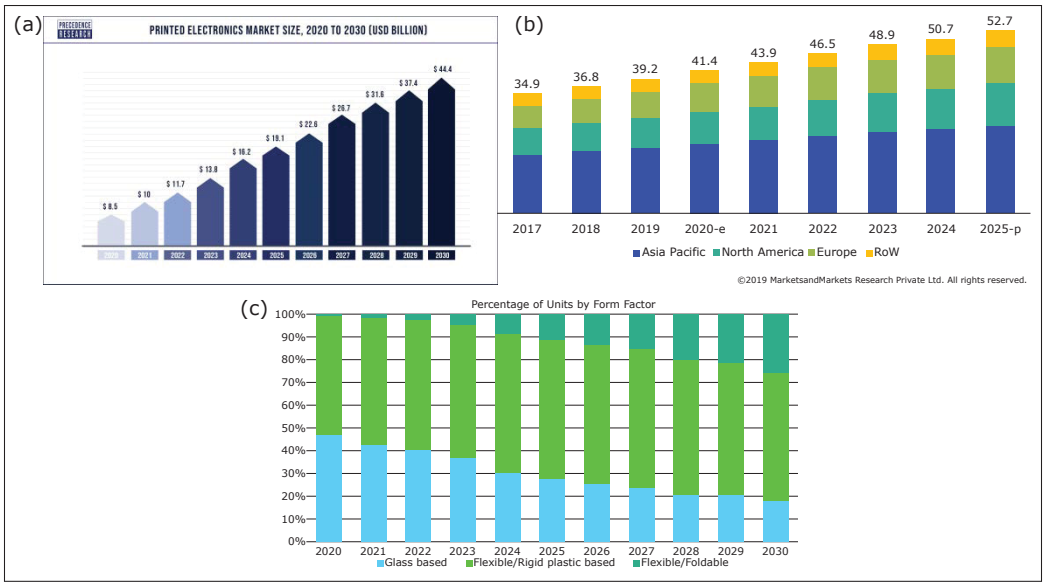

Figure 0.1 Market studies and projections for flexible printed electronics and optoelectronic devices (a) Printed electronics market size worldwide 2020-2030 (b) Optoelectronic components market size by region (USD$ Billion) (c) Projection for change in form factor of OLED displays into flexible devices[1]

Photonic processing of materials was born as an alternative to the traditional thermal treatments employed in industry. It provides answers to well established industrial hurdles such as high thermal requirements (thermal power), long processing times, energy loss related to the rising and lowering temperature of the oven, incompatibility with heat-sensitive substrates (polymers, amorphous alloys) and inability to induce spatially resolved thermal effects (i.e curing, welding and crystallization) in small and large-area applications. In addition, the use of optical and photonic processing of materials in optoelectronic devices has several advantages over traditional electronic processing:

- **Speed:** Optical processing is generally, faster than thermal processing.

[1] (a) Market Stats News (2021) (b) Markets and Markets (2020) (c) Das & He (2019)

- **Efficiency:** Photonic treatment of materials uses less energy than traditional thermally induced treatment. In similar manner, optical and photonic processing equipment tends to use less physical space than thermal processing equipment.
- **Versatility:** Photonic signals can be used to process a wide range of materials, including both conducting and non-conducting.
- **Customization:** Different processing parameters such as light intensity, pulsed or continuous wave pulse shape, speed, number of passes among others can be varied to attain the optimal material properties.
- **Scalability:** Large area devices can be readily produced at a fraction of the cost. Material deposition and processing can be done in the same production line.

Consequently, the dramatic increase in the use of photonic processing of materials for optoelectronic applications has fueled the development of new areas of research and industry. With the progress in direct laser and intense pulsed-light sintering, one can likely manipulate the optoelectronic properties of materials with the same degree of precision as with thermal processing. In addition, it is now possible to control chemical reactions that previously relied solely on external thermal energy sources. In general, these changes in properties are the result of the rapid release of energy from the light source, resulting in thermally-induced effects that allow precise control over the treated material's properties.

In particular, the emerging field of hybrid printed electronics benefits two-fold from the development and maturing of processing routes through light-induced treatment of materials. On one hand, it permits to take advantage of organic and inorganic materials for the production of flexible devices such as wearable sensors, displays and conformal photovoltaic devices (Ren *et al.*, 2021). On the other hand, as a consequence of the short processing times, the energy required to process materials is also lowered. For instance, metallic-based nanoparticle colloidal inks have been smoothly integrated into hybrid-flexible printed electronics production

lines, and their processing has been successfully tailored for optical treatment. Normally, processing these inks in an oven would take between 10 and 30 minutes, but photonic processing can be completed in seconds using a fraction of the energy. This successful transition resulted, in part, to the size of the nanoparticles inside these inks, which range from 1 to 100 nm. In this case, the melting temperature decreases with dimension by a factor of 10-100 °K (Buffat & Borel, 1976; Kaptay, 2012; Guisbiers, 2012; Ansari, 2021). This means, colloidal inks are easily sintered by optical means, even when applied in flexible, heat-sensitive substrates (Schroder, McCool & Furlan, 2006).

In similar fashion, 1-Dimensional metallic nanostructures are of special interest in the manufacturing of flexible, semi-transparent conductive electrodes. Once again, photonic processing of these materials allowed the rapid and efficient fabrication of transparent conductive films, compared to traditional thermal processing that takes several minutes (Sepulveda-Mora & Cloutier, 2012). This networks are intrinsically flexible and can be readily employed in displays, sensors and solar cells. However, proper quantification of the performance of transparent conducting electrodes (TCEs) fabricated with industry-ready equipment is required to establish the feasibility of including this technology in production lines (Gerlein, Benavides-Guerrero & Cloutier, 2021).

Semiconducting metal oxides (MOs) are widely used in optoelectronic devices and have desirable optical and electrical properties that can be achieved by sintering at high temperatures, typically greater than 300°C and for longer than 20 minutes. Comparatively, a continuous production line, the high energy requirements, and the slow processing speed of metal oxides will result in inefficient industrial processing. At 30 m/min, a common speed goal for flexible electronics manufacturing, a 20 minute annealing time would necessitate a 600 m long production line (Hsu, 2021). These stringent requirements render MOs incompatible with heat-sensitive substrates and impede the transition from thermal processing to more

efficient optical processing alternatives (Noh *et al.*, 2022). However, recent advances in material chemistry (Benavides, Trudeau, Gerlein & Cloutier, 2018; Daunis, Schroder & Hsu, 2020; Benavides-Guerrero *et al.*, 2022b), allowed the synthesis of light sensitive ceramics that can be crystallized under visible-light sources such as lasers and broad-band flash lamps. This development opens the door to additive manufacturing of *large-area*, ceramic thin-films that are compatible with optoelectronic devices and sensors (Luo *et al.*, 2017; Gerlein, Benavides-Guerrero & Cloutier, 2019). This, in turn, has the potential of reaching that *golden* 30 m/min processing speed mark.

Taking one step further, multi-material photonic processing of hybrid thin films in flexible substrates is something that, until now, has yet to be demonstrated. By taking advantage of the diverse photonic processing requirements of different materials, one can envision integrated production lines that take care of, for example, both sintering and crystallization by purely optical means. This can be translated into large area optoelectronic devices that can exhibit flexibility, performance and compatibility with temperature sensitive materials. Large-area, multi-material, transparent conductive films processed solely through optical means and compatible with high-speed production lines are unquestionably, an exciting area of research where novel, flexible optoelectronic devices and applications could be developed to meet the needs of a number of 4.0 industries.

0.2 Research objectives

Entitled Optoelectronic properties and photonic-based processing of printed conductive thin-film architectures, this doctorate thesis presents the work done to demonstrate the processing of single and multi-material transparent conductive electrodes by photonic and direct laser sintering. The results of this research enable future developments in flexible devices that require metal-oxide electron transport layers, such as for photodetectors and solar cells, all fabricated by simple and repeatable steps, with electric-to-optical characteristics on par

with those of the traditionally fabricated TCEs. With this in mind, the following secondary objectives have been identified:

- Establish the best processing parameters for the the materials used, so that the results are repeatable and can be easily translated to industry-ready manufacturing equipment
- Test the optical-to-electrical standard metrics for TCEs that prove the performance of the platforms
- Proof that flexible, multi-material TCEs can be fabricated using exclusively photonic processing methods

The main contributions of this research work are the following:

- Develop the necessary optimization process to produce large-area, on-demand crystallization of thin films of TiO_2
- Establish the feasibility of photonically sintered TCEs made of silver nanowires and compare their performance through well-established optical-to-electrical metrics
- Validation of the simulation tools present on industry-grade manufacturing equipment, establishing its strengths and short-comings when compared to published molecular dynamics simulations of the same phenomena
- Proposal of a new Figure-of-Merit for photonic treatment versus sheet resistance of TCEs
- Demonstrate the fabrication of large-area, flexible, multi-material TCEs made of silver nanowires networks in conjunction with photo-sensitive TiO_2. These platform was completely processed using photonic processing

0.3 Additional work done as part of my Doctorate studies

0.3.1 Research project: Synthesis and characterization of lead sulfide quantum dots. Presentation of results, application in optoelectronic devices and contributions in peer reviewed publications

In this chapter, a detailed description of the synthesis and optical characterization of lead sulfide quantum dots is introduced. Additionally, this chapter covers an integration and optimization project called: Bandgap engineering employing MWCNT in a TiO_2 sol-gel matrix in quantum dot sensitized photovoltaic devices. The purpose of this work was to better understand the properties and the role that of TiO_2 inside photovoltaic devices when it operates as a transport/barrier layer. It amied to explore the possibility of band-engineering to improve the operation of QD-sensitize solar cells made of lead-sulfide (PbS) nanocrystals. Once an operational device was obtained I ventured to improve the fill factor of the solar cell by creating sub-bandgap states inside the TiO_2 matrix by doping it with graphene, based on the results obtained in DSSC's where the introduction of carbon nanostructures improved charge collection on a photovoltaic device (Benetti *et al.*, 2016; Kim *et al.*, 2016). Graphene is a material that exhibits a favorable band-alignment for the device under analysis and indeed, improved the charge collection and thus, the fill factor and the efficiency of the cell. The experience gained in QD synthesis and characterization, and the obtained results were essential contributions in three peer-reviewed articles where the development PbS QD-based optoelectronic devices, show how these versatile nanocrystals can be readily integrated (Xu *et al.* (2015); Ka, Gerlein, M. Asuo, Nechache & Cloutier (2018); Ka *et al.* (2020)).

0.3.2 Industrial project: Study of optoelectronic properties of commercial graphene flakes for the formulation of screen printing inks

This work was done as part of a joint venture between ETS and and the company Carbosphere®. Thanks to the experience and understanding that I have acquired as part of the printed

electronics team in the NOMAD group, it was relevant for me to participate in this project, given the importance of graphene materials in the world of printed electronics. This project aimed to study the practical application of their graphene products as an additive or, as a base material in the formulation of screen printing inks. Indeed, the production methods employed at Carbosphere have enabled the synthesis of defect-rich, multi-layered graphene flakes at 5-10 times lower cost[2] compared to other commercial alternatives, depending on the desired quality characteristics. This material already proved useful in the creation of anti-corrosion coatings with conductive and self-healing properties (Benavides-Guerrero, Banerjee, Gedamu, Gerlein & Cloutier, 2022a). As such, the interest was to extend its application in high-performance screen printing inks for electrodes and devices.

This project was divided in two approaches: First, *metal-ink approach* whose aim was to improve state-of-the-art silver-based screen printing inks by adding Carbosphere's graphene flakes. Second, the *carbon-ink approach*, aimed to create, from scratch, a graphene-based screen printing ink. This required us to study its compatibility with the printing vehicle SOL725 provided by Henkel. To achieve both goals, two main aspects needed to be understood about Carbosphere's graphene: first, what is the layer composition of the graphene flakes delivered. For this analysis, confocal Raman spectroscopy and SEM imaging were the tools used for characterization. Second, how the graphene-based inks performed electrically and mechanically when applied as a screen printed ink in PET substrates. For this part, samples were fabricated using formulations made with different concentrations and additives, to test the electrical performance of the inks using stencil and screen printing masks.

0.4 Thesis organization

The contents of the upcoming chapters presented in this thesis are summarized as follows:

[2] Value estimation provided directly by Carbosphere

- CHAPTER 1 presents a background on the most important concepts that are related to the topics presented in the peer-reviewed publications. The topics covered include an explanation on the mechanisms that enable photonic curing of materials. An overview of metal-oxides and the role of TiO_2 in applications for optoelectronic devices, including light-induced, large-area crystallization of TiO_2. Additionally, theory about transparent conductive electrodes, characterization and processing of thin films of silver nanowires is also covered.
- CHAPTER 2 presents a review of nanocrystals as well as it's importance in optoelectronic devices. Particularly, lead-sulfide (PbS) photovoltaic devices and common amelioration techniques employed in increasing performance in TiO_2-based platforms. Finally, a short primer in graphene along a general description of the Raman spectroscopy used to complete the project with commercial graphene flakes for its application in screen printed inks.
- CHAPTER 3 is the published manuscript submitted to Advanced Engineering Materials called "Laser-Assisted, Large-Area Selective Crystallization and Patterning of Titanium Dioxide Polymorphs".
- CHAPTER 4 is the published manuscript submitted to Scientific Reports called "High-performance silver nanowires transparent conductive electrodes fabricated using manufacturing-ready high-speed photonic sinterization solutions".
- CHAPTER 5 is the manuscript submitted to the journal RSC Advances titled "Photonic sintering of a multi-material transparent conductive electrode architecture for optoelectronic device integration" that currently undergoes revision.
- CHAPTER 6 describes the work done with lead sulfide quantum dots for applications in photovoltaic devices, including detailed descriptions of the synthesis and QD properties, and its application in designing and optimizing a QD sensitized solar cell. The research project presented, aimed to enhance the fill-factor of a solar cell made of PbS quantum

dots and TiO_2 by adding graphene to create sub-bandgap states that improved the charge collection and as a result, the fill factor doubled. Finally, a summary of my contributions to peer-reviewed articles based on the work done with this nanocrystals.

- CHAPTER 7 describes the procedures, results and conclusions obtained during the project with the commercial graphene flakes for their application as a screen printing inks.
- Finally, this thesis ends with a conclusion and recommendations chapter. In there, I discuss the scientific contributions of my work, their continuity avenues and prospects of my PhD. After, a comprehensive list of the publications where I have participated.

CHAPTER 1

LITERATURE REVIEW

1.1 Processing of materials with intense pulsed light from a Xenon flash lamp

Whether it is called intense pulsed-light sintering, flash-light processing, photonic curing (PC) or sintering, all of these terms refer to the treatment of materials by means of exposure to a high energy, short flash of unpolarized, white light coming from an xenon lamp[1](Kinney & Tompkins, 1969). This form of material processing leads to expeditious, high throughput, cost saving, high temperature thermal processing of thin films made from a variety of materials, deposited on flexible polymers such as PET, PEN or Kapton (polyimide), paper and fabrics (Im *et al.*, 2021). These short pulses of light, in the range of tenths of microseconds to milliseconds, can be tailored to deliver specific amounts of energy density by varying the charging voltage, the speed of discharge to which the lamp is subjected and the modulation of the emitted pulse, carefully influencing the material's response to the pulsed light (Akhavan, Schroder, Pope & Farnsworth, 2013). This flexibility allows to dry, sinter, anneal, crystallize, polymerize and modulate chemical reactions, hence the variety of names for such technique (Schroder, Rawson, Pope & Farnsworth, 2011). Optimization of processing parameters have enabled researchers and industry alike, to fully demonstrate the potential of this technique: printed electronic circuits whose conductive paths are completely photonically sintered (Kamyshny, Steinke & Magdassi, 2011; Schroder *et al.*, 2011; Serpelloni, Cantù, Borghetti & Sardini, 2020), fabrication photovoltaic cells in which the transport layer, the active material, or both, are photonic cured (Das *et al.*, 2015; Xu, Piper, Daunis, Schroder & Hsu, 2020; Piper, Daunis, Xu, Schroder & Hsu, 2021); nanostructure-based precursors for the fabrication of transparent conductive films (Kim, Chikamatsu, Azumi, Saito & Minami, 2013; Gerlein *et al.*, 2021; Gilshtein, Tacneng, Bolat, Torres Sevilla & Romanyuk, 2021) and also, smart IoT sensors, capable of measuring their environment while being able communicate with other

[1] For the purpose of this document, the terms *photonic curing or sintering* will be used interchangeably when referring to the processing parameters and characteristics

devices(Borghetti, Cantù, Sardini & Serpelloni, 2020), are amongst the many applications that greatly benefited of employing photonic processing in the fabrication of low-cost devices.

The most common source of light for photonic processing is an inert, sealed xenon flash lamp designed to produce non-coherent, high intensity, full spectrum pulses of white light via voltaic-arc discharge. Ionized xenon gas converts electrical energy to light with around 50% efficiency, making it the most efficient gas for light emission in the visible range (Oliver & Barnes, 1969). The emission spectrum lies between 200 and 1100 nm, where the visible portion accounts for >60% and the UV and IR regions between 20-40% of the whole spectrum, as shown in the Figure 1.1(a) where a single 200µs pulse is shown when the lamp has been charged a different voltages.

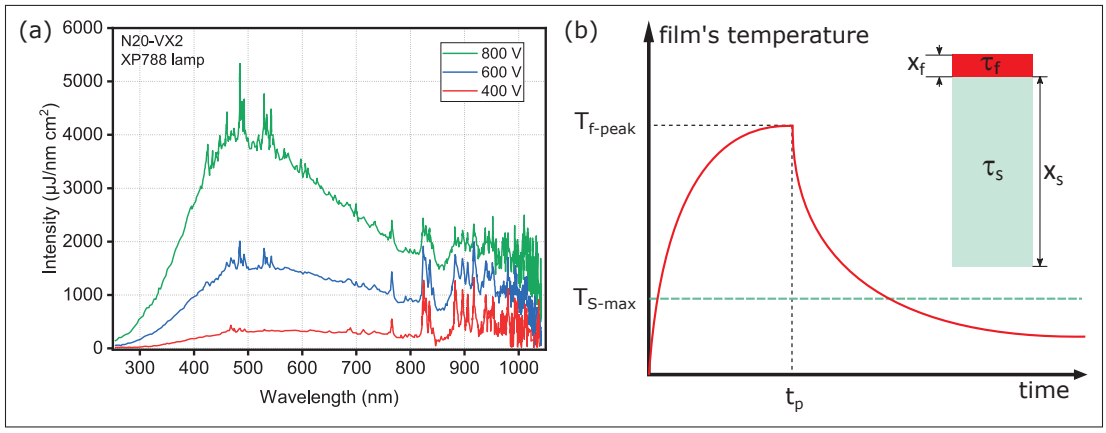

Figure 1.1 (a) Optical spectrum emitted from a Xenon lamp, data by Novacentrix (b) Transient mechanisms of photonic curing. *Inset:* Representation of a thin film on a substrate
(b) Adapted from Schroder (2011)

A more in-depth analysis of the dynamics of photonic curing on the processing of a thin film of material is depicted in Figure 1.1(b), where *T* is temperature, *t* is time, *x* is thickness, *S* is substrate, *f* is film and *p* for pulse. Starting with a thin film deposited atop the substrate, both with thermal equilibration times τ_f and τ_s, illustrated in the inset schematic of Figure 1.1(b). The thermal equilibration time is defined as a function of the following coefficients: c_p the specific heat capacity [$J.K^{-1}.kg^{-1}$], ρ the volumetric density [$Kg.m^{-3}$], κ the thermal

conductivity [$W.m^{-1}.K^{-1}$] and the film/substrate thickness x_i, which are all related in equation 1.1 (Wikipedia, 2021, 2022).

$$\tau_i = \frac{c_i \rho_i x_i^2}{4\kappa_i} \tag{1.1}$$

In the transient plot of Figure 1.1(b), heating of the film induced by the absorption of the pulsed-light is represented with the continuous red line. This heating will continue for the duration of the pulse, t_p, reaching a maximum temperature shown as $T_{\text{f-peak}}$. This value can be much higher than the substrate's melting temperature, $T_{\text{S-max}}$, represented by the light green dashed line. Thereafter, the film rapidly cools down by siphoning excess heat back into the substrate.

The behavior described above is possible when three conditions correlating the film and substrate's characteristics are met to yield optimal photonic treatment results (Schroder, 2011). First, the film must be much thinner than the substrate (equation 1.2) so that the thermal mass of the substrate helps cool down the film via conduction. Second, the pulse duration must be much shorter than the thermal equilibration time of the substrate (equation 1.3), meaning that the heating happens faster than the substrate's ability to warm up. Finally, the thermal equilibration time of the film must be shorter than that of the pulse duration (equation 1.4), meaning that a short pulse must be enough to heat and process the film.

$$x_f << x_s \tag{1.2}$$

$$t_p << \tau_s \tag{1.3}$$

$$\tau_f << t_p \tag{1.4}$$

Indeed, photonic curing reconciles working with heat-sensitive substrates with high-temperature, material thermal processing, enabling manufacturing of flexible devices on a wide variety of

low-cost substrates. As explained elsewhere, there are three mechanisms that apply during fast photonic processing of different types of materials (Luo *et al.*, 2017):

1. *High absorptivity and low thermal dissipation*: For one-dimensional nanomaterials, they quickly absorb the arriving energy from a pulsed-light source of emission but, they are very slow in transferring this energy to their surroundings, which translates into almost instantaneous heating
2. *UV induced polymerization*: In polymer films, this means UV-induced cross-linking and treatment
3. *Rapid internal heating*: For materials with high attenuation of light such as metals and inorganic non-metals, internal heating will be the result of large optical-to-heat conversion rates and the photo-decomposition of precursors that gives way to crystallization processes, e.g. metal-oxides

For example, in metallic nanoparticles, surface plasmon resonance in the visible range of the spectrum is responsible for the fast and localized heating, thanks to the increased absorption of light, that results in the subsequent sintering and treatment of films (Jang *et al.*, 2020). At the same time, their poor thermal conductivity is what prevents the absorbed energy to be fully transferred into the substrate or other thermal sensitive materials. This means that as long as the light pulse duration is shorter than the time it takes to reach thermal equilibrium between the film and the substrate, sintering of nanoparticles is possible.

1.2 Semiconducting metal-oxide materials in optoelectronics

In general, oxides are one of the most abundant and stable compounds on earth. Their study and subsequent use have, inescapably, played an integral part in humanity's technological advance, ranging all the way from medicine, construction to microelectronics (Palneedi *et al.*, 2018). This widespread use originates, in part, from how easily oxygen forms bonds (electronegativity of 3.44) by strongly attracting electrons from almost any other element. Semiconductor metal oxides (SMOs) are commonly present in optoelectronic devices, operating in a wide range of roles such as insulators, semiconductors and trans-

port/blocking layers. This is possible thanks to their versatility, chemical stability, and compatibility with a large array of materials and rigid, flexible and semitransparent substrates (Scheideler & Subramanian, 2019; Piper *et al.*, 2021; Daunis *et al.*, 2020). Also, most SMOs do not react with water and other common solvents, making them great candidates for outdoor applications. Their synthesis routes usually require simple steps, are low-cost, highly scalable and lifetime stable (Chang & Waclawik, 2014). Additionally, SMOs have been found to perform in other areas such as resistive memory devices, transistors, photocatalysis, water treatment, and gas sensing applications (Stathopoulos *et al.*, 2017; Scheideler & Subramanian, 2019; Xiao, Yang, E & Li, 2023; Yu *et al.*, 2023; Huang *et al.*, 2021b; Garzella, Comini, Tempesti, Frigeri & Sberveglieri, 2000; Chahrour, Yam & Eid, 2020; Wong, Abuzalat, Mostafa, Kim & Park, 2019). As wide bandgap semiconductors, many intrinsic SMOs exhibit poor electrical conductivity, a property that can be tuned by means of doping to a degenerate state turning SMOs into oxide transparent conductive electrodes (TCE), integral parts in optoelectronic devices. Such is the case of tin-doped indium oxide (In_2O_3:Sn), otherwise known as ITO; other examples are aluminium-doped zinc oxide (AZO, ZnO:Al) and fluorine-doped tin oxide (FTO, SnO_2:F). For example, in vertically layered photovoltaic devices, at least one of the electrodes must be a TCE that allows the light to reach the active area of the device and trigger the generation of electron-hole pairs that will be separated and collected with the help of transport/blocking layers, which can also be made of thin layers of MO materials (Fortunato, Ginley, Hosono & Paine, 2007; Delahoy & Guo, 2010).

1.2.1 The role of TiO_2 in optoelectronic applications

One SMO stands out for its diverse properties, versatility, stability and wide range of applications depending upon its polymorphism (Bai & Zhou, 2014; Bai, Mora-Seró, De Angelis, Bisquert & Wang, 2014). Titanium dioxide (TiO_2), or Titania, can be found in various crystalline forms, where anatase and rutile are the most commonly known. As a wide bandgap material (3.2 eV) it has been employed as a UV absorber in photodetectors as well as in dye-sensitized

solar cells (DSSC), although the UV portion of the solar spectrum only constitutes about 5% (Ullattil, Narendranath, Pillai & Periyat, 2018; Banerjee, Asuo, Pignolet, Nechache & Cloutier, 2020; Chen, Retamal, Lien, He & Liao, 2015). Combining TiO_2 with other narrow bandgap MOs such as copper(I) oxide (Cu_2O) and iron oxide (FeO) helps expand its operation in the visible range of the spectrum (Yuhas & Yang, 2009; Rühle *et al.*, 2012; Pavan *et al.*, 2015).

Being a transition metal oxide, TiO_2 works well as an electron transport material (ETM) showing improved electron mobility in conventional layered solar cells (Lira-Cantu & Krebs, 2006). In n-i-p devices, TiO_2 is found interfacing the transparent electrode and the inner active material layers (Vaenas, Konios, Stergiopoulos & Kymakis, 2015; Mali & Hong, 2016), where *n* refers to the electron transport layer, *i* refers to the intrinsic absorber and *p* refers to the hole transport layer. Similarly, dye-sensitized solar cells (DSSC) is a configuration where a thin film layer of textured TiO_2 atop a transparent conductive electrode, usually a doped metal oxide, is coated with an organic dye absorber, promoting intimate contact and efficient charge carrier separation at the interface between the dye and the TiO_2 (O'Regan & Grätzel, 1991; Chiba *et al.*, 2006; Roose, Pathak & Steiner, 2015). Nanostructured solar cells, derive their name from the fact that one or both blocking layers are nanostructured: whether is nanoparticles, nanorods, or any other nanoscopic-sized entity made of TiO_2 (Benetti *et al.*, 2016; Xu, Benavides, Ma & Cloutier, 2012; Zhang *et al.*, 2018). Mesoscopic solar cells where a layer of TiO_2 nanoparticles are deposited atop a TCE, are commonly found in halide perovskite solar cells and quantum dot sensitized solar cells (Kojima, Teshima, Shirai & Miyasaka, 2009; Vaenas *et al.*, 2015; Ju *et al.*, 2010; Im, Lee, Lee, Park & Park, 2011; Lee, Ryu, Lee & Yim, 2018). In depleted heterojunction solar cells, the band alignment plays a definite role in creating a strong electric field that will help break the photo-generated excitons that reach the interface between the active material and the transport/blocking layers (Pattantyus-Abraham *et al.*, 2010; Ding *et al.*, 2014, 2016).

As a wide bandgap semiconductor, 3.2 eV, thin film layers of TiO_2 favorably fit a wide variety of devices whose bandgap aligns in such way that electrons are easily transported towards the TCE by the TiO_2 layer, while effectively blocking the free holes when acting as

a electrically high-barrier to overcome (Ju *et al.*, 2010; Kontos *et al.*, 2011; Vaenas *et al.*, 2015; Banerjee, Benavides, Guo & Cloutier, 2018). Better electronic properties for TiO_2 have been achieved when doped with compatible carbon nanostructures that introduce sub-gap states that increase their electron transport while maintaining the advantageous compatibility previously described (Dembele *et al.*, 2013; Taleshi, 2015; Latif *et al.*, 2020; Wong *et al.*, 2019).

In other optoelectronic applications, again the chemical stability, low-cost of fabrication and non-toxicity of MOs and in particular, that of TiO_2, have made it a preferred constituent material (Li, Huang, Zheng & Zheng, 2020). In industrial, military and aerospace applications, UV photodetectors are required to perform in difficult and likely, elevated temperature conditions (Alaie, Mohammad Nejad & Yousefi, 2015). High performance photodetectors have been fabricated taking advantage of the compatibility of thin film TiO_2 with very simple architectures (Banerjee *et al.*, 2020). High-responsive nanostructured TiO_2based photo-diodes take advantage of its wide bandgap for UV and visible detection (Selman & Hassan, 2015; Cao *et al.*, 2011; Zou, Zhang, Huang & Marzari, 2010). In similar fashion, nanorod-based field electron emission (FE) devices made of TiO_2 exploit the nanorods' periodicity, geometry and proximity, and are of great commercial interest for applications in displays, X-ray sources and microwaves emission (Wu, Shih & Wu, 2005; Li *et al.*, 2009b; Zhai *et al.*, 2011b). Finally, thin films of TiO_2 have been widely used as coatings in dielectric mirrors (Meng, Huang, Liu, Zeng & Bu, 2012; zhang, Liu, Gan & Cui, 2017).

1.2.2 Large-area, light-induced crystallization of TiO_2

Optoelectronic devices made with TiO_2 use a crystalline version of this material that possess those desired optical and electrical properties, whether it is anatase or rutile. Therefore, it is beneficial for their production that an amorphous TiO_2 precursor exists that can be crystallized using the least amount of energy, facilitating their upscale fabrication. Ideally, handling of this precursor should take place at room temperature, without the need of specialized atmospheric conditions or the inclusion of additional chemical triggers to achieve

crystallization. Exploration of laser-induced crystallization of TiO_2 has been a subject of intense research as of late, starting with high intensity UV laser sources and later, moving onto the visible range (Nakajima, Shinoda & Tsuchiya, 2014; Palneedi *et al.*, 2018; Benavides *et al.*, 2018; Gerlein *et al.*, 2019; Siuzdak, Haryński, Wawrzyniak & Grochowska, 2020; Benavides-Guerrero *et al.*, 2022b). It has been shown that optimization of chemical routes, addition of dopants or controlled atmospheric conditions facilitate the crystallization of TiO_2 precursors using optical sources. Indeed, it is now possible to completely crystallize large-area thin films of TiO_2 into a single phase, a spatial combination of anatase and rutile, or a mixed transient phase that exhibits features of both phases in the same sample, using laser green or low-cost blue-purple (Benavides *et al.*, 2018; Gerlein *et al.*, 2019; Benavides-Guerrero *et al.*, 2022b) sources in the visible range under regular atmospheric conditions.

Photonic-driven crystallization of photosensitive metal-oxide precursors is an active area of research that directly benefits the development of new generation of printed, flexible, optoelectronic devices (Das *et al.*, 2016; Zhu *et al.*, 2017). Recently, amorphous organo-metallic thin-films of TiO_2 were found to be photosensitive and exhibited crystallization into rutile while participating in the photocatalytic oxidation of methylene blue (Krylova & Na, 2015). Activation of the crystalline phase took place after *continuous* irradiation from a Xenon lamp during one hour. Similarly, the partial transition from anatase to rutile in TiO_2 nanoparticles has been demonstrated using intese pulses of light, however, this effect was possible because of the presence of metallic atoms and carbon nanostructures in the device (Wong *et al.*, 2019). It has been reported that perovskite solar cells whose electron transport layer (ETL) is made of photonically cured TiO_2 exhibit similar performance to those made with oven crystallized TiO_2 ETLs on glass substrates (Das *et al.*, 2016; Feleki, Bex, Andriessen, Galagan & Di Giacomo, 2017).

Luo et *al.* reported the crystallization of amorphous thin films done under atmospheric conditions but with no control over the dominant crystalline phase, using intense, short pulses of light using a Xenon flashlamp (Luo *et al.*, 2017). In that case, a large number of pulses (200), were necessary to achieve a dendrite-nanostructured TiO_2 film with large

surface area. The photo-initiated decomposition of organo-metallic precursors, followed by the oxidation and crystallization of the metal component was be explained by two factors: first, while TiO_2 thin films show poor visible light attenuation, generation of hot electrons is attributed to absorption of light under the 300nm wavelength. Additionally, the photogenerated electrons and holes recombined non-radiatively inside the thin film, generating additional heat that provides enough energy to trigger the phase transition (Krylova & Na, 2015). As a consequence, the film's temperature increased almost instantaneously. The second fact becomes evident when framed around the material properties: the internal heat cannot be efficiently dissipated thanks to the ceramic nature of the titania films with low thermal conductivity (Luo *et al.*, 2017). These results highlight the potential compatibility of photonic sintering of TiO_2 with roll-to-roll fabrication systems.

1.3 Transparent conductive electrodes for optoelectronic devices

By definition, an optoelectronic device is an optical-to-electrical or electrical-to-optical transducer. This means that light has to have a way to enter the device to interact with it, or to leave it as the product of some electrically triggered phenomenon. Depending on the physical configuration and operation of said device, the presence of a transparent conductive electrode (TCE) for the light to pass through, might be necessary. These electrodes must be optically transparent while, at the same time, conduct the electricity that is either generated by light-matter interactions or, consumed in the process of producing light. For devices such as organic light emitting devices (OLED), liquid crystal displays (LCD), touch panels, photovoltaic devices and photosensors, TCEs are an integral component for their correct operation. With all TCEs, the most important parameters for optimization are a trade-off, presented in Figure 1.2(a), that exists between optical transparency and electrical conductivity: highly transparent electrodes are achieved in detriment of the TCE's conductivity and vice versa.

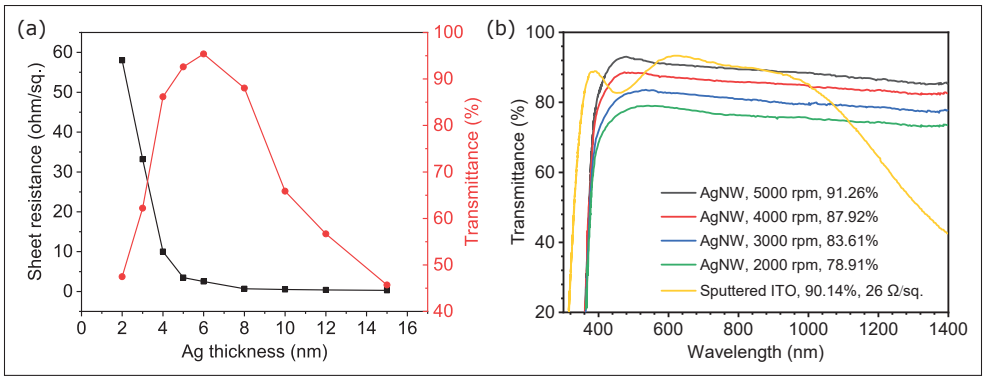

Figure 1.2 Properties of TCEs (a) Dependence between film thickness, sheet resistance and transmittance (b) UV-VIS-IR transmittance for AgNWs and ITO
(a) adapted from Sahu *et al.* (2006), (b) adapted from Liu *et al.* (2018)

Doped metal-oxides such ITO, FTO and AZO, are widely known for their performance in the visible range, and are common platforms used in touch screens, solar cells and photodetectors. Their optical-to-electrical characteristics mostly depend on the thickness of the layer applied where thicker films improve conductivity while sacrificing the optical transparency. However, they come at a high production price, particularly due to the high vacuum process required to deposit a highly-uniform thin film via sputtering deposition. Furthermore, their brittle, ceramic nature limits their use to rigid applications.

Metal-free TCE's are an emerging line of research, with crystalline carbon allotrope nanostructures leading the way (Iijima & Ichihashi, 1993; Novoselov *et al.*, 2005). When free of defects, graphene and metallic carbon nanotubes (CNT) are highly conductive, stable, and mechanically strong materials that offer high optical transparency in the visible range of the spectrum, thanks to their single atomic layer structure. These are important candidates for stretchable optoelectronic applications (Siwal, Saini, Rarotra, Zhang & Thakur, 2021; Ren *et al.*, 2021). However, there are shortcomings that need further work: in the case of CNTs, the high resistance present at the junction of neighbouring nanotubes makes thin films effectively less conductive than ITO films (Hirotani & Ohno, 2019). Additionally, the problem

remains in the high production costs associated in producing large scale of high quality yields (Siwal *et al.*, 2021).

In contrast, metallic nanostructures can be solution processed and fabrication of TCE's can be mass produced. They possess the electrical characteristics close to those of their bulk counterparts, can be malleable, stretchable and at the nanometer size, percolated networks offer high transparency comparable to those offered by doped MOs as can be seen in Figure 1.2(b).

1.3.1 Silver nanowires TCEs

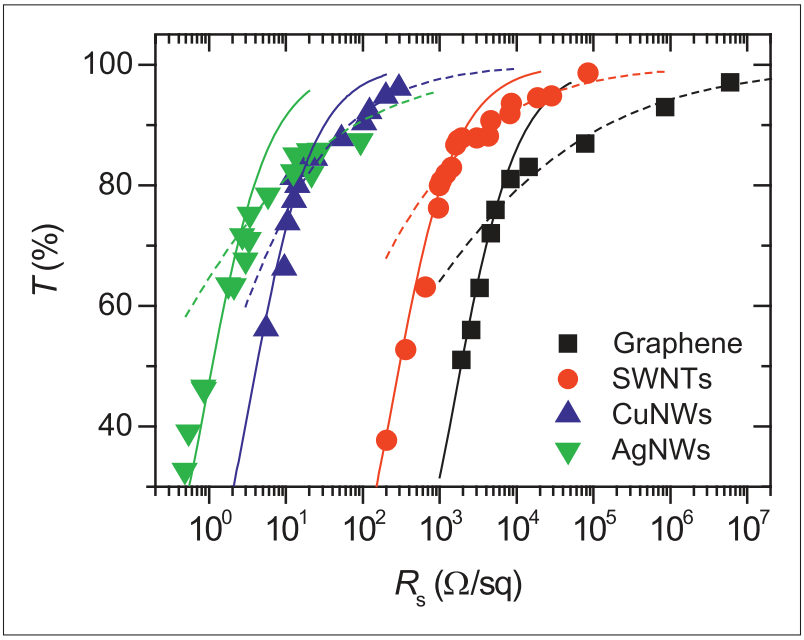

Figure 1.3 Comparison of metallic and inorganic nanostructures for TCEs
Taken from De & Coleman (2011)

The fabrication of metallic, transparent, and conductive electrodes has been revolutionized by advancements in nanotechnology. Silver stands out as a highly conductive metal but it is not cost-effective on a macroscopic scale. However, at the nanoscale, the required quantity for creating transparent conductive electrodes (TCEs) is sufficiently small, resulting in a total production cost that remains competitive with other materials, such as metal oxides (MOs)

or inorganic nanomaterials, while delivering comparable or superior performance. Shown in Figure 1.3, the transmittance versus the sheet resistance for different metallic nanowires such as copper nanowires (CuNWs), silver nanowires (AgNWs) and carbon nanostructures such as graphene and single wall carbon nanotubes (SWNTs). Not only silver nanowires (AgNWs) offer competitive transparency and conductivity in comparison to traditional MOs transparent electrodes, but they display better ultraviolet and near-infrared transmittance as shown in Figure 1.2(b). As can be seen, ITO starts incrementing exponentially its absorption of light beyond 1000 nm, limiting applications for sensors that operate in the IR and telecommunication wavelengths. Production of metallic nanowires is done in solution under ambient conditions (Tokuno *et al.*, 2011; Li, Wang & Yan, 2011; Madeira, 2018). This, makes them compatible with coating techniques that meet the demands for large-area, high deposition speed and high quality of films, aiming to form a random and continuous conductive mesh of interconnected nanostructures (Sepulveda-Mora & Cloutier, 2012; Gerlein *et al.*, 2021). Highly transparent networks of silver nanowires have been widely used in photovoltaics, photodetectors, sensors (pressure, biocompatible), antennas, etc (Min *et al.*, 2017; Aurang, Doganay, Bek, Turan & Unalan, 2017; Yi, Zhu & Deng, 2018).

The conductivity of the mesh can be improved by sintering and/or, pressing togehter the nanowires at their junction points, maintaining it's optical properties and improving on the mechanical characteristics, with the possibility to obtain optical transmittance of 90% for a sheet resistance of 10 Ω/sq. (Hosseinzadeh Khaligh & Goldthorpe, 2014; Aurang *et al.*, 2017; Gerlein *et al.*, 2021). These characteristics can also be manipulated following the rule-of-thumb for TCEs: more conductivity is obtained sacrificing optical transmittance. Indeed, when more conductive films are required, denser films of nanowires rapidly boost conductivity, incrementing the paths for electrons to travel. Oven sintering is the main route to process AgNW thin films for various applications, achieving high conductivity and reproducible performance. This however, limits the applications of TCEs to rigid substrates and compatibility with materials that can withstand the processing temperatures, around 250 °C.

CHAPTER 2

LITERATURE REVIEW FOR THE ADDITIONAL PROJECTS

2.1 The importance of nanocrystals

Figure 2.1 The famous Lycurgus cup
The British Museum CC BY-NC-SA 4.0

Nanoparticles lay at a intermediate size regime, being larger than single atoms or molecules species but much smaller than common bulk solid objects. These are the most fundamental component utilized in the fabrication of nanostructures and their optical, electrical and magnetic properties greatly depend on their dimensions (Murray, Kagan & Bawendi, 2000). For example, gold nanoparticles around 20 nm exhibit a wine red color and silver nanoparticles are yellowish-gray (Rao, Kulkarni, Thomas & Edwards, 2000) and these characteristics can create beautiful effects like the famous Lycurgus cup shown in Figure 2.1, where regular opaque green color turns red when the cup is illuminated from inside thanks to the combination of gold and silver ~70 nm nanoparticles inside the dichroic glass composition.

Synthesis of very small particles far beyond from what's normally perceptible, has happened since ancient times. Generally, there are two general approaches to the preparation of nanomaterials: the top-down breakdown method where external forces act upon solids to

fracture them into ever smaller pieces. The bottom-up approach starts from materials in gas or liquid form and the particles build-up as the result of a chemical reaction. At the nanoscale, being able to control the physical size of materials allows to finely tune the material's properties.

The study of monodispersed, nanometer-sized crystals, otherwise known as nanocrystals (NCs) synthesized in colloidal solutions dates back to the 1980's when scientists from Bell labs, MIT and other research centers realized that these structures displayed the atomic arrangement of bulk solid materials, but their optical and electronic properties of nanoparticles developed slowly as their size changed (Rossetti & Brus, 1982; Rossetti, Nakahara & Brus, 1983; Ramsden & Grätzel, 1984; Kubo, Kawabata & Kobayashi, 1984; Steigerwald *et al.*, 1988; Steigerwald & Brus, 1990; Murray, Norris & Bawendi, 1993; Murray *et al.*, 2000).

Quantum confinement in all three dimensions is the result of effectively reducing the size of the crystalline particles smaller than the bulk exciton's Bohr radius (Brus, 1984). In semiconductors, excitons are electron-hole pairs electrostatically linked by Coulomb forces, that are de-localized in space. This electrostatic link depends on the distance separation and is known as the Bohr radius (as an analogy between Bohr's hydrogen atomic model and an excited electron inside a semiconductor), and it's a material-dependent property. In bulk semiconductors, this radius is much smaller than the crystal lattice distance and the effect of confinement is negligible. In contrast, the lattice in nanocrystals is smaller than the Bohr radius and the exciton's energy is affected by quantum confinement, the density of states separates in discrete energy levels and the bandgap of the material not only becomes size-dependent (Rogach, Eychmüller, Hickey & Kershaw, 2007), but is also larger than its bulk counterpart and thus, the light absorption/emission properties of nanocrystals are also dependent on the particle size. Incidentally, the more familiar absorption bands present in bulk materials are developed as the crystallite size increases beyond the Bohr radius limit (Bawendi, Steigerwald & Brus, 1990).

2.1.1 Optoelectronic applications of nanocrystals

Colloidal synthesis of nanocrystals is a bottom-up approach that takes place inside a heated dispersion medium (typically between 150-300°C), a coordinating solvent, where the nanocrystals start forming in a nucleation reaction: a condensation process where molecules or ions aggregate, following the rapid injection of an metal-organic precursor. The rate of growth is controlled by the coordinating solvent's temperature at the moment of injection as well as the growth time allotted after the initial nucleation takes place (Bose *et al.*, 2008; Zhang *et al.*, 2015; Giansante *et al.*, 2015), yielding a colloidal dispersion of quantum dots of relatively monodispersed diameter. Optical characterization of the resulting colloidal dots such as photoluminescence and absorption spectroscopy deliver accurate information about the size, polydispersity, optical bandgap and concentration of the quantum dots reaction (Baskoutas & Terzis, 2006). Additionally, the hot-injection synthesis yields neutrally-charged nanocrystals surrounded by long chain molecules, whose high steric hindrance supply enough van der Waals repulsive force to keep closing nanocrystals apart, by generating osmotic pressure between them (Wu & Ning, 2023). As a result, the colloidal QDs will stay well dispersed when they are in solution. Indeed, the robust surface passivation of the QDs by the oleic acid ligands makes them highly stable and less labile. In contrast, highly labile QDs result in degradation or reactivity with the solvents, a factor that leads to poor dispersion (Cao, Stavrinadis, Lasanta, So & Konstantatos, 2016).

Similar to the role atoms and molecules play as the building blocks of condensed matter, nanocrystals also play this role when assembled in closely packed solids. The narrow distribution of shape, size, surface chemistry and internal structure enables the deposition of nanocrystals in compact, glass-like, ordered assemblies whose properties remain, in principle, dictated by those of the single particles but, at the same time, new or enhanced collective properties arise from the creation of these so-called *quantum dot solids* (Giansante *et al.*, 2015; Wang *et al.*, 2016; Brown *et al.*, 2014; Borriello *et al.*, 2015). While optical absorption and emission are dictated by the nanocrystallite size, electrical properties such as charge transport ability in QD solids are controlled with the help of chemical ligands that

bring the quantum dots ever closer (Murray *et al.*, 2000; Xu *et al.*, 2015; Borriello *et al.*, 2015). Thus, the overall optoelectronic properties of the solid can be tuned to boost for example, the film's conductivity or transparency, which will have a direct impact in the performance of devices built around them.

2.1.2 Lead-sulfide nanocrystals and quantum dot-based photovoltaic devices

In the periodic table, chalcogens can be found in the group 16 (VI-A) where the non-metals elements Oxygen (O), Sulphur (S), Selenium (Se) and the semi-metals Tellurium (Te) and Polonium (Po) lie. In particular, S, Se and Te are of interest in the synthesis of colloidal, semiconductor, metal-chalcogenides (MeCh) nanoparticles such as CdS, ZnS, PbS, CdTe and CdSe, whose size dependent photo-emission (See Figure 2.2) and absorption, as well as their quantum confinement effects are especially attractive in photovoltaic and optoelectronic sensing devices (Bawendi *et al.*, 1990; Steigerwald & Brus, 1990; Joo *et al.*, 2003). These MeCh QDs display narrow and stable light absorption and emission bands, and the devices exhibit high quantum yield (Hinds *et al.*, 2007; Moreels *et al.*, 2009, 2011; Ma, Xu, Benavides & Cloutier, 2012). Additionally, these MeCh QDs have proven useful in biology and medicine for imaging, sensing and fluorescent bio-labeling (Park *et al.*, 2011; Ma *et al.*, 2014; Oluwafemi, Sakho, Parani & Lebepe, 2021).

Semiconductor nanostructures such as lead-chalcogenides colloidal quantum-dots (QDs) which are synthesized through simple chemical routes (Murray *et al.*, 1993; Zhang *et al.*, 2015), are a compelling alternative for the development of solution processed, thin-film, large-area, low-cost, air-stable and potentially flexible depleted-heterojunction quantum dot sensitized solar cells (Pattantyus-Abraham *et al.*, 2010; Ju *et al.*, 2010). Closely packed films of quantum dots function as the active area of these photovoltaic devices. In here, the film's packing density is determined by the binding molecule that enables the overlapping of electron wave functions in nearly adjacent QDs, facilitating the subsequent dissociation of excitons that translates in the transport of charge carriers (Choi *et al.*, 2010b; Rekemeyer, Chuang, Bawendi & Gradečak, 2017; Xu *et al.*, 2015).

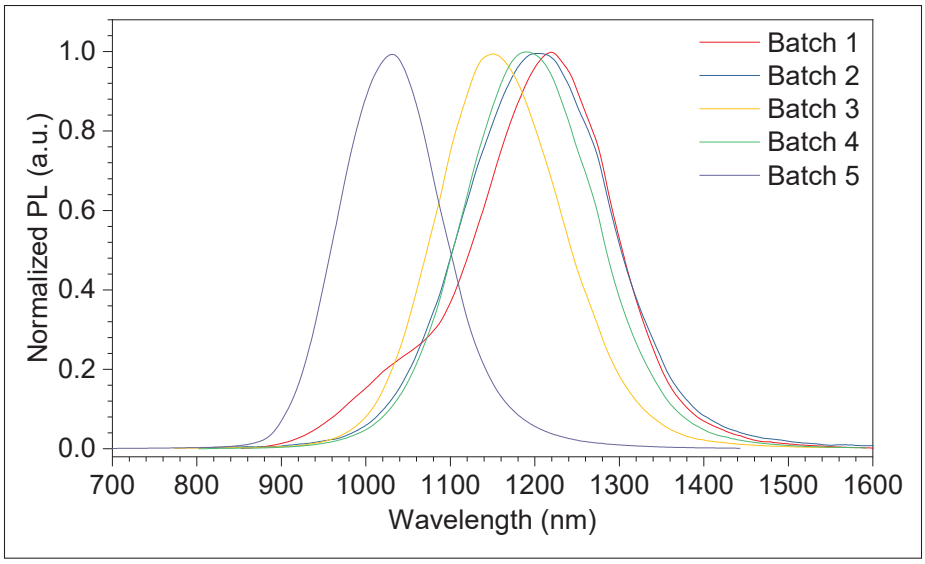

Figure 2.2 Photoluminescence of various size of PbS QDs produced in the laboratory

Lead-based chalcogenide semiconductors are major players in the production of optoelectronic devices that take advantage of the infra-red regime such as solar cells, photodetectors, light sources, lasers, and thermoelectric. In PbS, the effective mass of the electrons and holes are small and relatively similar, $0.085 \cdot m_0$, and the Bohr radius (a_B) is very large, 20 nm (Wise, 2000; Nanda, Kruis, Fissan & Behera, 2004; Rogach *et al.*, 2007). Since the crystallite's size is smaller to that of the exciton Bohr radius of the bulk material, $R \ll a_B$, quantum confinement is possible (Wise (2000)). Furthermore, in PbS, this large Bohr radius indicates stronger quantum confinement compared to similarly-sized quantum dots fabricated with other II-VI or III-V materials; these, in turn, also show asymmetric Bohr radii for holes and electrons; for example, in CdSe quantum dots, the exciton Bohr radius a_B is ~6 nm. On the other hand, in PbS QDs, the Bohr radii for both excitons are very similar, indicating strong confinement for both types carriers. (Peterson & Krauss (2006)).

PbS QDs exhibit high quantum efficiency and offer the possibility of tuning their emission/absorption across the infrared region, as shown in Figure 2.2, where the effect of changing various synthesis parameters is presented (Zhang *et al.*, 2015). These variations lsited in Table **??**. This is especially useful in designing photovoltaic devices (Sargent, 2012) that fall

Table 2.1 Variation of synthesis parameters to produce Batches 1-5

Batch	Oleic acid (g)	Octadecene (g)	HMDS (µl)	Hot injection (°C)
Batch 1	1.34	13.156	105	120
Batch 2	1.34	13.156	105	120
Batch 3	2.67	14	105	120
Batch 4	2.67	14	210	100
Batch 5	2.67	14	210	80

within one of the two categories: First, as the main active component, PbS QD solids have shown promising results in heterojunction solar cell devices whose performance depends on efficient charge transfer between neighboring QDs and the adjacent electrodes. This is dependant on the ligand(s) used to create the solids that favor the transport and collection of charges and, the thickness of each layer (Xu *et al.*, 2011; Ma *et al.*, 2012; Xu *et al.*, 2015; Pattantyus-Abraham *et al.*, 2010; Wang *et al.*, 2016; Proppe *et al.*, 2017; Ka *et al.*, 2018). Conversely, in quantum-dot sensitized solar cells, they complement traditional platforms by efficiently adding charges generated from the absorption of photons in the IR region, thus expanding the range of operation at a very low cost (Ning *et al.*, 2015; Ka *et al.*, 2018). When assembled into quantum dot solids, their electronic and optical properties depend on both, the initial characteristics of the synthesized nanocrystals and, the solid's assembly quality: how closely packed are the quantum dots so that the charge transport becomes more efficient (Lingley, Lu & Madhukar, 2014; Wang *et al.*, 2016; Hong *et al.*, 2016; Rekemeyer *et al.*, 2017) within the solid as well as the transfer to the device's charge collection electrodes (Ju *et al.*, 2010; Kramer *et al.*, 2012; Lee *et al.*, 2018). Furthermore, the solution processability of colloidal PbS QDs is advantageous to produce low-cost and large area devices, that offer integration flexibility with other platforms, including silicon-based optoelectronic applications (Klimov *et al.*, 2000; Kamat, 2013; Kim *et al.*, 2016; Saran & Curry, 2016; Ka *et al.*, 2018).

Despite the straight-forward and low-cost fabrication process, planar TiO_2-based lead-sulfide (PbS) QDs photovoltaic cells show low efficiency of around 3%, low short-circuit current and low fill-factor (Ju *et al.*, 2010). This is due to the planar architecture that does not fully prevent the recombination of charge carriers in the quasi-neutral region of the junction as a result of the

short diffusion length in colloidal quantum dot films versus the depletion length (Kramer *et al.*, 2012). Other causes stem from the effect the solid-state ligand exchange has on the energy levels and band-gap conditions of the treated quantum dots (Brown *et al.*, 2014) that could render them incompatible with traditional platforms used in QD-based photovoltaics(Kamat, 2013).

2.1.2.1 Chemical ligands and quantum dot assemblies for device applications

The use of organic thiol molecules such as 1,2-Ethanedithiol (EDT) or 1,3-benzenedithiol (BDT) for solid state ligand exchange, is especially popular in photovoltaic device fabrication (Ju *et al.*, 2010; Brown *et al.*, 2014). These short molecules bring the quantum dot solids closely packed increasing the carrier mobility and in turn, the short circuit current density (Xu *et al.*, 2015; Lingley *et al.*, 2014). However, the solid-state ligand exchange process that involves removing the oleic acid (OA) capping molecule, which is left from the solution synthesis process. It also removes Pb atoms from the dots (Hughes *et al.*, 2012), changing them from cation rich to anion rich quantum dots, sacrificing the surface passivation that OA offers. This impacts the overall efficiency of devices (Brown *et al.*, 2014). Subsequent oxidation of these nanocrystals decreases the photovoltaic device's performance over time (Zhai *et al.*, 2011a).

As an alternative, halide-based ligands (I-, Br-, Cl-) became one promising strategy to deliver successful passivation at the surface of PbS quantum dots while making the film of QDs closely packed, through solid-state ligand exchange. Thanks to the affinity between Pb and the halide ions (Hong *et al.*, 2016; Balazs *et al.*, 2015; Zhang, Gao, Miller, Luther & Beard, 2014) it is possible to increase the photovoltaic performance and environmental resilience (Hong *et al.*, 2016; Kim *et al.*, 2016; Chuang, Brown, Bulović & Bawendi, 2014; Tang *et al.*, 2011; Cao *et al.*, 2016). While devices fabricated with organic thiols like EDT exhibit higher open-circuit voltages, devices making use of Tetra-n-butylammonium iodide (TBAI) for solid-state ligand exchange display higher short-circuit current density (Brown *et al.*, 2014). Additionally, this improved passivation helps maintain the initial operation characteristics for longer times

compared to traditional thiol molecules such as EDT or BDT (Ma *et al.*, 2012; Xu *et al.*, 2015; Kim *et al.*, 2016; Klem *et al.*, 2008). A combination of layers of both TBAI-treated and EDT-treated has been demonstrated to improve the performance in planar QD-based solar cells thanks to the formation of a p-n junction at the interface between these two (Rekemeyer *et al.*, 2017), where the EDT-treated QDs exhibit a light p-type behavior and the TBAI-treated QDs exhibit n-type characteristics (Chuang *et al.*, 2014) that facilitates and enhances the charge carrier separation.

In conjunction with the choice of ligands, the interaction of the QD solids interaction with other layers present devices such as QD sensitized solar cells, plays an important role in the final device's performance. Titanium Dioxide (TiO_2) is a good choice of cathode material for its optical transparency, chemical resistance, non-toxicity, simple preparation and stability as a hole blocking/electron transport layer (HBL/ETL). A heterojunction interface with the TBAI-treated QDs takes advantage of a favorable band alignment and the low-cost sol-gel synthesis of high quality films. However, this heterojunction suffers from the presence of Schottky barriers that lower the performance and are attributed as the cause of the presence of s-shaped current-voltage (J-V) characteristics (Hu *et al.*, 2014; Mandelis, Hu & Wang, 2016). Multiple strategies aim to increase charge collection in TiO_2-based sensitized solar cells, involving one dimensional (1D) nanostructures like nanorods (Jiao, Zhou, Zhou & Wu, 2013; Zhang *et al.*, 2018), nanowires and nanotubes (Xu *et al.*, 2012; Benetti *et al.*, 2016) based electrodes. Carbon nanotubes are of particular interest due to their extraordinary electrical and mechanical properties (Wilder, Venema, Rinzler, Smalley & Dekker, 1998; Dembele *et al.*, 2013), making them very adequate for applications in flexible photovoltaics.

Indeed, for photovoltaic applications, interface optimization is a driving factor for boosting the performance of heterojunction quantum dot sensitized solar cells with TiO_2 transport layers. The use of hybrid TiO_2 layers with one-dimensional carbon nanostructures makes an excellent alternative to overcome this hurdle (Dembele *et al.*, 2013; Benetti *et al.*, 2016). Devices fabricated with ZnO/PbS QD/SL-Graphene achieve efficiencies up to 6% however,

fabrication of single-layer graphene based devices remains challenging due to its volatility and elevated manufacturing costs(Kim *et al.*, 2016).

2.2 A short primer in graphene

For many years two-dimensional (2D) atomic crystals were an impossibility regarded only as mathematical tool to study single-atom thick films of materials. In 2004, Novoselov and co-workers showed that "atomically thin carbon films" were attainable by mechanical exfoliation of a highly oriented pyrolytic graphite (HOPG) block, depicted in Figure 2.3(a), where the blue lines show where the inter-layer overlapping takes place and the red lines where it does not. Different layer colors are used to aid visualization. They produced environmentally stable, chemically inert and optically transparent films who were installed into devices for characterization. Furthermore, they showed how their simple exfoliation method was applicable to other crystalline materials (Novoselov *et al.*, 2004; Novoselov *et al.*, 2005) as an efficient way of obtaining single-atom thin-films, finally allowing researchers to directly study their properties and applications. Some examples of these are shown in Figure 2.3(b), where the inset notation correspond to (a) $NbSe_2$ (b) graphite (c) $Bi_2Sr_2CaCu_2O_x$ and (d) MoS_2 and all the scale bars represent 1 μm. Since then, graphene is regarded by many as a wonder material that in theory, will open new doors in electronics, sensors, membrane technologies, composites, heat transfer and energy storage, among others.

Graphene is a 2-dimensional, allotrope network of sp^2 hybridized carbon atoms arranged in honey-comb fashion, with the carbon-carbon distance of 1.42 Å (Castro Neto, Guinea, Peres, Novoselov & Geim, 2009). It is considered that only single and double layer graphene behave as "zero-gap semiconductors", while bandgap overlaps appear for films between 3-10 layers (Novoselov *et al.*, 2005). Anything beyond this point, from 10 to 10th's of layers, should be regarded as "thin films of graphite" (Geim & Novoselov, 2007), and whose properties start resembling those of three-dimensional graphite. Under an electric field excitation, graphene exhibits ambipolar charge carrier concentrations of up 10^{13} cm^{-2} and mobility around from 2.5 x 10^5 $cm^2/V^{-1}.s^{-1}$ with a weakly dependence on ambient temperature or chemical doping

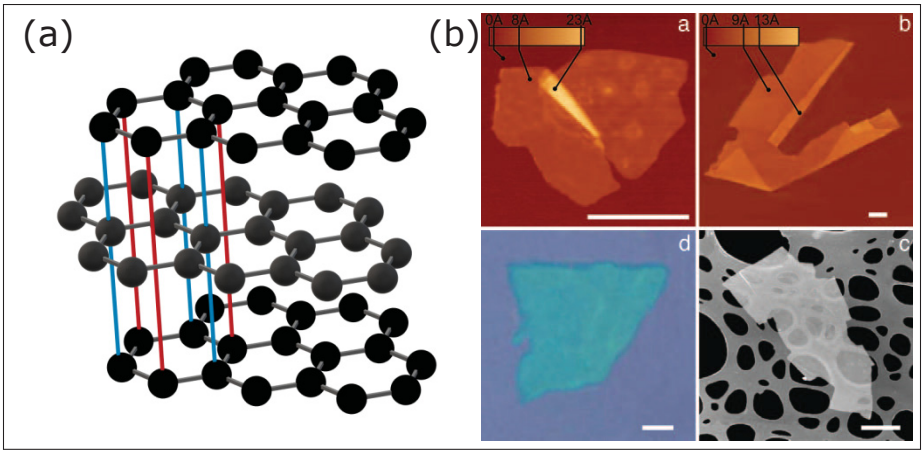

Figure 2.3 (a) HOPG structure and (b) 2D crystals by obtained by mechanical exfoliation
(b) Taken from Novoselov *et al.* (2005)

(Novoselov *et al.*, 2012). These high mobility characteristics are what makes graphene most attractive for electronic applications.

Initially, the possibility of graphene was confirmed through mechanically exfoliating HOPG with single layer sheets exceeding 100µm in size (Weber, Calado & van de Sanden, 2010) and, it is through this method that the highest quality single-layer graphene sheets were obtained, showing those 'miraculous' properties. In contrast, repeatable and uniform production requires advanced techniques such as chemical vapor deposition (CVD) (Li *et al.*, 2009a) and indeed, large areas of almost single layer graphene are readily possible (Bae *et al.*, 2010). Other chemical synthesis routes (Park & Ruoff, 2009) yield larger quantities than CVD but the presence of defects and added chemical species in the resulting crystalline structure means graphene with poor electrical properties. As such, these types of graphene or graphene oxide flakes are more suited for applications in conductive paints and coatings, smart composites and shielding (Benavides-Guerrero *et al.*, 2022a). High quality graphene better suited to operate in high-performance optoelectronic devices will be out of the scope of the project developed in this thesis. In the end, it is the improvement of such production techniques (Figure 2.4) what will allow full integration of graphene into the current technological landscape

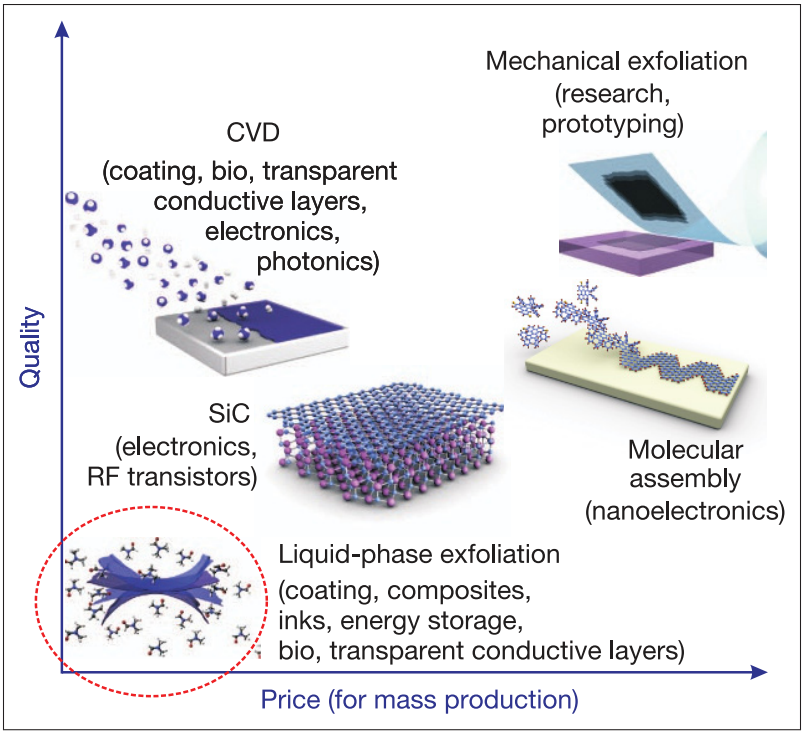

Figure 2.4 Potential applications of graphene based on the quality of its synthesis. *Red circle:* Type of graphene that will be analyzed in this application project Adapted from Novoselov *et al.* (2012)

or better yet, fully disrupt it with unforeseen developments as it certainly possesses the potential for that.

2.3 An overview to Raman spectroscopy

Raman spectroscopy is a technique that takes advantage of a phenomenon called inelastic scattering of photons, known as the *Raman effect*, first discovered in 1928 by Sir Chandrasekhara Venkata Raman, who was awarded the 1930 Nobel prize in Physics "for his work on the scattering of light and for the discovery of the effect named after him"[1].

[1] The Nobel Prize in Physics 1930. NobelPrize.org

Even though this technique has been around for almost a century, it was only after the invention of the **laser** in the 1960's, that it started to be widely used in research and industrial facilities as a way of characterize and analyze compounds. The main principle of the Raman effect is explained as follows: Molecules are quantized systems that can exist in various discrete energy levels or vibrational modes, where the ground is the lowest energy state and any other level represents higher vibrational energy in the molecule. When a source of light emits photons of an specific known wavelength which interact with said molecule, some will be scattered in all directions, e.g. light interacting gas molecules. Raman's discovery states that a small portion of this scattered light will emerge with a shift from its original wavelength as a result of the light-matter interactions that took place. This shift corresponds to the fraction of initial photon's energy transferred to the molecule who in turn, was excited to a higher vibrational state. This is known as a Stokes shift and is proportional to the photon's energy lost.

If the molecule starts from an excited state and the scattered photon emerges with higher energy than the source, it means the molecule gave up this energy to relax back to the ground state. This positive energy shift is known as anti-Stokes. If there is no energy shift in the scattered photon, this is called Rayleigh scattering. The three types of scattering are depicted in Figure 2.5. In there, ν_{L} is the laser source and ν_{R} is the Rayleigh scattered light of the same energy (both green color). The orange arrow represents the Stokes (ν_{S}) and the blue arrow the anti-Stokes (ν_{AS}) energy shifts, respectively. The molecular vibrational modes are the black straight lines and the virtual transient excited states are the oscillating lines. Colors are used for visual aid only and do not represent the reality.

The Raman effect is material dependent and different shifts are associated with specific materials, since each molecule has specific vibrational modes given from the atomic organization. Thus, Raman spectroscopy measures the scattered photon's energy shift comparing it to the source's energy and from there, it is possible to analyze the nature of the molecule under study, including, crystallinity.

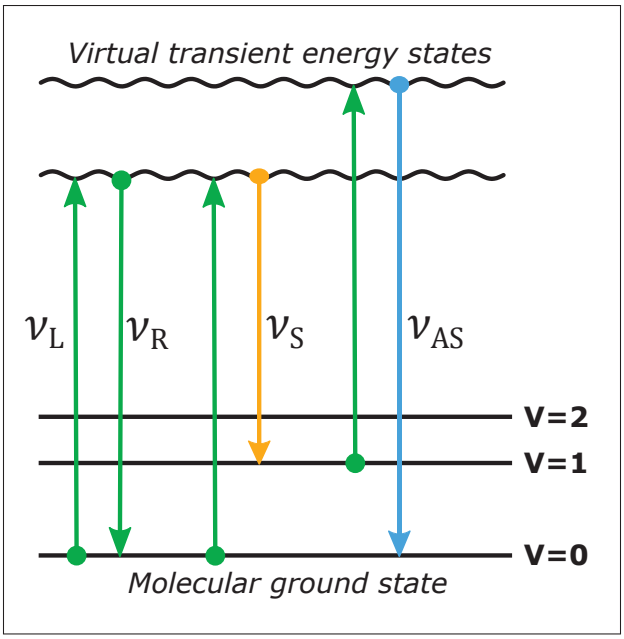

Figure 2.5 Schematic representation of Raman scattering effects

2.3.1 Raman spectroscopy of graphene

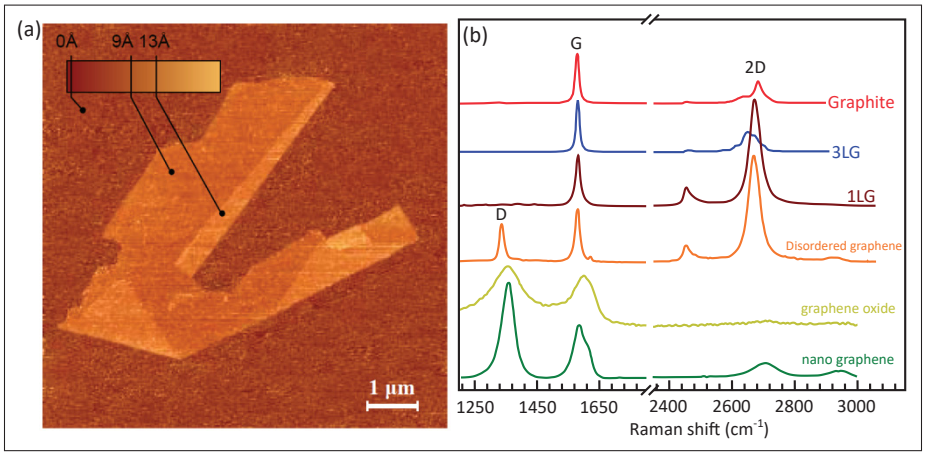

Figure 2.6 Characterization of graphene by AFM and Raman spectroscopy (a) AFM image of free standing single-layer graphene (b) Raman signals for different graphite forms (a) Taken from Ferrari *et al.* (2006), (b) Adapted from Wu *et al.* (2018)

It was important to establish the quality level of the mass-produced commercial graphene flakes as a high number of layers or strong presence of defects will yield low electrical conductivity results. While the number of layers on a sample can be directly identified using AFM (Ferrari *et al.*, 2006; Schniepp *et al.*, 2008) and shown in Figure 2.6(a), Raman spectroscopy is a quick, non-destructive tool that allows characterization of graphene samples, including the presence of defects and it is also possible to estimate the number of layers present in the sample (Wall, 2011; Barron, 2019; Silva *et al.*, 2020) as shown in the different spectra in Figure 2.6(b). The most prominent bands in the Raman spectrum of graphene and their role in layer characterization are described as follows:

- **D-band:** Being weaker in graphite, this band is commonly found between 1340 - 1350 cm^{-1} in graphene. This band is sensitive to the apparent presence of defects such cracks, dislocations and vacancies. In essence, this band is caused by phonon scattering that originates at the defect sites, which explains why it is a measure of the disorder in the structure (Malesevic *et al.*, 2008; Li *et al.*, 2010). It can also give information about disorder in the lattice, when the sampling is done in close proximity of an edge or, if there are chemical modifications made to the graphene sample. This band represents a ring breathing mode from the sp^2 carbon rings, which are the carbon atoms in-plane of the graphene sheet. If significant, it represents high defect density. This is a resonant band, which means that the vibration and peak position is dependent on the laser excitation wavelength and also depends on the presence of defects for activation (Ferrari, 2007).
- **G-band:** This band is located between 1580-1587 cm^{-1}. Large-quantity fabrication methods have also reported this band to be located at around 1560 cm^{-1}, producing large-area doped graphene samples by arc-discharge methods (Li *et al.*, 2010), producing many-layers graphene, similar to that used in this project. The peak position and relative intensity of the Raman signal are sensitive to the layer thickness, doping of the sample and the strain in the lattice. It's been proposed that the intensity of this peak can be linearly correlated with the number of layers for samples with a small number of layers ($N<10$) (Wall, 2011; Silva *et al.*, 2020) when compared with a common reference intensity peak. As this is a sharp band, the peak position is also dependent on the number

of layers (Wang, Wang, Cao, Feng & Lan, 2009). Similarly, for samples with a small number of layers it was discovered that location of the peak follows the empirical relation $\omega_G = 1581.6 + 11/(1 + n^{1.6})$ derived by Wang and co-workers, whose representation is shown in Figure 2.7(a). As the number of layers increases the band position red-shifts as a consequence the relaxation of the lattice with each additional layer. This band is common to all sp^2 carbon systems, as it comes from the in-plane C-C bond stretching in graphite-based materials. In the presence of impurities, there's is the possibility of a band splitting into the normal G-band and an additional so-called D'-band, that can be located as far as 1620 cm^{-1}.

- **2D-band:** This is the second order from the D-band, meaning that this peak originates from a two-phonon lattice vibration process. It is located between 2660 - 2710 cm^{-1} İts peak position, band shape and intensity are sensitive to the number of layers, inter-layer orientation and strain. It is always a strong band in graphene and it does not depend on defects for activation and does not provide information about the presence of defects in the lattice. However, increasing the number of layers breaks the band symmetry, inducing peak splitting, making it useful to directly determine the number of layers up to 4 (Wall, 2011), by fitting a number of fundamental Lorentzian functions (Hao *et al.*, 2010) that match the number of peaks/bumps of the signal, exemplified in 2.7(b). Complex computational algorithms have expanded this capabilities for the determination of higher number of layers in mass-produced, low-cost graphene samples (Silva *et al.*, 2020). It exhibits strong dispersive behavior, meaning peak position and shape are also affected by the laser excitation wavelength.

2.3.1.1 Relation between peak's intensity and FWHM for layer estimation

It's been proposed that a ratio between the 2D and the G peak's intensity can provide information about the number of layers for graphene samples with a small number (N) of layers, N<5. For high quality single layer graphene the ratio between the intensities of the two peaks should be, $I_{2D}/I_G >= 2$ (Kumar *et al.*, 2014). Also, there is a distinct absence

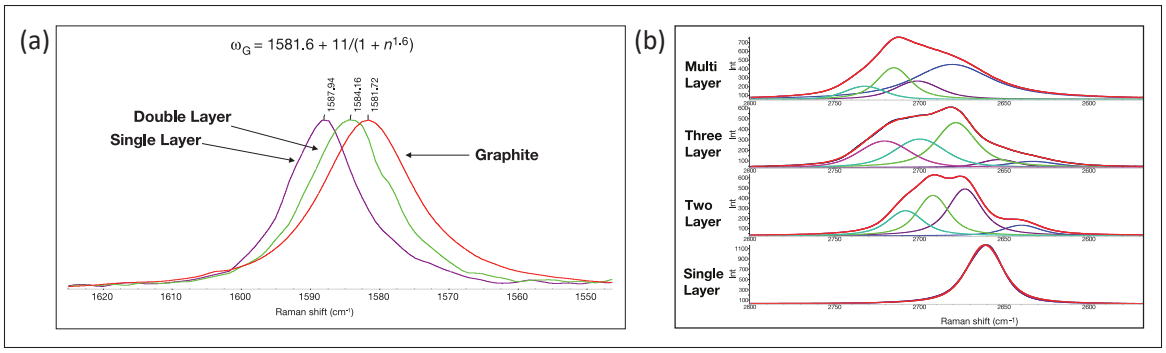

Figure 2.7 (a) G-band peak position based on the number of graphene layers (b) 2D-band peak decomposition that correlates the number of layers Taken from Wall (2011)

of the D-band peak and the 2D-band is a sharp peak with symmetric wings. For few-layers graphene with N=2,3,4, the ratio I_{2D}/I_G varies: for N=2 is between 1 and 2 and, for N=3,4 is larger than 0.8. For many layers graphene with $I_{2D}/I_G < 0.5$, this ratio loses significance as it becomes difficult to provide an exact measure. Additionally, it has been shown that the full-width half-maximum of the 2D-band provides reliable information about the number of layers (Hao *et al.*, 2010) for up to 5 layers. Unfortunately, for samples containing of more than 5 layers, estimation of the number of layers using the FWHM of the 2D-band is no longer accurate as the band shape becomes very close to that of bulk graphite (Ferrari *et al.*, 2006; Ferrari, 2007).

CHAPTER 3

LASER-ASSISTED, LARGE-AREA SELECTIVE CRYSTALLIZATION AND PATTERNING OF TITANIUM DIOXIDE POLYMORPHS

Luis Felipe Gerlein[1] , Jaime Alberto Benavides-Guerrero[1] , Sylvain G. Cloutier[1]

[1] Département de Génie Électrique, École de Technologie Supérieure,
1100 Notre-Dame Ouest, Montréal, Québec, Canada H3C 1K3

Article published in « Advanced Engineering Materials », September 2019
https://onlinelibrary.wiley.com/doi/abs/10.1002/adem.201901014

Abstract: While ubiquitous in multiple industrial applications, the widespread use of solution-based precursors for crystalline titanium dioxide (TiO_2) for optoelectronic device integration remains limited due to its high processing temperature. This limitation generates material compatibility issues and complicates the fabrication steps, especially for low-temperature substrates used in flexible hybrid electronics and low-cost photovoltaics. It is currently possible to crystallize TiO_2 at lower processing temperatures, but it requires a carefully-controlled atmosphere or metallic doping of the amorphous precursor and can only achieve a low-yield conversion of the precursor. This paper presents a qualitative method for the processing of an amorphous photo-sensitive precursor in order to achieve high-yield conversion to highly-crystalline TiO_2 at room-temperature and in ambient environment without added dopants using a low-energy laser. Moreover, it demonstrates the ability to controllably convert locally to anatase or rutile TiO_2 only by adjusting the laser power density. This work shows real potential for the additive manufacturing of TiO_2 structures for photo-catalysis, printable flexible hybrid electronics and low-cost photovoltaics using low-energy laser processing that is compatible with heat sensitive materials and flexible substrates.

3.1 Introduction

Titanium dioxide (TiO_2) powders possess advantageous properties including chemical stability, non-toxicity and low manufacturing costs that are exploited in a wide variety of industrial appli-

cations (Hanaor & Sorrell, 2011; Diebold, 2003) These applications include water treatment (Lee & Park, 2013), water splitting for hydrogen production (Ni, Leung, Leung & Sumathy, 2007; Wang *et al.*, 2011; Miyoshi, Nishioka & Maeda, 2018), surfaces modification (Wang *et al.*, 1997, 1998; Chawengkijwanich & Hayata, 2008; Liu, Cao, Fujishima & Jiang, 2014), photocatalysis (Fujishima & Honda, 1972; Linsebigler, Lu & Yates, 1995), microelectronic circuits (Wu & McCreery, 2009; Stathopoulos *et al.*, 2017), sensors (Chen & Lu, 2005; Akbar, Dutta & Lee, 2006; Bai & Zhou, 2014) and solar cells (Bai *et al.*, 2014; Duraisamy, Muhammad, Kim, Jo & Choi, 2012), amongst others. Most properties of TiO_2 stem from its crystallization into two polymorphs, namely anatase and rutile. Depending on the desired application, the anatase structure will appear when annealing the amorphous TiO_2 around 450 °C while the rutile structure will appear between 800 °C to 1100 °C (Sun, Egawa, Zhang & Yao, 2002a). However, all these applications would greatly benefit from the ability to fully-convert precursor solutions into anatase or rutile TiO_2 in ambient environment and at much lower temperatures. This is especially true in applications that involve multiple materials and fabrication steps. This would significantly reduce the energy consumption during manufacturing and could expand the use of TiO_2 to the additive manufacturing of energy conversion, wearable and flexible hybrid electronic devices and systems.

In recent years, careful control of the phase transition and phase stability of TiO_2 polymorphs induced by low-power visible light gained attention in the scientific community (Vásquez *et al.*, 2015; Ricci, Casu, Salis, Corpino & Anedda, 2010; Russo, Liang, Xiu He & Norman Zhou, 2017; Dam, Jena & Pradhan, 2016; Zhang, Chen & Wang, 2017; Ricci *et al.*, 2013; Zhang, Jin & Li, 2016; Benavides *et al.*, 2018; Yu *et al.*, 2018). Indeed, it is possible to promote or inhibit the laser-induced phase transition from anatase to rutile TiO_2 by the addition and careful control of the concentration of metallic ions in the TiO_2 matrix (Choi, Park & Hoffmann, 2010a). Such is the case of doping with iron (Fe) or aluminum (Al). Induced by laser radiation, iron promotes the phase transition from anatase to rutile, while aluminum inhibits it (Vásquez *et al.*, 2015). However, this process still involves temperatures over 350 °C to achieve only partial crystallization of the TiO_2 nanoparticles. Meanwhile, scandium (Sc)

and vanadium (V) can also be used as dopants in TiO_2 nanoparticles to shift the transition temperature from anatase to rutile (Zhang *et al.*, 2016). Others achieved phase transition at lower-temperature, but under partial oxygen pressure (Ricci *et al.*, 2010) or in in high-vacuum chambers (Ricci *et al.*, 2013) to enable the photoactivation of the TiO_2 precursor. However, this dramatically increases the manufacturing costs and limits its use for modern low-cost additive manufacturing applications. Finally, other approaches achieved complete control of the synthesis of only one specific crystalline phase of TiO_2 nanoparticles (Dam *et al.*, 2016; Zhang *et al.*, 2017) with considerably lower temperatures compared to traditional crystallization techniques.

Although direct laser writing of crystallized TiO_2 is not a new approach (Yu *et al.*, 2018), recent efforts require a 24-hour aged amorphous precursor and a femtosecond IR laser source. Crystallization is only possible after the addition of a two-photon absorber chemical and takes place under a controlled nitrogen atmosphere, while achieving only the conversion to rutile phase.

These previous efforts all arise from the profound need for high-quality crystalline TiO_2 converted at room temperature in ambient environment. Yet, important fundamental hurdles prevent their scaling-up to modern industrial-like environments. In particular, the inclusion of TiO_2 precursors into laser-based 3D printers and digital inkjet printing systems, including electrohydrodynamic inkjet, has been limited by two defining factors: the high processing temperatures (beyond 400 °C) still necessary to crystallize into different polymorphs (Duraisamy *et al.*, 2012; Arin *et al.*, 2011), and/or the specific atmospheric conditions required to crystallize under visible light at room temperature (Ricci *et al.*, 2010, 2013; Yu *et al.*, 2018). Both factors are highly detrimental for the widespread integration of TiO_2 precursors into large volume manufacturing of many photo-catalysis, energy conversion, wearable and flexible hybrid electronic solutions.

Previously, our group reported a novel TiO_2 precursor formulation relying on an incomplete nonhydrolytic sol-gel ester elimination to yield films of amorphous TiO_2 suitable for laser-

induced conversion in ambient conditions (Benavides *et al.*, 2018). This formulation allows low-energy laser-induced conversion of amorphous-to-anatase, amorphous-to-rutile, anatase-to-rutile or amorphous-to-mixture of anatase/rutile in ambient environment and at room temperature without metallic ions or specific atmospheric conditions.

In this article, we demonstrate large-scale laser-assisted conversion of amorphous TiO_2 films under ambient conditions with an inexpensive approach using a low-cost commercially available 3D printer platform with a 405 nm laser engraving attachment module to spatially control the TiO_2 crystallization. To this end, we describe in detail how this unique formulation can be used to achieve selective conversion of this amorphous TiO_2 into combined anatase and rutile patterns over large surface area. The laser-induced conversion process is carefully optimized (laser velocity, laser power setting and number of passes) in order to achieve selective conversion of the TiO_2 over large surface area. The highly crystalline TiO_2 is characterized by Raman spectroscopy and X-ray diffraction (XRD), while the morphology and integrity of the converted areas are analyzed using laser-scanning microscopy.

3.2 Experimental results

3.2.1 Sample preparation

We prepared a dispersion of TiO_2 nanoparticles following a procedure fully-described elsewhere (Benavides *et al.*, 2018; Joo *et al.*, 2005). The average size of the amorphous nanocrystals are stablished by means of atomic force microscopy (AFM), yielding an average particle size of 8.020 nm, as measured by the AFM software (See supplementary Figure I-1). We placed pieces of standard glass slide inside a plastic container containing a solution of as-synthesized amorphous TiO_2 nanoparticle suspension in hexane. The container is subsequently sealed within a box with breathing holes to avoid external contamination and, guarantee a slow and uniform evaporation of the hexane, yielding smoother films. After 12 hours inside the fume hood, a densely packed film of amorphous TiO_2 nanoparticles remains atop the glass after all the solvent has evaporated. This method aims to create a thick film,

hence the amount of amorphous precursor inside the container is twice the height of the glass slide to provide good coverage. The resulting film displays a reddish coloration and covers all the area of the glass as presented in Figure 3.1. The physical microscopic quality of the amorphous, as-deposited film can be seen in Figure 3.1(b) and the overall look of the film atop glass is in Figure 3.1(c).

The simplicity of this deposition method makes it adaptable to a variety of substrates, not limited to glass, including flexible ones like cellulose acetates and biocompatible substrates.

3.2.2 Conversion and optimization

All experiments we report here are performed in normal laboratory environment. No special inert gas or vacuum chamber nor additional substrate heating are required to trigger the crystallization of the amorphous TiO_2 film after deposition.

The laser head consists of a 405 nm CW blue-violet source with a maximum 500 mW power output. Because of the transistor-transistor logic (TTL) fan controller, the laser head does not exhibit a linear power density evolution when adjusting the power setting from 0-255 in the printer fan control, as shown in Figure 3.1(a). Perceivable emission occurs from power setting 2 (with about 5 mW of laser power). At maximum power, with the power setting set at 255, the laser emission reaches 465 mW from the 500 mW nominal specification for the module (Figure 3.1(a)). Additionally, because of the poor design for thermal dissipation in the module, the laser head heats quickly and it can lead to permanent damage under constant operation after a few minutes. Under low power operation, with the power control set under 50 (about 388 mW measured emission), the laser emission will not damage the unit and the impact of the poor cooling is less dramatic but, this lack of stable emission reflects in the results obtained. While we managed to achieve conclusive outcomes, this is something to keep in mind while analyzing the results presented in this report.

The laser head offers a manual control to adjust the focal distance of the laser beam. In our case, we set this focal point to be at 40 mm from the emission point and to that number, one

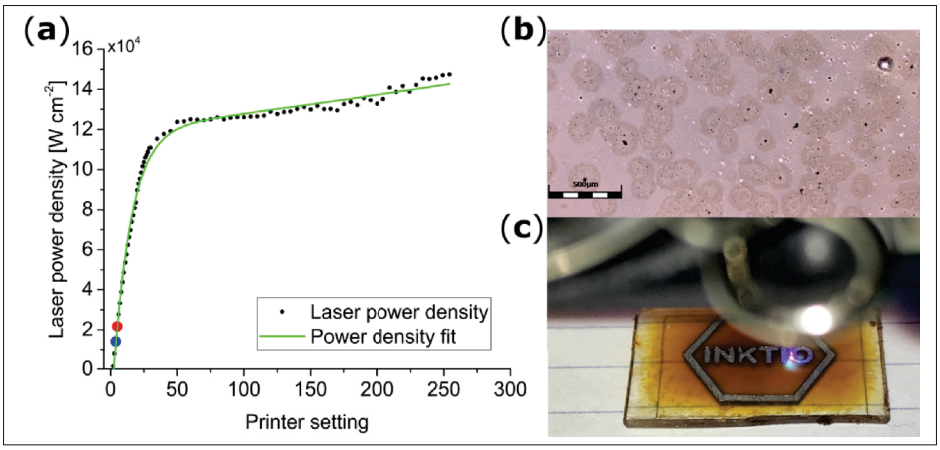

Figure 3.1 Laser and film characteristics (a) Evolution of the laser emission power of the 405 nm laser unit used to convert the TiO_2 as a function of the setting number (b) Micrograph of an amorphous film atop glass after complete drying (c) Photograph of the conversion process using the 405nm laser source atop the amorphous TiO_2 film

must add the height of the sample under test to ensure the focal point is at the surface of the sample. At this focal point, the trace width of the laser trace measures 20 µm and with this value we calculated the laser power density.

In addition to the power setting, the BIBO printer offers four other parameters that can be adjusted. The travel speed corresponds to the head movement speed when the laser is not active. This parameter was set to match the laser speed, minimizing the acceleration/deceleration of the head during writing that influences the quality of the films by changing the exposure time compared to the rest of the film. The laser speed is the head's velocity when the laser is on. Passes refers to the number of times the pattern is repeated in the same place. Pass depth sets the bed's height after each pass. Given that our film's thickness is always between 20 - 30 µm, we did not change this parameter even at a high number of passes. We focus on three key parameters of interest to optimize the conversion process. The order of importance for the optimization explained in the following sections are (1) laser power setting, (2) the laser speed and (3) the number of passes.

For optimization, conversion of the TiO_2 amorphous film must be evaluated for different power settings. Initially we will provide the power setting as a value from 0-255 that corresponds to the levels available to the laser controller. Each value has a corresponding laser emission power density, as previously presented in Figure 3.1(a) and the chosen values will be available in the summary table for each step.

3.2.2.1 Rutile conversion optimization

Initial experiments, present in Figure 3.2, show square areas of the film fully-converted to crystalline TiO_2 using the BIBO printer's laser module. Each area is filled with a simple square mesh pattern shown in Figure 3.2(a) which guarantees uniform converted areas by keeping the lines close enough to each other to trigger conversion along the area of interest. Each square is about 2.5 mm x 2.5 mm and made using different laser power settings, from 25 to 255 in increments of 25 each (Figure 3.2(b)). Confocal Raman microscopy analysis of each square shows a fully crystallized rutile TiO_2 phase, with the typical peaks found at 145, 232, 452 and 610 cm^{-1} (shown in Figure 3.2(c)). The parameters used in this initial test are summarized in the supplementary section, Table I-1.

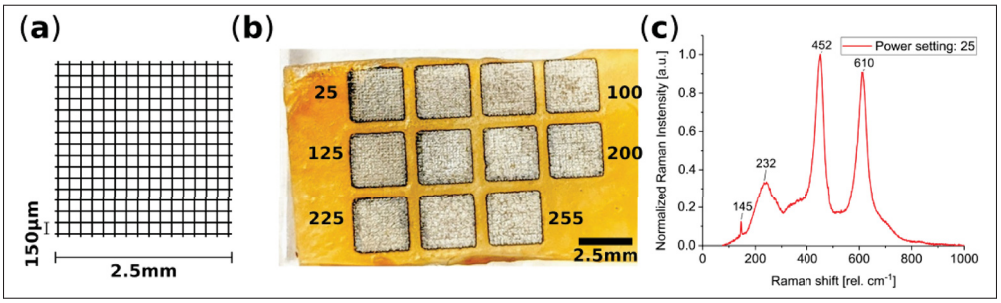

Figure 3.2 Pattern used in high power conversion (a) Mesh pattern composed of 16 by 16 crossed lines covering an area of roughly 6.25 mm^2. Each line is 20 µm thick and the dimensions of each inner square are 150 µm x 150 µm (b) Photograph of the squares fabricated using different power settings, starting from 25 in increments of 25 up to 250, and an extra square at 255 (c) Typical micro-Raman spectrum showing complete crystallization to rutile TiO_2 with a power setting of 25

Microscopic analysis of the square patterns from Figure 3.2 reveals a strong penetration of the laser throughout the film to the point of complete ablation of the material, exposing the substrate as shown in Figure 3.3(a,b). The laser traces strip large areas of the TiO_2 film leaving the glass substrate uncovered, while the space between the traces show mounds of fully crystallized rutile TiO_2 in random shapes (Figure 3.3(c)), which ultimately does not render a uniform and continuous film (3.3 and Supplementary Figure I-1).

We had to carefully control the excitation power of the laser source present in our confocal Raman microscope system to avoid triggering unwanted crystallization and alter the results obtained from the large area crystallization. For this reason, we performed the analysis at low excitation power, where the only signal detectable is always coming from the crystallized TiO_2 left in the substrate.

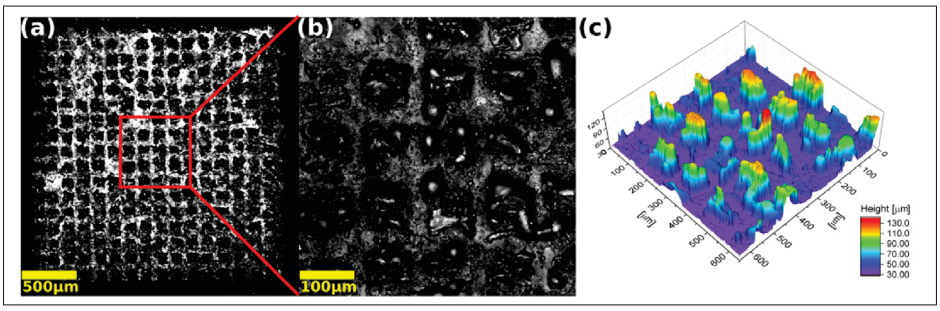

Figure 3.3 Microscopic analysis of the morphology of the square features created using the power setting 25 (a) Low-resolution image of the whole square (b) Magnified portion of the red square in (a); (c) 3D reconstruction of the topology of the magnified portion of the square

Our main goal is to minimize this material ablation while promoting exclusively the crystallization of the amorphous TiO_2 layer under environmental conditions, delivering a uniform film in which the presence of both, anatase and rutile crystalline phases is possible. Because of this unwanted material etching, we explored lower laser power settings going from 1-16, corresponding to power emission between 4 to 230 mW (13.7 – 732 $W.mm^{-2}$). With a new film deposited atop glass using the same described procedure, the patterns of choice are lines 100 µm thick created by doing 5 contiguous traces of 20 µm each (Figure 3.4).

For each pattern, the power setting of the laser is fixed and ranges from 16 down to 1, in single steps. To further reduce the material displacement, we increase the laser speed parameter from 50 to 100 mm min^{-1}. Of course, this also reduces the total dosage received by the film. The travel speed, number of passes and pass depth remain unchanged from the previous run. From laser power setting 16 down to 6, the resulting line patterns exhibit complete crystallization to rutile. These results are like those previously obtained in the square patterns realized with higher power settings (Figure 3.3), with important material displacement and/or ablation, leaving bare areas of exposed glass where the amorphous TiO_2 was previously present (see Supplementary Figure I-2).

At power setting 5, the equivalent laser power density is 216 ± 10 $W.mm^{-2}$ (3.1(a)). At this emission power, one can already observe a smoother and more uniform, fully-crystallized film (Figure 3.4(b)). We largely attribute the presence of cracks in the film after crystallization to the natural densification of the material and subsequent volume loss due to the atomic reorganization. Reported values in density for both anatase and rutile phases are 3830 kg m^{-3} and 4240 kg m^{-3} respectively (Diebold, 2003), highlight the structural differences of both phases. Indeed, the unit-cell volume of anatase is 130.36 $Å^3$ while for rutile is 62.45 $Å^3$, factor that explains the stronger fracturing present in the rutile conversion (Benavides *et al.*, 2018) when coming from an amorphous state. This fracture effect also depends on the film thickness, being more prominent in thicker films. Here, we estimate the thickness of the film used to pattern these lines to be 24 µm as seen in Figure 3.4(c).

We tested the quality of the crystalline phase by confocal Raman microscopy and X-ray powder diffraction (XRD), shown in Figure 3.5. The Raman characterization of the sample line number 5 (Figure 3.5(a,b)) shows complete crystallization in the rutile phase with Raman peaks located at 236, 450 and 610 cm^{-1}; typical values for rutile TiO_2 (Figure 3.5(a)). XRD characterization allows the identification of the crystalline phase of TiO_2 by the presence of strong peaks located at 27°, 36°, 55° degrees (Figure 3.5(b)) dominant in the identification of the rutile phase (Thamaphat, Limsuwan & Ngotawornchai, 2008). The presence of residual anatase peaks will be analyzed in the discussion section. In the Table I-2 in supplementary

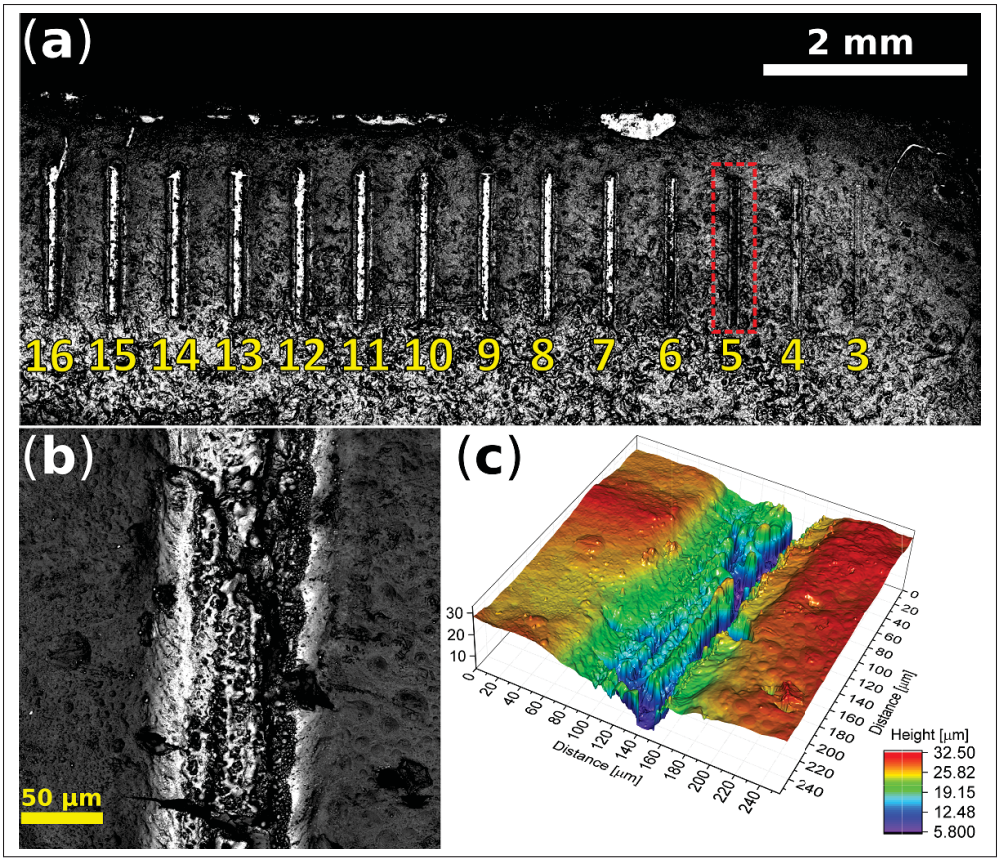

Figure 3.4 Line patterns produced with a laser speed of 100 mm/min and varying the power setting from 25 to 1 on a 24 µm-thick film of amorphous TiO_2 (a) Line patterns from 16 to 3. Lines produced with power settings 2 and 1 do not affect the area and are not visible in the image (b) Micrograph from the line pattern produced with power setting 5 (c) 3D laser micrograph reconstruction from the image on (b)

section, we provided the summary of the other BIBO laser parameters to achieve this low-fragmentation rutile conversion.

Starting from the settings in Supplementary Table I-2, we fixed the pass depth and the power setting. Leaving the laser speed and number of passes open for optimization provides the flexibility required to achieve the best structurally sound yield for both rutile and anatase crystallization. In this test, we follow the same line pattern than before with lines 100 µm wide and each line created with a different set of parameters. We vary the laser speed from 100

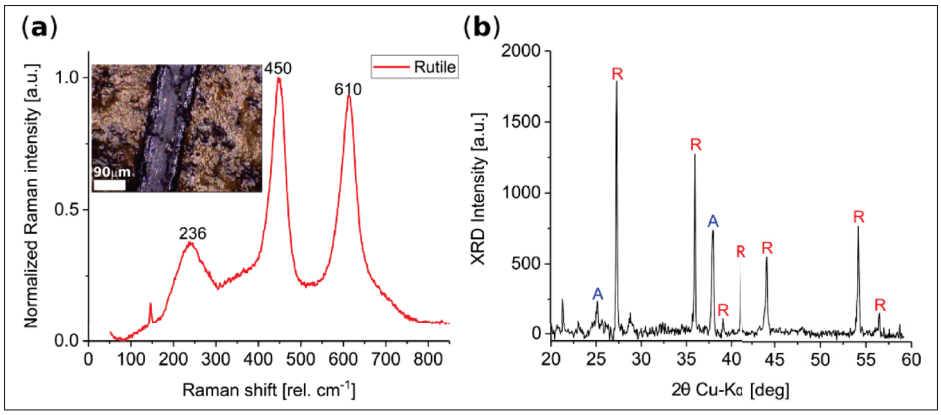

Figure 3.5 Characterization of the crystallization at power setting 5 (a) Confocal Raman spectra. Inset: Micrograph of the area analyzed (b) XRD of the crystallized area showing fully converted rutile structure

mm.min^{-1} to 500 mm.min^{-1}, being that the maximum value allowed in the machine. We used increments of 20 mm.min^{-1} for a total of 25 lines in this test.

At a laser speed of 300 mm.min^{-1} and 2 passes, the rutile crystallization is cleaner with less fractures in the film. These are the final parameters of choice to make rutile films, summarized in Table 3.1.

Table 3.1 Optimal parameters chosen for the creation of rutile films

Travel speed [mm min^{-1}]	Laser speed [mm min^{-1}]	Passes	Pass depth [mm]	Laser setting	Emission power [mW]	Emission power density [W.mm^{-2}]
300	300	2	0	5	68	216

3.2.2.2 Anatase conversion optimization

Between both phases, rutile proves the easier phase to optimize given it is the most stable phase of TiO_2. Conversely, anatase crystallization requires precise tuning given the photosensitivity of the film and the unstable power output of the laser module. This translates in an exceedingly small range where the correct crystallization happens before the film receives

an excess of radiation and continues the atomic rearranging towards the more stable rutile phase and produces a mixed (Benavides *et al.*, 2018) anatase/rutile phase.

For this reason, and to achieve better control in obtaining anatase phase, we set the laser emission power down to 45 ± 2 mW (power setting 4), then vary the laser speed settings while increasing the number of passes. Starting from 300 mm.min^{-1} to 500 mm.min^{-1} with increments of 25 mm.min^{-1} and for each speed setting, we change the number of passes was 2, 3, 4, 5. With a laser speed at 450 mm.min^{-1} and 3 passes, the anatase phase has a strong presence in the film, although well-marked spots of rutile appear, as shown in Figure 3.6 and supplementary Figure I-3 in the supplementary section. This crystallized smooth film, shows little presence of cracks and the strong Raman signature of a fully converted anatase phase (Figure 3.6(a)). This is also confirmed by the XRD analysis in Figure 3.6(b) showing the presence of both phases within the same film. Further increment of the laser speed to 475 and 500 mm.min^{-1} reduces the rutile spots, but it also reduced the presence of fully converted anatase.

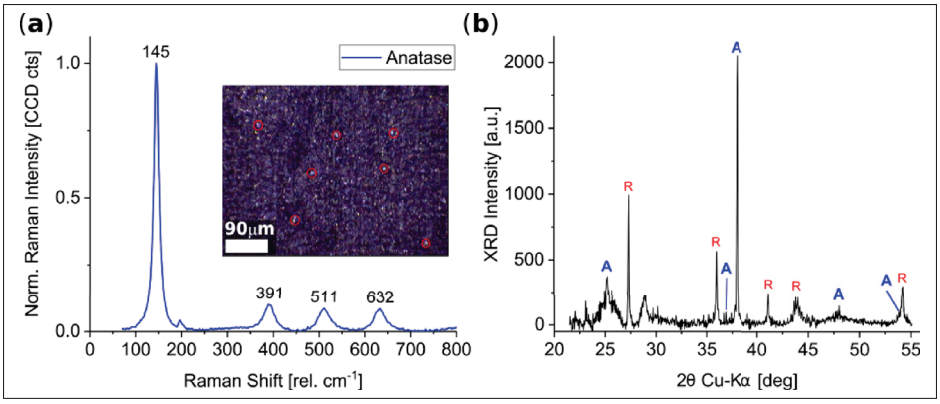

Figure 3.6 Characterization of the anatase phase obtained at 450 mm min^{-1} laser speed and 2 passes (a) Confocal Raman spectrum. Inset: micrograph of the film after conversion. The red circles mark the presence of rutile within the anatase film and (b) XRD spectrum highlighting the anatase peaks

Confocal Raman and XRD confirms the complete crystallization of the specified area. The main Raman peaks at 145, 391, 511 and 632 cm^{-1} in Figure 3.6(a) clearly suggest a dominant

anatase phase. The strong diffraction peaks for anatase at 25°, 37° and 48° in the XRD spectrum of Figure 3.6(b) are also consistent with this result. All the values presented for both anatase and rutile are in good agreement with the standardized values. The optimal parameters to achieve anatase crystallization are present in Table 3.2.

Table 3.2 Optimal parameters chosen for the creation of anatase films

Travel speed [mm min^{-1}]	Laser speed [mm min^{-1}]	Passes	Pass depth [mm]	Laser setting	Emission power [mW]	Emission power density [$W.mm^{-2}$]
450	450	3	0	4	45	140

3.2.3 Large-area laser-induced conversion to anatase/rutile TiO_2

To showcase the endless possibilities of this TiO_2 solution and low-energy conversion process for additive manufacturing, we chose to print a geometric pattern that has both rutile and anatase areas coexisting along with amorphous unconverted sections, as presented in Figure 3.7. In the initial pattern design, as shown in the inset in Figure 3.7(a), there are three distinctive colors: dark brown is the amorphous film, dark gray is the anatase section and light gray is the rutile section.

Optical characterization of the sample, shown in Figure 3.7(b), clearly shows each section labeled (Am) amorphous, (A) anatase-rich and (R) rutile-rich regions easily recognizable in this intimately dense mixed film. We analyzed the transition between phases at the interface between the anatase-rich and the rutile-rich sections using Raman spectroscopy (see Supplementary Figure I-4) in search for unconverted areas. The transition is abrupt and consistent with the visual results; however, the interface requires further optimization that is limited by the quality yield of the laser. In the nanoscale regime, the properties of metal oxides such as TiO_2 are very sensitive to the oxygen content in the lattice, factor that helps explain the dark color (Ullattil *et al.*, 2018) of the resulting film, especially in the anatase form.

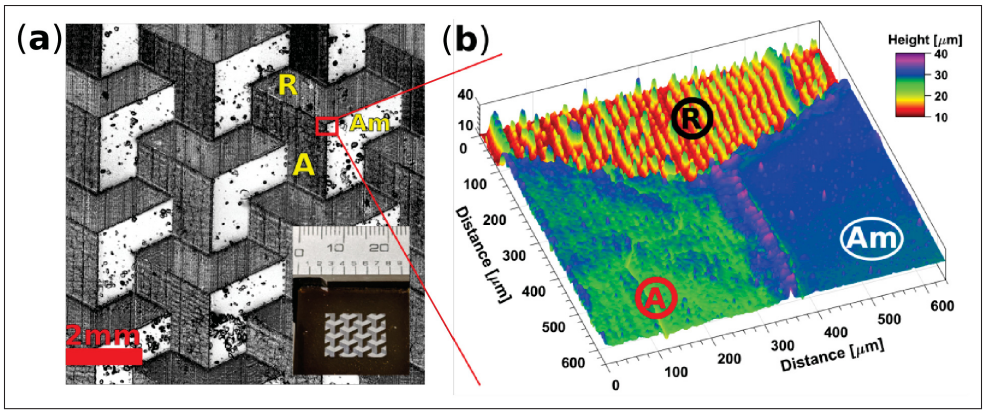

Figure 3.7 Large-area on-demand crystallization of the TiO_2 film (a) Micrograph of the patterned film with the presence of the both phases next to each other and an amorphous part left unconverted in between. Each section corresponds to either amorphous, anatase or rutile. Inset: photograph of the patterned sample (b) Magnified 3D reconstruction of a section of the sample. The unconverted amorphous (Am) area represented in blue color. The rutile area (R), the more red-yellow section and the anatase area (A) is the green-blue area. These colors are automatically assigned by the 3D reconstruction software

It is well established the advantageous and synergistic effects associated with having both phases in the same environment for photocatalytic applications. This setting reduces charge recombination boosting the degradation of organic contaminants (Benavides *et al.*, 2018; Thamaphat *et al.*, 2008; Ullattil *et al.*, 2018). However, previous results require the use of two types of independent nanoparticles working together, without the level of spatial control offered here. As demonstrated by our results, this is the first time that a TiO_2 large-area film can be produced on-demand where the ratio anatase:rutile is controlled directly by the geometry of each.

3.3 Discussion

Just recently, approaches that involve the use of TiO_2 as part of the active material in photovoltaic applications (Rajbongshi & Verma, 2018) and the potential of the heterojunction composed of both phases in light harvesting have just being explored (Banerjee *et al.*, 2018).

This is done using a Degussa P25 (biphasic TiO_2 nanoparticles) with a fixed ratio of anatase to rutile presence in the mix. The results included in this letter describe the possibility of having spatially-selective bi-phasic TiO_2 layers compatible with conventional laboratory fabrication techniques for optoelectronic devices in addition to the possibility of large-scale production lines.

However, integration in large production lines requires more adept control of the crystallization conditions, specifically the quality and stability of the source of illumination: whether is a low power laser source or a high-power photonic curing flash-lamp (Das *et al.*, 2016) using a mask for faster, large area conversion. In our case, the laser unstable emission tends to variate the power delivered and creating partially converted spots in the wings. This configuration does not guarantee a uniform conversion all over the area of interest. A square profile emission present in much more expensive and reliable sources (Bolduc, Trudeau, Beaupré, Cloutier & Galarneau, 2018) will increase the yield of a single crystalline phase per unit area.

Under the current conversion conditions, the limited presence of rutile phase within the anatase area come from specific spots whose location is random and unpredictable. Despite the low-cost of our approach, good spatial resolution, control and reproducibility, the lack of proper thermal and emission stability in our laser unit, makes it inappropriate to meet high-precision industrial standards. We, however, believe this proof-of-concept is concrete evidence that it is possible to crystallize TiO_2 under ambient environmental conditions, using a low-cost approach, with the possibility of obtaining spatial control of the phases by only adjusting the emission parameters of a laser source.

3.4 Conclusions

As a wide band-gap semiconductor, titanium dioxide is an attractive candidate, especially for application into dye-sensitized solar cells (DSSCs) (O'Regan & Grätzel, 1991; Lim, Pandikumar, Lim & Huang, 2016), where the light absorption role and the charge transport

role are separated. The integration of TiO_2 in novel organic and inorganic photovoltaic devices is limited to a charge transporting role due to the incompatibility of the crystallization process of TiO_2 that damages the other materials involved in the fabrication of the device. Crystallized TiO_2 whether as anatase (3.2 eV band-gap) or rutile (3.0 eV band-gap), exhibits optical absorption at the violet portion of the optical spectrum and with our technique it is possible to fabricate and integrate devices that take full advantage of this asset.

By utilizing a defect-rich synthesis of non-hydrolytic of titanium dioxide that shows enhanced sensibility to photoconversion while avoiding costly and lengthy thermal crystallization procedure, we demonstrate that it is possible to have large area deposition and conversion of biphasic thin layers of TiO_2 . Complete area-selective conversion to either anatase or rutile is possible, while preserving the state of the other one.

In addition to create fully crystallized large area patterns with “a la carte” ratio of each phase, it is now possible to experiment with unconventional patterns between these two phases. Also, this improvement brings new possibilities for low-cost printed flexible electronics, wearable devices and novel additive manufacturing schemes. Most importantly, with our approach, this procedure could be automated and repeated by a machine learning platform for large scale production of devices.

3.5 Experimental Section

Chemicals. Oleic acid (90%, Aldrich) (OA), titanium(IV) isopropoxide (TTIP, Aldrich, 97%), ethanol (ACS reagent, ≥ 99.5% (200 proof, absolute), and hexane.

TiO_2 precursor synthesis. This synthesis follows the recipe published elsewhere (Benavides *et al.*, 2018; Joo *et al.*, 2005). TiO_2 nanoparticles are synthesized through an incomplete nonhydrolytic sol-gel ester elimination reaction of titanium isopropoxide (TTIP, 3.36g) and oleic acid (OA, 10 g). The mixture of both takes place at room temperature under nitrogen atmosphere inside the glove-box. The temperature of mixture is raised to 280 °C using a hot plate and it is kept at this temperature for 2 h. The clear yellow solution gradually changes

color to dark brown. At this point, the solution is cooled to room temperature and can be removed from the glove-box. An excess of ethanol is added to yield a beige precipitate. The remaining ethanol solutions solution is centrifuged for 30 min to recuperate the nanoparticles. After disposal of the ethanol, the solution is dispersed in hexane and ready to use.

Material characterization. Optical imaging and laser 3D reconstruction made using the Olympus Laser Confocal Microscope LEXT OLS4100. Raman imaging and analysis made using the WITEC Alpha300 confocal Raman microscope equipped with a 60mW fiber-coupled continuous-wave laser at 532 nm and a mechanical attenuator. X-ray diffraction patterns obtained using a Bruker, D8 Advance with a Cu source.

3D printer equipment. The 3D printer of choice is the BIBO-2 Touch printer that possesses a positional accuracy in the Z direction resolution of 20 μm. This accessible 3D printing system can be purchased for under $850 USD with a laser engraving module that replaces the extruder heads and is controlled by the fan transistor-transistor logic (TTL) control circuit. The laser module can be purchased separately through the ANNOY TOOLS store at the website Aliexpress.com for under $35 USD.

Supporting Information

Supporting Information is available from the Wiley Online Library or from the author.

Acknowledgements

S.G.C. thanks the Canada Research Chair and the NSERC Discovery programs for their support.

Conflict of Interest

The authors declare no conflict of interest.

Keywords

anatase, laser-assisted conversion, rutile, titanium dioxide

CHAPTER 4

HIGH-PERFORMANCE SILVER NANOWIRES-BASED TRANSPARENT CONDUCTIVE ELECTRODES FABRICATED USING MANUFACTURING-READY ULTRAFAST PHOTONIC SINTERIZATION PROCESS

Luis Felipe Gerlein[1] , Jaime Alberto Benavides-Guerrero[1] , Sylvain G. Cloutier[1]

[1] Département de Génie Électrique, École de Technologie Supérieure,
1100 Notre-Dame Ouest, Montréal, Québec, Canada H3C 1K3

Article published in *Scientific Reports*, December 2021
https://www.nature.com/articles/s41598-021-03528-w

Abstract: On the long road towards low-cost flexible hybrid electronics, integration and printable solar energy harvesting solutions, there is an urgent need for high-performance transparent conductive electrodes produced using manufacturing-ready techniques and equipment. In recent years, randomly-distributed metallic nanowire-based transparent mesh electrodes have proven highly-promising as they offer a superb compromise between high performances and low fabrication costs. Unfortunately, these high figure-of-merit transparent mesh electrodes usually rely heavily on extensive post-deposition processing. While conventional thermal annealing yields good performances, it is especially ill-suited for deposition on low-temperature substrates or for high-throughput manufacturing solutions. Similarly, laser-induced annealing severely limits the processing time for electrodes covering large surfaces. In this paper, we report the fabrication of ultra high-performance silver nanowires-based transparent conductive electrodes fabricated using optimized manufacturing-ready ultrafast photonic curing solutions. Using conventional indium tin oxide (ITO) as our benchmark for transparent electrodes, we demonstrate a 2.6-2.7× performance gain using two different figure-of-merit indicators. Based on these results, we believe this research provides an ideal manufacturing-ready approach for the large-scale and low-cost fabrication of ultra high-performance transparent electrodes for flexible hybrid electronics and solar-energy harvesting applications.

4.1 Introduction

New critical applications ranging from internet-of-things (IoT) & biomedical sensors to wearable & energy-harvesting devices are currently forcing the consumer electronics industry to revise its manufacturing paradigms. To meet this new and exponentially-growing demand, the industry is seeking new flexible hybrid electronic solutions using printable circuits and components. Many of those key applications including solar cells (Camic *et al.*, 2020; Pereira & Hatton, 2019), light emitting devices (Yin *et al.*, 2020), haptic displays & touch screens (Cann *et al.*, 2016), wearable electronics (Yin *et al.*, 2020; Kwon *et al.*, 2018; Hwang *et al.*, 2018) and biomedical sensors (Han, Park, Oh, Jung & Kim, 2017) usually require a high-performance transparent conductive electrode (TCE) technology compatible with high-speed manufacturing techniques and equipment. Ideally, a printable solution-based TCE solution would be compatible with traditional rigid substrates, but also with flexible substrates using polyethylene or polyimide, amongst others (Bolduc *et al.*, 2018; Yeo *et al.*, 2014). Unfortunately, extensive post-treatment steps are usually necessary to achieve the best TCE performance (Lee, Han, Choi & Moon, 2010; Kou, Yang, Chang & He, 2017; Tang *et al.*, 2018; Ali, Shuhaimi & Hassan, 2014). This significantly affects the manufacturing capabilities and costs.

Today, the most established TCE technology is by far the Sb-doped indium oxide (or so-called ITO) glass films (Chen *et al.*, 2013; Dauzou *et al.*, 2016). However, brittleness, material availability and high processing costs make it ill-suited for many emerging applications when it comes to large-scale manufacturing (Dauzou *et al.*, 2016; Linnet *et al.*, 2018). While they can offer some advantages, other doped metal-oxides including aluminum-doped zinc oxide (AZO) and fluorine-doped tin oxide (FTO) (Dauzou *et al.*, 2016) also suffer from structural and manufacturing limitations akin to ITO's. Conductive conjugated polymer solutions can be more easily processed; however, they are also limited when it comes to performances and large scale manufacturing (Cao, Li, Chen & Xue, 2014). Besides their organic nature makes them prone to oxidation and photodegradation, which requires additional post-treatment steps (Nardes *et al.*, 2008; Vitoratos *et al.*, 2009). More recently, graphene-, nanotube- or nanowire-

based conductive mesh electrodes have proven a promising alternative to oxide-based TCE films.

Metallic nanowire-based mesh electrodes are especially promising contenders to replace ITO as the next-generation TCE standard. This is largely due to their facile and low-cost processing in ambient conditions, low sheet resistance, high transparency and flexibility (Jang *et al.*, 2020; Ding *et al.*, 2016). Indeed, they show low sheet resistance (R_{sh}), exceeding 90% of optical transparency (Jiu *et al.*, 2012; Sun *et al.*, 2020; De *et al.*, 2009). As such, they have become especially attractive for low-cost printable photovoltaic devices architectures (Chen *et al.*, 2012). For haptic displays and sensing applications (Han *et al.*, 2017; Ding *et al.*, 2016), requirements for sheet resistance are on the order of 500 Ω/sq. (Bae, Kim, Shin, Ahn & Hong, 2012). As such, metallic nanowire-based TCEs are also well suited for these applications. They also provide the added benefit of a better tolerance to mechanical bending for flexible device integration (Han *et al.*, 2017; Yang *et al.*, 2016).

4.1.1 State-of-the-art

Traditionally, percolated silver nanowire mesh electrodes require thermal annealing above 300 °C in order to properly connect the nanowires together and achieve the best performances (Sepulveda-Mora & Cloutier, 2012). The conventional thermally-induced sintering process imposes a stringent time-to-temperature trade-off restriction, such that lower annealing temperatures generally require much longer processing times (Langley *et al.*, 2014). Previously, incremental densification of the silver nanowire-based film through pressure rolling clearly established the direct relationship between the post-processing treatment and the electrodes' improved electrical and mechanical properties (Yeo *et al.*, 2014; Hauger, Al-Rafia & Buriak, 2013; Tokuno *et al.*, 2011). Indeed, these lengthy post-processing treatments can successfully yield spectacular sheet resistance values, under 14 Ω/sq., together with an improved mechanical bending capability (Hosseinzadeh Khaligh & Goldthorpe, 2014). Unfortunately, imposing such high temperature treatments on most sensitive low-temperature substrates will also yield severe degradation. In contrast, reducing the process temperature

will necessarily require increasing the processing time and significantly slow-down the manufacturing process (Langley *et al.*, 2014).

As an alternative to conventional thermal annealing, light-assisted post-processing such as laser-induced sintering (Bolduc *et al.*, 2018) and broadband pulsed-light or high-intensity photonic curing (Schroder *et al.*, 2006; Schroder, 2011; Kim, Dhage, Shim & Hahn, 2009; Bansal & Malhotra, 2016; Dexter, Gao, Bansal, Chang & Malhotra, 2018) can allow for room-temperature processing of a variety of nanoparticles ranging from metallic (Kim *et al.*, 2009; Sarkar, Gupta & Gupta, 2017) to chalcogenides (Dexter *et al.*, 2018) and semi-conducting (Hwang *et al.*, 2020; Dharmadasa, Lavery, Dharmadasa & Druffel, 2014) aggregates. It also enables a wider variety of low-cost and low-temperature substrates (Schroder, 2011). Carefully-optimized photonic curing can deliver results akin to conventional thermal annealing process, but in much faster processing times (Schroder, 2011; Chung, Kim & Kim, 2016). This is done by exciting plasmon resonance-induced heating, without damaging the underlying substrate. With silver nanowires, visible light excites a plasmonic resonance and heat dissipation occurs rapidly along their longitudinal axis thus facilitating their interconnection (Chung *et al.*, 2016). Meanwhile, thermal equilibrium can be reached within milliseconds within the substrate (Schroder *et al.*, 2006; Schroder, 2011). Moreover, the heat can't reach the opposite side of the substrate, thus preventing unwanted warping, expansion or cracks in the substrate (Dexter *et al.*, 2018). As a result, functional materials can be processed at temperatures much higher than those tolerated by the underlying substrates. Therefore, a small number of high fluence, short pulses could potentially densify the film of silver nanowires on a low-temperature substrate, hopefully reaching sheet resistance values comparable to values obtained after several minutes, or hours, of conventional thermal annealing.

It was previously established that good conductivity can be obtained using photonic curing with low-energy density fluence, but at the cost of using an elevated number of pulses (Bansal & Malhotra, 2016). Indeed, excitation with over 150 pulses can already yield sheet resistance values under 0.15 Ω/sq., for films composed of silver nanoparticles of 40 nm in diameter (Bansal & Malhotra, 2016). In contrast, reducing the number of pulses usually

requires very thick silver nanoparticle films. Indeed, resistivity down to 6.9 μΩ/sq. was previously achieved using only 6 pulses, but only for silver films over 4.35 μm in thickness (Dexter, Bhandari, Chang & Malhotra, 2017).

Two key parameters play a definite role in the fabrication of any high-performance transparent conductive electrodes, (1) the optical transparency T and, (2) the sheet resistance R_{sh}. These key parameters are commonly combined using two different figures-of-merit indicators. The first one can be defined as the electrical to optical conductivity ratio (De, King, Lyons, Khan & Coleman, 2010) σ_{DC}/σ_{OP}, while the second represents the figure of merit for transparent conductive materials (Haacke, 1976; Sannicolo *et al.*, 2016) Φ_{TC}. These figures-of-merit indicators are most useful to evaluate and compare the optimal trade-off between transparency and sheet resistance for different TCEs (De *et al.*, 2009; Sepulveda-Mora & Cloutier, 2012) given a specific application (Sun *et al.*, 2020). By using a manufacturing-grade photonic curing engine (Novacentrix, PulseForge Invent), we now seek to explore the optimal post-processing conditions required to enable the introduction of this silver nanowire-based TCE technologies into state-of-the-art printed electronics manufacturing lines.

4.1.2 Summary of this work

This report describes how we take advantage of simulation and careful control of the high-speed photonic curing of an interconnected network of silver nanowires, in order to manufacture the best high-performance transparent conductive electrodes. Using standard commercial ITO as our comparison benchmark, we achieve a 2.6-2.7× performance gain over ITO using two distinct figure-of-merit indicators. Under optimal conditions, these electrodes can reach transparencies over 90% and sheet resistance values down to 9.8 Ω/sq., compared to 30 Ω/sq. for standard ITO. While their performance equals the best results achieved with high-temperature pressure-rolling (Yeo *et al.*, 2014; Hauger *et al.*, 2013; Hosseinzadeh Khaligh & Goldthorpe, 2014), this photonic curing process is also compatible with low-temperature substrates and with the stringent requirements of high-speed roll-to-roll manufacturing lines (Sannicolo *et al.*, 2016; Novacentrix, 2018). As such, we firmly

believe this low-cost transparent conductive electrode fabrication process using high-speed photonic sintering will greatly facilitate the large-scale manufacturing of multiple new disruptive technologies including low-cost printed solar cells, lighting, haptics, wearable electronics and biomedical sensors.

4.2 Results and discussion

In Figure 4.1, we show the Pulseforge simulation results of the optimal pulse configuration used to process our TCE samples on glass. Our typical pulse has a fluence of 23.4 J.cm^{-2}, with an envelope duration of 30,000 µs. This irradiation is delivered using a sequence of 15 consecutive pulses to complete the photonic treatment of the film. As shown in Figure 4.1(a) the process brings the film's temperature to 300 °C, a well established temperature value for a proper welding of silver nanowires in thermally-annealed TCE's (Sepulveda-Mora & Cloutier, 2012). If we look more closely, Figure 4.1(b) reveals how each of these fifteen (15) 30,000 µs-long pulses is really made of 18 shorter µ-pulses with a duty cycle set at 50%.

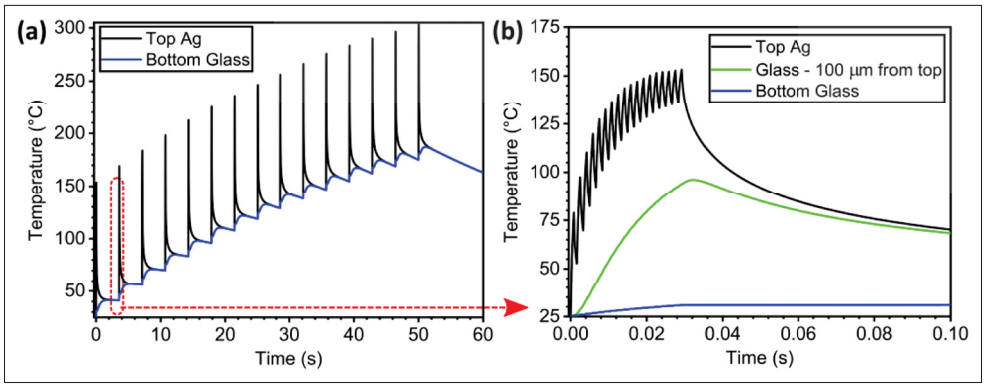

Figure 4.1 SimPulse simulation of the pulse-train used to process AgNW TCE's in glass in the Pulseforge (a) 15 consecutive pulses. The red oval points to a detailed version of the first pulse in (b) Simulation of the effects of a single pulse. For comparison, the green line depicts the simulated temperature profile at 100 µm under the top surface of the glass substrate and the blue line shows the simulated temperature at the bottom surface

As a reference, in Figure 4.1 we show the temperatures reached in the glass substrate at 100 µm under the top surface (green curve) and at the bottom surface (blue curve), in order to properly illustrate the heat dissipation process taking place during this photonic processing. As expected, those temperatures are too low to cause damage in most low-temperature substrates currently used in flexible electronics.

Previous works by Bansal and Malhotra discuss in detail the consequences of intense pulsed-light sintering on nanoparticle necking and the overall temperature profile in metal nanoparticle-based films, both theoretically and experimentally (Bansal & Malhotra, 2016). They describe how the temperature in the films reaches a maximum before cooling down due to increased heat dissipation of the joined nanoparticles as a whole. This phenomenon occurs as a result of the plasmon resonance-induced heating and subsequent welding described by their coupled model (Bansal & Malhotra, 2016). As such, we can confidently conclude, the Novacentrix SimPulse physical modelling tool is closer to their non-coupled model and does not account for this inter-particle necking effect during the film processing. Our basis for reaching this conclusion is fully described in the supplementary material. This first-order approximation can be perfectly acceptable for most industrial processing applications, as long as the users remain aware of this model limitation. Still, the better heat dissipation by the processed film (tailing-off) is already a satisfactory indicator of the correct welding of the nanostructures and the model can serve as a rough indicator of the steady-state temperatures reached in our system. While the PulseForge Invent is capable of delivering higher pulse fluence that could potentially further reduce significantly the processing time, it remains essential to carefully avoid extreme peak temperatures that can damage both the functional material and the substrate. Carefully avoiding these situations is the key to a successful photonic annealing, thus achieving the maximum peak temperature in the thin-film with the lowest substrate temperature possible thanks to the rapid thermal equilibrium reached between the thin-film and the substrate's surface (Schroder *et al.*, 2006; Schroder, 2011). Indeed, carefully-controlled pulse shaping includes dividing the main pulse into several μ-pulses that help deliver the pulse energy in more specific ways to prevent burning or blowing

off the material while reaching the desired temperature goal (Schroder *et al.*, 2006; Schroder, 2011). In the end, the good agreement between the literature results and our SimPulse predictions shown in Supplementary Figure II-1, are enough to make us highly confident about its capability to analyze the overall behavior of our TCEs under photonic curing conditions.

4.2.1 Optical and electrical properties of the TCE's

4.2.1.1 Optical characteristics

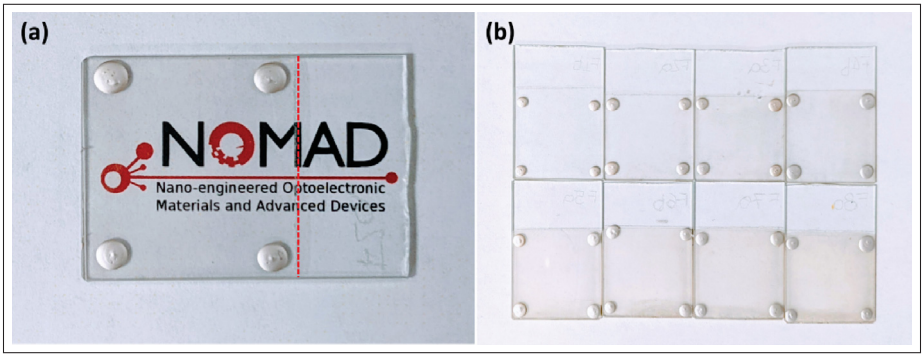

Figure 4.2 TCE electrodes on glass after photonic annealing (a) Two-layer sample on a piece of paper to highlight its good transparency. The red dashed line shows where the film ends (b) Samples showing an increasing number of silver nanowire layers and how their transparency is progressively reduced

Visual inspection of the samples before and after photonic sintering shows no significant changes in transparency or film quality. Photograph of a typical sample with a double layer of silver nanowires after photonic curing is shown in Figure 4.2(a), highlighting how the logo can be easily distinguished through the glass and the TCE layer. Photonic treated samples with a range of layers also maintain integrity upon visual inspection as shown in Figure 4.2(b).

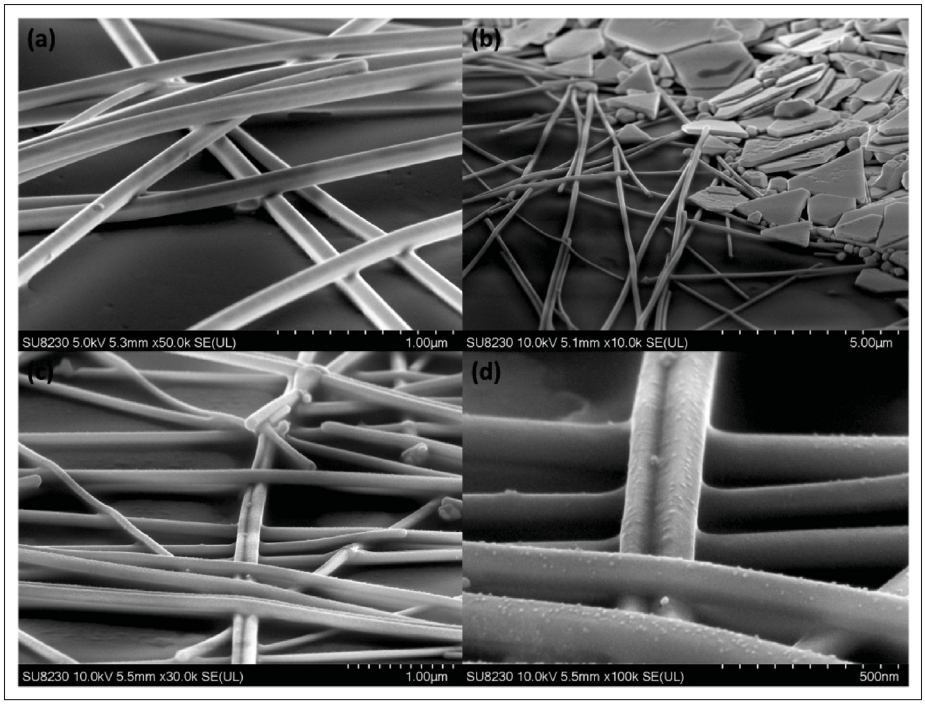

Figure 4.3 SEM images of the nanowires before and after photonic treatment (a) Pristine untreated nanowire films (b) Photonic-treated films showing the interface with the silver flakes from the electrical contacts (c,d) High-resolution micro-graphs to highlight the successful interconnection of the nanowires yielding better electrical properties after photonic curing

Scanning electron microscopy (SEM) analysis shown in Figure 4.3 allows to compare the morphology of the nanowire-based electrodes before and after photonic curing. Figure 4.3(a) exposes how the nanowires maintain their original shape and texture before photonic curing, as well as avoiding potential spherodization of the nanowires (Kwan, Le & Huan, 2016). Visual artifacts of the SEM imaging technique gives an appearance of joint nanowires, but in reality this film conducts poorly due to the presence of the PVP coating surrounding the nanowires (Jiu *et al.*, 2012). Figure 4.3(b) suggests that the application and low-temperature treatment of the paste does not affect the integrity of the treated film and there is good physical contact with the nanowire network. After photonic curing treatment, the high-resolution SEM images in Figures 4.3(c-d) reveal morphologies that are expected from a highly-conductive, transparent, thin-film of silver nanowires where deformations resulting from welding between

the nanowires can be observed (Chung *et al.*, 2016). The nano-textured surfaces for the nanowires as revealed in Figure 4.3(d) appear as a result of the removal of the PVP layer as previously described in the literature (Jiu *et al.*, 2012).

4.2.1.2 Transmittance and surface coverage fill factor

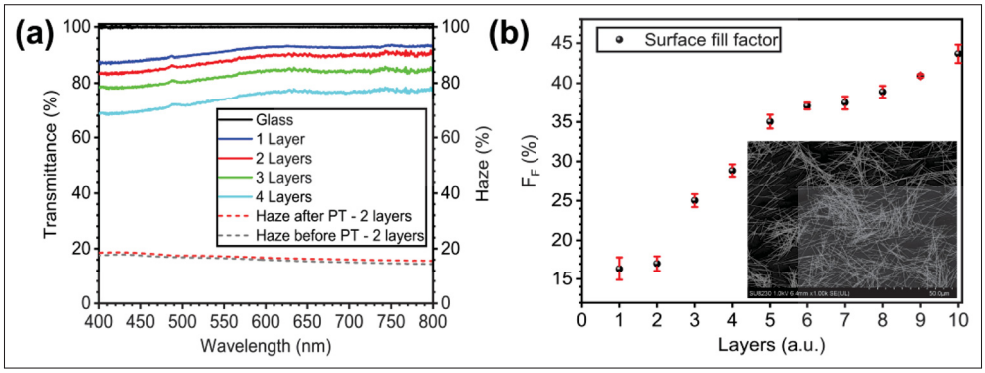

Figure 4.4 Optical transmittance and haze of the TCEs (a) Transmittance spectrum for samples with 1-4 nanowire layers (left axis). The haze characteristics of the sample with 2 layers before and after photonic treatment (dashed lines - right axis) (b) Surface coverage fill factor F_F from 1 to 10 layers of deposited nanowires. Inset: SEM image of a 2-layer sample

These electrodes are all fabricated using a solution of 10 mg/mL of silver nanowires in ethanol, with lengths ranging from 20-30 µm and an average diameter of 120 nm. The optical transmittance evolution as a function of the number of layers deposited by dip coating is presented in Figure 4.4(a) for samples with 1-4 layers, and using pristine glass as the baseline. Averaging the TCE transmittance values over the visible spectrum (400-800 nm), we obtain 91.5%, 88.3%, 82.8% and 74.7% for samples with 1, 2, 3 and 4 nanowire layers respectively. Haze is another optical parameter that provides information about the light scattering in the film and points to the utility of a TCE in diverse applications. Haze values lower than 1% make TCE's very useful for display applications whereas higher values highlight their utility in photovoltaic devices (Menamparambath *et al.*, 2016). Our champion sample made with 2 layers, presents an average haze over the visible range of 16% before photonic treatment and 16.9% after, shown in Figure 4.4(a). Even with the change in NW's texture after treatment

shown in Figure 4.3(d), its haze remains close to its initial value and demonstrates potential use in photovoltaic devices. Finally, the surface coverage fill factor (F_F) evolution with an increasing number of layers is shown in Figure 4.4(b). The values of F_F for samples with number of layers 1-4 are 16.4%, 17.0%, 25.0% and 28.8% respectively.

4.2.1.3 Optoelectronic characteristics

The values for transmittance (T), surface fill factor (F_F), sheet resistance (R_{sh}) and Non-Uniformity Factor (NUF) (Jia *et al.*, 2016) were obtained following the procedures described in the methods section. In Figure 4.5 the evolution of T and F_F are shown as a function of the measured R_{sh}. Based on the simulation results (Figure 4.1), the values of sheet resistance can be obtained using the established pulse conditions and number of pulses for photonic treatment of the samples. The sheet resistance values thus achieved for the samples with 1-5 layers are 15.3, 9.8, 6.1, 5.4 and 3.0 Ω/sq. respectively. *NUF* for our champion electrode was calculated from 12 regions in the sample and resulted in NUF=26%. This value highlights an innate disadvantage of the dip-coating fabrication method, regardless of its low-cost and ease of processing. Other fabrication methods, like Meyer rod method (Jia *et al.*, 2016; Wang, Yang, Zhao & Zhang, 2019) yield better uniformity but were unavailable at the moment of fabrication of our samples.

For TCEs, the transparency of the film usually refers to the transmittance and can be related to R_{sh} using the form $T = e^{-\alpha/\sigma_{DC,B}R_{sh}}$. There, α represents the absorption coefficient and $\sigma_{DC,B}$ is the bulk DC conductivity of the film (De *et al.*, 2010). By fitting the experimental data from Figure 4.5, we obtain the empirical relation for T as a function of R_{sh}:

$$T = -1.15 \cdot e^{-0.39/1.05 \cdot R_{sh}} + 0.92 \tag{4.1}$$

where the fitting parameters $\alpha = 0.3906 cm^{-1}$, $\sigma_{DC,B} = 1.051$ and the values -1.155 and 0.92 represent scaling and translation factors. The R^2 value for equation 4.1 is 0.99. As expected,

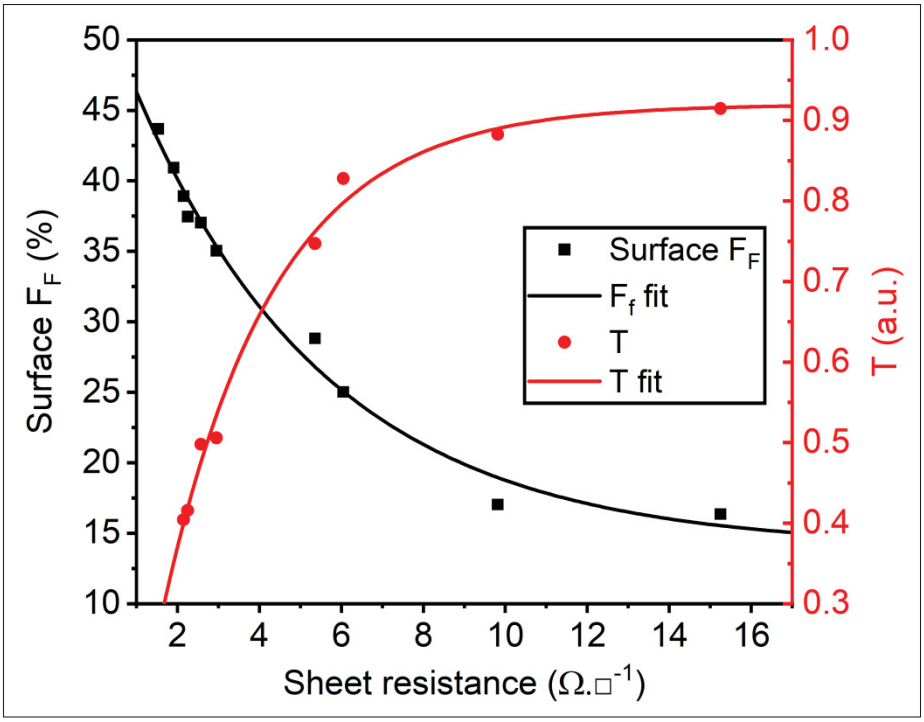

Figure 4.5 Surface fill factor (F_F) and transmittance (T) as a function of the sheet resistance (R_{sh}) values for electrodes with varying number of layers. The smooth lines correspond to the nonlinear fit functions

smaller nanowire fill factor result in higher optical transmittance and higher sheet resistance values. In turn, reducing the sheet resistance requires increasing the coverage density, thus reducing the optical transmittance. Expressing equation (4.1) in the form $R_{sh} = f(T)$ yields the following empirical relation:

$$R_{sh} = -2.69 \cdot ln\left(\frac{0.92 - T}{1.15}\right) \tag{4.2}$$

which can now be used to calculate our electrodes figures of merit.

4.2.2 Figures-of-merit for the transparent conductive electrodes compared with conventional ITO

When evaluating the performance of transparent conducting electrodes, it is important be able to qualify their characteristics against known variables. Established figures-of-merit (FoM) indicators (De *et al.*, 2009; Zhang & Engholm, 2018) help establish the optimal trade-off between the transparency T and the sheet resistance R_{sh} and achieve meaningful comparisons.

4.2.2.1 Figure of merit: Electrical to optical conductivity ratio $(\sigma_{DC}/\sigma_{OP})$

The first figures-of-merit (FoM) indicator looks at the ratio between the electrical and optical conductivity $(\sigma_{DC}/\sigma_{OP})$. The value used for the electrical conductivity σ_{DC} represents the bulk DC conductivity of the TCE film. In contrast, the optical conductivity defined as σ_{OP} can be seen as the ratio between the optical absorption coefficient α and the impedance for free space, $Z_0 = 120\pi$. As such, one can use the relationship established (De *et al.*, 2009, 2010) between the transmittance value T with the sheet resistance values R_{sh}:

$$T = \left(1 + \frac{Z_0}{2 \cdot R_{sh}} \frac{\sigma_{OP}}{\sigma_{DC}}\right)^{-2} \tag{4.3}$$

To derive the following expression for the FoM indicator, σ_{DC}/σ_{OP}:

$$\frac{\sigma_{DC}}{\sigma_{OP}} = \frac{188.5}{R_{sh} \cdot \left(T^{-1/2} - 1\right)} \tag{4.4}$$

As expected, achieving the highest ratio σ_{DC}/σ_{OP} requires both high electrical conductivity (meaning low R_{sh} values), coupled with low optical transmittance (meaning high T values). By using the empirical relationship obtained for our TCE electrodes in equation (4.2) and substituting for R_{sh} into equation (4.4), the relationship for this FoM indicator only as a function of T for our TCE electrodes can be re-expressed as:

$$\frac{\sigma_{DC}}{\sigma_{OP}} = \frac{-70.07}{ln\left(0.8 - \frac{T}{1.155}\right) \cdot \left(T^{-1/2} - 1\right)} \tag{4.5}$$

Using this semi-empirical expression, it is now possible to establish the FoM values for our TCE devices, which are shown in the Figure 4.6. The maximum TCE performance of $\sigma_{DC}/\sigma_{OP} = 317\ \Omega^{-1}$, is reached with 2 layers of silver nanowires ($T = 88.3\%$, and R_{sh}= 9.8 Ω/sq.). As seen in Figure 4.6(a), this FoM value is 2.67× higher than a conventional glass-covered ITO substrate. This is mostly due to a significantly lower sheet resistance value (T = 90.2%, and R_{sh}= 30 Ω/sq.), corresponding to a $\sigma_{DC}/\sigma_{OP} = 118.7\ \Omega^{-1}$ obtained using Equation (4.5) (Chen *et al.*, 2013).

4.2.2.2 Figure of merit: Transparent conductive materials Φ_{TC}

A different FoM indicator aims at quantifying and comparing the performance of transparent conductive electrodes with different thickness, sheet resistance and transparency values. To do so, Haacke proposed the following figure of merit indicator (Haacke, 1976):

$$\Phi_{TC} = \frac{T^{10}}{R_{sh}} \tag{4.6}$$

It is important to mention that this Φ_{TC} is not dimensionless, as one might expect from a conventional figure-of-merit indicator. Here again, we can use the empirical relationship obtained for our TCE electrodes (Equation 4.2), to substitute R_{sh}into Equation (4.6). In doing so, this second FoM indicator as a function of T for our TCE electrodes can be described as:

$$\Phi_{TC} = \frac{T^{10}}{-2.69 \cdot ln\left(\frac{0.92-T}{1.155}\right)} \tag{4.7}$$

It is obvious from both Equations (4.6) and (4.7) that this second FoM indicator will greatly favor the TCEs transparency (high T values) over their conductivity (low R_{sh}values). Figure

4.6(b) compares this second FoM indicator for our TCE electrodes and for the standard ITO-coated glass.

Once again, the maximum FoM value is found near T=90%, and corresponds to the 2-layer TCE sample ($T = 88.27\%$, and R_{sh}= 9.81 Ω/sq.). The corresponding FoM value is $\Phi_{TC} = 0.031\ \Omega^{-1}$. In contrast, accepted values (Chen *et al.*, 2013) for commercial ITO (T = 90.2%, and R_{sh}= 30 Ω/sq.) correspond to a $\Phi_{TC} = 0.012\ \Omega^{-1}$. As expected, this FoM indicator is 2.58× higher than ITO for our 2-layer TCE electrode, which is nearly identical to the previous FoM enhancement value (2.67×).

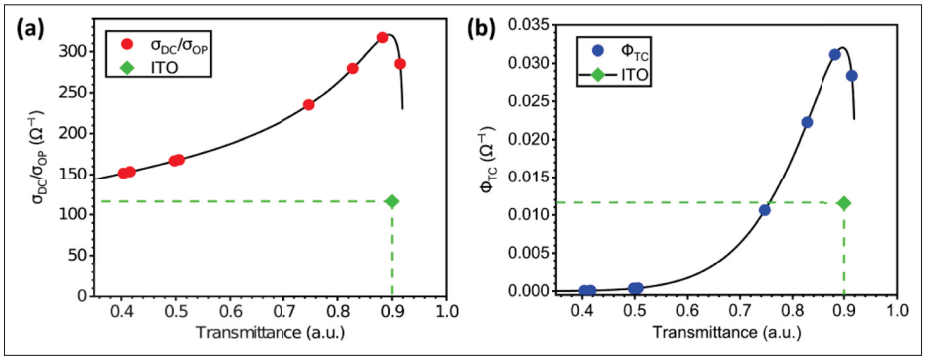

Figure 4.6 Figures of merit for transparent conductive electrodes (a) σ_{DC}/σ_{OP} and (b) Φ_{TC}. Both figures of merit conclude that the sample with 2 layers offers the best balance between transparency (T=88.27%) and sheet resistance (R_{sh}=9.81 Ω/sq.). The FoM values for ITO on glass are represented by the green diamond for reference

4.2.2.3 Figure of merit for photonic treatment versus sheet resistance of TCEs, Φ_{PT}

So far, both FoM indicators are based on the relationship between optical transmittance and sheet resistance values. The transmittance is of course defined as the fraction of the incident light intensity that reaches the opposite side (varying between 0 and 1) and it also relates to both the film's absorption coefficient α and its thickness t using the Beer-Lambert law of absorption to obtain $T = I/I_0 = e^{-\alpha \cdot t}$.

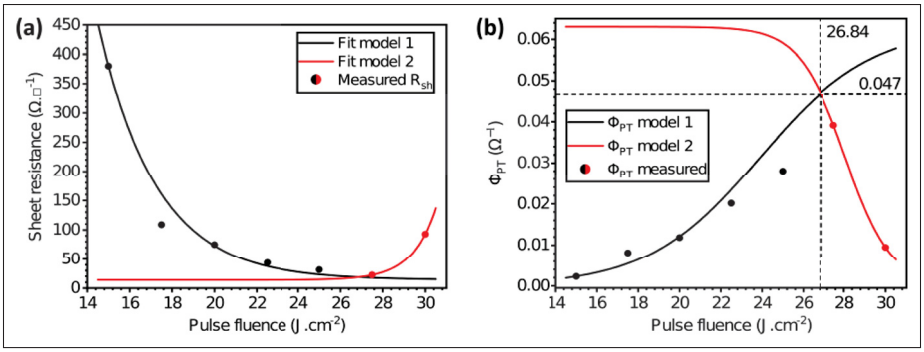

Figure 4.7 Figure-of-merit redefined for photonic treatment of transparent conductive electrodes Φ_{PT}. Dashed lines mark the highest value of the FoM corresponding to 0.0535 Ω^{-1} and a pulse fluence of F_p=26.4 J.cm^{-2}

Meanwhile, the sheet resistance, $R_{sh} = 1/\sigma t$ measures the resistance of a squared area, regardless of the area of the square and it is expressed in terms of the conductivity of the film σ and the film's thickness *t*. As such, the ratio T/R_{sh} is maximized when the thickness $t = 1/\alpha$ and $T = 0.37$. This value of transparency does not sit well with TCE's and it is why Haacke redefined the FoM giving more weight to the transmittance T using the general form (Haacke, 1976) $\Phi_{TC} = T^x/R_{sh}$.

We can now propose a new figure-of-merit indicator for photonic curing that relates the sheet resistance values of the TCE film with the pulse fluence F_p (instead of T). First an empirical relation between F_p and R_{sh} can be derived from the plot in Figure 4.7(a). Given the evolution of R_{sh} at higher values of F_p (introducing light-induced damage), it becomes necessary to split the fitting function into two models that will represent a specific set of values (black and red circles in Figure 4.7). The obtained models are represented in equations (4.8) (below the damage threshold) and (4.9) (above the damage threshold).

$$R_{sh}^{(1)} = 15 + 360 \cdot e^{(-0.4\cdot(F_P-15))} \tag{4.8}$$

$$R_{sh}^{(2)} = 15 + 1 \cdot e^{(0.88\cdot(F_P-25))} \tag{4.9}$$

Based on our preliminary results, we define this figure-of-merit for photonic treatment of transparent conductive electrodes as $\Phi_{PT} = 1/R_{sh}$. Incorporating the empirical equations (4.8) and (4.9) into this new expression for Φ_{PT} yields the FoM equations (4.10) and (4.11):

$$\Phi_{PT}^{(1)} = \frac{1}{R_{sh}^{(1)}} = \frac{1}{15 + 360 \cdot e^{(-0.4\cdot(F_P - 15))}} \tag{4.10}$$

$$\Phi_{PT}^{(2)} = \frac{1}{R_{sh}^{(2)}} = \frac{1}{15 + 1 \cdot e^{(0.88\cdot(F_P - 25))}} \tag{4.11}$$

This non-dimensionless semi-empirical FoM indicator's evolution as a function of the pulse fluence is shown in Figure 4.7(a) for samples with 2 layers of silver nanowires. The maximum value for this FoM is $\sigma_{PT} = 0.0535\ \Omega^{-1}$ with a F_p=26.4 J.cm^{-2}. As previously explained, we chose a pulse fluence value of 24.5 J.cm^{-2}, which gives a $\Phi_{PT} = 0.0364\ \Omega^{-1}$ for the sake of speed and ease of processing. Just like for the thermal annealing of silver nanowire-based electrodes, a maximum performance is reached before the electrode starts to degrade due to light-induced damage. Certainly, different factors can affect this FoM indicator, which is also based on empirical results as the other two established indicators. However, we believe it is consistent and further supports the previous conclusions drawn from the SimPulse simulations. In industrial production lines, we believe great benefits can arise from quickly characterizing and predicting the optimal fluence conditions for a given process using this indicator in conjunction with the SimPulse industrial simulation toolboxes.

4.3 Conclusions

In this work, we successfully produce high-performance transparent conductive electrodes (TCEs) made of a silver nanowire meshes on glass substrates. The photonic sintering post-processing speeds are compatible with industrial manufacturing equipment used for printed electronics. The silver nanowire films are deposited using carefully-controlled dip-coating to precisely control the nanowire densities and processed using light-pulses from a state-

of-the-art manufacturing-grade photonic curing machine (Novacentrix, PulseForge Invent). These electrodes display performances akin to thermally-annealed silver nanowire-based electrodes.

We first use SimPulse simulations and compare with known results available on the literature (for validation). While the SimPulse simulation results are consistent with the literature, we observe it does not account for the interaction between nanoparticles (inter-particle necking). As long as this model limitation is well understood, the simulation tool is accurate, and we conclude that it can be used for rapid optimization of the photonic treatment parameters for industrial-grade manufacturing purposes. We then use this simulation tool to estimate the optimal curing parameters for our nanowire electrodes.

Observing the nanowire morphology before and after the photonic curing process, we confirm that the photonic sintering significantly benefits from the metallic nanowires' morphology. The radiation energy delivered by the lamp is efficiently absorbed through surface plasmon resonance, rapidly increasing their temperature sintering the wires into a highly-conductive interconnected nanowire network.

Looking at our TCEs properties, we find that two (2) deposited layers of nanowires yield the best balance between transmittance (88.3%) and sheet resistance (9.8 Ω/sq.) values. As expected, the same sample exhibited the best performance when analyzed using the two most common figures-of-merit indicators for TCEs, namely $\sigma_{DC}/\sigma_{OP} = 317.1\ \Omega^{-1}$ and $\Phi_{TC} = 0.031\ \Omega^{-1}$. These performance values are 2.6-2.7× higher than commercial-grade ITO glass, the reference for commercial transparent conductive electrodes.

Finally, we propose a new figure-of-merit indicator for photonic curing that describes the balance between pulse fluence and sheet resistance for a constant transparency value. We observe that the photonic treatment of the silver nanowire films exhibits a bi-exponential behavior originating from the light-induced damage from exposure to excessive fluence. These results can be replicated at lower pulse fluence by incrementing the number of pulse repetitions and the emission frequency. This however, may not be convenient in fast-paced

industrial manufacturing environments but it leaves room for further investigation. We show that the optimal fluence value of 24.5 J.cm^{-2} (experimental) is consistent with the theoretical value of 23.9 J.cm^{-2} predicted by this FoM (Φ_{PT}) model. We believe using this figures of merit presented here, will help the community to better understand and predict the metallic nanowire photonic treatment phenomenon.

We believe that the results presented in this paper may help to accelerate the development of printed electronics technology. Particularly, in the rapid fabrication and integration of high-performance silver nanowire-based transparent conductive electrodes in multiple opto-electronic, energy-harvesting and sensing applications.

4.4 Methods

TCE deposition. A dispersion of silver nanowires in ethanol is purchased from ACS material chemical supplier. The average nanowire diameter is 120 nm and their lengths range from 20-30 µm. The nanowire dilution is adjusted to a concentration of 10 mg/ml and then used as is. Commercial glass substrates with dimensions 1×1.5 inches are obtained from Micro-mechanics. The glass slides are cleaned according to the following protocol: First, thorough washing with alconox detergent and rinsing with de-ionized water. Second, 15 minutes sonication in isopropanol. Finally, 15 minutes sonication in acetone. The silver nanowire mesh electrodes are deposited by dip-coating. The nanowire solution is placed in a beaker of appropriate size and the glass slides are coated using an immersion still time of 5 seconds and the withdrawal velocity was set to 200 mm/min. The holder height is adjusted so that the nanowire-covered surface area is 1 sq. inch. Kapton tape is used to cover the back of the glass substrates to prevent covering of both sides of the glass.

Photonic annealing of the samples. Each sample is processed using the Novacentrix PulseForge Invent system. The samples are taped to the system tray and only the area covered by the silver nanowires is exposed to the light pulses. To do so, the uncovered top section of the glass is covered by a metal plate (mask) held by magnets embedded in the tray.

The pulse conditions, number of pulses and exposure method were kept the same for all samples. Only the number of layers in the sample fabrication is changed to vary the nanowire density (and the TCE transparency). Using a single flash, we optimized the pulse fluence in order to achieve the lowest sheet resistance values for TCE samples with 2 layers of silver nanowires. The lowest sheet resistance was obtained with a pulse fluence of 27.5 J.cm^{-2} with the single pulse characteristics presented in Figure 4.1(b). At this fluence value, the emission frequency of the machine is limited and the processing time increases. For this reason we chose a slightly lower fluence at 24.5 J.cm^{-2} to enable faster processing, achieving low sheet resistance while reaching the target temperature of 300 °C as predicted in our simulations from Figure 4.1(a). From the simulation, the number of pulses to reach 300 °C is set to 15 and is the value used for processing all the samples. After photonic processing, commercial silver-flake paste (Novacentrix, Metalon HPS-021LV) is used to apply the electrical contacts on the four corners of the silver nanowire films by drop casting a small amount and curing at 80 °C for 60 minutes. This paste facilitated measuring the electrical conductivity of the films without damaging or affecting the film's acquired electrical properties in any way.

Sample characterization. After photonic curing and drying of the the silver paste pads, the sheet resistance is measured with a Keithley 2400 source unit to measure the resistivity values across the contacts. The non-uniformity factor (NUF) was done dividing the total area of the sample in 12 regions and measuring the sheet resistance on each region using a Four-point Probe system from Ossila. The calculation of the NUF value was done following the procedure described elsewhere (Jia *et al.*, 2016) Nanowire surface fill factor F_F was measured using a 3D laser confocal microscope LEXT OLS4100 from Olympus. Ten 120 by 120 µm images are taken at random places in the films, using the 100X objective. For each image, the auto-enhance setting from the microscope's own software is applied to improve clarity and contrast. Afterwards all images were binarized using Matlab, where white pixels corresponded to nanowires while black pixels to areas devoid of them. The surface fill factor F_F is then computed by dividing the number of white pixels over the total pixel count of the image. Finally, the value for F_F of each of the ten images taken per sample are averaged

to obtain the overall F_F value for a given sample. Scanning electron microscopy (SEM) characterization is performed using a SU8230 microscope from Hitachi. Transmittance T was measured using a Ocean Optics Flame spectrometer and a LS-1 tungsten halogen lamp that covers the full visible spectrum from 400 - 800 nm. The 100% transmittance baseline is set using a clean glass slide to obtain only the transmittance value for the TCE. The film's transmittance value is obtained by dividing the measured transmittance over the glass transmittance at that respective wavelength (baseline correction), then averaged over the whole spectrum (400-800 nm). Finally, these ten transmittance values are again averaged to provide the final transmittance value for any given sample. Haze was measured using the UV-VIS-NIR spectrophotometer Perkin Elmer, Lambda 750 with an integrating sphere. This measure required four scans, two of them with the sample located at the entrance of the integrating sphere providing the total transmittance (T2) and the forward scattered light of the sample (T4). The other two scans were done without the sample to remove the scattering of light originated in the equipment itself, with one scan using the white standard (T1) and one open-ended (T3). Haze is then calculated with the following relation:

$$Haze = \left(\frac{T4}{T2} - \frac{T3}{T1}\right) \cdot 100\%$$

Acknowledgements S.G.C. thanks the Canada Research Chair and the NSERC Discovery programs for their support

Author contributions statement L.F.G. contributed to design, fabrication and analysis of samples as well as writing of this manuscript. J.A.B-G. contributed in the photonic sinterization of the samples and manuscript writing. S.G.C. contributed to analysis and the extensive revision of the manuscript. All authors reviewed the manuscript.

Competing interests The authors of this manuscript declare no competing conflict of interests in its publication.

Keywords nanowires, photonic curing, simulation, simpulse, pulseforge, electrodes

CHAPTER 5

PHOTONIC POST-PROCESSING OF A MULTI-MATERIAL TRANSPARENT CONDUCTIVE ELECTRODE ARCHITECTURE FOR OPTOELECTRONIC DEVICE INTEGRATION

Luis Felipe Gerlein[1] , Jaime Alberto Benavides-Guerrero[1] , Sylvain G. Cloutier[1]

[1] Département de Génie Électrique, École de Technologie Supérieure,
1100 Notre-Dame Ouest, Montréal, Québec, Canada H3C 1K3

Article ID: RA-ART-10-2023-007103 under peer-review in *RSC Advances*. Submitted in October 2023

Abstract: Emerging flexible optoelectronic devices require multi-material processing capabilities to fully enable the use of temperature-sensitive substrates and materials. This report demonstrates how photonic sintering enables the processing of materials with very different properties. For example, charge carrier transport/blocking metal-oxides, and transparent conductive silver nanowire-based electrodes ought to be compatible with low-energy and high-throughput processing for integration onto flexible low-temperature substrates. Compared to traditional post-processing methods, we show a rapid fabrication route yielding highly-stable hybrid electrode architectures on polyethylene terephthalate (PET). This architecture consists of an interconnected silver nanowire network encapsulated with a thin crystalline photo-sensitive titanium dioxide (TiO_2) coating, allowing both layers to be treated using independent photonic post-processing sintering steps. The first step sinters the nanowires, while the second completes the conversion of the top metal-oxide layer from amorphous to crystalline TiO_2. This approach improves on the fabrication speed compared to oven processing, while delivering optical and electrical characteristics comparable to the state of the art. Optimized transparency values reach 85% with haze values down-to 7% at 550 nm, while maintaining a sheet resistance of 18.1 Ω/sq.. However, this hybrid architecture provides a much stronger resilience to degradation, which we demonstrate through exposition to harsh plasma conditions. In summary, this study shows how carefully-optimized photonic curing

post-processing can provide more-stable hybrid architectures while using a multi-material processing suitable for high-volume manufacturing on low-temperature substrates.

5.1 Introduction

Flexible hybrid optoelectronic integration faces several fundamental challenges before achieving low-cost manufacturing of high-performance devices on low-temperature flexible substrates. These low-cost substrates generally bring stringent processing requirements, leading to critical manufacturing issues. Emerging techniques such as laser- or flashlamp-based (so-called photonic) post-processing sintering offer promising alternatives to conventional oven-based processing for heat-sensitive substrates (Das *et al.*, 2016; Daunis *et al.*, 2020; Feleki *et al.*, 2017; Jang *et al.*, 2020; Jiu *et al.*, 2012; Piper *et al.*, 2021; Schroder, 2011; Song *et al.*, 2015a). By carefully tuning the processing conditions for each individual material, it becomes possible to process multiple thin films independently on the same device, without thermal annealing and at high speeds. Thin films made of metallic nanoparticles need to be processed with a small number of high power density pulses to achieve high-density conductive films (Bansal & Malhotra, 2016; Dexter *et al.*, 2017). For ceramic materials, a larger number of lower power-density pulses tends to achieve improved densification and crystallization (Noh *et al.*, 2022). While these general rules may seem incompatible, they can be combined to process multi-material devices using the same rapid-processing equipment. Indeed, this possibility to process multiple materials using a minimal set of tools could prove a great advantage for the rapid assembly of flexible devices by reducing the number of fabrication steps and increasing their throughput.

One important component of many flexible hybrid optoelectronic devices is the transparent conductive electrode (TCE). However, they can be especially difficult to integrate on low-temperature flexible substrates. Similarly, carrier transport/blocking metal-oxide layers also often require processing steps incompatible with low-temperature substrates. These common materials widely-used in optoelectronics were previously treated using photonic post-processing (Feleki *et al.*, 2017; Jang *et al.*, 2020; Zamanpour *et al.*, 2021). However,

combining them brings a whole new level of complexity for the processing technique to remain unchanged.

Percolated networks of silver nanowires are ideal candidates for indium-tin-oxide (ITO) film replacement due to higher conductivity (Gerlein *et al.*, 2021; Sepulveda-Mora & Cloutier, 2012; Sun, Gates, Mayers & Xia, 2002b; Sun, Yin, Mayers, Herricks & Xia, 2002c), improved substrate adhesion (Song *et al.*, 2015a; Song *et al.*, 2015b), high optical transmission (Azulai, Belenkova, Gilon, Barkay & Markovich, 2009; Menamparambath *et al.*, 2016; Preston, Xu, Han, Munday & Hu, 2013) and flexibility (Jiu *et al.*, 2012; Park *et al.*, 2017). Photonic sintering of metallic nanowires can be successful in creating semitransparent, conductive percolated networks, because of the light-induced plasmonic welding that can occur at the nanowire junction (Niittynen, Sowade, Kang, Baumann & Mäntysalo, 2015; Garnett *et al.*, 2012). Most metallic nanostructures exhibit surface plasmon resonance throughout the visible spectrum, making them strong light absorbers compared to non-plasmonic nanoparticles (Chan, Zhao, Hicks, Schatz & Van Duyne, 2007). This is why photonic sintering systems rely on high-power and wide-spectrum xenon flash lamps (Jang *et al.*, 2020).

Meanwhile, emerging solution-based metal-oxide precursors offer a great potential for integration on low-temperature flexible substrates using high-throughput industrial manufacturing processes (Lee, Chang, Herman & Chang, 2007; Scheideler & Subramanian, 2019; Weidling, Turkani, Luo, Schroder & Swisher, 2021). Titanium dioxide (TiO_2) is of particular interest for a wide range of optoelectronics devices, both as an active material and as an electron transport layer (Bai & Zhou, 2014; Bai *et al.*, 2014). For example, inkjet-printed UV photodetectors exploiting the synergistic relationship between TiO_2 and silver nanowires have been demonstrated, highlighting the potential of these two materials for printed optoelectronic device development (Bai & Zhou, 2014; Chen *et al.*, 2015). Similarly, printed oxide thin-film transistors (TFTs) on memory polymers were also previously demonstrated (Daunis *et al.*, 2018). There, the metal-oxide layer is exposed to UV through shadow-masks in a roll-to-roll configuration. Ongoing research on large-area light-induced sintering & crystallization of metal-oxide materials such as titanium dioxide for optoelectronic devices can be divided

into three main areas: UV source-induced (Di Giacomo *et al.*, 2015; Hwang *et al.*, 2014; Jeong *et al.*, 2016; Nakajima *et al.*, 2014), visible and NIR light-induced (Benavides *et al.*, 2018; Benavides-Guerrero *et al.*, 2022b; Gerlein *et al.*, 2019; Qian & Shen, 2013; Zocca, Colombo, Gomes & Günster, 2015) and broadband, pulsed light-induced crystallization (Das *et al.*, 2016; Feleki *et al.*, 2017; Hwang & Kim, 2015; Luo *et al.*, 2017; Zamanpour *et al.*, 2021). Traditionally, most metal oxides are transparent in the visible part of the spectrum, and photonic post-processing requires higher energy than that required to process metallic nanostructures (Noh *et al.*, 2022).

Previous reports describe hybrid composite architectures combining TiO_2 and silver nanowires (Song *et al.*, 2015b; Chung, Song, Bob, Zhu & Yang, 2012; Huang, Cheng, Ho & Huang, 2021a; Lee, Lee, Yoo, Lee & Jung, 2016; Yeh, Chen, Yang, Chen & Chen, 2017). These hybrid platforms have demonstrated improvements to the wire-to-wire junction resistance (Song *et al.*, 2015b; Huang *et al.*, 2021a), the chemical stability of the network (Lee *et al.*, 2016), the thermal resilience and overall electrode longevity when exposed to higher temperatures than those supported by bare nanowire networks (Yeh *et al.*, 2017; Ramasamy, Seo, Kim & Kim, 2012). This is mainly achieved using conformal coatings through atomic layer deposition techniques or decorating the silver nanowires with metal-oxide nanoparticles (Chung *et al.*, 2012; Yeh *et al.*, 2017). These improved operating conditions enabled the development of thin-film transistors on rigid substrates and flexible memristors (Song *et al.*, 2015b; Resende *et al.*, 2021). However, these current methods of deposition and treatment of the TiO_2 layer still rely on amorphous metal-oxide films, traditional sol-gel chemical routes, use of rigid substrates, complicated and expensive and low-yield depositing techniques. Overall, these methods miss out on the potential advantages of using crystalline materials and the possibility for integration into streamlined roll-to-roll fabrication facilities (Song *et al.*, 2015b; Resende *et al.*, 2021).

This report describes a simple fabrication method for producing a multi-material, stable hybrid TCE architecture on PET using two separate photonic post-processing treatment steps. The detailed processing conditions illustrate how to exploit the response of each material to tune

the flashing parameters, allowing each material to be processed independently of the others. The use of photo-sensitive TiO_2 not only provides important environmental protection and stability to these films, while further improves their electrical properties. These hybrid TCE architectures offer a platform that can be integrated into the fabrication of next-generation optoelectronic components at low fabrication costs by incorporating straightforward fabrication techniques.

5.2 Results

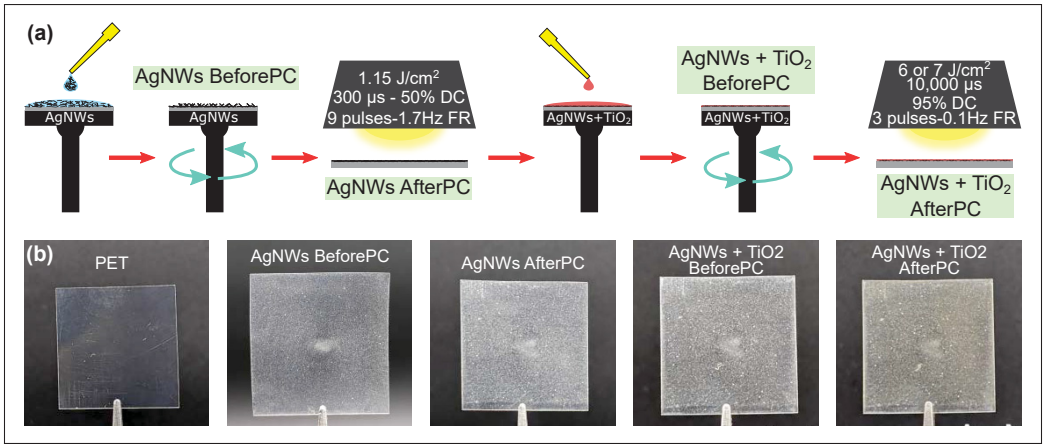

Figure 5.1 Schematic representation and pictures of the fabrication steps for the hybrid TCE architecture (a) Step-by-step graphical depiction of the fabrication steps and the necessary photonic curing conditions (b) Photographs of samples at each stage of the fabrication of the hybrid TCE architecture

A step-by-step overview of the fabrication process for the hybrid TCEs is shown in Figure 5.1, comparing the pristine and coated PET substrates. It is worth noting that the dark background greatly enhances the contrast of the images compared to a white background, but visually exaggerates the apparent loss of transparency and haze of the films, which will both be quantified later. The labels highlighted in green identify each processing step, and this nomenclature will be used throughout the manuscript. As explained in the experimental section, plasma is used to clean and prepare the flexible PET substrates. For both layers, similar spin-coating conditions of 4000 rpm for 30 seconds are used for material deposition.

Optimal photonic sintering parameters for the welding of the AgNWs atop the PET substrates are based on a previously-published study (Jiu *et al.*, 2012). A rapid succession of 9 pulses at a firing rate of 1.7 Hz, fluence of 1.15 J.cm^{-2}, an envelope of 300 µs with 50% pulse duty-cycle are enough to weld the silver nanowires, creating a highly conductive layer. In this stage, the pulse conditions and the number of pulses are optimized to achieve the best sheet resistance (R_{sh}) value for the TCE films, while preserving the bulk structural and optical properties of the PET. Photographs of samples at each fabrication stage are shown in Figure 5.1(b).

Subsequently, a solution consisting of a 10% w/w dilution of the photo-sensitive TiO_2 in anhydrous ethanol was prepared and deposited by spin-coating. This photo-sensitive TiO_2 precursor is synthesized following a previously-published procedure (Benavides-Guerrero *et al.*, 2022b), which is also briefly summarized in the experimental section. This special chemical route yields a defect-rich TiO_2 sol-gel precursor, for which the visible-light absorption is significantly enhanced (Rajaraman, Parikh & Gandhi, 2020). This amorphous precursor is shown to crystallize using 405 or 532 nm laser sources, under environmental conditions (Benavides *et al.*, 2018; Benavides-Guerrero *et al.*, 2022b; Gerlein *et al.*, 2019). It is also suitable for photonic post-processing using a wide-spectrum light source such as a Xenon flash lamp. This crystalline TiO_2 layer can be used in the fabrication of optoelectronic devices, whether as the active layer of a photodetector or as an electron transport layer (Chen *et al.*, 2015; Huang *et al.*, 2021a; Lee *et al.*, 2016).

The coated samples are then exposed a second time to crystallize the TiO_2 layer using a slow progression of 3 pulses, delivered at a firing rate of 0.1 Hz, with an envelope of 10,000 µs with a 95% duty cycle. The energy density delivered depends on the crystalline phase desired depending on the target application, using 6 J.cm^{-2}, or 0.6 kW.cm^{-2}, to convert to anatase. To crystallize into rutile, 7 J.cm^{-2} or 0.7 kW.cm^{-2}, were necessary. This crystallized TiO_2 layer provides increased protection of the nanowire-based electrode in this hybrid TCE architecture.

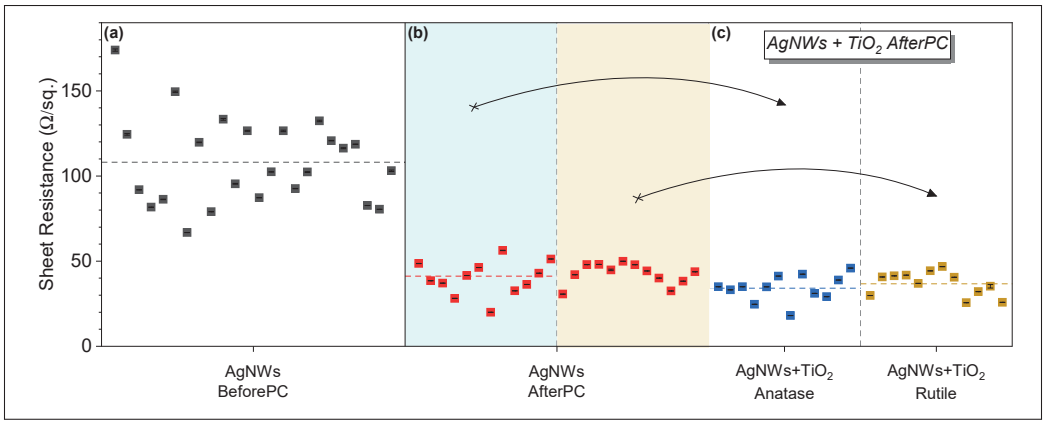

Figure 5.2 Sheet resistance of a group of 24 hybrid TCE samples at different stages of the fabrication process. The horizontal dashed lines denote the mean R_{sh} value for each group of samples. (a) Initial R_{sh} values for all the samples *AgNWs BeforePC*. (b) Resulting R_{sh} for all samples at *AgNWs AfterPC* stage. After deposition of the photo-sensitive TiO_2 precursor, half the samples are crystallized to form anatase TiO_2, while the other half is converted to rutile. This is shown by the blue and yellow shaded areas in the (b) section of the plot. (c) The arrows indicate the resulting R_{sh} values for each subgroup after the second round of photonic post-processing, the *AgNWs + TiO_2 AfterPC* stage

The electrical properties measured after each fabrication stage are compared in Figure 5.2. There, individual statistics are presented for multiple groups of devices. Indeed, the average sheet resistance for the percolated silver nanowire network is R_{sh} = 108 Ω/sq. before treatment, and it is shown in Figure 5.2(a). After the photonic sintering of the AgNWs, Figure5.2(b) shows an average R_{sh}= 41 Ω/sq. for the same 24 samples. This represents a 62% average reduction of the sheet resistance due to better contacts between the nanowires, as illustrated by the dashed gray and red lines. After the deposition of the photo-sensitive TiO_2 precursor on all the samples, 12 samples are converted to anatase and 12 are converted to rutile. They are separated into the blue- and yellow-shaded areas in Figure 5.2(b). The average sheet resistance of the 12 samples covered with anatase is R_{sh}= 34 Ω/sq., compared R_{sh}= 37 Ω/sq. for the samples covered with rutile TiO_2. These averaged values represent an additional 6% reduction, compared with the standalone AgNWs electrodes. This additional reduction is attributed to the densification that occurs with the crystallization of TiO_2 (Song

et al., 2015b). The presence of oxygen vacancies in the TiO_2 precursor makes it sensitive to visible light, and crystallization is possible using photonic post-processing. These oxygen vacancies could contribute to enhance the conductivity in the films by facilitating charge transport, thanks to the vacancies acting as dopant states that shift the material's Fermi level close to the conduction band (Maarisetty & Sundar Baral, 2020; Pham & Wang, 2014). Testing of this effect is out of the scope of this communication given its minor contribution to the TCE's final sheet resistance.

SEM images of the silver nanowire electrodes before, in Figure 5.3(a), and after photonic sintering are shown in Figure 5.3(b-c). These results suggest a good welding of the nanowire network as well as moderate penetration in the surface of the PET substrate after photonic treatment. In Figure 5.3(c), we notice what appears to be a substrate's surface morphology change that comes as a result of the intense heat generated locally. This leads to partial melting of the substrate in the regions that are directly around and in close contact with the heated nanowires (Park *et al.*, 2017). This partial substrate melting did not globally change the optical properties and flexibility of the bulk film, but it has been reported that it can contribute to improving the adhesion to the substrate and the overall sturdiness of the film (Jiu *et al.*, 2012; Park *et al.*, 2017; Song *et al.*, 2015a). The embedding of the nanowires and the local modification of the small regions of the PET substrate around the heated nanowire parts was resolved with the help of atomic force microscopy (AFM). These effects can be clearly appreciated in Figure III-1 of the Supplementary information, showing a sample of *AgNWs AfterPC*. In the areas without nanowires, the surface of the PET film remained unchanged, thus, the surface bumps are attributed to the excess heat generated at the nanowires during the photonic processing.

The silver nanowire electrodes covered with the TiO_2 coating before photonic treatment are shown in Figures 5.3(d, e). The same electrode after photonic treatment is shown in Figure 5.3(f). This additional layer has been shown to provide thermal stability, environmental protection, sustainability and protection against UV degradation for the nanowire film (Lee *et al.*, 2016; Ramasamy *et al.*, 2012; Song *et al.*, 2015b; Yeh *et al.*, 2017). It also provides the

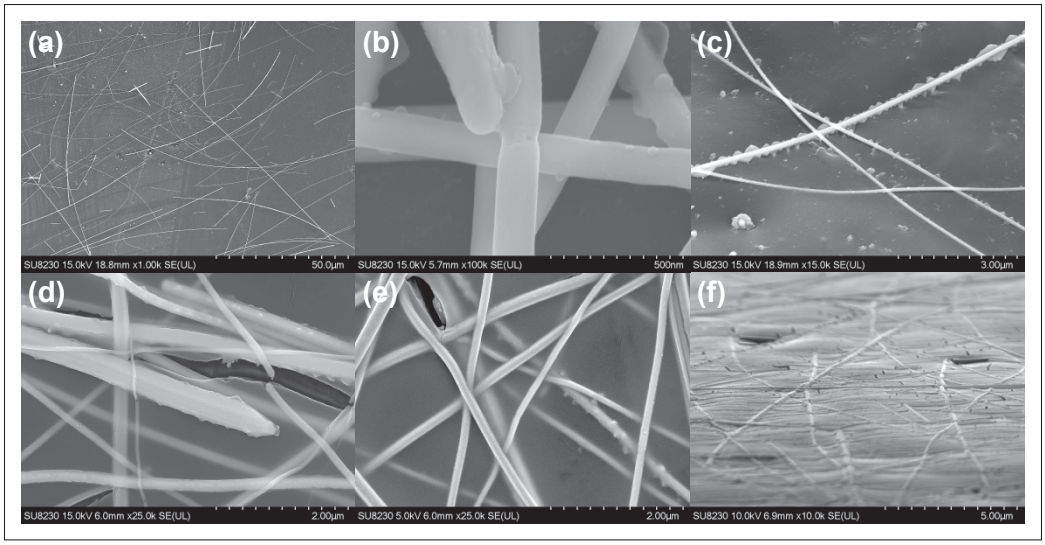

Figure 5.3 SEM micrographs of the silver nanowire films on PET. (a-c) Silver nanowire networks after photonic curing at different magnifications. (d-f) Silver nanowires covered with the TiO_2 coating (d-e) before and (f) after photonic sintering

benefit of an additional functional layer of metal-oxide material that can be useful for device integration. Surface coverage with energy-dispersive X-ray spectroscopy (EDS) results are presented in Figure III-2 of the supplementary section, showing an approximately 400 nm TiO_2 layer covering the nanowire film. The densification resulting from the crystallization of the amorphous TiO_2 layer is known to potentially increase the close contact between the adjacent nanowires, leading to slight improvements in the overall sheet resistance of the film even after the initial flash-driven plasmonic welding (Song *et al.*, 2015b). The versatility of the photonic sintering process also allows to dry and process films where residual solvents may be present, by using long-envelope pulses that facilitate the drying process and trigger the film's crystallization (Noh *et al.*, 2022). This is shown in the secondary post-treatment step described in Figure 5.1.

Atomic force microscopy (AFM) analysis was employed to investigate the surface topography of crystallized TiO_2 films atop the AgNWs. Samples with AgNWs after photonic sintering (*AgNWs AfterPC*) were partially covered in transparent scotch tape. Then, the same TiO_2 deposition and crystallization procedures took place. Finally, the tape was removed revealing

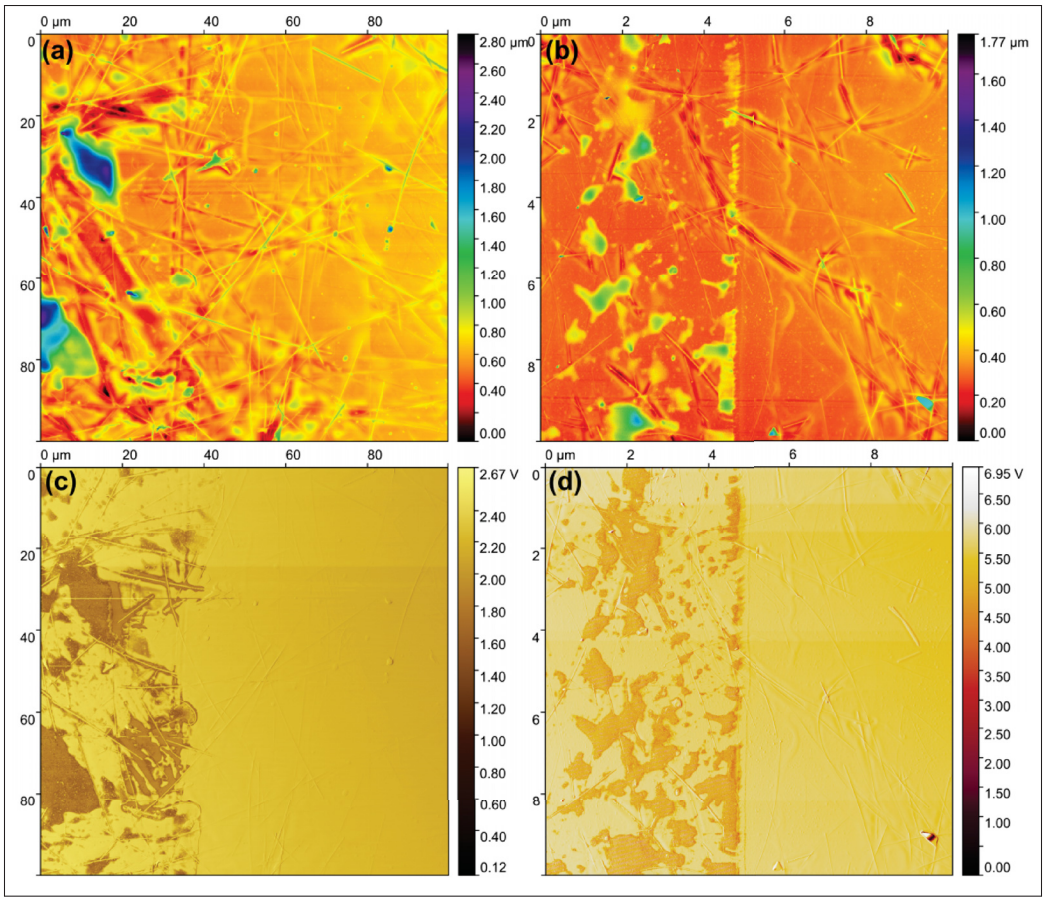

Figure 5.4 Topographic images for samples crystallized into (a) anatase and, (b) rutile. Inphase images for samples crystallized to anatase (c) and rutile (d), showing complete coverage of the AgNWs by the TiO2 film. In (a) and (c), the areas whose height color correspond to green and higher, are glue residues left by the tape after removal. The AgNWs however, remain fixed to the PET substrate

an area with bare AgNWs next to an area completely covered by crystallized TiO_2. The resulting AFM topography analysis shown in Figure 5.4(a) and (b) presents the partial coverage of anatase and rutile TiO_2, respectively. The scotch-tape tests also confirm the presence of AgNWs after its removal, showing the permanence of the nanowires embedded in the PET. Although precise film height estimation from AFM profiles proved challenging, a qualitative assessment was achieved by comparing image colors with the scale bar. The height of anatase film was estimated to be around 600 nm, shown in Figure 5.4(a). The rutile-covered sample, Figure 5.4(b), displayed an average height of around 400 nm. Inphase

images in Figures 5.4(c) and (d), facilitated the discrimination of coated and uncoated areas, demonstrating robust coverage of AgNWs by crystallized TiO_2 films, as presented in Figure 5.3. Importantly, the scotch-tape glue was affected by the photonic processing and transferred to the films upon removal. This is evidenced by regions whose height registered above the hybrid films, corresponding to green and above colors in the Figures 5.4(a) and (c) and the darker regions in Figures 5.4(c) and (d).

With respect to the optical properties of these hybrid TCEs, the deposition of the TiO_2 layer impacts the overall transparency of the film by a small margin, with losses ranging between 1% and 2% when measured at 550 nm. In contrast, the amorphous TiO_2 layer does increase the haze factor in the films, which is then changed by the photonic-induced crystallization process. The comparisons for visible transmittance and haze can be observed in Figure 5.5(a, b). The transmittance is measured for all samples presented in Figure 5.2, while the haze was measured in one randomly-selected sample after each fabrication step. The values presented in Table 5.1 correspond to the average transmittance and the haze values measured at 550 nm at each step of the fabrication process. Haze values are obtained using the technique described in the supplementary information in Figure III-4, while the transmittance spectra for the 12 anatase and rutile samples are shown in Figure III-5.

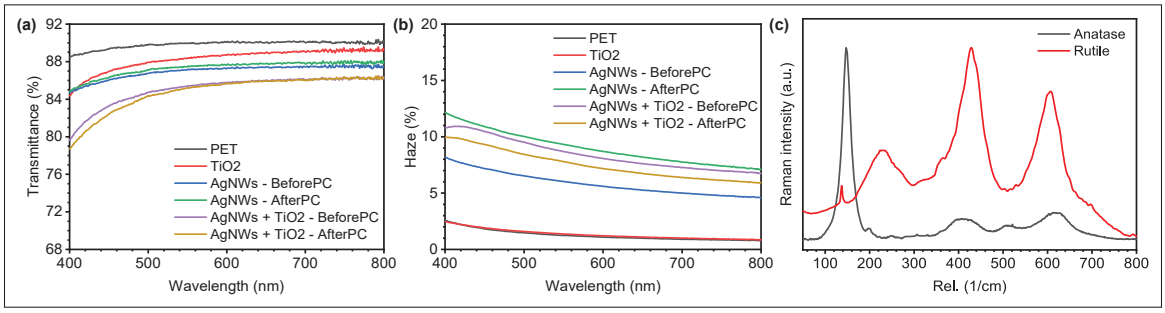

Figure 5.5 Optical properties of the hybrid TCE architecture samples at various stages of the fabrication process. (a) Transmittance of the samples at each stage of the fabrication process. (b) Haze of the samples at each stage of the fabrication process. (c) Confocal Raman micro-spectroscopy results from the crystallized samples after 6 and 7 $J.cm^{-2}$exposure, which are consistent with the anatase and rutile TiO_2 phases respectively

Table 5.1 Averaged transmittance and haze values at 550 nm measured at various stages of the fabrication process

	Transmittance (%)	**Haze (%)**
PET	89.8	1.3
PET + TiO_2	88.4	1.3
AgNWs BeforePC	86.9	5.8
AgNWs AfterPC	86.5	8.9
AgNWs + TiO_2 AfterPC (Anatase)	85.0	7.8
AgNWs + TiO_2 AfterPC (Rutile)	85.2	7.7

Two independent methods are used to confirm the crystallization of the TiO_2 layer. First, we can use a modified developing solution (*DevSol*), whose preparation is described in the Methods section. This *DevSol* test is known to wash away the non-crystallized TiO_2, while the crystalline TiO_2 remains (Daunis *et al.*, 2018, 2020). This simple method helps to quickly determine the optimal pulse conditions to yield a crystalline structure, as a 15 second immersion and subsequent washing in DI water are enough to establish the crystalline state of our films. Figure 5.6(a) shows a sample with an amorphous TiO_2 layer (*AgNWs + TiO_2 BeforePC*) that failed the *DevSol* test. Because of the transparency of the TiO_2 film, the red dashed line in Figure 5.6(a) helps to distinguish between the top washed-away region from the unwashed bottom. For contrast, a sample where the layer is fully crystallized (*AgNWs + TiO_2 AfterPC*) is shown in Figure 5.6(b) and, that same sample after it was immersed in the *DevSol* for 15 seconds in Figure 5.6(c) maintaining its integrity and the coverage properties of the TiO_2 layer.

In turn, Raman spectroscopy can be used to assess the samples that passed the *DevSol* test. Raman micro-spectroscopy results from Figure 5.5(c) clearly show the anatase and rutile TiO_2 signatures after the proper photonic treatment. As such, these results confirm that this precursor can be controllably-converted to anatase or rutile TiO_2 depending on the target application. Most importantly, this can be done with little consequences on both the R_{sh} values and the optical transmittance of this hybrid TCE architecture as shown in Figure 5.2 and Figure 5.5(a). It is very hard to obtain conclusive XRD measurements from smooth thin films

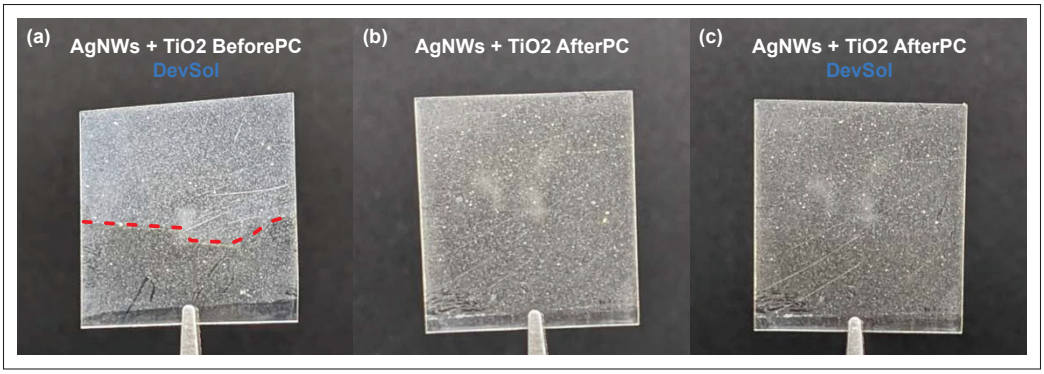

Figure 5.6 Effects of the developing solution on the TiO_2 layer atop the silver nanowires. (a) A sample with an amorphous layer after *DevSol* immersion for 10s. The red dashed line helps distinguish the TiO_2 layer left from the washed away region. (b) A sample after photonic curing of the TiO_2 layer to yield a fully crystallized coating. (c) The same sample after 10s immersion in the *DevSol* showing the permanence of the TiO_2 layer

of TiO_2 atop a PET substrate and AgNWs in between. The PET substrate generates a strong signal that completely obscures any other signal coming from the hybrid-TCE constituents. Dried TiO_2 precursor, compressed in pellet form enables proper XRD characterization of the crystalline state after the photonic processing has taken place. Figures III-3(a,b) show the crystallization of these pellets processed to yield anatase and rutile phases.

Finally, it was previously shown that conformal coatings using TiO_2 to cover silver nanowire films offer environmental protection against degradation and oxidation of the silver, thus preserving its electrical properties (Song *et al.*, 2015b; Lee *et al.*, 2016; Yeh *et al.*, 2017; Huang *et al.*, 2021a). We chose to test the additional protection offered by the crystallized TiO_2 coating by exposing a new set of samples to oxygen plasma during a brief period. Experimental results shown in Figure 5.7 clearly indicate that only 40 seconds of plasma exposure at 50 W ionization power is enough to increase the sheet resistance of the unprotected electrodes by several orders of magnitude. Higher ionization power or longer exposure times easily break the unprotected films, and it becomes impossible to measure the sheet resistance value throughout the whole film. Figure 5.7(a) shows that unprotected samples turned dark as a

result of the forced oxidation of the silver (Akinsinde *et al.*, 2021), unlike the samples protected by a thin crystallized TiO_2 coating and shown in Figure 5.7(b). Figures 5.7(c-d) compare the sheet resistance values for the hybrid TCEs before and after the oxygen plasma treatment. In Figure 5.7(c), bare silver nanowire films (samples S1-S4) show a pronounced increase in their R_{sh} compared to the samples S5-S7 that were protected by the thin crystallized TiO_2 coating. These changes in R_{sh} are highlighted in Figure 5.7(d).

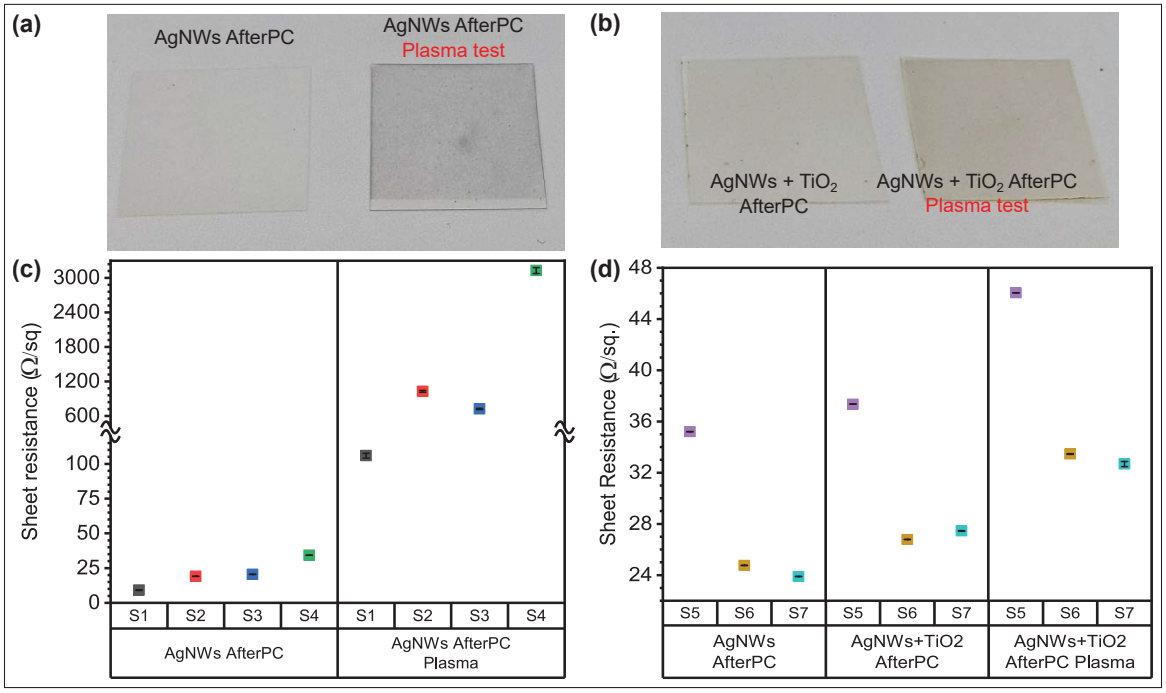

Figure 5.7 Effects of plasma etching on a new set of samples. (a) *AgNWs AfterPC* samples only and (b) *AgNWs + TiO_2 AfterPC* samples. (c) This plot shows *AgNWs AfterPC* samples S1-S4 before and after they were subject to plasma exposure and its impact on their R_{sh}. Note the y-axis break that facilitates data display. (d) This plot shows the $R_{sh}$for samples S5-S7 after the photonic sintering of the AgNWs, then after the photonic crystallization of the TiO_2 layer and finally, after the plasma treatment

A useful tool to visualize the heat dissipation during both rounds of photonic sintering is through the SimPulse simulation tool available within the PulseForge Invent system. This simulation can allow us to better understand the macroscopic effects of the photonic post-processing parameters on the substrate to avoid thermally-induced structural damage. There, layers of material can be stacked atop each other, and the simulation shows the temperature

time profile at each interface and at specific chosen depths. In Figure 5.8(a), simulations suggest that direct heating of the silver nanowires occurs during the first 150 µs of the first pulse. Then, rapid cooling dominates thanks to the thermal mass present in the substrate. As expected, the whole nanowire film and the surface of the PET follow the same temperature profile. Moving deeper into the substrate after 25% of the total thickness, the temperature profile stays below 200 °C as represented by the dashed blue line. The continuous green line illustrates how the bottom of the PET barely registers any temperature increase throughout the entire process due to the significant thermal gradient.

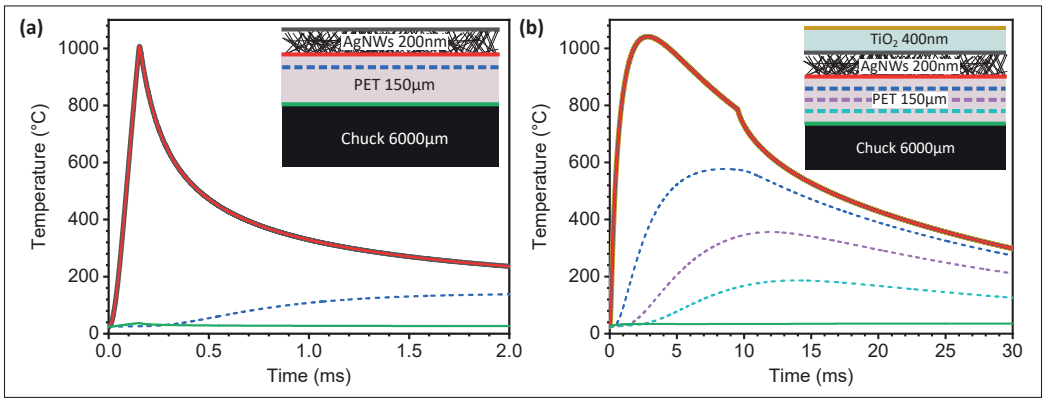

Figure 5.8 Thermal profile simulations of both photonic sintering processes obtained with the SimPulse simulation tool. (a) Thermal profile over time between the silver nanowire film and the substrate. The blue dashed line shows the temperature profile at 25% of the total thickness of the substrate, starting from the interface with the nanowire film. (b) Thermal profile over time for the hybrid TCE during the photonic sintering treatment. The temperature profile inside the substrate is calculated at three distances (25%, 50% and 75% from its surface) represented by the dashed lines. In both figures, the legend is shown by a schematic of the device under analysis, where the horizontal lines correspond to the plotted lines

In contrast, the transient temperature profile of the device with the TiO_2 coating shows a synergistic effect. We assume that both the silver nanowires and amorphous TiO_2 follow the same temperature progression as their simulated profiles are perfectly superimposed in Figure 5.8(b) as shown by the yellow, dark grey and red continuous lines. Of course, this heating profile is most likely to be non-uniform, with a local heating effect more pronounced

around the nanowires. Even though the system reaches temperatures of over 1000 °C, the nanowire network easily transfers this excess heat to both the substrate and the TiO_2 coating, helping with the crystallization process (Lermusiaux, Mazel, Carretero-Genevrier, Sanchez & Drisko, 2022). In this case, we analyze the temperature profile inside the PET substrate at 25, 50 and 75% of the PET's total thickness, shown in Figure 5.8(b). At around 75% of the substrate's thickness, the temperature never surpasses 200 °C, which is in line with the thermal specifications of the PET substrate thus avoiding damage to it.

5.3 Discussion

Conceptually, it is somewhat surprising to observe that the silver nanowire film's properties remain mostly unchanged when a long pulse is used to crystallize the thin amorphous TiO_2 coating. Pulses of 10's to 100's of microseconds in duration quickly raise the temperature of the metallic nanowires, enabling the formation of strong joints at the points where the nanowires are in contact. This occurs thanks to the almost instantaneous localized heat generation along the nanowire network as a result of the surface plasmon resonance that metallic nanostructures exhibit in the visible portion of the electromagnetic spectrum (Garnett *et al.*, 2012; Luo *et al.*, 2017). Because plasmon-induced welding is self-limiting, the heat accumulation at the intersections stops once the joining process occurs (Bansal & Malhotra, 2016). When the absorbed photonic energy converts into heat, it then spreads throughout the whole percolated nanowire network before being dissipated in the substrate. This suggests that heat dissipation from the AgNWs is facilitated by the superior heat capacity and low thermal conductivity of the substrate (Jang *et al.*, 2020). Additionally, direct contact with the aluminum chuck cools the substrate's back, creating a large thermal gradient. Finally, increasing the pulse fluence by adjusting the time envelope can facilitate greater heat transfer from the nanowires to the substrate (Jang *et al.*, 2020). For the case of the longer pulses used to crystallize the TiO_2 layer, the heating is much slower. This favors the ceramic crystallization process while still giving sufficient time for the surface of the substrate to reach thermal

equilibrium, preventing any thermally-induced damage, even though the temperature reached at the substrate's surface is much higher, as seen in Figure 5.8(b).

This can be understood from the thermal equilibration time τ calculated for each of the materials involved (Schroder, 2011). Based on the material parameters available in the SimPulse simulation, a 150 µm-thick PET substrate possesses a τ_{PET} = 23 ms, for a 200 nm-thick film of silver nanowires is τ_{AgNWs} = 58 ps approximately (Ji, He, Wang, Ran & Ye, 2014) and the TiO_2 coating possesses a τ_{TiO_2} = 7 ns approximately, a value that is obtained from the database present in the SimPulse software. One of the conditions necessary to achieve successful photonic curing of materials is that the pulse duration (t_p) must be much shorter than the thermal equilibrium time of the substrate (τ_{PET} = 23 ms, from SimPulse material database). In this case, the heat generation coming from the silver nanowire film can be dissipated into the substrate. If the nanowires are processed using a longer pulse envelope comparable to τ_{PET}, the absorbed energy will transfer to the substrate too fast to properly weld the film of nanowires. This also explains why the pulse conditions used to crystallize the TiO_2 layer does not affect the $R_{sh}$of the already treated nanowire film, even if the pulse fluence is about 6x times higher than the pulses used to process the nanowires. Indeed, higher fluence in longer pulses does not necessarily translate into higher peak power density (PPD). The short pulse used in the photonic treatment of the silver nanowires possesses a PPD of 7.21 $kW.cm^{-2}$, whereas the long pulse with higher fluence used in the crystallization of the TiO_2 only delivers a PPD of 0.69 $kW.cm^{-2}$using a Gaussian pulse profile.

Although the τ_{TiO_2} is almost 1000x greater than that of the AgNWs, it remains shorter than the pulse's duration, meaning that the crystallization process should not damage the substrate, as shown in Figure 5.8(b). However, photonic crystallization of the TiO_2 layer atop the silver nanowire layer requires a more advanced analysis. The presence of oxygen vacancies in the TiO_2 precursor modifies its optical absorption levels, extending them to longer wavelengths (Pan, Yang, Fu, Zhang & Xu, 2013; Sarkar & Khan, 2019). As such, photons with less energy than the nominal TiO_2 bandgap can still be absorbed and trigger the crystallization (Benavides *et al.*, 2018; Gerlein *et al.*, 2019; Benavides-Guerrero *et al.*, 2022b). The presence of the

silver nanowires also helps inducing the crystallization of the TiO_2 coating by converting their absorbed photonic energy as heat, because silver is a much better absorber than TiO_2 (Lermusiaux *et al.*, 2022; Yang, Hirose, Nakao, Hoang & Hasegawa, 2012). Additionally, the presence of the metallic atoms promotes the reorganization of the Ti-O bonds into lower energetic states, which improves the crystallization (Wong *et al.*, 2019; Yang *et al.*, 2012). Indeed, we tested the TiO_2 film crystallization atop the PET substrate without the AgNWs using the same photonic post-processing conditions reported for both anatase and rutile phases. These results shown in the Supplementary Figure III-6 demonstrate that we cannot obtain a crystalline layer. As a result, these samples all failed the *DevSol* immersion test. These results confirm the contribution of the silver nanowires to the metal-induced crystallization of the TiO_2.

5.4 Conclusions

We report a facile fabrication route to produce hybrid transparent conductive electrodes (TCEs) on flexible PET. Their optical and electronic properties are comparable with previously-reported single-material silver nanowire-based TCEs. Our best devices consist of a layer of AgNWs covered with anatase TiO_2. They boast an average optical transparency of 84% and haze value of 7.7% at 550 nm, with a sheet resistance down to 18 Ω/sq. These results are obtained through the carefully-controlled photonic treatment of each layer separately. Indeed, a single 1x1 inch hybrid TCE sample can be entirely fabricated in less than an hour, including the cleaning and preparation of the PET substrate and the post-processing of each of the layers.

The successful welding of silver nanowires on flexible polymeric substrates and the optically-induced crystallization of TiO_2 layers for applications in optoelectronic devices have been previously demonstrated independently. However, integrating both materials and post-processing together is a new development in the field of additive manufacturing for flexible electronics. We demonstrate that this understanding the synergistic post-processing effects

of each material allows to treat simultaneously a wide array of materials using industry-grade photonic sintering machine.

We use a known developing solution test as a fast and reliable approach to test the crystallization of thin-film metal-oxides, a method that can be efficiently incorporated in production lines for effective quality control at any point of the fabrication processes. It also tests the compatibility of our TCE's with fabrication processes for devices where contact with solvents and other chemicals could potentially damage either the AgNWs or TiO_2. Also, oxygen plasma is used for quality control and to test the accelerated degradation of our TCEs.

To the best of our knowledge, this is the first hybrid-material transparent conductive electrode architecture that is completely treated by photonic sintering methods. Taking advantage of the diverse processing demands of different materials, it is possible to envision higher number layers of different materials that can be assembled this way, to create functional devices with very short processing times. As such, we firmly believe that this work helps bring flexible hybrid TCEs closer to large-scale manufacturing capabilities.

5.5 Experimental section

Material preparation. Silver nanowires with average diameter of 100 nm and length from 100-200 µm dispersed in ethanol with a concentration of 20 mg/mL were purchased and used as-received from ACS Materials (Agnw-L100). The substrate is heat stabilized polyester film purchased from Tekra (Melinex ST505). Titanium(IV) butoxide (TNBT), ethanol anhydrous, acetylacetone (acac) and acetic acid anhydrous >99% were procured from Millipore Sigma and used as-purchased. To prepare the defect rich, light sensitive, amorphous TiO_2 precursor, 28.853 g of ethanol mixed with 1.474 g of acac were placed under magnetic stirring for 20 minutes. Then, 1.860 g of TNBT were added, while maintaining the stirring for additional 40 minutes. Hydrolysis was triggered by adding dropwise 0.84 mL of DI water. This solution is covered in parafilm to restrict contact with air and contaminants and then, is left aging for 8

months. The resulting solution was diluted in anhydrous ethanol at 10% w/w concentration ready for deposition.

Assembly of the silver nanowire networks and deposition of titanium dioxide layer. The PET substrates were cleaned with IPA alcohol and prepared for oxygen plasma cleaning for 10 minutes at 150 Watts using a PE-100 system from PlasmaEtch. After, the PET substrates were cut in 22 x 22 mm squares and placed on the spin coater chuck. The deposition of the AgNW film was done applying 300 µL of Agnw-L100 solution on the still substrate, ensuring complete area coverage. The spin coating process is then started at 4000 rpm for 45s. Afterwards, the first round of photonic sintering processing took place using a PulseForge Invent system from Novacentrix. Subsequently, 200 µL of the amorphous TiO_2 precursor was drop-casted completely covering the sample and a second spin coating process took place at 4000 rpm for 45s. After, the second round of photonic sintering processing took place to crystallize the TiO_2 layer.

Developing solution (*DevSol*) preparation and testing. The solution was prepared by adding 2 mL of acetic acid in 20 mL of 1:3 DI water to methanol mix. To help identify the effects of the DevSol test, the samples were partially immersed, leaving half of the sample untouched. The immersion took place for 15 seconds and after, de-ionized water was used to wash the samples.

Sample characterization. Sheet resistance was measured using the 4-point probe system from Ossila. Optimization of the best photonic curing conditions to weld the AgNW film was done by only measuring the samples before and after in the same center spots, previously marked for uniformity of the measures. Rapid proof of crystallization of the TiO_2 precursor was done following a modified version of rinse-in developing procedure reported elsewhere (Daunis *et al.*, 2020, 2018). Plasma ageing was done using the same PE-100 PlasmaEtch system, set to 50 Watts for 40 seconds. Raman characterization is done using a WITec Alpha300 confocal Raman microscope equipped with a 60 mW fiber-coupled CW laser at 532 nm emission wavelength and a mechanical attenuator. SEM and EDS imaging was done

using a SU8230 from Itachi. XRD was done using a Bruker D8 Advance, equipped with a Cu source. Atomic force microscopy analysis was done using a Bruker MultiMode8-HR AFM. Optical transmittance and haze analysis were done using a UV–VIS–NIR spectrophotometer Perkin Elmer, Lambda 750 with an integrating sphere. Haze measures were performed following the procedure described in the supplementary information.

Author Contributions

The concept and methodology were planned and done by L.F.G. and S.G.C.; Fabrication of the samples and testing done by L.F.G.; Synthesis of the TiO_2 precursor done by J.A.B.; Characterization done by L.F.G and J.A.B. and analysis of the results was done by L.F.G., J.A.B., S.G.C.; The first version of manuscript was written by L.F.G. and S.G.C. The manuscript was reviewed and commented by L.F.G., J.A.B., S.G.C.

5.6 Conflicts of interest

The authors declare no conflict of interests for the publication of this manuscript.

CHAPTER 6

SYNTHESIS AND CHARACTERIZATION OF LEAD SULFIDE QUANTUM DOTS. RESULTS AND PRACTICAL APPLICATIONS

As previously explained, lead-chalcogenide colloidal quantum dots (QDs) are nanostructures that are easily synthesized in solution. Their size can be easily tuned to produce a wide range of narrow optical emission bands. They have a strong photoluminescence response in the near infrared, which is helpful for making photodetectors and light-emitting devices. They can be easily dispersed in solvents or assembled in quantum dot solids. In our research group, we have extensively studied the synthesis, properties, and applications of these versatile nanocrystals. My understanding and experience researching the synthesis and characterization of these nanostructures yielded meaningful contributions that led to the publication of three peer-reviewed articles (Xu *et al.* (2015); Ka *et al.* (2018, 2020)).

6.1 Colloidal synthesis of PbS quantum dots

The synthesis of quantum dots in solution is a fairly simple and inexpensive process that produces particles on the nanometer scale with a narrow size distribution. The oleic acid (OA) ligand-passivated surface of the QDs imparts excellent solubility in various solvents. These ligands can be dispersed in a wide range of polar, non-polar, and water-based solvents by chemical exchange (Bakueva *et al.* (2004); Jumabekov *et al.* (2014)). In contrast, epitaxially grown QDs rely on two critical factors: the substrate chosen for growth must possess a high level of crystallinity, and the essential lattice mismatches must be present to achieve the optimal growth orientation and geometry for the nanoparticles (Tan, Chen, Wu & Zhang (2018)). Lastly, it is difficult to make densely packed, thin-film quantum dot solids using epitaxial growth methods; in contrast, it's a straight-forward process to clump colloidal QDs together using ligand exchanges during layer-by-layer deposition.

The methodology reported by Hines and Scholes serves as the foundation for the synthesis process (Hines & Scholes (2003)). They reported on a method for synthesis that involved a

reaction between a lead precursor and disilathiane molecules in a coordinating solvent at elevated temperatures. By manipulating the reaction parameters, it is possible to produce robust, highly luminescent PbS nanocrystals with a narrow size distribution and whose optical bandgap can be tuned across a wide range in the near-IR.

The reaction takes place inside a 3-neck reactor, as seen in Figure 6.1(a), with the controlled nucleation of the QD seeds followed by the continuous growth of the rock salt crystallites. A molecular ratio of 4:2:1 of OA/Pb/S was established for a good QD yield (Hines & Scholes (2003)). Through the hot-injection method, the sulfur precursor is swiftly added to the reactor containing the solution that has the lead dissolved in it. The growth of the nanocrystals can be quenched by immersing the reactor in cold water or, by adding a solvent that is miscible with the initial reaction solvent, octadecene, but immiscible with the surfactant groups, oleic acid. This second solvent, usually acetone, destabilize the nanocrystals in dispersion so they flocculate at the bottom of the reactor.

6.1.1 Size control of the Quantum Dots

Variations in the reaction parameters will affect the final size of the quantum dots: reaction time, injection temperature, reactant and surfactant concentration, and surfactant chemistry (Zhang *et al.* (2015)). As a general rule, the size of the nanocrystals will be larger when the reaction time is longer because precursor molecules will attach to the QD seeds, resulting in larger crystallites. High concentrations of the surfactant, in this case oleic acid, mean smaller crystal seeds. This is because OA functions as a stabilizing agent in colloidal synthesis, exerting control over nucleation and growth kinetics. The surfactant adsorbs onto the surface of the nanocrystals, forming a protective layer that hinders further aggregation and coalescence. This enhanced surface passivation effectively restricts attachment of the precursor molecules, which not only control the final size of the quantum dots but also influence the amount of seed formation.

Executing the hot injection of the sulfur precursor at various reactor temperatures determines the kinetics of nucleation and subsequent crystal growth (Soni, Joshi & Ningthoujam (2021)). Higher temperatures generally result in increased precursor solubility and faster nucleation, leading to the formation of smaller nanocrystals.

6.1.2 Detailed description of the synthesis of PbS quantum dots

The role of each of the constituents involved in the synthesis of PbS QDs is explained in Table 6.1.

Table 6.1 List of chemicals involved in the synthesis of PbS quantum dots with peak emission is centered at 1050nm

Name	Chemical formula	Quantity	Function
1-Octadecene (ODE)	$CH_3(CH_2)_{15}CH{=}CH_2$	10+4 grams[1]	Coordinating solvent
Oleic acid (OA)	$CH_3{-}(CH_2)_7{-}CH{=}CH{-}(CH_2)_7{-}COOH$	2.67 grams	Surfactant molecule
Lead oxide (PbO)	PbO	0.45 grams	Lead precursor
Hexamethyldisilathiane (HMDS)	$(CH_3)_3SiSSi(CH_3)_3$	210 µl	Sulfur precursor

Detailed below is the procedure for synthesizing PbS QDs whose photoluminescence peak is centered at around 1050 nm:

1. On a 3-neck flask mix 10 g of ODE, 2.67 g of OA and 0.45 g of PbO.
2. Introduce the magnetic stirrer. Using rubber caps, install the heat sensor, nitrogen flow and vacuum pump according to the setup presented in Figure 6.1(a).
3. Once the nitrogen and vacuum flows are balanced, using the heating mantle, bring the temperature of the mixture to 150 °C and let it rest for 2h under vigorous stirring.
4. In the meantime, inside a nitrogen purged glove box, prepare the injection mixing 4 g of ODE and 210 µl of HMDS.
5. Do multiple gas purges of the exchange chamber of the glove box to avoid propagation of the bad sulfur smell coming from the HMDS.
6. Bring the temperature of the reactor down to 75 °C, stabilize, and proceed with the hot injection of the HMDS solution. The contents inside the reactor should instantly change

[1] The two values correspond to necessary amounts for both the reactor and the injection, respectively

from transparent to a dark brown color, signaling the appearance of the QDs in the solution.

7. Maintain the temperature and the nitrogen/vacuum flow for another 2 to 5 minutes to promote the controlled growth of the QDs.
8. Remove the heating mantle, remove the vacuum and nitrogen connections, and quench the reaction by immersing the reactor in ice water.
9. Pour the contents of the reactor into six centrifuge tubes and proceed with the washing process.

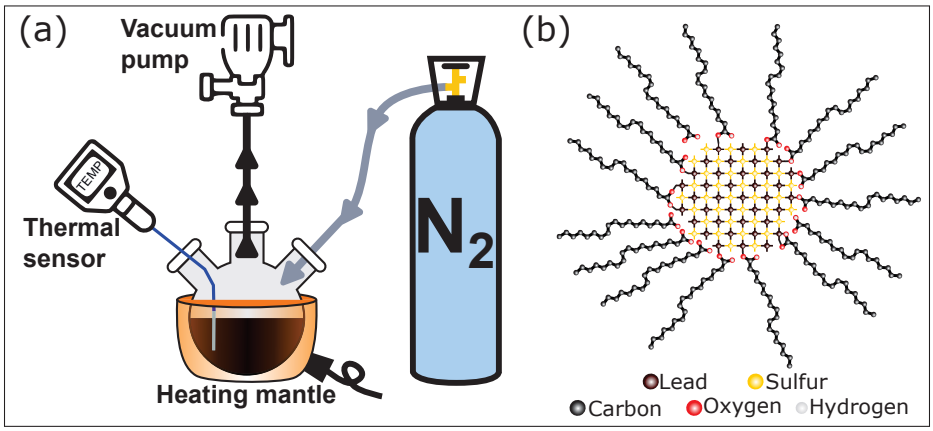

Figure 6.1 (a) Experimental setup for the synthesis of PbS quantum dots (b) QDs as-synthesized showing long chains that correspond OA molecules

This washing procedure helps to remove the excess of OA left from the QD synthesis reaction. Once the contents of the reactor have been equally distributed on all six centrifuge tubes, fill the rest with an excess of acetone. This will precipitate the QDs to the bottom of the tubes helped by 5 minutes of centrifugation at 2000 r.p.m.. Once finished, the QDs have agglomerated at the bottom of the tubes and the acetone should appear translucent without contaminants. Dispose of the acetone carefully, so that the QDs at the bottom remain. Fill again with hexane in small amounts, enough to properly disperse the QDs (1-2 ml should suffice) and fill the rest of the tube with excess acetone. Repeat the centrifugation, acetone disposal and hexane redispersion. Finally load the QDs dispersed in hexane inside a syringe and pass all the solution through a 0.2 µm PTFE syringe filters. More than one filter will be

necessary for this final step. These QDs dispersed in hexane are passivated with OA on their surface. This protects the nanocrystals from the environment but renders them insoluble in polar solvents such as ethanol or IPA. The OA attaches to the QD surface through the carboxyl group in the chain, as shown in Figure 6.1(b). This keeps the hydrophobic tails facing outward and stops the quantum dots from aggregating. This is advantageous for creating well-dispersed colloidal solutions of QDs but OA is a very long organic chain, whose length is approximately 2.68nm, comparable to the QD average size. This makes the electron transport between adjacent QDs assembled in solids very poor (Xu *et al.* (2015)). For this reason, when assembling the QDs in thin-film solids, this bulky aliphatic ligand needs to be removed so that much shorter ligands can bring the QDs closer. In comparison, the molecule length of EDT, BDT and MPA, which are common ligands used in QD assemblies, are 0.66 nm, 0.647 nm and 0.66 nm, respectively.

6.1.3 Results obtained: Synthesis and characterization of QDs

As previously mentioned, a direct way to control the final size of the quantum dots is by changing the temperature at which the hot injection of the sulfur precursor is done. This effect is depicted in Figure 6.2(a), where other conditions such as the amount of OA and the lead/sulfur precursors do not change. The photoluminescence peak increases nearly monotonically, showing careful control in the synthesis process, shown in Figure 6.2(b). Modeling the dependence between OA concentration, hot-injection temperature and the lowest energy exciton peak (λ_{1S}) has been previously reported, where the position of λ_{1S} shows a linear relationship with the concentration of OA in the reaction (Zhang *et al.* (2015)). The optical absorption of the smallest PbS QDs produced is shown in Figure 6.2(c), and the absorption spectrum fitting of that batch is analyzed in Figure 6.2(d), pointing to the optical bandgap of the QDs as represented by the green linear fit (Ghobadi (2013)) and whose value was calculated to be around $E_{gap} = 1.6$ eV. The yellow linear fit projects to $\lambda = 918$ nm, is closely related to the emission peak at λ= 936 nm. The absorption spectrum fitting

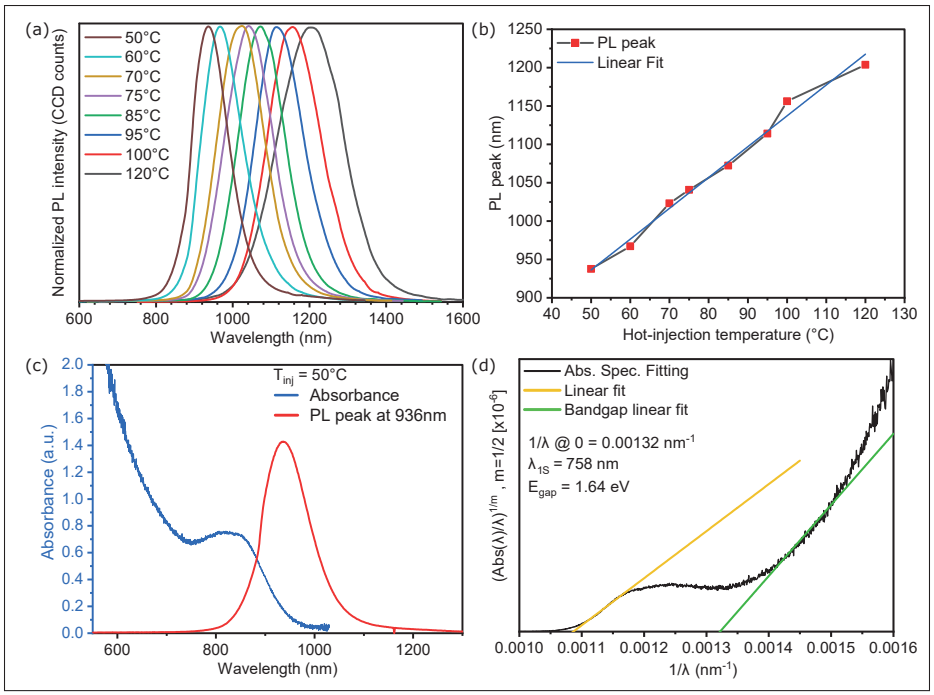

Figure 6.2 (a) Photoluminescence of PbS QDs synthesized at various hot injection temperatures (b) PL peak versus hot-injection temperature showing a linear relation (c) Absorbance and PL of QDs synthesized at 50 °C (d) Absorption spectrum fitting of the absorbance spectrum

method allows for the determination of the optical bandgap of nanocrystals, requiring only the absorbance spectrum and not the film's thickness or reflectance spectrum (Ghobadi (2013)).

The difference between the absorption and the emission peaks is called the Stokes shift, which is a characteristic feature of quantum dots and depends on factors such as the size, shape, and surface properties of the quantum dots (Leitsmann & Bechstedt (2009)). In photoluminescence, an excited electron-hole pair is quickly created because optical absorption is an extremely fast phenomenon. In contrast, the semiconductor lattice has time to reorganize in the presence of this exciton, causing relaxation of its initial energetic state, and the radiative emission is thus red-shifted from the original absorbed photon energy. In PbS quantum dots, the Stokes shift can be as high as 200 meV between λ_{1S} and the emission peak (Fernée, Thomsen, Jensen & Rubinsztein-Dunlop (2006)). This means the

difference between the absorption peak and the emission peak could be as pronounced as 400nm.

6.2 Application project: Employing MWCNT in TiO_2 sol-gel matrix to boost the fill factor of quantum dot-sensitized heterojunction solar cells

This study is a simple approach to enhancing the cathode charge extraction by building a device that involves a functionalized multi-walled carbon nanotubes (MWCNTs). The functional groups in the MWCNTs increase the interactions with the TiO_2 nanocrystals, improving dispersibility into the matrix while avoiding the formation of cracks. The devices display photovoltaic efficiency of up to 3%, doubling the performance of the device with only TiO_2 as the hole blocking layer. This improvement originates solely from the enhancement of the fill-factor coming from the addition of MWCNTs into the TiO_2 matrix, which is the result of improvement in the band alignment between TiO_2 and the FTO covered-glass electrode, facilitating an efficient pathway for collection and transport of photogenerated charge carriers. This in turn, increases the short-circuit current in our device. Additionally, no further treatment or surface modification was necessary in the fabrication of the TiO_2 cathode matrix for these devices. This is an all solution-based, simple and easy to fabricate method that increases the FF of the depleted heterojunction quantum dot sensitized solar cells. It is believed this solution can find further applications in current architectures that already exhibit superior performance.

6.2.1 Interoperability of TiO_2 sol-gel with QD solids made with iodine-based ligands

Traditionally, the band alignment between EDT-PbS solids and anatase TiO_2 favors the transport of photo-generated electrons from the quantum dots towards the TiO_2 and after, they will be subsequently extracted by the FTO electrode. In contrast. the photo-generated holes shall find a direct path to the Au anode in contact with the QD layer. However, in a more complex setting having two type of ligands interfacing quantum dot solids, interfacial band bending occurs between EDT-linked and TBAI-linked PbS solids. This is evidenced

by the ligand-dependent work function leveling that yields a type II heterojunction (Chuang *et al.*, 2014). This heterojunction blocks the flow of electrons and facilitates the extraction of holes by the anode, increasing the open circuit voltage of the device. The interface between TBAI-PbS and TiO_2 electron transport layer is pray to the displacement of the PbS work function, creating a small barrier that counters a direct charge extraction pathway, as shown in Figure 6.3.

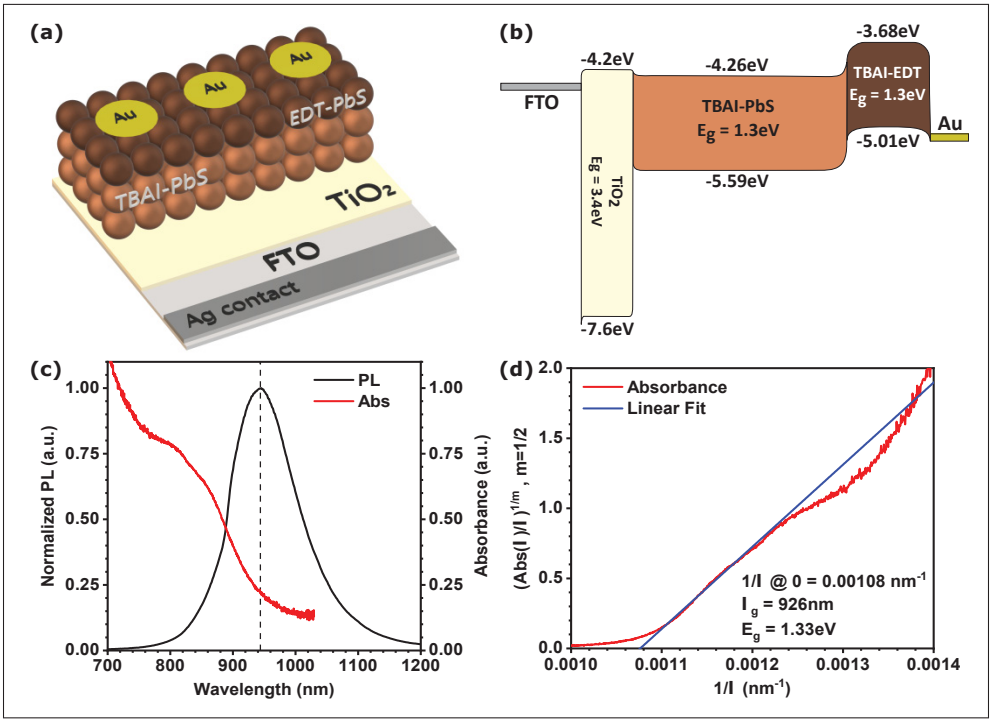

Figure 6.3 Characteristics of the fabricated solar cell (a) Device schematic (b) Band diagram (c) Photoluminescence (black signal - left axes) with the emission peak highlighted by the dashed line at 943 nm and absorbance (red signal - right axes) (d) Bandgap determination using the absorption spectrum fitting technique with a QD bandgap of E_g = 1.33 eV

The general structure of the device starts with an approximately 50 nm layer of anatase TiO_2 deposited atop a FTO covered glass. Afterwards, layers of PbS QDs are deposited through solid-state ligand exchange using first TBAI and then, EDT for the final two layers. Finally, Au contacts are evaporated through a mask. The general schematic of the device is presented in Figure 6.3(a) where each set of PbS layers is represented by a different shade of brown

color. The band alignment of the device is shown in Figure 6.3(b). Optical characterization of the as-synthesized PbS QDs is displayed in Figures 6.3(c) showing the photoluminescence emission peak located at 943 nm, as well as the absorbance spectrum of the same QDs. Using a method published elsewhere (Ghobadi, 2013), we estimated the optical band-gap for our synthesized QDs to be E_g = 1.3 eV as can be seen in the linear fit in Figure 6.3(d).

6.2.2 Devices fabricated with pure TiO_2 sol-gel as the cathode

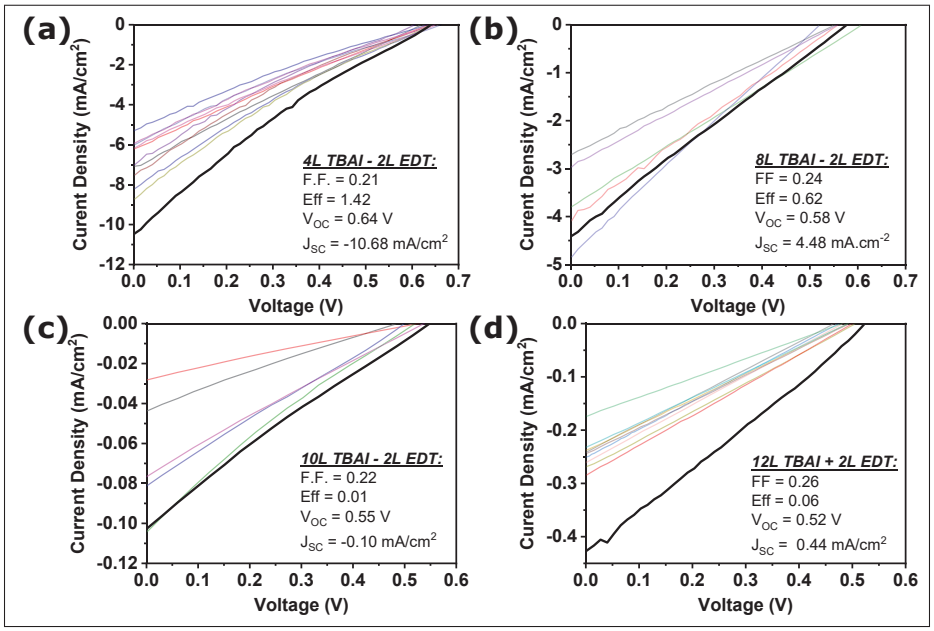

Figure 6.4 J-V characterization of solar cells fabricated with a pure TiO_2 layer and 4 (a), 8 (b), 10 (c) and 12 (d) layers of TBAI-PbS. The rest of the device structure remains the same for all samples: 2 layers of EDT-PbS and 100nm of gold

The deposited layer of TiO_2 atop the FTO glass possesses high transparency while preserving the beneficial optoelectronic characteristics (Xu *et al.*, 2012; Kontos *et al.*, 2011) of the anatase TiO_2. Optimization of the thickness of active area was done by varying the number of TBAI-PbS layers deposited, as explained in the methods section. The number of layers of EDT-PbS remained fixed at 2. An maximum photo-conversion efficiency of 1.42% with a V_{OC}=0.64 V and J_{SC}=10.68 mA.cm^{-2} was obtained with a structure comprising 4 layers of TBAI-PbS. The

low performance showed in these devices can be easily attributed to high interface resistance whose effects can be traced back to the energy barrier created at the interface of the TiO_2 cathode and the TBAI-PbS solid (Lee *et al.*, 2018; Pandey *et al.*, 2020). The complete set of results shown in 6.4 depicts the performance of devices varying the number of active region layers from 4 to 12. The different characteristics of all the devices fabricated using pure TiO_2 in the cathode are summarized in the Table 6.2.

Table 6.2 Summary of results for devices made with pure TiO_2 cathode layer

TiO_2+ TBAI-PbS + 2L EDT-PbS + Au				
No. Layers	**Fill Factor (%)**	**Efficieny (%)**	**V_{OC} (V)**	**J_{SC} (mA.cm^{-2})**
4L TBAI-PbS	20.7	1.42	0.64	10.68
8L TBAI-PbS	24.09	0.62	0.58	4.48
10L TBAI-PbS	21.3	0.01	0.55	0.11
12L TBAI-PbS	25.9	0.01	0.52	0.44

6.2.3 Effects of the MWCNTs in the TiO_2 matrix

The inclusion of multi-walled carbon nanotubes in the sol-gel matrix introduced inter-band states at the TiO_2-FTO interface that helped reducing interface resistance of the device, allowing an increased flow of charge carriers out of the solar cell, effectively improving its performance (Taleshi, 2015; Benetti *et al.*, 2016). Based on results published elsewhere, and the transparency analysis outcome provided in 6.5(d), where the loss in transparency for different MWCNTs concentrations ranging from 1-4% was analyzed, a concentration of 2% by weight as the optimal value of MWCNTs, was chosen to test the effect of this nanofiller in the TiO_2 matrix (Benetti *et al.*, 2016).

The exact weight of the MWCNTs necessary to meet a desired concentration was calculated after the crystallization of the TiO_2 precursor took place. It was established that the weight of pure TiO_2 left after the annealing process at 500°C during 1 hour, was an average of 3% of the total initial weight of the sol-gel solution. Therefore the amount of MWCNTs added into the mix is 2% of the 3% of the total weight of the TiO_2 solution in the container. The

use of functionalized MWCNTs facilitated temporal dispersion and compatibility with a TiO_2 precursor dissolved in ethanol.

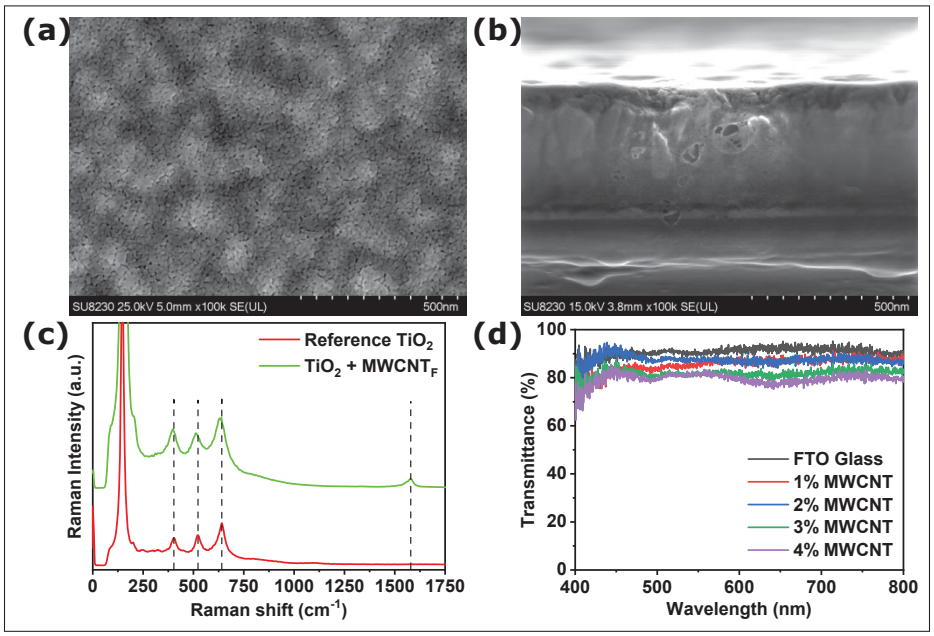

Figure 6.5 TiO_2 matrix with MWCNTs (a) Top SEM image of the film with 2% w/w concentration (b) Cross-section of an approximately 65 nm thick film (dark gray) atop FTO layer (c) Raman spectroscopy of the film with (green) and without (red) MWCNTs and (d) Transmittance of the TiO_2+ MWCNTs at various concentrations

Confocal Raman spectroscopy confirms the presence of both, the anatase TiO_2 phase and the MWCNTs in the same sample. The correspondent Raman peaks for Anatase TiO_2 located at 399, 516 and 639 cm^{-1} are clearly distinguishable when compared to that of a reference sample without MWCNTs. The additional peak at 1580 cm^{-1} in 6.5(c) corresponds to the G-band present in MWCNTs (Mali, Betty, Bhosale & Patil, 2012). Given the low concentration of MWCNTs in the sample and the limitations of our confocal Raman setup, it was not possible to locate a better spot that displayed a more complete set of Raman peaks for the MWCNTs. We detected a slight shift in the location of the peaks of the mixed matrix structure. We believe, this shift does not represent a detrimental change in the quality of the crystallization

of the TiO_2 matrix and can be attributed to crystal strains introduced by the presence of the MWCNTs (Taleshi, 2015). SEM imagery in Figure 6.5, shows the top view of the film. It is a uniform and yet porous TiO_2 matrix helps to maximize the area of contact with the QDs solids (Lee *et al.*, 2018). The cross-sectional SEM analysis in 6.5(b) shows a top dark gray layer of around 60 nm thick that contains the TiO_2 + MWCNT matrix. The following layer, with a thickness of 400 nm, corresponds to the FTO electrode covering the glass slide.

The inclusion of the MWCNTs in the TiO_2 matrix boosted the device's performance sensibly 6.6. In this case, the champion device was comprised of 8 layers of TBAI-Pbs and 2 layers of EDT-PbS and displayed stable results with V_{OC}=0.45 V and J_{SC}=13.88 mA.cm^{-2}. The fill-factor of the champion device was calculated to be 46.97% and the overall photovoltaic conversion efficiency was 2.92%, as presented in 6.6(c). Although not as strong increment, the I-V characteristics of the devices with 4 TBAI-PbS layers, shown in Figure 6.6(b), also show improvement compared to the previous attempt without the presence of MWCNT in the structure. These results confirm that adding MWCNTs in the TiO_2 matrix favors extraction of electrons out of the device, improving its overall performance. The compilation of results in this stage are present in Table 6.3

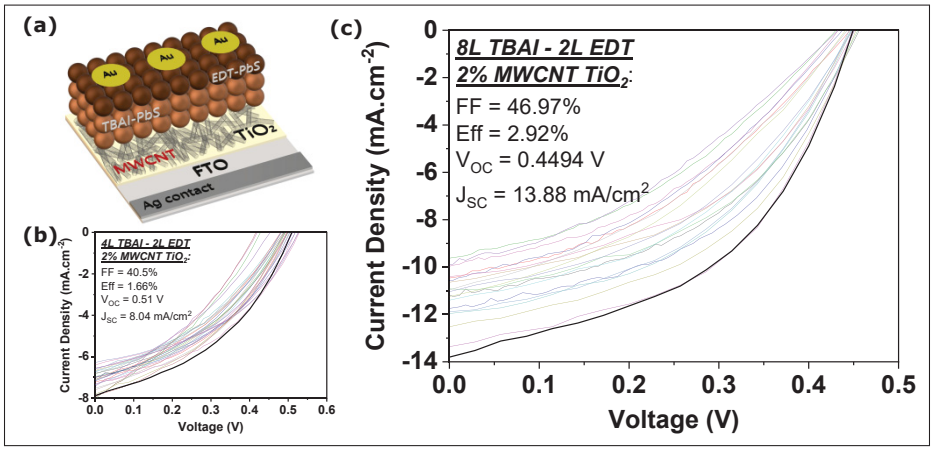

Figure 6.6 Devices fabricated with of 2% MWCNTs in the TiO_2 matrix. (a) Schematic of the device (b) Devices fabricated with 4 layers of TBAI-PbS QDs (c) Devices fabricated with 8 layers of TBAI-PbS QDs showing our champion device

For the devices with 8 layers of TBAI-PbS, the effect of the presence of the MWCNTs in the TiO_2 matrix granted a substantial increase in its photovoltaic characteristics. From the information presented in Tables 6.2 and 6.3, it is clear how the fill factor went from 24% to 48% and the J_{SC} increased from 4.5 to 13.9 $mA.cm^{-2}$. This confirms the advantages to interface engineering by the addition of 1-Dimensional nanofillers in charge carrier transport layers for photovoltaic devices made of colloidal quantum dots.

Table 6.3 Summary of results for devices fabricated with TiO_2 + f-MWCNTs collector

TiO_2+ f-MWCNT (2%) + TBAI-PbS + 2L EDT-PbS + Au				
No. Layers	**Fill Factor (%)**	**Efficieny (%)**	**V_{OC} (V)**	**J_{SC} ($mA.cm^{-2}$)**
4 Layers	40.51	1.66	0.51	8.04
8 Layers	47.97	2.93	0.45	13.88

6.2.4 Study conclusions

This project has shown a straightforward strategy to improve the operation of depleted heterojunction PbS QDs solar cell architecture by successfully incorporating MWCNTs within the TiO_2 electron transport/hole blocking layer. It is known that the fill-factor is strongly affected by the series resistance that exists at the interface with the extraction electrode. Thus, the presented results showing 2x fill factor and 2.5x photocurrent increments, are attributed to the enhanced charge transport and the successful reduction in the at the interface's series resistance. This was achieved by the addition of 2% MWCNTs into the metal-oxide matrix. As demonstrated by the absorbance measures, the addition of MWCNTs minimally affects the optical transparency of the TiO_2 thin film. The SEM analysis show that the presence of MWCNTs transform the smooth TiO_2 surface, offering porosity and texture to the film, increasing the effective surface area of contact between the PbS solids and the TiO_2 layer. This resulted on a better path for extraction of the photogenerated charge carriers out of the active area of the device.

This simple approach takes advantage of the enhanced dispersibility that functionalized MWCNTs display in the TiO_2 precursor. Thanks to the presence of carboxyl group (COOH)-, these nanotubes are compatible with the ethanol solvent present. However, inclusion of the MWCNTs suppose an additional step in the fabrication process of the solar cell. Despite this, this finding offers a simple-implementation solution to boost the fill factor of quantum dot-based solar cells and provide valuable guidance towards improved material design.

6.3 Contribution to peer reviewed articles

The experience gained in the understanding of the synthesis, size control and characterization of PbS quantum dots, allowed me to actively participate in the following peer-reviewed articles (Xu *et al.* (2015); Ka *et al.* (2018, 2020)).

Impact of Different Surface Ligands on the Optical Properties of PbS Quantum Dot Solids

*Xu, F., **Gerlein, L. F.**, Ma, X., Haughn, C. R., Doty, M. F., & Cloutier, S. G. (2015). Materials, 8(4), 1858-1870. DOI: 10.3390/ma8041858*

Contributions: In this publication, my contributions are for the synthesis and photoluminescence characterization of the PbS QDs used in the experiments, as well as the sample preparation used in the time-resolved spectroscopy. I collaborated with the main author of the manuscript writing about the synthesis process and the preparation of the manuscript figures and overall manuscript text revision.

An ultra-broadband perovskite-PbS quantum dot sensitized carbon nanotube photodetector

*Ka, I., **Gerlein, Luis F.**, M. Asuo, I., Nechache, R., & Cloutier, S.G. (2018). Nanoscale, 10(19), 9044-9052. DOI: 10.1039/C7NR08608C*

Contributions: In this publication, I have done the synthesis of the PbS quantum dots for all the five sizes used in the photodetector devices and performed the photoluminescence characterization for all of them. Additionally, I was in charge of the process of deposition of the QD layers doing ligand-exchange with EDT. I participated in the writing of the manuscript and its revision.

Solution-Processed p-Type Copper Thiocyanate (CuSCN) Enhanced Sensitivity of PbS-Quantum-Dots-Based Photodiode

*Ka, I., **Gerlein, L. F.**, Asuo, I. M., Bouzidi, S., Gedamu, D. M., Pignolet, A., Cloutier, S. G. (2020). ACS Photonics, 7(7), 1628-1635. DOI: acsphotonics.0c00491*

Contributions: In this publication, I have done the synthesis and photoluminescence analysis and characterization of the PbS QDs used in the photodetector devices. I participated in the revision and correction the manuscript.

CHAPTER 7

INDUSTRIAL PROJECT: STUDY OF OPTOELECTRONIC PROPERTIES OF COMMERCIAL GRAPHENE FLAKES FOR THE FORMULATION OF SCREEN PRINTING INKS

7.1 Project goals

This project was conceived to explore the electrical properties of mass-produced commercial graphene nanoplatelets (GNP) synthesized by the industrial partner Carboshpere - Graphene Division. These are carbon nanostructures that exhibit corrugated stacks of graphene sheets with dimensions ranging from a few micron up to hundreds of microns. The graphene references received were early development of their manufacturing technology and therefore, it was expected to find high defect density, as will be shown in this document. The references provided by Carbosphere for testing were P141, P30C, P237, P239. Additionally, the reference P221 was later received and characterized in SEM only. This project included analyzing the commercial screen-printing inks EDAG725 and EDAG440B provided by Henkel and their compatibility with Carbosphere's GNP. As such, it was divided into two main approaches with a different set of goals:

- **Metal ink approach:** In this approach, the baseline was the commercial silver microparticle paste EDAG725 provided by Henkel. This is a silver screen-printing paste with 60% solid contents, low electrical resistivity, $R_{sh} \leqslant 0.015\ \Omega/\square/25\mu m$, and flexibility. This approach comprised the addition of Carbosphere's graphene nanofillers into the existing EDAG725 to study the effects of the graphene dispersed in a well designed, commercial screen printing paste. This strategy aimed to preserve the current electrical properties of EDAG725 with the addition of graphene, hence reducing manufacturing costs.
- **Carbon ink approach:** In the second approach, using Henkel's SOL725 as the printing vehicle and graphene from Carbosphere as the primary component, the main objective was to create a carbon based screen printing paste that matched the performance of the commercially available, graphite-based paste EDAG440B. This strategy targeted a

sheet resistance between 1 and 10 Ω/□/25µm. In this approach, graphene exfoliation and stabilization were explored, aiming to enhance dispersibility and facilitate the use of various solvents. Similarly, the addition of metallic nanoparticles in the paste helped reducing the final sheet resistance of the paste.

7.1.1 Sheet resistance characterization method

For this industrial project, the characterisation techniques were adapted to match those of the industrial partners. Henkel uses the unit of measure [R_{sh}]=[Ω/□/25µm] for sheet resistance. To obtain this value, the formula below must be used:

$$R_{sh} = \frac{R(tr) * H(tr)}{N(tr) * 25} \tag{7.1}$$

Where *R(tr)* is the measured resistance in Ohms, *H(tr)* is the thickness of the coating in µm, *N(tr)* is the number of squares in the strip and 25 corresponds to the standard coating thickness of 1 *mil*. Using this approach requires using a specific rectangular strip geometry deposited by screen printing. To measure the sheet resistance of the screen printed samples, it was decided to emply a 5 x 25 mm rectangle where the number of 5 x 5 mm squares in the strip, *N(tr)*, is equal to 5. The resistance measure was done using Keithley 2400 source-measuring unit in 2-wire mode connected to pogo-pins manipulated with micro-actuators.

7.2 Characterization and processing of the graphene samples

7.2.1 Raman characterization

All analyses were done using a Witec Alpha 300 RS confocal Raman imaging microscope, with a 532 nm laser excitation source with a power density of $\approx 10^5$ W.cm^{-2}(Benavides *et al.* (2018)). According to the manufacturer's, the process of fabrication of the graphene samples involved a high pressure, pyrolysis reaction to synthesize the graphene nanoplatelets,

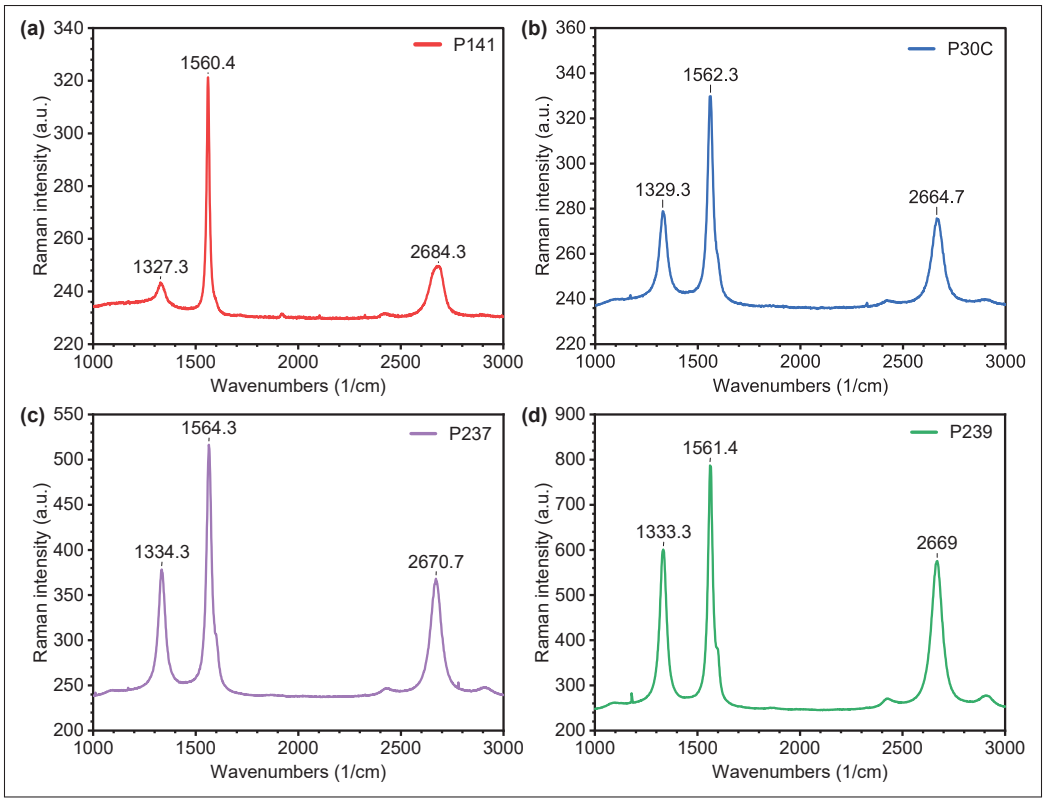

Figure 7.1 Raman characterization of various references of graphene nanoplatelets provided by Carbosphere. Each plot shows the location of the D, G and 2D bands

resembling the arc-discharge method reported elsewhere (Li *et al.*, 2010). At the time of working on this project, this fabrication process was still under development and tuning, which meant that the results varied from one batch of graphene to the next. Because of the aggressive nature of the production process, this also meant precise control over the number layers and defects was not optimized. This was clearly visible in the Raman spectroscopy analysis performed for the four references of Carbosphere's graphene product.

In Figure 7.1, different references of graphene are presented with their corresponding main peaks labeled for reference. The shape of the 2D-peaks for all samples resemble that of traditional multi-layer graphene (Malesevic *et al.*, 2008), contrary to thin layers of graphite where the characteristic peak doublet $2D_1$ and $2D_2$ is present at around 2700 cm^{-1} (Ferrari *et al.*, 2006). The *R-factor* defined as the ratio I_D/I_G, is a qualitative measure to examine

the nature of graphitic materials and it is inversely proportional to their quality. It approaches zero at the centre of a HOPG block and at the center of a high-quality single-layer graphene (Kastner *et al.*, 1994; Malesevic *et al.*, 2008). Also, the dispersibility of the graphene played a major role in deciding which reference was better for the intended application. In the case of the provided reference samples, the D-peak height and both ratios: the R-factor and I_{2D}/I_G, were calculated after subtraction of the data baseline and are presented in table 7.1:

Table 7.1 Summary of the Raman characterization peaks for various Carbosphere's graphene references

Reference	**D-peak height**	**R-factor**	I_{2D}/I_G
P141	10	0.11	0.21
P30C	39	0.41	0.4
P237	133	0.49	0.45
P239	339	0.65	0.59

According to Carbosphere, the reference P239 was heat treated and intentionally doped with NH_3 after the synthesis process, aiming to improve its electrical properties and exfoliation properties (Li *et al.*, 2010; Jiang, Yu, Feng & Song, 2018). This change that was noticeable in the metallic-ink approach where P239 dispersed better than the other graphene references and thus, it was the reference of choice for this part of the project. The effect of the NH_3 doping can be seen in Figures 7.1(d) and 7.2(b), with the G-peak bump located at around 1600 cm^{-1}. This bump indicates the presence of impurities in the graphene structure and red-shifts proportionally to the impurity availability, down to around 1620 cm^{-1} at higher concentrations.

As shown in Table 7.1, the lowest D-peak intensity and R-factor of P141 made it the best candidate to evaluate in the carbon-ink approach, as it is the reference with the highest potential conductivity. In the case of references P237, it did not disperse better than other references as it needed further homogenization and other unit operations to achieve the same result. Therefore, its use did not represent a fabrication improvement and thus, was not considered for screen printing ink testing during this project. Also, P237's handling posed a serious ink fabrication hurdle and health risk, as it will fly away easily and even keeping a small amount in place for characterization posed a challenge.

7.2.1.1 In-depth Raman signal analysis of references P141, P239 and P30C

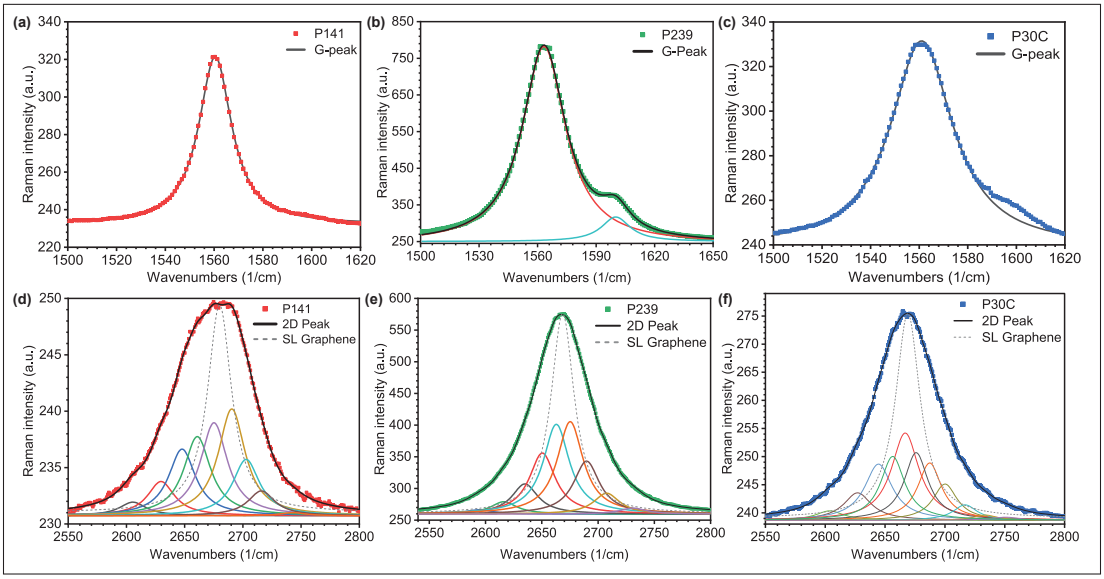

Figure 7.2 Analysis of the G and 2D Raman peaks for references P141, P239 and P30C. The G-peak is shown in (a), (b) and (c) while the 2D-peak is shown in (d), (e) and (f) for all references respectively. For reference, the dashed-lines in (d), (e) and (f) represent the 2D-band of a theoretical single layer graphene sample at the same location

In an attempt to establish the number of layers in references P141, P239 and P30C, further analysis of the 2D and G bands was done using the decomposition of the peak using Lorentzian functions of the form:

$$\mathcal{L}(x) = \frac{a * \omega^2}{4 * (x - x_c)^2 + \omega^2} \tag{7.2}$$

where *a* is the amplitude in arbitrary units, ω is the FWHM of the signal and x_c the shifting factor of the peak, both in units of cm^{-1}. In the case of the G-band, the peak's symmetry is diminished as a result of inter-layer interactions, and the shifting of the peak's location is affected by an increase in the number of layers. Additionally, the height of the G-peak increases monotonically with increasing the number of layers up to $N \leq 10$, but lacking a base reference sample, this approach was not pursued in this project (Silva *et al.*, 2020). The

2D-peak can be assumed to be a superposition of Lorentzian functions, each representing the theoretical contribution from each single layer in the many-layer coupled graphene structure. In practice, the 2D-peak fitting method is mostly used to distinguish single-layer graphene from few-layer graphene and to estimate the number of layers between 2 to 5 (Ferrari, 2007; Malard, Guimarães, Mafra, Mazzoni & Jorio, 2009; Hao *et al.*, 2010; Silva *et al.*, 2020).

The fitting of the Lorentzian functions was done in Matlab using the Curve Fitting Toolbox (*cftool*). The following fitting conditions were established for each function: the FWHM was set between 24 and 28 cm^{-1}. This values were chosen from reports of the 2D-peak's FWHM for single layer graphene, usually varying between 25-30 cm^{-1} (Ferrari *et al.*, 2006; Hao *et al.*, 2010; Wall, 2011). For convenience, a medium range value was chosen that allowed to consequently set the number of functions according to the convergence of the fitting process. When the number of Lorentzian functions was small, all the FWHM parameters (ω_i) will be maximized at 28 cm^{-1} and a convergence warning was presented. This warning meant that the fitting is not optimal and two options were possible: increase the limiting FWHM parameter or, increment the number functions, both aiming to better cover the original data-set. Therefore, it was necessary to add more functions up to the point where most fitting parameters converged without being limited by the established fitting settings. This is why, most of the (ω_i) values in Tables 7.2 are 28 cm^{-1} or close but, were obtained triggering the convergence warning. Adding more functions will only give room to smaller FWHM results. For reference, ideal Lorentzian functions with FWHM of 25 cm^{-1} have been plotted in Figures 7.2(d-f) in dashed gray lines, simulating a single-layer graphene and how a sharp 2D-band would look like.

In Figure 7.2, the G and 2D peaks of references P141, P239 and P30C are plotted in detail, with the corresponding fitted functions for each case. The fitting parameters are presented in the Table 7.2 using the same variable names from equation 7.2.

For the other parameters, the minimum amplitude (a_i) for each function was set to 0.1. The central wavenumber (x_{ci}), which corresponds to the starting iteration point of each function,

Table 7.2 Lorentzian fitting parameters obtained for the 2D-peak of the three references under analysis. The offset fit parameter (c_{REF}) for each reference is $c_{P141} = 230.7$, $c_{P239} = 259.6$ and $c_{P30C} = 238.7$

P141

a_1	a_2	a_3	a_4	a_5	a_6	a_7	a_8	a_9
1.211	3.043	5.916	7.025	8.255	9.477	5.01	2.209	0.2786
ω_1	ω_2	ω_3	ω_4	ω_5	ω_6	ω_7	ω_8	ω_9
28	28	28	28	28	28	27.87	27.81	26
x_{c1}	x_{c2}	x_{c3}	x_{c4}	x_{c5}	x_{c6}	x_{c7}	x_{c8}	x_{c9}
2606	2630	2648	2661	2675	2690	2703	2716	2743

P239

a_1	a_2	a_3	a_4	a_5	a_6	a_7	a_8	a_9
6.58	19.51	47.57	96.31	141.7	145.9	83.53	32.87	9.444
ω_1	ω_2	ω_3	ω_4	ω_5	ω_6	ω_7	ω_8	ω_9
28	28	28	28	28	28	28	28	28
x_{c1}	x_{c2}	x_{c3}	x_{c4}	x_{c5}	x_{c6}	x_{c7}	x_{c8}	x_{c9}
2595	2616	2635	2650	2663	2675	2690	2708	2731

P30C

a_1	a_2	a_3	a_4	a_5	a_6	a_7	a_8	a_9	a_{10}	a_{11}
1.677	48.87	10	6.448	15.52	10.2	12.04	2.752	0.9307	0.5505	11.36
ω_1	ω_2	ω_3	ω_4	ω_5	ω_6	ω_7	ω_8	ω_9	ω_{10}	ω_{11}
28	28	28	24.35	27.92	24	24	24	24	27.99	24.46
x_{c1}	x_{c2}	x_{c3}	x_{c4}	x_{c5}	x_{c6}	x_{c7}	x_{c8}	x_{c9}	x_{c10}	x_{c11}
2604	2627	2644	2700	2667	2687	2676	2717	2734	2750	2656

was chosen according to the number of functions available. Compared to the ideal 2D-band plotted in dashed lines in Figure 7.2(d-f), it is clear that the presence of many layers contribute to the widening and distortion of the 2D-bands in the reference samples. For both references P141 and P239, nine Lorenztian functions were necessary to cover the entire data set. For sample P30C, this number increased to 11, as presented in Table 7.2. From these numbers, it can be suggested that these samples contain at least 9 layers in the case of references P141 and P239, and at least 11 layers for P30C. This can be appreciated in Figure 7.2 where the 2D peaks of references P141 and P239 are clearly narrower than that of reference

P30C. While this is only *a posteriori* observation, it is likely that on average, reference P30C contained graphene with a higher number of layers than the other two references, and for that reason it was not considered for experiments in this project.

7.2.2 Electron microscopy of some of the references provided by the partner Carbosphere

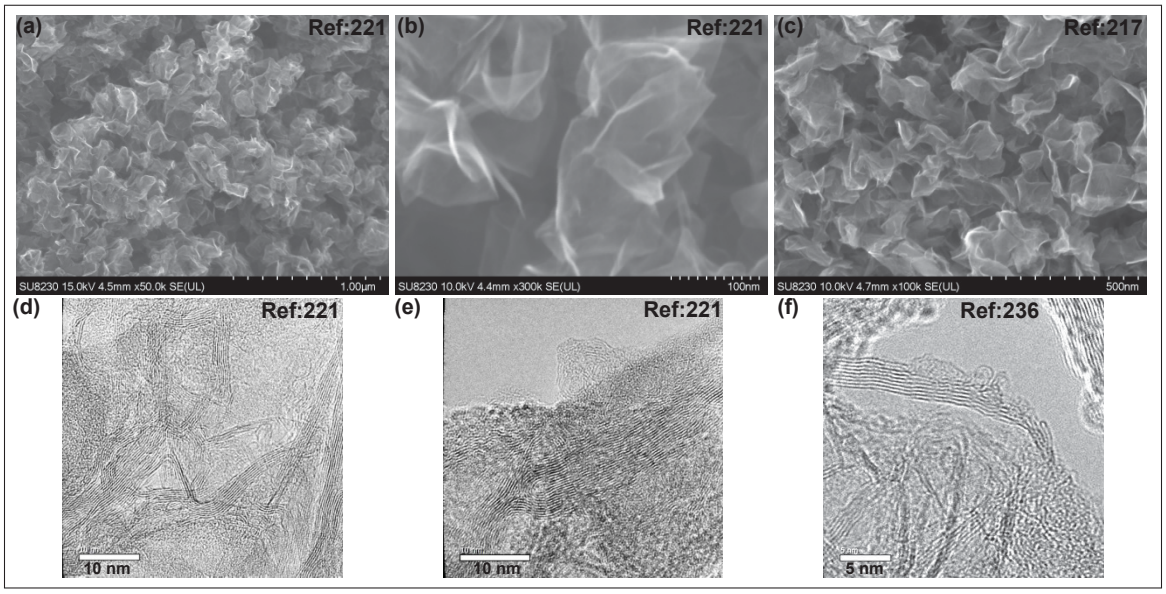

Figure 7.3 SEM and TEM analyses of various references (a-c) SEM images taken at ÉTS facilities (d-f) TEM images kindly provided by Carbosphere graphene

Overall, the fabrication process is the same for all reference samples. However, it was known that the production parameters varied for each but it was unknown in what measure. Keeping in mind the nature of this low-cost, high-yield graphene flake manufacturing, it was noted the wide distribution in number of layers and flake sizes within the same sample. This is shown by the SEM analysis in Figures 7.3(a-c) done on additional references later received, 221 and 217. In addition, transmission electron micrographs were kindly provided by Carbosphere from references 221 and 236 are shown in 7.3(d-f). In there, samples with a wide range of number of layers can be clearly appreciated, with sections showing as little as 4 to 5 layers and as many as 15+ layers.

The graphene images presented permit to draw important conclusions: first, the graphene flakes produced by Carbosphere display a corrugated, ever-changing nature, a factor that complicates the Raman and SEM analyses. Second, this structural variability makes the Raman signature of a sample drastically change depending on the probing location. Third, the laser source in the Raman system is focused down to a region 10µm in diameter, which means that the received signal is more of an average of the characteristics of many flakes, with many edges and defective regions contributing to the final measure. Fourth, there is a strong correlation with the conclusions extracted from the Raman analysis from Figure 7.2 and the fittings, and the images presented in Figure 7.3. For additional results, Benavides et al., used graphene reference P218 to develop anti-corrosive coatings for aerospace applications. That graphene shows similar structure to those presented in this work (Benavides-Guerrero *et al.*, 2022a).

7.2.3 Exfoliation and stabilization processing

Graphene exfoliation is performed to overcome the van de Waals forces that dominate inter-flake attractive interactions, allowing the separation of graphene layers from graphite flakes and making it easier to disperse while decreasing agglomeration in numerous solvents (Hernandez, Lotya, Rickard, Bergin & Coleman, 2010; Li *et al.*, 2013). When performed in liquids, there are three cost-effective methods that can be utilized: *Acoustic ultra-sonication* generates acoustic cavitation in which high-pressure and temperature differentials promote strong turbulence and shearing in the particles. This causes agitation, dispersion, and homogenization of graphene flakes (Khan, O'Neill, Lotya, De & Coleman, 2010b; Khan, May, O'Neill & Coleman, 2010a). This process can be performed in a wide range of conditions and solvents, but expensive equipment is required to generate ultrasonic vibrations via an acoustic probe transducer. *Shear/wet ball milling* aids in the reduction of large chunks of material and, when combined with the proper solvents, reduces the inter-layer forces, thereby facilitating the separation of graphene nanosheets. It is a lengthy process that can easily take more than 10 hours, but it is scalable and can produce large quantities of exfoliated

graphene (Paton *et al.*, 2014; Majee, Song, Zhang & Zhang, 2016). *Electrochemical*, it has a high output, is simple to execute in salt-based electrolytes, and permits functionalization of graphene flakes (Parvez *et al.*, 2013; Chen & Xue, 2014; Parvez *et al.*, 2014). Graphene stabilization is usually done after the exfoliation process. Its main purpose is to improve the dispersibility of the graphene (Yamuna, Sundaresan & Chen, 2019).

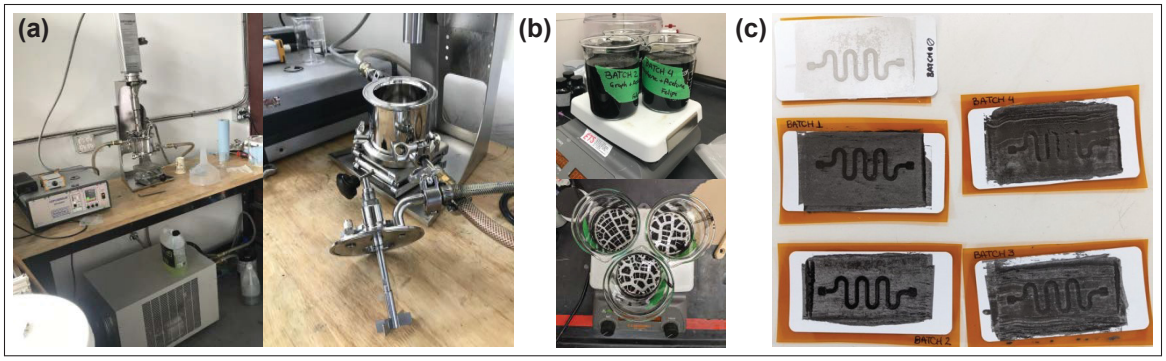

Figure 7.4 (a) Exfoliation of graphene using ultrasonication turret (b) Dispersed graphene after ultrasonication and graphene after evaporation of the solvent (c) Stencil printing of samples which allowed for evaluation of the ink adhesion

The process and tools used for exfoliation are presented in Figure 7.4. In this work, two exfoliation solvents were tested, acetone and acetyl cellulose. Exfoliated samples were used to create a high loading, 5% or 10% w/w, formulation ink made exclusively from Carbosphere graphene. To improve dispersibility in acetone, polyvinylpyrrolidone (PVP) at 10% was used with graphene references P239 and P141 (Marra, Minutillo, Tamburrano & Sarto, 2021). The exfoliation process was done using a industrial ultrasonic equipment delivering either 100 or 200 Watts for 15 minutes. This result of this process was tested creating a formulation with high weight loading by weight dispersed in SOL725 vehicle.

7.3 Analysis of results: Metal-ink approach

The baseline was established using a screen printing paste supplied by Henkel with the reference EDAG725; a commercial paste made with silver microparticles at a 60% concentration

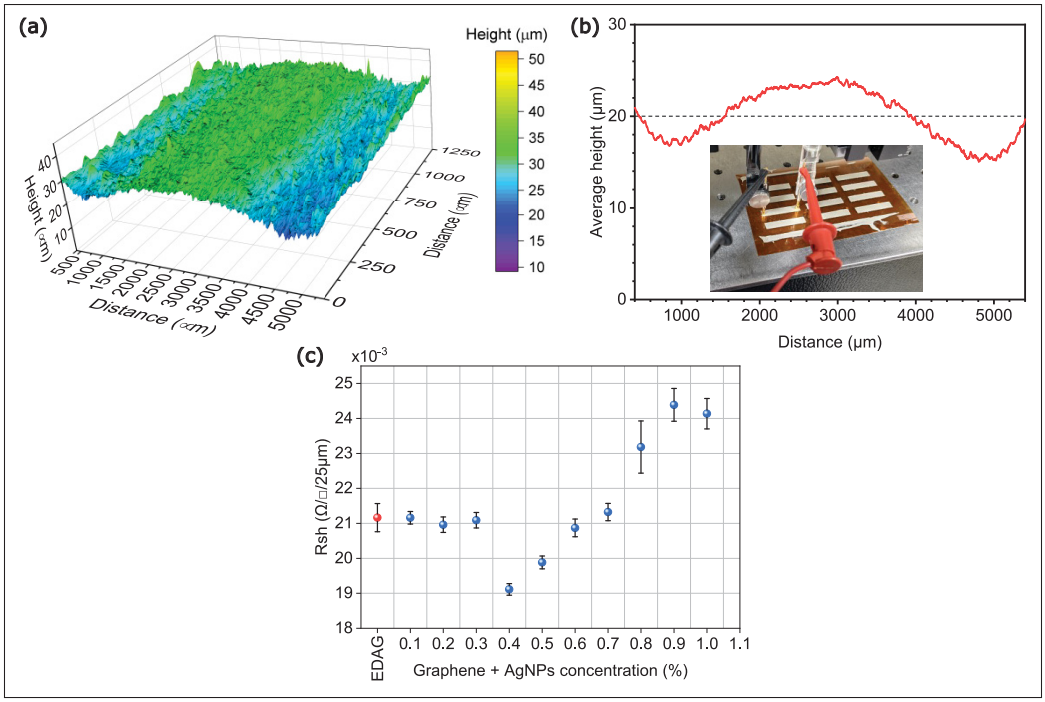

Figure 7.5 (a) 3D reconstruction of a ribbon made of EDAG725 (b) Average height from the 3D reconstruction. *Inset:* applied ribbons and measuring probes (c) Sheet resistance versus graphene P239 concentration + AgNPs

by weight. In accordance with the values on the data-sheet, the measured sheet resistance was 0.016 Ω/□/25μm. Diluting the formulation to a 50% silver concentration using SOL725 printing vehicle only changed the sheet resistance to 0.021 Ω/□/25μm. The 3D reconstruction of the surface structure and a complete sample of 12 ribbons can be appreciated in 7.5(a) and (b), of a printed sample of EDAG725 paste. The average of all the measured line profiles is shown in 7.5(b), where an average ribbon height can be calculated. The double-S shape of the ribbon is a result of using stencil rather than a screen for printing. With this technique, there is always heavy accumulation of material in the edges of the print. Using a screen, the paste is applied evenly and flatter results are possible, but it was not present at the moment of doing these trials.

Because of the high concentration of silver in this paste, the amount of nanofillers that was possible to be dispersed remained limited. This required diluting the formulation to a 30%

solid contents of silver, whose R_{sh} is shown by the red data point in Figure 7.5(c). Adding a combination of graphene plus silver nanoparticles (AgNPs), it was possible to bring down the R_{sh} of the 30% diluted EDAG725. Tests showed that concentrations of both components superior to 1% provided no benefits. The reference P239 was chosen for these experiments as it showed better mixing affinity with the EDAG725 paste, with the sheet resistance results plotted in Figure 7.5(c). The mixing and incorporation of the graphene plus AgNPs was done using the Thinky planetary mixer. Each concentration was printed using a 1-mil thick, laser-cut sticker paper stencil, creating 12 ribbons just like the inset in Figure 7.5(b). Thus, the value of R_{sh} provided is the average of 12 independent measures per equal concentrations of graphene P239 and AgNPs. It can be seen that between 0.1 and 0.3% added nanofillers, the R_{sh} more or less remained the same. At 0.4% concentration, there is a sudden drop to about 0.019 Ω/□/25µm, that is lower than that of the original 30% EDAG725 formulation. Afterwards, it picks up until it eventually becomes larger than the baseline, from 0.7 to 1% graphene plus AgNPs concentration. These results point to a possible improvement of the EDAG725 by addition of equal parts of 0.4% w/w of graphene P239 and AgNPs. Additional adhesion and long-term performance test were not done during these tests. Also, comparison of the paste's performance using traditional screen-printing is necessary to have a complete picture of how much the addition of graphene changed the initial characteristics of these high-performance paste. Although the results show a promising contribution from the addition of these nanofillers, the mixing and post-processing times do not represent a substantial gain from an economical point of view.

It was found that an excess of graphene P239 beyond the optimal concentrations increased the sheet resistance of the printed areas and acted in detriment of the excellent EDAG725 conductive properties. This can be explained taking into account: (i) Being such poor electrical conductor, the addition of graphene P239, even at a low concentration of 1%, competed with percolated network formed by the silver microparticles, affecting the electrical transport raising the overall sheet resistance of the film. Additionally, high graphene loads compromised the viscosity and adhesion properties of the formulation. (ii) Further characterization proved

that KWI's graphene flakes were mostly a stack of more than 10 layers with high defect density, factors that account for its low electrical mobility and thus, low electrical conductivity (Geim & Novoselov (2007)).

7.4 Analysis of results: Carbon-ink approach

The benchmark for this part of the project was established using the carbon-based formulation EDAG440B from Henkel, with 38% solid contents by weight. Common applications of this type of inks involve membrane keyboards and flexible printed circuits. The deposition of the EDAG440B paste was made using an 80 mesh screen on PET. Printed samples are shown in Figure 7.6(a) and a laser confocal 3D reconstruction of the ribbon is shown in 7.6(b). The sheet resistance based on a sheet of 24 printed ribbons was 27.2 Ω/□/25µm with an average ribbon thickness of 31 µm, as shown in Figure 7.6(c).

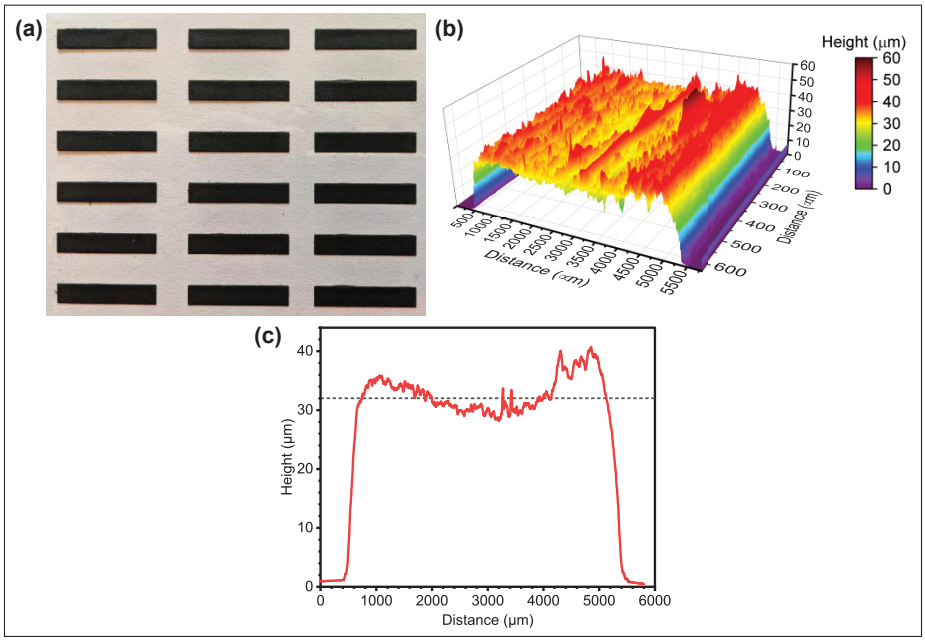

Figure 7.6 (a) Carbon-based EDAG440B screen printed ribbons (b) 3D reconstruction of a ribbon (c) averaged ribbon thickness

In this second phase of the project, the aim was to produce a graphene-based screen printing paste with lower R_{sh} than that of the EDAG440B paste, between 1-10 Ω/□/25µm. This paste would be created with only SOL725 as a dilution/vehicle agent and KWI's graphene product. In this case, it was important to study the effects of graphene exfoliation and stabilization to improve the dispersion of Carbosphere's graphene flakes.

7.4.1 Determination of the maximum concentration of graphene allowed by SOL725 printing vehicle

The process started establishing the highest concentration of Carbosphere's graphene that could be added to the printing vehicle SOL725. As it was previously studied, the reference P141 was chosen as it showed the most promising electrical characteristics. Various concentrations of the reference P141 in combination with metallic nanoparticles were added to the SOL725 printing vehicle, ranging from 1% to 5% w/w each. A paste with only graphene was difficult to spread and yielded no measurable conductivity. A maximum concentration of 5% of GNP was found to preserve the adhesion properties of the SOL725 while enabling the deposition of the paste via stencil printing, shown in Figure 7.7.

The defective nature and the high number of corrugated layers, made the graphene platelets poor electrical conductor and thus, it was necessary to introduce additional conductive nano-fillers to help bridging the graphene flakes, improving the percolation of the matrix and facilitating the electrical transport by reducing the resistivity of the printed films (Benavides-Guerrero *et al.*, 2022a). It was found that a combination of reference P141 exfoliated graphene flakes dispersed in acetone and silver nanoparticles of 200-400nm in size, yielded the best conductive paste, at equal concentrations of 5% w/w. By itself, the printing vehicle SOL725 displayed excellent adhesion to the PET substrate and this became the limiting factor when studying the maximum graphene/Ag-nanoparticles loading. The integration of the nanoparticles in the printing vehicle was done using the Thinky planetary mixer in 3 cycles of 30 seconds at maximum rotation speed of 2000 r.p.m. and orbiting speed of 800 r.p.m., as can be seen in the Figure 7.7(a). The effect of the orbital mixing can be appreciated in the

before and after pictures shown in Figure 7.7(b). In the Figure 7.7(c), stencil-printed squares are shown, corresponding to formulation with the maximum allowed concentration of both graphene flakes and nanosilver. Indeed, higher concentrations of graphene resulted in a very thick paste, hard to push through to a screen or even stencil mask. Examples of screen printed samples are shown in Figure 7.7(d-e), where samples with 3% contents of graphene and silver nanoparticles show good adhesion but, overloading the ink with 6% contents of graphene and silver nanoparticles greatly affect the ink's addition.

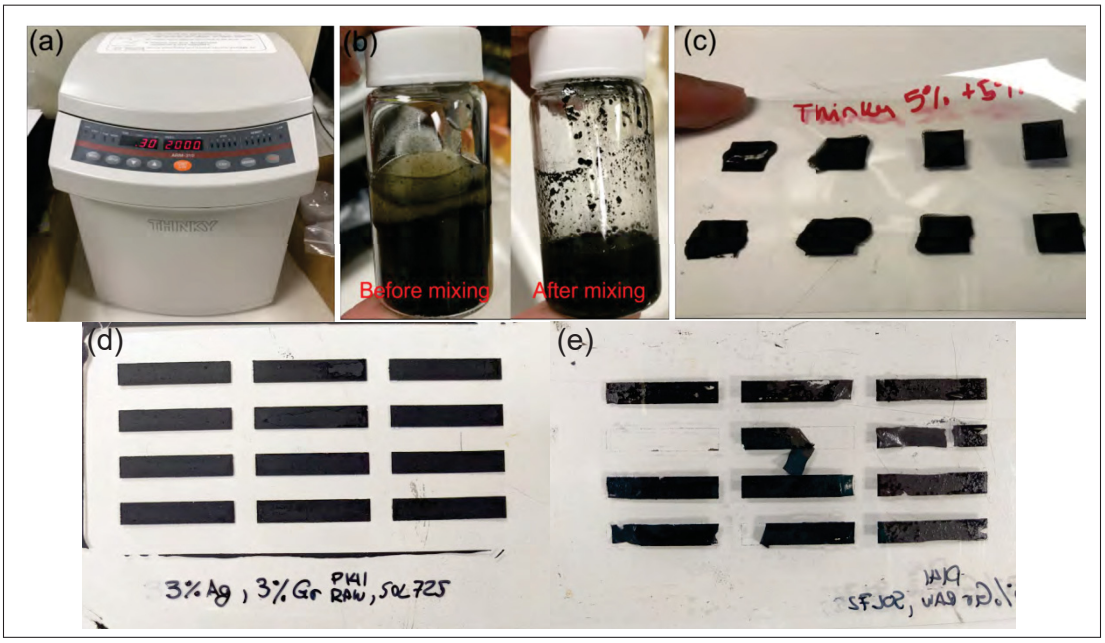

Figure 7.7 Highest concentration of P141 graphene in SOL725 + AgNPs (a) Thinky mixer (b) Before and after the mixing processes (c) Stencil-printed squares (d-e) Screen printed ribbons done at different nanofiller concentrations

The best result for this paste was measured to be $3 \pm 1k\Omega$ after the introduction of silver nanoparticles ranging from 200-400 nm in size and a concentration of 5% w/w. Measurements of layer thickness, to calculate the value in Ω/□/25µm were not done, as only the resistance measures were enough to draw conclusions. It is important to note that dispersing the graphene in acetone, followed by sonication aided substantially in the mixing process (Marra *et al.*, 2021). The acetone solvent completely evaporates during curing process and did not affect the final adhesion properties of the printing vehicle SOL725 as its evaporation

temperature is lower than the curing temperature. The adhesion tests were done accordingly to the guidance of standard ASTM D3359-17 and were done following the standard IPC-TM-650 instructions using Scotch tape grade 600.

From previous works with Carbosphere's graphene, incorporation of zinc nanoparticles was also tested as a substitute for the silver nanoparticles (Benavides-Guerrero *et al.*, 2022a). Equal concentrations of zinc and graphene set to 3% by weight yielded the best results in terms of dispersion, adhesion, application and lowest resistance, with a value of 0.9 ± 0.4 MΩ. Similarly, the print thickness was not measured in this case to calculate the values in terms of Ω/□/25µm. The advantage of using zinc nanoparticles was demonstrated as a sacrificial component in anti-corrosive films, but as a bridging conductor for the graphene nanoplatelets it did not perform as expected.

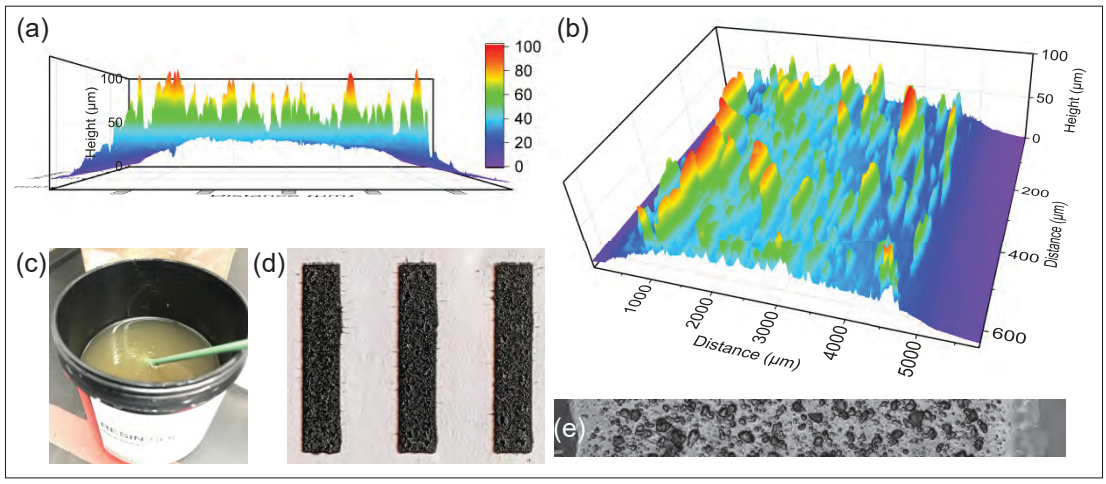

Figure 7.8 High-loading formulation at 10% graphene concentration (a-b) 3D reconstruction of a printed ribbon (c) SOL725 printing vehicle pure (d) Printed samples of the 10% loading formulation (e) Confocal laser micrograph highlighting the ribbon's surface roughness

It was possible to obtain a high-loading screen printing paste using graphene exfoliated in acetone and stabilized in acetyl cellulose. The 80-mesh screen was used for to print this paste, shown in Figure 7.8. Unfortunately, both the poor quality of the print and high sheet resistance of this approach, meant less than ideal results. The average thickness for these prints was 45 µm and the average sheet resistance was 8.45 MΩ/□/25µm. Because

of the high graphene loading, this paste was hard to spread on the manual screen printer, and the deposition suffered from lack of uniformity, as the paste was not evenly pushed through the mask yielding curved prints, as can be seen in Figure 7.8(a-b). It is important to note that the printing vehicle is optimized for screen printing formulations and is currently under use in several projects in the NOMAD research group, and is depicted in Figure 7.8(c) (Fourmont & G. Cloutier, 2022). Visual analysis of the printed ribbons demonstrate high rugosity as shown in Figure 7.8(d-e) which is not the case, in comparison, for commercial screen printed conductive formulations.

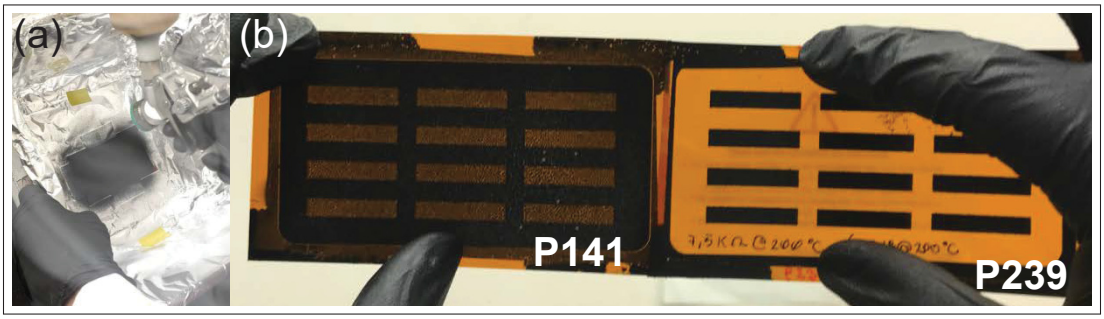

Figure 7.9 Spray-painted high loading formulations with references P141 and P239 (a) Spray-coating process (b) Resulting samples

Additionally, two high loading 10% w/w pastes made with different graphene references were spray-painted using the stencil mask onto Kapton substrates and cured at 200 °C. The process is shown in Figure 7.9(a). It is noteworthy to see how different references yielded completely different dispersion and adhesion results as can be seen in Figure 7.9(b), even though all fabrication and deposition conditions were the same. This was a final exploration of alternative deposition methods beyond screen printing. Previous experiences with spray-painted graphene-based coatings showed that spray coating helped disperse better the graphene. The nozzle size was 0.5 mm and the spray pressure was 2 bar. The 10% loaded paste had to be dissolved in acetone in a 1:1 ratio to be able to spray onto the substrate, effectively bringing the concentration to 5%.

7.5 Project conclusions

From the results obtained working in this project the following concluding remarks were delivered to the industrial partner, Carbosphere graphene:

- Carbosphere's graphene best application lies in the smart coating/paint fields as it was proven previously
- Carbosphere's graphene demanded additional unit operations to be operational with the targeted applications of the project: Exfoliation, stabilization, confirmation of number layers, characterization
- Stabilization and exfoliation did not boost the conductivity of the formulations
- Carbosphere's graphene production is unstable and each batch behaves differently: for example, P141 and P239 were supposed to behave closely
- Carbosphere's production method is able to yield large quantities of graphene, at the lowest cost compared to other commercial multi-layered graphene providers. While this is an important advantage, there is plenty of room for improvement and optimization to improve the uniformity of the product
- Graphene is a great conductor when it is low on defects and number of layers, however the many-layers graphene references provided by Carbosphere show high defect density and a wide range of sheet number that lowers its ability to freely conduct electricity.
- As they are, screen printing inks from Henkel are top performers

It is important to remind the reader that at the moment of execution of this project in 2021, the samples received from Carbosphere were early development and much of the synthesis process was still under optimization. By the time of finishing writing this document in 2023, Carbosphere reached out to show the latest results of a much more stable and controlled processing with better control over the number of layers and strong reduction of the defect density per batch production. As such, further characterization of these new results is being currently planned.

CONCLUSION AND RECOMMENDATIONS

Summary of this work

This thesis aimed to demonstrate the flexibility, applicability and speed of photonic processing of materials for the integration of transparent, large-area and multi-material conductive films built using heat-sensitive substrates. To achieve this result, it was necessary to develop the necessary know-how to process competitive single-material electrodes whose performance can be comparable with the ones fabricated using traditional methods. The first contribution of this PhD was demonstrating that large-area, on-demand crystallization of TiO_2 thin films using common, low cost tools was possible. These tools not only facilitated and sped-up the crystallization process, but also showed the possibility of direct laser writing of ceramics in heat sensitive substrates for additive manufacturing of TiO_2 films. These results open the door for future applications in low-cost photocatalysis electrodes, printed devices for electronics and low-cost flexible optoelectronic devices. The second contribution of this PhD encompasses the careful evaluation and bench-marking the performance of silver nanowire-based transparent conductive electrodes processed using additive manufacturing tools. Silver nanowire-based electrodes are known for their high performance and versatility. Characterizing the electrical-to-optical figures of merit in electrodes processed using photonic sintering is useful for a wide audience interested in additive manufacturing of this nanomaterial. Additionally, a new figure of merit (FoM) was proposed aiming to evaluate the effect of photonic processing in the sheet resistance of the films, as this processing method introduces a new variable that has an impact in the final electrical performance of the silver-nanowire network. The third contribution of this PhD, builds upon the knowledge acquired in the previous works and, my acquired expertise developing the optimal photonic sintering conditions for thin films of TiO_2 on flexible substrates. To this end, a multi-material electrode that was fully processed using photonic sintering was presented. This highlights the deep understanding of photonic

processing, where it was possible to adjust the conditions of one material without affecting the properties of the other. This high degree of flexibility and fabrication speed, is not possible in traditional processing techniques.

Discussion and recommendations

In order to continue with the work presented in the Doctorate thesis, the following recommendations can be made. These relate to applications of the optical processing of metal-oxides and the expansion of the multi-material processing capabilities using photonic sources and state-of-the-art additive manufacturing techniques.

The first recommendation concerns applications of direct laser laser processing of thin films of TiO_2. Being this the first time large-area devices can be fabricated with complete spatial control of the crystalline phase, it represents an opportunity to explore surface combinations that can maximize the performance of catalysts and sensors. Presently, applications such as photo-catalysts and water-splitting have demonstrated that the presence of a homo-junction formed by adjacent anatase/rutile phases, facilitates the charge carrier separation and reduce recombination, exploiting the favorable migration of photo-generated carriers from rutile to anatase (Xiao *et al.*, 2023; Yu *et al.*, 2023; Huang *et al.*, 2021b; Chahrour *et al.*, 2020). In optical sensors, the distinct photo-luminescent properties of anatase and rutile can be exploited when present together in the same sensor (Lettieri, Pallotti, Gesuele & Maddalena, 2016). These applications rely on complicated synthesis routes and small-scale production to achieve their results. In contrast, the possibility of a quick fabrication route plus spatial crystallization on demand, makes the study presented, very relevant to bring the fabrication of low-cost, large-area prototypes from a small laboratory-size device into an industrial-size prototype (Gerlein *et al.*, 2019). To further explore direct laser crystallization of large-area films, it is important to move away from spin coating because it is hard to implement at a

large scale. Thus, it would be beneficial to incorporate deposition techniques that are in line with modern additive manufacturing processing such as inkjet and screen printing.

The second recommendation concerns the continuation of the work for the Figure of Merit (FoM) for photonic treatment of transparent conductive electrodes. This new FoM aroused from the optimization process that took place to minimize the sheet resistance of the silver nanowire TCE. It aims to quantify the impact that radiant energy used for sintering has on the sheet resistance of the film. Because of the nature of photonic sintering, there is more than one parameter of the pulse used that can yield a highly conductive yield. Indeed, the relationship between transparency and sheet resistance can be separated from the sintering temperature of the oven, that remains always constant. In the case of photonic sintering, the fluence and sheet resistance can be related to optimize for the best processing results, when the transparency has been maximized through the fabrication step. This study, however, would be better done in flexible substrates such as PET or PEN, since the use of glass as a substrate results in much higher energetic demands to obtain the same sheet resistance in the films Schroder (2011). It is possible to envision a 3-dimensional figure of merit where the X-axis is the pulse fluence, the Y-axis the pulse duration and, the Z-axis is the sheet resistance.

The third recommendation concerns the photonic sintering of multi-material devices. As demonstrated, it was possible to exploit the requirements of two different materials to process them in independent processing steps, on the same platform. However, the fabrication method is not compatible with additive manufacturing of large area devices. Indeed, deposition of transparent silver nanowires films using slot-die or spray coating could be an alternative to generate larger devices, specially compatible with low-cost, flexible photovoltaics. Early in 2023, the chemistry of the amorphous TiO_2 precursor has been optimized for inkjet printing, with a single layer deposition of less than 1 µm thick, with a high degree of uniformity and

precision. Not only this allows for the creation of large-area samples but also improves in the amount of material used for the creation of devices, as it is known that spin coating can be a wasteful fabrication technique.

Contributions

The main contributions of the research work and presented in this thesis by articles are as follows:

Develop the necessary optimized parameters for direct laser writing to generate large-area, on-demand crystallization of thin-films of TiO_2

Large scale production of metal-oxide materials for flexible optoelectronics has yet to be realized. The possibility to controllably select the presence of each TiO_2 phase show advantages that until know, only have been explored in terms of particle concentration. The applications where spatial engineering of the TiO_2 phases would be more beneficial is precisely, where large-area devices are required, as it is in the case of photovoltaics and photocatalysis. The optimized parameters presented in this publication have already been applied in other research works with proven success (Benavides-Guerrero *et al.*, 2022b).

This first contribution has been published on a scientific journal: *L.F. Gerlein, J.A. Benavides-Guerrero, & S.G. Cloutier (2019). "Laser-Assisted, Large-Area Selective Crystallization and Patterning of Titanium Dioxide Polymorphs." ACS Applied Engineering Materials* and it has been presented in CHAPTER 3.

Analyze the qualities of photonically sintered, transparent conductive electrodes made of silver nanowires comparing them to traditionally fabricated electrodes using two well-established optical-to-electrical metrics

Silver nanowire-based, transparent conductive electrodes are very strong candidates to replace the more expensive indium-doped tin oxide. While their properties have been well studied, an updated characterization of films processed through photonic sintering was missing in the literature. This work aimed to fill that gap, by using common Figures-of-Merit to compare with previous works and also common transparent conductive materials such ITO and FTO.

This second contribution has been published on a scientific journal: *L.F. Gerlein, J.A. Benavides-Guerrero, & S.G. Cloutier (2019). "High-performance silver nanowires transparent conductive electrodes fabricated using manufacturing-ready high-speed photonic sinterization solutions." Scientific Reports* and it has been presented in CHAPTER 4.

Proposal of a new Figure-of-Merit for photonic treatment versus sheet resistance of TCEs

This new Figure-of-Merit (FoM) gives more relevance to the processing technique than previous FoM metrics. Throughout the work done for this publication, it became evident that the photonic sintering conditions played a major role on the final sheet resistance of the films, only second to the optical transmittance value. Identical films would exhibit electrical characteristics, only by changing the pulse envelope at the same radiant energy. That's why it is important to develop this FoM that allows to quantitatively analyze the optimal photonic processing parameters for a specific type of nanowires and a specific solution concentration.

This third contribution has been published on a scientific journal: *L.F. Gerlein, J.A. Benavides-Guerrero, & S.G. Cloutier (2019). "High-performance silver nanowires transparent conductive*

electrodes fabricated using manufacturing-ready high-speed photonic sinterization solutions." Scientific Reports and it has been presented in CHAPTER 4.

Fabrication of large-area, flexible, multi-material TCEs made of silver nanowires networks in conjunction with photo-sensitive TiO_2, for applications in optoelectronic devices. These platform was completely processed using photonic processing

Multi-material processing using photonic sintering is a new avenue of fabrication that could open the door to large scale fabrication of optoelectronic devices. One of the components in these devices that is usually the hardest to process is the metal-oxide layer because it requires the highest oven temperatures. Optimizing the photonic sintering conditions required for this type of material, without altering the properties of the underlying transparent conductive electrode makes for a straight-forward processing route that can be expanded to other materials as well. It is also relevant to note how phonon-assisted crystallization played an important role in reducing the energy density requirements of the second processing step, and how this phenomenon can be taken advantage of for photonic processing of materials.

This fourth contribution has been submitted on a scientific journal: *L.F. Gerlein, J.A. Benavides-Guerrero, & S.G. Cloutier (2023). "Photonic post-processing of a multi-material transparent conductive electrode architecture for optoelectronic device integration" RSC Advances* [1] and it has been presented in CHAPTER 5.

Thesis prospects

Study of the impact of inkjet printed TiO_2 ink on a MEMs resonator

In 2023, I am participating in a project where the photo-sensitive amorphous TiO_2 ink is being inkjet printed on MEMs resonators. This represents an interesting approach because it allows

[1] By the time this thesis was submitted, this article was undergoing peer revision

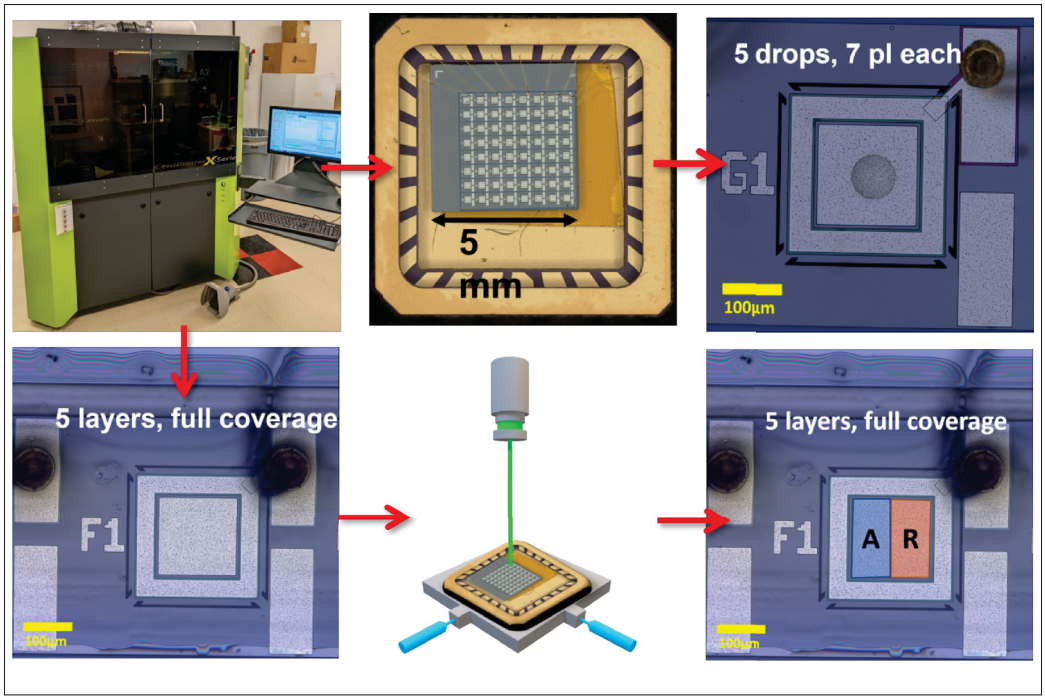

Figure 8.1 Schematic of the project for printing TiO_2 on MEMs

to controllably change the resonant frequency of the actuators according to the number of drops deposited on each device. Once we characterize the amount of change that can be induced by the printed drops, the next step in the project is to crystallize the TiO_2 atop the resonators using direct laser crystallization and provide them with new properties as sensors. The Figure 8.1 shows a detailed diagram of the process.

First, I printed the same specific number TiO_2 drops of atop a series of resonators, as shown in the upper three photos in Figure 8.1. Alternatively, it is possible to print and cover the whole resonator row and in this case, the control parameter becomes the number of layers per print. This case is shown in the bottom-left image in Figure 8.1. Using a laser source, it is possible to create areas with different crystalline phases within the same resonator, at different spatial ratios. This is the case represented by the bottom-center and -right illustrations in Figure 8.1. Conversely, with the help of photonic crystallization, we can crystallize the TiO_2 print atop the resonator into fully converted areas of anatase or rutile.

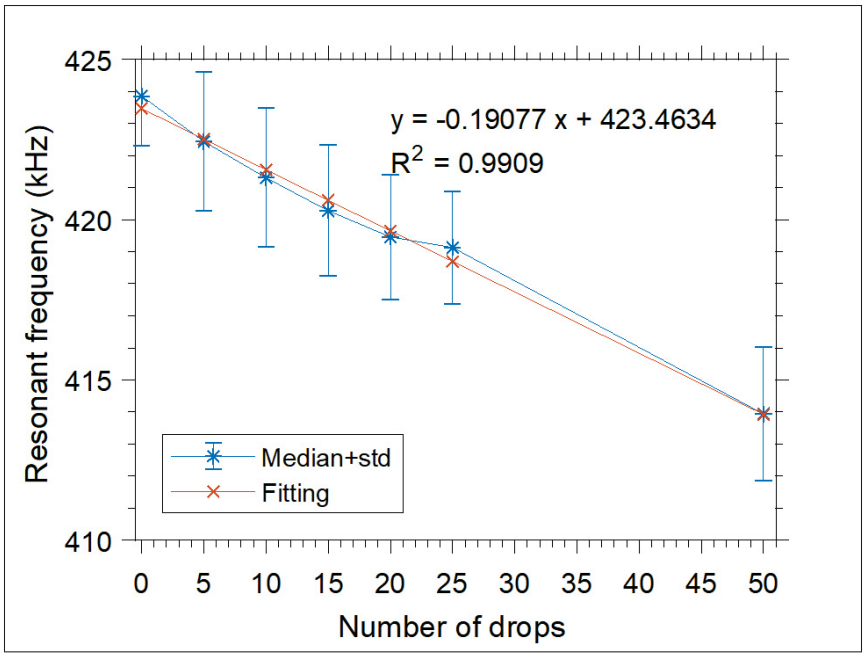

Figure 8.2 Average change in resonant frequency of eight MEMs resonators after printing various number of drops

After each printing process, the change in the resonant frequency each MEMs resonator was measured and annotated. The preliminary results, averaged from 8 devices per row are presented in Figure 8.2. The second part will be printing a full coverage of the devices, so that the deposition is uniform throughout the area. With this project we are aiming to give new properties to these resonator devices that can be correlated with the changing resonant frequency of the device.

Photonic crystallization of inkjet printed TiO_2 electrodes for photocatalysis

In 2023, we have initiated a project to bring to practical use the knowledge acquired for photonic crystallization of inkjet printed TiO_2 films. The tuning of the ink has been carefully optimized by my colleague Dr. Jaime Alberto Benavides, and I have been in charge of optimizing the photonic crystallization parameters using the Novacentrix Pulseforge. The results are large-area, anatase electrodes with great adhesion to flexible substrates and

photocatalytic response in the visible spectrum of light. These electrodes have been tested for the degradation of the organic molecule Rhodamine B.

Development of PbS QDs based inks for printed electronics

Thanks to all the experience gained in the synthesis, characterization and integration of lead sulfide quantum dots, I have a deep understanding of the procedures for device fabrication based on these versatile nanocrystals. However, the current synthesis process yields quantum dots that are only miscible in non-polar solvents like hexane and toluene, which toxic under continuous manipulation and are incompatible with current printing technologies as they tend to destroy the plastic reservoirs in printing cartridges. Also, these solvents quickly evaporate as it was evidenced by the screen printing pastes developed in the industrial project presented as part of this thesis. This problematic solvents could result in the clogging of the delicate piezoelectric jetting nozzles inside inkjet printers or clogging the small openings in screens used in screen printing. In this front, work has been initiated to create colloidal dispersion of PbS QDs that are miscible in polar solvents as water, ethanol and ethylene glycol, as shown in Figure 8.3(a). This is achieved through the ligand exchange process where the OA molecule is replaced by L-glutathione (GSH), yielding water-soluble, air-stable colloidal solutions of PbS QDs (Deng *et al.* (2012); Jumabekov *et al.* (2014)). From left to right: first vial, GSH solution in DI water. Second vial, GSH solution carefully deposited on top of the colloidal PbS QDs dispersed in chloroform. Water and chloroform are immiscible and thus the two solutions remain separated. Third vial, after hand shaking the vial for a few seconds, the ligand exchange takes place and the PbS QDs are now dispersed in water. The lower phase is the chloroform devoid of QDs.

These preliminary results show PbS QDs dispersed in DI water showing similar but reduced photoluminescence response, shown in Figure 8.3(b). This colloidal dispersion could be potentially be printed once the right balance of solvents is optimized to achieve the right vapor

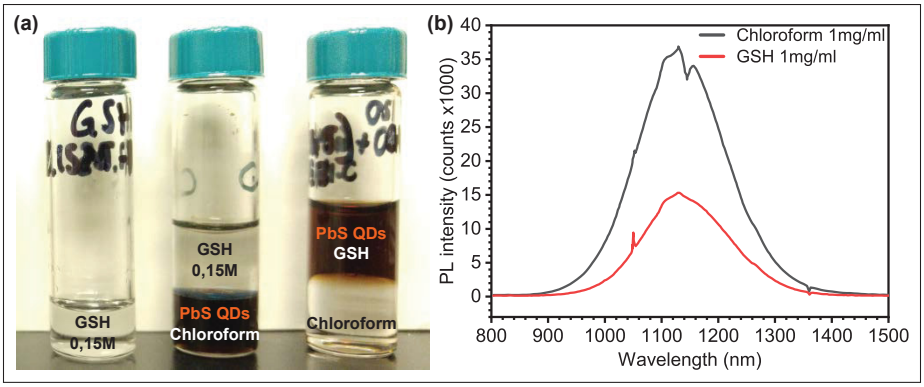

Figure 8.3 (a) Water solubilization of PbS QDs by ligand exchange with L-gluthatione (b) Photoluminescence of the QDs in chloroform and in water

pressure and viscosity values. Thanks to their small size, compatibility with digital printed is almost guaranteed. This opens the possibility for rapid prototyping of optoelectronic devices with strong response in the IR.

INKTIO: an entrepreneurial consolidation for semiconducting, photo-sensitive ceramic inks for printed electronics

As a direct result of my participation in developing the photo-sensitive ink of TiO_2 for printed electronics, the team INKTIO whose members were Dr. Charles Trudeau, Dr. Jaime Benavides and me, had the chance to participate in the contest Génie en Affaires from ACFAS in the 2019 edition. In this contest, our team was awarded the First prize of the jury.

Along this prize, came the subsequent patent application done in 2021 to protect our technology, filed in Canada and the USA under the name: “AN AMORPHOUS TITANIUM DIOXIDE PRECURSOR MATERIAL. METHOD OF PRODUCING THEREOF AND METHOD OF CONTROLLING CRYSTALLINE PHASES THEREOF”[2]. This patent allowed Dr. Benavides and I to pursue the incorporation of our company in 2023, of which I am co-founder and

[2] CA 3097600 - Available at: https://www.ic.gc.ca/opic-cipo/cpd/eng/patent/3097600/summary.html

CEO. We plan to extend the knowledge gathered during the creation of the TiO_2 ink into other metal-oxide formulations for next-generation printable SnO_2, ZrO and ZnO inks. This photo-sensitive ink platform that we have created, requires the precise know-how of the photonic crystallization conditions necessary to offer end-user applications in photocatalysis, bio-sensors and optoelectronic devices.

Most importantly, I want to acknowledge the opportunity provided by my advisor, Dr. Sylvain G. Cloutier, to have access to state-of-the-art equipment and pursue our daring ideas to make this company a reality.

Additional scientific publications

During this doctorate, I've had the chance to contribute in the work that led to several scientific publications. These peer-reviewed journal articles are referenced below:

- Gerlein, L. F., Benavides, J. A. & Cloutier, S. G. (2023). *Photonic Sintering of a Multi-Material Transparent Conductive Electrode Architecture for Optoelectronic Device Integration*. Submitted for Revision
- Vaussenat, F., Bhattacharya, A., Payette, J., Benavides-Guerrero, J. A., Perrotton, A., Gerlein, L. F. & Cloutier, S. G. (2023). Continuous Critical Respiratory Parameter Measurements Using a Single Low-Cost Relative Humidity Sensor: Evaluation Study. *JMIR Biomedical Engineering*, 8(1), e47146. doi: 10.2196/47146
- Gerlein, L. F., Benavides-Guerrero, J. A. & Cloutier, S. G. (2021). High-Performance Silver Nanowires Transparent Conductive Electrodes Fabricated Using Manufacturing-Ready High-Speed Photonic Sinterization Solutions. *Scientific Reports*, 11(1), 24156. doi: 10.1038/s41598-021-03528-w

- Gerlein, L. F., Benavides-Guerrero, J. A. & Cloutier, S. G. (2019). Laser-Assisted, Large-Area Selective Crystallization and Patterning of Titanium Dioxide Polymorphs. *Advanced Engineering Materials*, 22(2), 1901014. doi: 10.1002/adem.201901014
- Benavides-Guerrero, J. A., Gerlein, L. F., Trudeau, C., Banerjee, D., Guo, X. & Cloutier, S. G. (2022b). Synthesis of Vacancy-Rich Titania Particles Suitable for the Additive Manufacturing of Ceramics. *Scientific Reports*, 12(1), 15441. doi: 10.1038/s41598-022-19824-y
- Bhattacharya, A., Benavides, J. A., Gerlein, L. F. & Cloutier, S. G. (2022). Deep-Learning Framework for Fully-Automated Recognition of TiO2 Polymorphs Based on Raman Spectroscopy. *Scientific Reports*, 12(1), 21874. doi: 10.1038/s41598-022-26343-3
- Benavides-Guerrero, J., Banerjee, D., Gedamu, D., Gerlein, L. F. & Cloutier, S. G. (2022a). Conductive, Anti-Corrosion, Self-Healing Smart Coating Technology Incorporating Graphene-Based Nanocomposite Matrix. *Frontiers in Materials*, 9, 12. doi: 10.3389/fmats. 2022.835855
- Ka, I., Gerlein, L. F., Asuo, I. M., Bouzidi, S., Gedamu, D. M., Pignolet, A., Rosei, F., Nechache, R. & Cloutier, S. G. (2020). Solution-Processed p-Type Copper Thiocyanate (CuSCN) Enhanced Sensitivity of PbS-Quantum-Dots-Based Photodiode. *ACS Photonics*, 7(7), 1628–1635. doi: 10.1021/acsphotonics.0c00491
- Benavides, J. A., Trudeau, C. P., Gerlein, L. F. & Cloutier, S. G. (2018). Laser Selective Photoactivation of Amorphous TiO2 Films to Anatase and/or Rutile Crystalline Phases. *ACS Applied Energy Materials*, 1(8), 3607–3613. doi: 10.1021/acsaem.8b00171
- Asuo, I. M., Gedamu, D., Ka, I., Gerlein, L. F., Fortier, F.-X., Pignolet, A., Cloutier, S. G. & Nechache, R. (2018). High-Performance Pseudo-Halide Perovskite Nanowire Networks for Stable and Fast-Response Photodetector. *Nano Energy*, 51, 324–332. doi: 10.1016/j.nanoen.2018.06.057

- Fourmont, P., Gerlein, L. F., Fortier, F.-X., Cloutier, S. G. & Nechache, R. (2018). Highly Efficient Thermoelectric Microgenerators Using Nearly Room Temperature Pulsed Laser Deposition. *ACS Applied Materials & Interfaces*, 10(12), 10194–10201. doi: 10.1021/acsami.7b18852
- Ka, I., Gerlein, L. F., M. Asuo, I., Nechache, R. & Cloutier, S. G. (2018). An Ultra-Broadband Perovskite-PbS Quantum Dot Sensitized Carbon Nanotube Photodetector. *Nanoscale*, 10(19), 9044–9052. doi: 10.1039/C7NR08608C
- Ka, I., Gerlein, L. F., Nechache, R. & Cloutier, S. G. (2017). High-Performance Nanotube-Enhanced Perovskite Photodetectors. *Scientific Reports*, 7, 45543. doi: 10.1038/srep45543
- Banerjee, D., Trudeau, C., Gerlein, L. F. & Cloutier, S. G. (2016). Phonon Processes in Vertically Aligned Silicon Nanowire Arrays Produced by Low-Cost All-Solution Galvanic Displacement Method. *Applied Physics Letters*, 108(11), 113109. doi: 10.1063/1.4944334
- Xu, F., Gerlein, L. F., Ma, X., Haughn, C. R., Doty, M. F. & Cloutier, S. G. (2015). Impact of Different Surface Ligands on the Optical Properties of PbS Quantum Dot Solids. *Materials*, 8(4), 1858–1870

APPENDIX I

CHAPTER 3: SUPPLEMENTARY INFORMATION

Table A I-1 Summary of crystallization parameters used in the squares test

Travel speed [mm min^{-1}]	**Laser speed [mm min^{-1}]**	**Passes**	**Pass depth [mm]**	**Laser setting**	**Settings increment stepsize**
50	50	2	0	25-255	25

Table A I-2 Laser power optimization results. Crystallization parameters for low-fragmentation yield of the rutile phase

Travel speed [mm min^{-1}]	**Laser speed [mm min^{-1}]**	**Passes**	**Pass depth [mm]**	**Emission power [mW]**	**Emission power density** $[W\ mm^{-2}]$
100	100	2	0	68	216

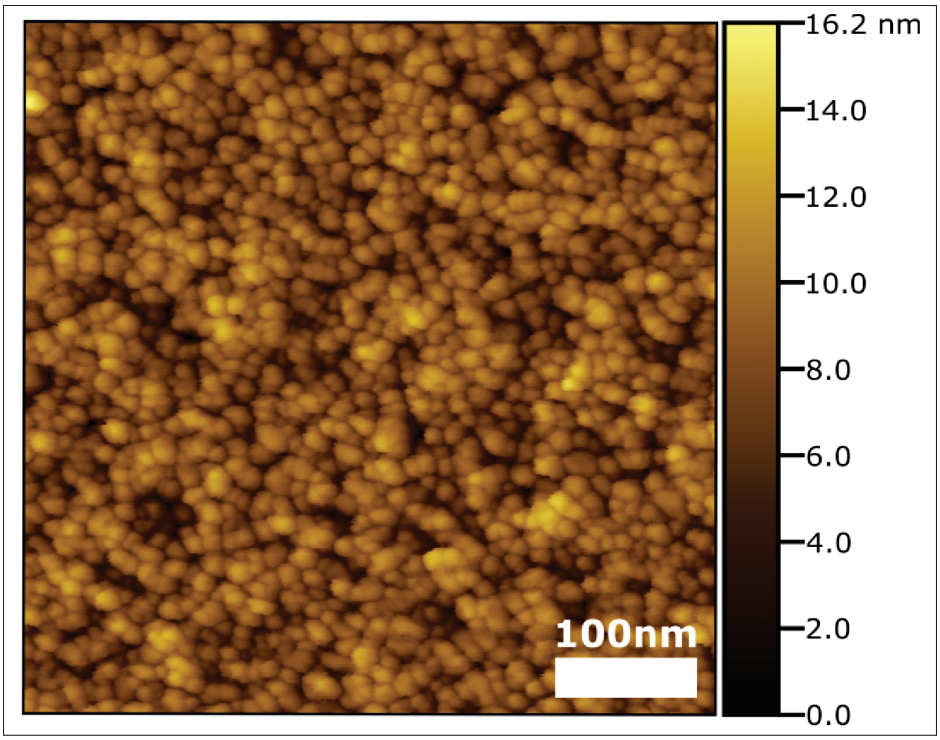

Figure A I-1 AFM imaging of an amorphous thin film of the as-synthesized TiO_2 precursor produced by the incomplete nonhydrolytic sol-gel ester elimination reaction

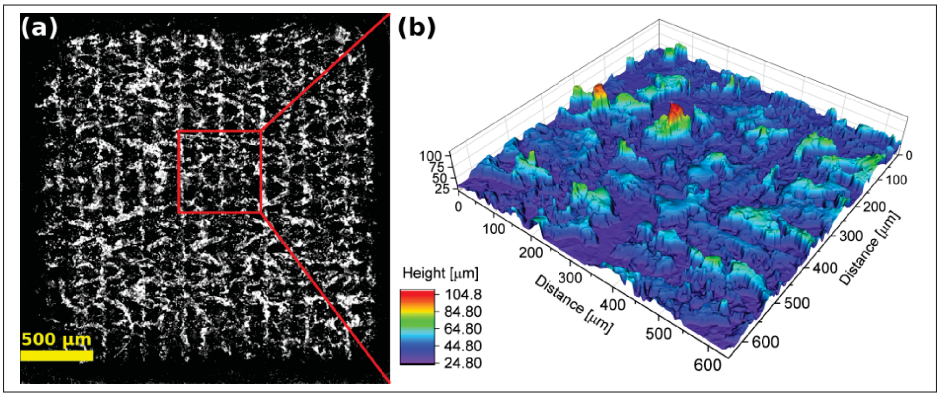

Figure A I-2 3D reconstruction of the square pattern done at power setting 255 (a) Full square micrograph (b) Magnified 3D laser reconstruction of the red square in (a)

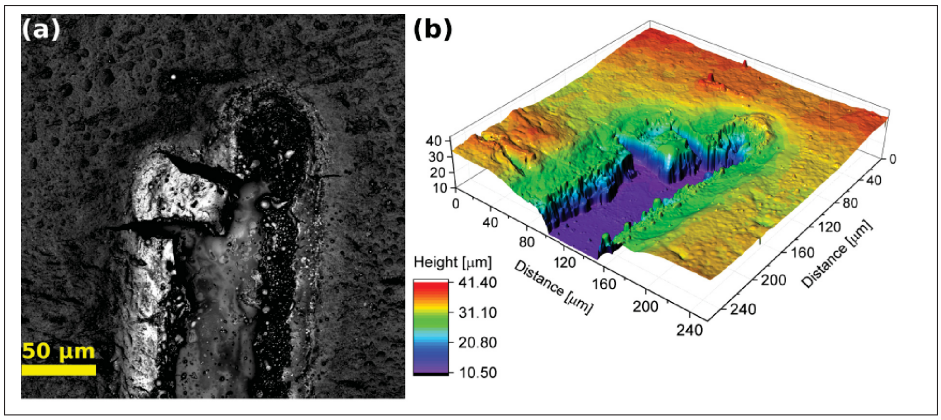

Figure A I-3 3D reconstruction of the line pattern done at power setting 7 (a) Top view micrograph (b) 3D laser reconstruction of the ablated line. The purple area corresponds to the glass

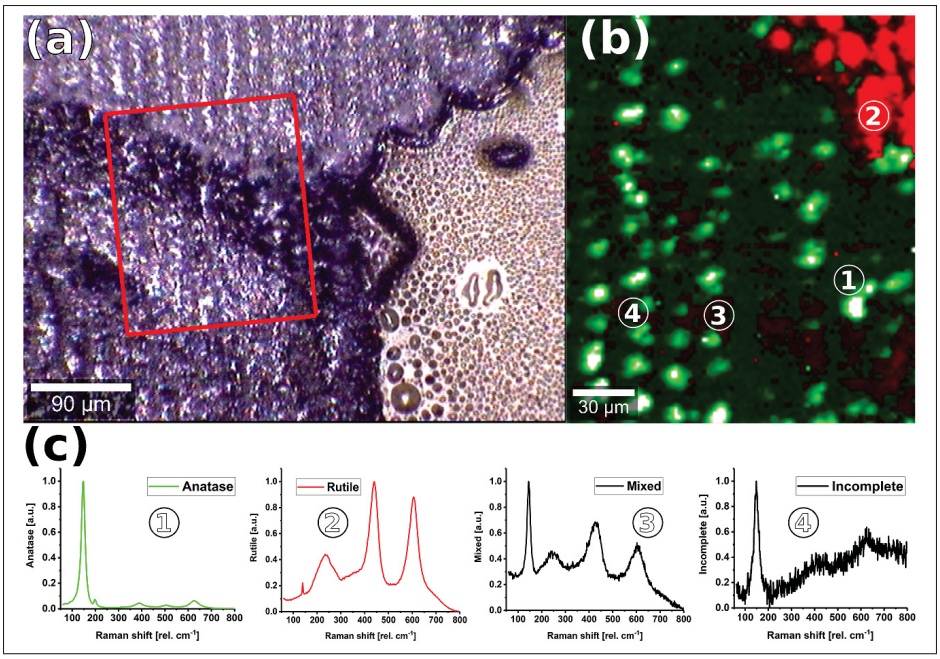

Figure A I-4 Confocal Raman image analysis of the interface between anatase and rutile sections in the geometric pattern (a) Micrograph of the interface showing the three regions (b) Raman color coded image showing the strong presence of anatase and rutile sections. The green section is the anatase area while the red section is the rutile area. The numbers correspond to different Raman signals presented below (c) Raman signals showing the crystallization state of various points inside the red square in (a)

APPENDIX II

CHAPTER 4: SUPPLEMENTARY INFORMATION

1. Validation of the SimPulse simulations

This detailed comparison intends to validate the SimPulse simulation tool and its application for the post-processing treatment of our silver nanowires thin-film electrodes. This commercial integrated photonic curing simulation tool is intended to reduce processing times in industrial environments. The sample's material stack can be created with their corresponding thicknesses to match real conditions as closely as possible. It yields the appropriate processing parameters for photonic curing and sintering a variety of commercial metallic nanoparticles inks and slurries, widely employed in the printed electronics world. Here, we compared the SimPulse model's prediction with reports from the literature.

Indeed, Bansal et *al*. and Dexter et *al*. already provided a comprehensive framework to elucidate the behavior of nanowires under intense pulse light sinteringBansal & Malhotra (2016); Dexter *et al.* (2017). Based on their experimental parameters and results, we can replicate the same thermal behavior using the SimPulse tool. To do so, one must set the simulator parameters in order to match the pulse fluence conditions reported and adjust the machine parameters within the inherent speed limitations of the machine. The results shown in Figure II-1(a-c) depict the behavior predicted by SimPulse tool using the same pulse fluence conditions as previously reportedBansal & Malhotra (2016); Dexter *et al.* (2017). The material stack is configured to be the same, from top to bottom: 20 nm layer of silver, 250 µm of polyimide substrate, 1500 µm of borosilicate glass buffer. The pulse settings were set as follows: single pulse duration 5000 µs, duty cycle of 50%, pulse frequency of 3 Hz, no micro-pulses.

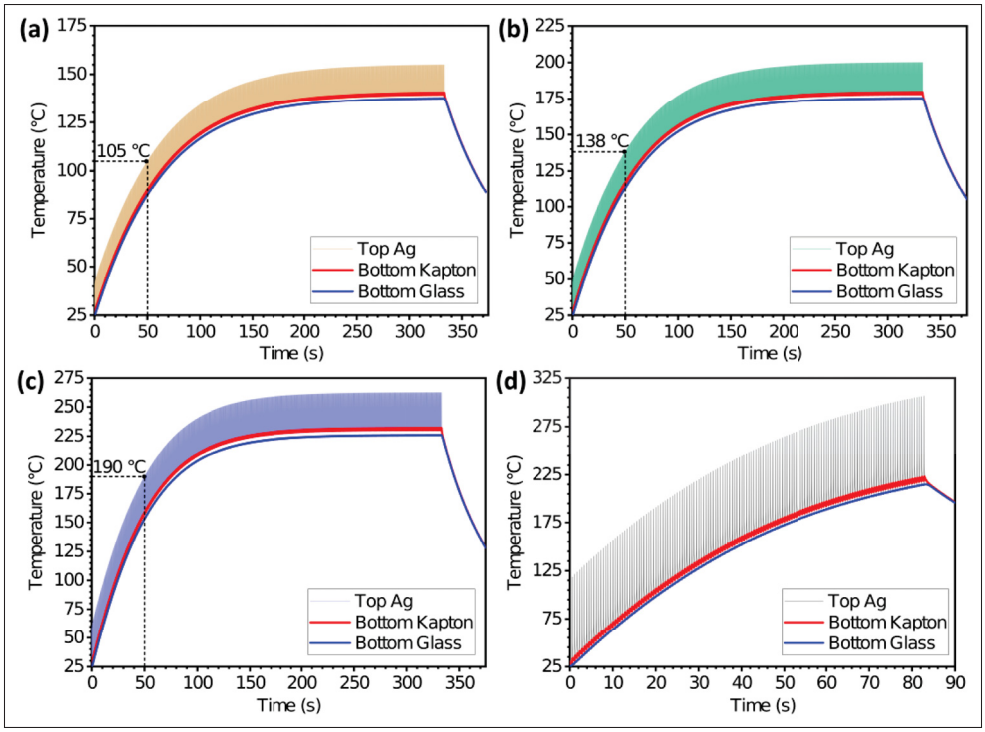

Figure A II-1 Validation of the Simpulse simulation for nanoparticles. SimPulse temperature predictions using 1000 pulses to match the results reported by Bansal et al. at different energy densities Bansal & Malhotra (2016): (a) E1=0.85 J.cm^{-2}, (b) E2=1.2 J.cm^{-2} and (c) E3=1.8 J.cm^{-2}. The dashed lines represent the 150th pulse count and the respective temperature reached up to that point (d) Simulated pulse conditions matching the thermal behavior of E3 with 150 pulses

We then extended the pulse number from 150 (shown in Figure II-1(a-c) dashed lines) used in the literatureBansal & Malhotra (2016); Dexter *et al.* (2017), to 1000 pulses to achieve a steady state temperature matching the top surface's temperature predicted by the non-coupled model already analyzed. Also, our pulse emission frequency is different at these fluence conditions, a factor that affects the heating rate of the metallic nanowires. Aiming to match the thermal behavior of our simulations to those previously reportedBansal & Malhotra (2016); Dexter *et al.* (2017), E3 in this case, we changed the voltage applied to the lamp diode and adjusting for pulse frequency, the fluence required to obtain a peak temperature around 300 °C after 150 pulses is 3.49 J.cm^{-2}, as shown in Figure II-1(d). Interestingly, the

delta of temperature within the Kapton layer from top to bottom oscillates around 100 °C, according to the simulations. Because of the rapid cooling between layers, this does not affect the substrate.

APPENDIX III

CHAPTER 5: SUPPLEMENTARY INFORMATION

1. Siver nanowires embedding, and surface modification, on the PET substrate as a result of the photonic sintering processing

The results presented in Figure S1 corroborate the SEM observations in Figure III-1, showing that the PET surface was locally affected by the heated nanowires, which in this case, is represented by the dark colored pits in both AFM images. The surface variations between the pits and the surrounding high areas are the result of excess heat generated at the nanowires.

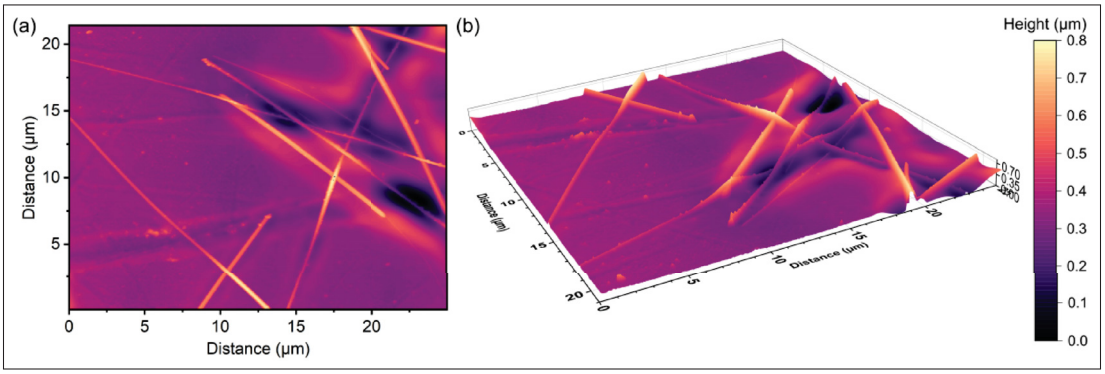

Figure A III-1 AFM topographic reconstruction of the AgNWs AfterPC. Both (a) 2D reconstruction and (b) 3D projection show how the nanowires penetrated the PET substrate locally affecting it's structure

2. EDS analysis report of the hybrid TCE architecture

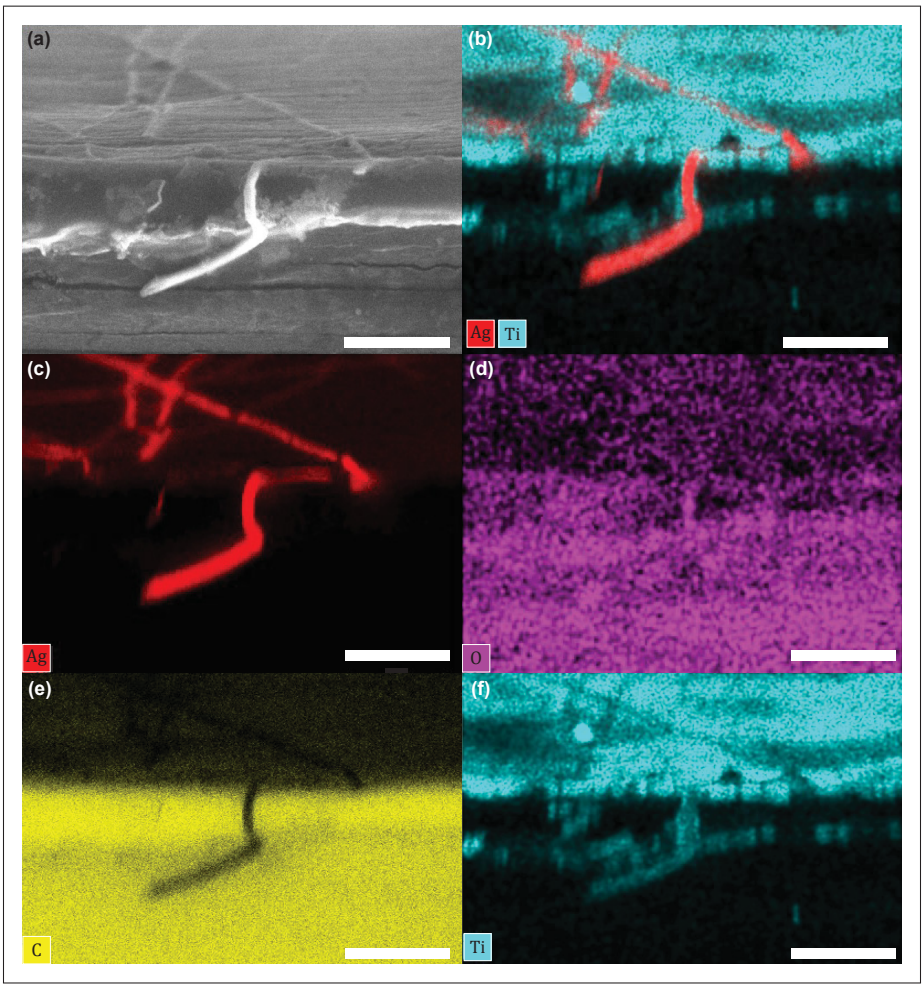

Figure A III-2 EDS analysis of a cross sectional cut of a film of AgNWs covered in TiO_2 (a) Initial SEM image (b) composite image of detected Ag and Ti elements (c) Silver only highlighting the distribution of the nanowires in the matrix (d) Oxygen only image, which is present in both the substrate and the covering layer (e) Carbon only image that is mostly present in the substrate (f) Titanium only which corresponds to the coverage film atop the nanowires, the TiO_2 layer was estimated to be 400nm in thickness from this image. All scale-bars correspond to 2 µm in length

3. Crystallinity analysis the TiO_2precursor by XRD

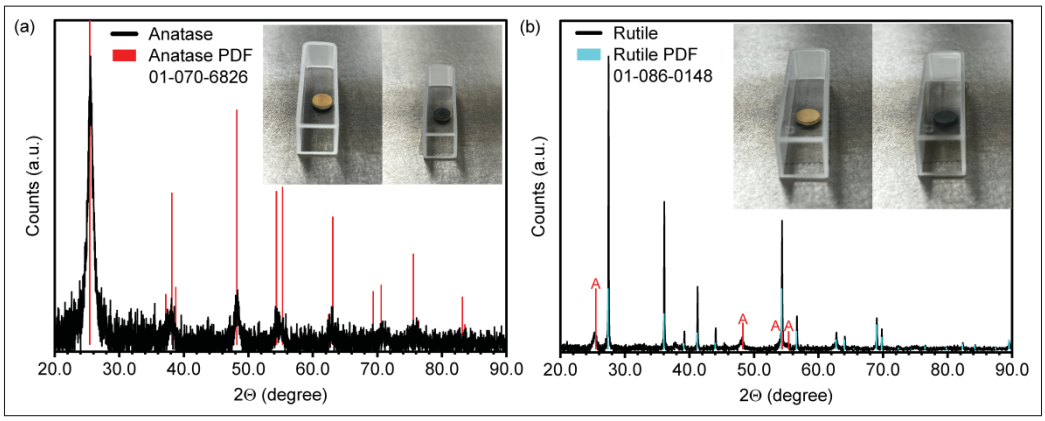

Figure A III-3 XRD of pellets made of the same TiO_2 precursor, dried in powder form. These pellets are subject to photonic crystallization to obtain anatase phase in (a) and rutile phase in (b). Four peaks coming from anatase are detectable when analysing the rutile pellet in (b), this is a by-product of the rutile photonic crystallization processing on thicker samples. The inset pictures in both figures show the pellets before and after photonic crystallization

4. Method for measuring of haze in nanowire-based semitransparent films

Using a UV/VIS spectrometer and an integrating sphere following the relation H = (T4/T2-T3/T1)·100%, where T2 and T4 are the sample's total transmittance and forward scattered light and, T1 and T3 represent the correction factor from the equipment using the white standard and the open-ended sphere, respectively (Preston *et al.*, 2013; Yu, Hsiao & Liu, 2006a). The general scheme is depicted in the Figure S2.

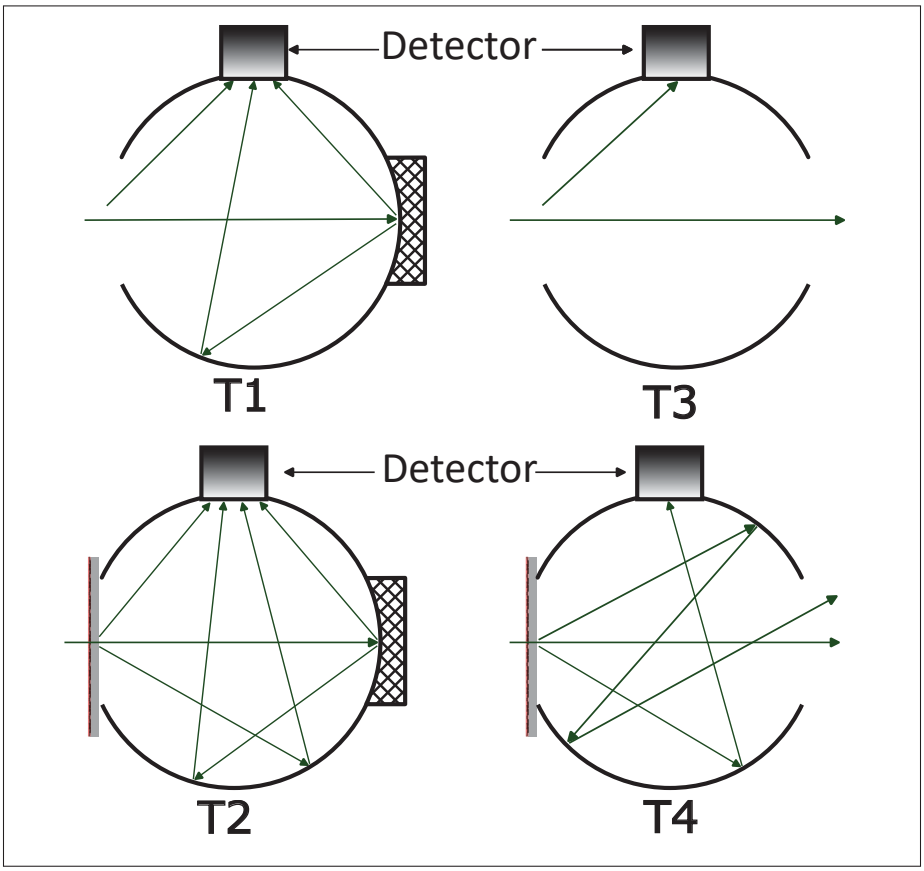

Figure A III-4 Schematic representation of the four measures necessary to calculate the haze of a sample using an integrating sphere

5. Transmittance data for all samples AgNWs + TiO_2 AfterPC crystallized in anatase and rutile

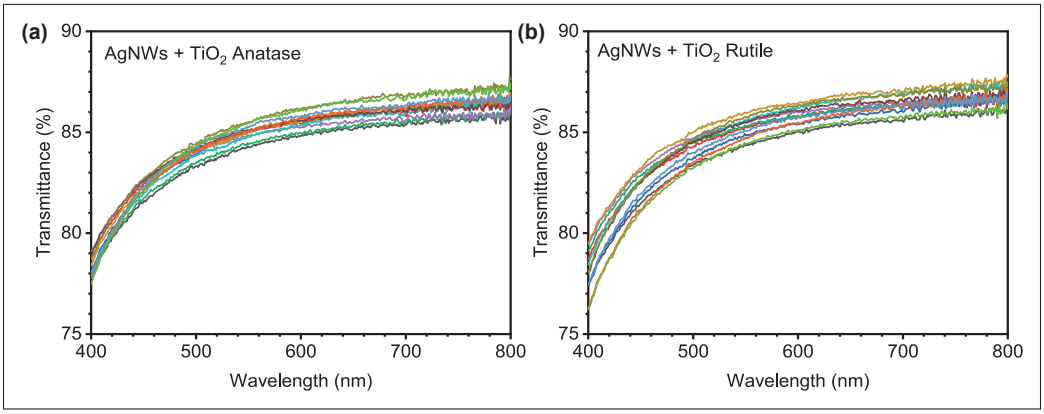

Figure A III-5 Transmittance for the finalized samples after the last photonic curing processing, AgNWs + TiO_2 AfterPC (a) Samples crystallized into anatase (b) Samples crystallized into rutile

6. Additional developing solution test results

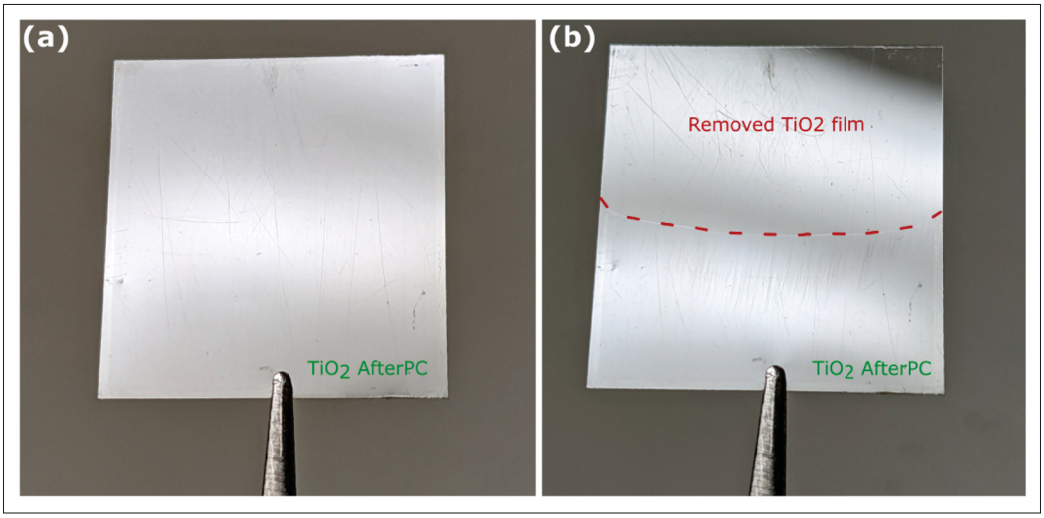

Figure A III-6 Only TiO_2 layer deposited atop PET unsuccessfully crystallized (a) In here, the film was treated using the same photonic sintering conditions presented in the manuscript to obtain the rutile phase (b) The same film after 10s of submersion in the *DevSol* test and subsequent washing using DI water, showing the removal of the TiO_2 in the exposed area. The red dashed line follows the thin film line and facilitates the discrimination of the two areas

APPENDIX IV

CHAPTER 6: SUPPLEMENTARY INFORMATION

1. Experimental section

1.1 Materials

Lead(II) oxide (PbO, Puratonic 99.999%) was procured from Alfa Aesar and used is. Oleic acid (OA, technical grade, 90%), hexamethyldisilathiane (HMDS, synthesis grade, kept under hydrogen atmosphere in a glovebox), , 1-octadecene (ODE, technical grade, 90%), anhydrous hexane (95%), 1,2-ethanedithiol (EDT, technical grade, $\geq$ 90%), anhydrous acetonitrile (99.8%), and tetrabutylammonium iodide (TBAI, reagent grade, 98%) were purchased from Sigma Aldrich and used is. Titanium (IV) butoxide 99% (TBT, Aldrich), acetylacetone for synthesis (ACAC, Aldrich), ethanol (ACS reagent, $\geq$ 99.5% (200 proof, absolute), Acetone (HPLC grade) was acquired from EMD Millipore was used as purchased. The COOH-functionalized SWCNTs (purity 95%) were purchased at Nanolab.

1.2 PbS quantum dots synthesis

The synthesis method follows a modified chemical route reported by (Hines & Scholes, 2003; Zhang *et al.*, 2015) with a proportional molar ratio of 4:2:1 for the constituents OA:Pb:S, respectively. On a 3-neck flask atop a magnetic stirrer, mixing of 0.45 grams of PbO, 2.67 grams of OA and 10 grams of ODE under nitrogen atmosphere and continuous stirring with the heating mantle set at 120°C for at least 1 hour. Meanwhile, the sulfur precursor preparation took place inside the nitrogen-purged glovebox where 210 µL of the sulfur precursor, HMDS, is dissolved in 4 g of ODE and placed on a syringe ready for injection into the 3-neck flask. The heating mantle was set so that the temperature inside the mixture was reduced to a stable 50°C and then, the sulfur precursor syringe was injected in the flask. Given the low reaction temperature, the nucleation reaction of the PbS QD's took longer than reactions made at higher temperatures (Zhang *et al.*, 2015). The reaction was left under continuous

stirring and nitrogen flow for additional 5 minutes. To quench the reaction, the heating mantle is removed and the 3-neck flask is submerged in cold water for a minute.

Removal and washing-off the excess oleic acid is done by 10 min centrifugation of the reaction product in tubes filled with excess acetone. Once complete, the acetone was carefully removed leaving the QDs agglomerate to dry in the bottom. A small amount of hexane (1-2 mL) is enough to disperse the QDs slush and a second washing procedure with acetone took place again. Finally, a dispersion of the washed QDs in hexane was filtered through 0.2 µm polytetrafluoroethylene filters for final collection. The final PbS solution in hexane had a concentration of 50 mg/ml.

1.3 Sol-gel chemical route for synthesis of the anatase TiO_2 electrodes with and without MWCNTs

The TiO_2 solution has been synthesized using a modified sol-gel technique. A mixture of 28.8532 g of ethanol with 1.4748 g of ACAC was place in a beaker and covered with parafilm and stirred magnetically for 20 minutes. Then, 10.8604 g of TBT were combined with this mixture, covered with parafilm again and magnetic stirring for additional 40 minutes. Finally, 0.84 mL of de-ionized water was added to the mixture, covered with parafilm, and magnetically stirred for 120 min. This precursor will undergo a 24 hour aging process after which it will be ready for use. Adding ACAC reduces the TBT hydrolysis reaction kinetics, impeding the formation of precipitates or chunks.

Once the solution is ready for processing, the desired amount MWCNTs was incorporated into the solution and magnetically stirred for 30 minutes. Afterwards, the mixture was placed under ultrasonic bath for 1 hour to yield a very uniform dispersion of MWCNTs ready for processing.

1.4 Device assembly

Atop FTO covered glass (400nm layer thickness) a layer of amorphous solution of TiO_2 deposited by spin-coating at 6000 RPM for 30 sec. yielding a thin layer of 60 nm on average, followed by thermal annealing in a hot plate at 550 °C during 1 hour to completely achieve anatase TiO_2. The deposition of the TiO_2+MWCNTs mixture was done similarly. Because of the surrounding ceramic coating in the nanotubes, the annealing process does not destroy them allowing the to retain their optoelectronic properties. PbS quantum dot solids were fabricated layer by layer on top of the TiO_2 (+MWCNTs) layer using spin coating at 2500 RPM for 30 s. For each layer, 15 s of static solid-state ligand exchange with either a solution of 10 mg/ml of TBAI in methanol as inorganic ligand for the active region, or a 0.02 M solution of EDT in anhydrous acetonitrile as organic ligand for the hole transport layer/electron blocking layer (HTL/EBL). Gold was evaporated and used as front contact interfacing the EDT-treated layers. Fast-drying silver paste was applied to the uncovered FTO section for better connection.

1.5 Measurement and characterization

The current–voltage (I-V) characterization was done with a Keithley-2400 source-measure unit (SMU). The SEM imagery was obtained from a Hitachi SU 8230 field emission scanning electron microscope. Photoluminescence characterization was done using a Torus 532 nm laser (Laser Quantum, Cheshire, UK) for excitation and a Jobin-Yvon iHR320 triple-grating spectrometer (Horiba Scientific, Kyoto, Japan) equipped with a symphony thermoelectrically-cooled Synapse CCD detector array to collect the emission. Absorbance measures were taken using a Jaz spectrometer from Ocean Optics and a Xenon calibrated lamp. Raman characterization was done under a WiTEC alpha300 micro-Raman system equipped with a 532 nm fiber coupled laser as excitation source.

BIBLIOGRAPHY

Akbar, S., Dutta, P. & Lee, C. (2006). High-Temperature Ceramic Gas Sensors: A Review. *International Journal of Applied Ceramic Technology*, 3(4), 302–311.

Akhavan, V., Schroder, K., Pope, D. & Farnsworth, S. (2013). Processing Thick-Film Screen Printed Metalon CuO Reduction Ink with PulseForge Tools. *Coating International*, 46, 14–17.

Akinsinde, L. O., Glier, T. E., Schwartzkopf, M., Betker, M., Nissen, M., Witte, M., Scheitz, S., Nweze, C., Grimm-Lebsanft, B., Gensch, M., Chumakov, A., Baev, I., Schürmann, U., Dankwort, T., Fischer, F., Martins, M., Roth, S. V., Kienle, L. & Rübhausen, M. (2021). Surface Characterization and Resistance Changes of Silver-Nanowire Networks upon Atmospheric Plasma Treatment. *Applied Surface Science*, 550, 149362. doi: 10.1016/j.apsusc.2021.149362.

Alaie, Z., Mohammad Nejad, S. & Yousefi, M. H. (2015). Recent Advances in Ultraviolet Photodetectors. *Materials Science in Semiconductor Processing*, 29, 16–55. doi: 10.1016/j.mssp.2014.02.054.

Ali, A. H., Shuhaimi, A. & Hassan, Z. (2014). Structural, Optical and Electrical Characterization of ITO, ITO/Ag and ITO/Ni Transparent Conductive Electrodes. *Applied Surface Science*, 288, 599–603.

Ansari, M. A. (2021). Modelling of Size-Dependent Thermodynamic Properties of Metallic Nanocrystals Based on Modified Gibbs–Thomson Equation. *Applied Physics A*, 127(5), 385.

Arin, M., Lommens, P., Avci, N., Hopkins, S. C., De Buysser, K., Arabatzis, I. M., Fasaki, I., Poelman, D. & Van Driessche, I. (2011). Inkjet Printing of Photocatalytically Active TiO2 Thin Films from Water Based Precursor Solutions. *Journal of the European Ceramic Society*, 31(6), 1067–1074.

Asuo, I. M., Gedamu, D., Ka, I., Gerlein, L. F., Fortier, F.-X., Pignolet, A., Cloutier, S. G. & Nechache, R. (2018). High-Performance Pseudo-Halide Perovskite Nanowire Networks for Stable and Fast-Response Photodetector. *Nano Energy*, 51, 324–332. doi: 10.1016/j.nanoen.2018.06.057.

Aurang, P., Doganay, D., Bek, A., Turan, R. & Unalan, H. E. (2017). Silver Nanowire Networks as Transparent Top Electrodes for Silicon Solar Cells. *Solar Energy*, 141, 110–117. doi: 10.1016/j.solener.2016.11.021.

Azulai, D., Belenkova, T., Gilon, H., Barkay, Z. & Markovich, G. (2009). Transparent Metal Nanowire Thin Films Prepared in Mesostructured Templates. *Nano Letters*, 9(12), 4246–4249. doi: 10.1021/nl902458j.

Bae, S., Kim, H., Lee, Y., Xu, X., Park, J.-S., Zheng, Y., Balakrishnan, J., Lei, T., Ri Kim, H., Song, Y. I., Kim, Y.-J., Kim, K. S., Özyilmaz, B., Ahn, J.-H., Hong, B. H. & Iijima, S. (2010). Roll-to-Roll Production of 30-Inch Graphene Films for Transparent Electrodes. *Nature Nanotechnology*, 5(8), 574–578. doi: 10.1038/nnano.2010.132.

Bae, S., Kim, S. J., Shin, D., Ahn, J.-H. & Hong, B. H. (2012). Towards Industrial Applications of Graphene Electrodes. *Physica Scripta*, T146, 014024. doi: 10.1088/0031-8949/2012/T146/014024.

Bai, J. & Zhou, B. (2014). Titanium Dioxide Nanomaterials for Sensor Applications. *Chemical Reviews*, 114(19), 10131–10176.

Bai, Y., Mora-Seró, I., De Angelis, F., Bisquert, J. & Wang, P. (2014). Titanium Dioxide Nanomaterials for Photovoltaic Applications. *Chemical Reviews*, 114(19), 10095–10130.

Bakueva, L., Gorelikov, I., Musikhin, S., Zhao, X. S., Sargent, E. H. & Kumacheva, E. (2004). PbS Quantum Dots with Stable Efficient Luminescence in the Near-IR Spectral Range. 16(11), 926–929. doi: 10.1002/adma.200306458.

Balazs, D. M., Dirin, D. N., Fang, H.-H., Protesescu, L., Brink, G. H., Kooi, B. J., Kovalenko, M. V. & Loi, M. A. (2015). Counterion-Mediated Ligand Exchange for PbS Colloidal Quantum Dot Superlattices. 9(12), 11951–11959.

Banerjee, D., Trudeau, C., Gerlein, L. F. & Cloutier, S. G. (2016). Phonon Processes in Vertically Aligned Silicon Nanowire Arrays Produced by Low-Cost All-Solution Galvanic Displacement Method. *Applied Physics Letters*, 108(11), 113109. doi: 10.1063/1.4944334.

Banerjee, D., Benavides, J. A., Guo, X. & Cloutier, S. G. (2018). Tailored Interfaces of the Bulk Silicon Nanowire/TiO2 Heterojunction Promoting Enhanced Photovoltaic Performances. *ACS Omega*, 3(5), 5064–5070.

Banerjee, D., Asuo, I. M., Pignolet, A., Nechache, R. & Cloutier, S. G. (2020). High Performance Photodetectors Using Porous Silicon-TiO2 Heterostructure. *Engineering Research Express*, 2(3), 035021. doi: 10.1088/2631-8695/abb06d.

Bansal, S. & Malhotra, R. (2016). Nanoscale-Shape-Mediated Coupling between Temperature and Densification in Intense Pulsed Light Sintering. *Nanotechnology*, 27(49), 495602.

Baran, D., Corzo, D. & Blazquez, G. (2020). Flexible Electronics: Status, Challenges and Opportunities. *Frontiers in Electronics*, 1, 13.

Barron, A. R. (2019). 8.7: Characterization of Graphene by Raman Spectroscopy. In *Physical Methods in Chemistry and Nano Science*. Retrieved from: https://chem.libretexts.org/@go/page/55923.

Baskoutas, S. & Terzis, A. F. (2006). Size-Dependent Band Gap of Colloidal Quantum Dots. *Journal of Applied Physics*, 99(1), 013708. doi: 10.1063/1.2158502.

Bawendi, M. G., Steigerwald, M. L. & Brus, L. E. (1990). The Quantum Mechanics of Larger Semiconductor Clusters (" Quantum Dots"). *Annual Review of Physical Chemistry*, 41(1), 477–496.

Benavides, J. A., Trudeau, C. P., Gerlein, L. F. & Cloutier, S. G. (2018). Laser Selective Photoactivation of Amorphous TiO2 Films to Anatase and/or Rutile Crystalline Phases. *ACS Applied Energy Materials*, 1(8), 3607–3613. doi: 10.1021/acsaem.8b00171.

Benavides-Guerrero, J., Banerjee, D., Gedamu, D., Gerlein, L. F. & Cloutier, S. G. (2022a). Conductive, Anti-Corrosion, Self-Healing Smart Coating Technology Incorporating Graphene-Based Nanocomposite Matrix. *Frontiers in Materials*, 9, 12. doi: 10.3389/fmats. 2022.835855.

Benavides-Guerrero, J. A., Gerlein, L. F., Trudeau, C., Banerjee, D., Guo, X. & Cloutier, S. G. (2022b). Synthesis of Vacancy-Rich Titania Particles Suitable for the Additive Manufacturing of Ceramics. *Scientific Reports*, 12(1), 15441. doi: 10.1038/s41598-022-19824-y.

Benetti, D., Dembele, K. T., Benavides, J., Zhao, H., Cloutier, S., Concina, I., Vomiero, A. & Rosei, F. (2016). Functionalized Multi-Wall Carbon Nanotubes/TiO2 Composites as Efficient Photoanodes for Dye Sensitized Solar Cells. *Journal of Materials Chemistry C*, 4(16), 3555–3562.

Bhattacharya, A., Benavides, J. A., Gerlein, L. F. & Cloutier, S. G. (2022). Deep-Learning Framework for Fully-Automated Recognition of TiO2 Polymorphs Based on Raman Spectroscopy. *Scientific Reports*, 12(1), 21874. doi: 10.1038/s41598-022-26343-3.

Bolduc, M., Trudeau, C., Beaupré, P., Cloutier, S. G. & Galarneau, P. (2018). Thermal Dynamics Effects Using Pulse-Shaping Laser Sintering of Printed Silver Inks. *Scientific Reports*, 8(1), 1418.

Borghetti, M., Cantù, E., Sardini, E. & Serpelloni, M. (2020). Future Sensors for Smart Objects by Printing Technologies in Industry 4.0 Scenario. *Energies*, 13(22), 5916. doi: 10.3390/en13225916.

Borriello, C., Miscioscia, R., Mansour, S. A., Di Luccio, T., Bruno, A., Loffredo, F., Villani, F. & Minarini, C. (2015). Influence of Ligand Exchange on the Electrical Transport Properties of PbS Nanocrystals. 212(12), 2677–2685.

Bose, R., McMillan, J. F., Gao, J., Rickey, K. M., Chen, C. J., Talapin, D. V., Murray, C. B. & Wong, C. W. (2008). Temperature-Tuning of Near-Infrared Monodisperse Quantum Dot Solids at 1.5 µm for Controllable Förster Energy Transfer. *Nano Letters*, 8(7), 2006–2011. doi: 10.1021/nl8011243.

Brown, P. R., Kim, D., Lunt, R. R., Zhao, N., Bawendi, M. G., Grossman, J. C. & Bulović, V. (2014). Energy Level Modification in Lead Sulfide Quantum Dot Thin Films through Ligand Exchange. 8(6), 5863–5872.

Brus, L. E. (1984). Electron–Electron and Electron-hole Interactions in Small Semiconductor Crystallites: The Size Dependence of the Lowest Excited Electronic State. *The Journal of Chemical Physics*, 80(9), 4403–4409. doi: 10.1063/1.447218.

Buffat, P. & Borel, J.-P. (1976). Size Effect on the Melting Temperature of Gold Particles. *Physical Review A*, 13(6), 2287–2298.

Camic, B. T., Jeong, H. I., Aslan, M. H., Kosemen, A., Kim, S., Choi, H., Basarir, F. & Lee, B. R. (2020). Preparation of Transparent Conductive Electrode via Layer-By-Layer Deposition of Silver Nanowires and Its Application in Organic Photovoltaic Device. *Nanomaterials*, 10(1), 46.

Cann, M., Large, M. J., Henley, S. J., Milne, D., Sato, T., Chan, H., Jurewicz, I. & Dalton, A. B. (2016). High Performance Transparent Multi-Touch Sensors Based on Silver Nanowires. *Materials Today Communications*, 7, 42–50.

Cao, C., Hu, C., Wang, X., Wang, S., Tian, Y. & Zhang, H. (2011). UV Sensor Based on TiO2 Nanorod Arrays on FTO Thin Film. *Sensors and Actuators B: Chemical*, 156(1), 114–119. doi: 10.1016/j.snb.2011.03.080.

Cao, W., Li, J., Chen, H. & Xue, J. (2014). Transparent Electrodes for Organic Optoelectronic Devices: A Review. *Journal of Photonics for Energy*, 4(1), 040990. doi: 10.1117/1.JPE.4.040990.

Cao, Y., Stavrinadis, A., Lasanta, T., So, D. & Konstantatos, G. (2016). The Role of Surface Passivation for Efficient and Photostable PbS Quantum Dot Solar Cells. 1(4), 16035.

Castro Neto, A. H., Guinea, F., Peres, N. M. R., Novoselov, K. S. & Geim, A. K. (2009). The Electronic Properties of Graphene. *Reviews of Modern Physics*, 81(1), 109–162. doi: 10.1103/RevModPhys.81.109.

Chahrour, K. M., Yam, F. K. & Eid, A. M. (2020). Water-Splitting Properties of Bi-Phased TiO2 Nanotube Arrays Subjected to High-Temperature Annealing. *Ceramics International*, 46(13), 21471–21481. doi: 10.1016/j.ceramint.2020.05.246.

Chan, G. H., Zhao, J., Hicks, E. M., Schatz, G. C. & Van Duyne, R. P. (2007). Plasmonic Properties of Copper Nanoparticles Fabricated by Nanosphere Lithography. *Nano Letters*, 7(7), 1947–1952. doi: 10.1021/nl070648a.

Chang, J. & Waclawik, E. R. (2014). Colloidal Semiconductor Nanocrystals: Controlled Synthesis and Surface Chemistry in Organic Media. *RSC Advances*, 4(45), 23505–23527. doi: 10.1039/C4RA02684E.

Chawengkijwanich, C. & Hayata, Y. (2008). Development of TiO2 Powder-Coated Food Packaging Film and Its Ability to Inactivate Escherichia Coli in Vitro and in Actual Tests. *International Journal of Food Microbiology*, 123(3), 288–292.

Chen, K. & Xue, D. (2014). Preparation of Colloidal Graphene in Quantity by Electrochemical Exfoliation. *Journal of Colloid and Interface Science*, 436, 41–46. doi: 10.1016/j.jcis.2014.08.057.

Chen, S.-P., Retamal, J. R. D., Lien, D.-H., He, J.-H. & Liao, Y.-C. (2015). Inkjet-Printed Transparent Nanowire Thin Film Features for UV Photodetectors. *RSC Advances*, 5(87), 70707–70712. doi: 10.1039/C5RA12617G.

Chen, T.-G., Huang, B.-Y., Liu, H.-W., Huang, Y.-Y., Pan, H.-T., Meng, H.-F. & Yu, P. (2012). Flexible Silver Nanowire Meshes for High-Efficiency Microtextured Organic-Silicon Hybrid Photovoltaics. *ACS Applied Materials & Interfaces*, 4(12), 6857–6864. doi: 10.1021/am302011u.

Chen, Z., Li, W., Li, R., Zhang, Y., Xu, G. & Cheng, H. (2013). Fabrication of Highly Transparent and Conductive Indium–Tin Oxide Thin Films with a High Figure of Merit via Solution Processing. *Langmuir*, 29(45), 13836–13842.

Chen, Z. & Lu, C. (2005). Humidity Sensors: A Review of Materials and Mechanisms. *Sensor Letters*, 3(4), 274–295.

Chiba, Y., Islam, A., Watanabe, Y., Komiya, R., Koide, N. & Han, L. (2006). Dye-Sensitized Solar Cells with Conversion Efficiency of 11.1%. *Japanese Journal of Applied Physics*, 45(7L), L638. doi: 10.1143/JJAP.45.L638.

Choi, J., Park, H. & Hoffmann, M. R. (2010a). Effects of Single Metal-Ion Doping on the Visible-Light Photoreactivity of TiO2. *The Journal of Physical Chemistry C*, 114(2), 783–792.

Choi, J. J., Luria, J., Hyun, B.-R., Bartnik, A. C., Sun, L., Lim, Y.-F., Marohn, J. A., Wise, F. W. & Hanrath, T. (2010b). Photogenerated Exciton Dissociation in Highly Coupled Lead Salt Nanocrystal Assemblies. *Nano Letters*, 10(5), 1805–1811.

Chuang, C.-H. M., Brown, P. R., Bulović, V. & Bawendi, M. G. (2014). Improved Performance and Stability in Quantum Dot Solar Cells through Band Alignment Engineering. 13(8), 796–801.

Chung, C.-H., Song, T.-B., Bob, B., Zhu, R. & Yang, Y. (2012). Solution-Processed Flexible Transparent Conductors Composed of Silver Nanowire Networks Embedded in Indium Tin Oxide Nanoparticle Matrices. *Nano Research*, 5(11), 805–814. doi: 10.1007/s12274-012-0264-8.

Chung, W.-H., Kim, S.-H. & Kim, H.-S. (2016). Welding of Silver Nanowire Networks via Flash White Light and UV-C Irradiation for Highly Conductive and Reliable Transparent Electrodes. *Scientific Reports*, 6(1), 32086.

Dam, T., Jena, S. S. & Pradhan, D. K. (2016). Equilibrium State of Anatase to Rutile Transformation for Nano-Structured Titanium Dioxide Powder Using Polymer Template Method. *IOP Conference Series: Materials Science and Engineering*, 115(1), 012038.

Das, R. & He, X. (2019). Flexible, Printed OLED Displays 2020-2030: Forecasts, Markets, Technologies. IDTechEx. Retrieved from: https://www.idtechex.com/en/research-report/flexible-printed-oled-displays-2020-2030-forecasts-markets-technologies/693.

Das, S., Yang, B., Gu, G., Joshi, P. C., Ivanov, I. N., Rouleau, C. M., Aytug, T., Geohegan, D. B. & Xiao, K. (2015). High-Performance Flexible Perovskite Solar Cells by Using a Combination of Ultrasonic Spray-Coating and Low Thermal Budget Photonic Curing. *ACS Photonics*, 2(6), 680–686. doi: 10.1021/acsphotonics.5b00119.

Das, S., Gu, G., Joshi, P. C., Yang, B., Aytug, T., Rouleau, C. M., Geohegan, D. B. & Xiao, K. (2016). Low Thermal Budget, Photonic-Cured Compact TiO2 Layers for High-Efficiency Perovskite Solar Cells. *Journal of Materials Chemistry A*, 4(24), 9685–9690.

Daunis, T. B., Barrera, D., Gutierrez-Heredia, G., Rodriguez-Lopez, O., Wang, J., Voit, W. E. & Hsu, J. W. P. (2018). Solution-Processed Oxide Thin Film Transistors on Shape Memory Polymer Enabled by Photochemical Self-Patterning. *Journal of Materials Research*, 33(17), 2454–2462. doi: 10.1557/jmr.2018.296.

Daunis, T. B., Schroder, K. A. & Hsu, J. W. P. (2020). Photonic Curing of Solution-Deposited ZrO2 Dielectric on PEN: A Path towards High-Throughput Processing of Oxide Electronics. *npj Flexible Electronics*, 4(1), 1–7. doi: 10.1038/s41528-020-0070-4.

Dauzou, F., Bouten, P. C. P., Dabirian, A., Leterrier, Y., Ballif, C. & Morales-Masis, M. (2016). Mechanical Integrity of Hybrid Indium-Free Electrodes for Flexible Devices. *Organic Electronics*, 35, 136–141.

De, S. & Coleman, J. N. (2011). The Effects of Percolation in Nanostructured Transparent Conductors. *MRS Bulletin*, 36(10), 774–781. doi: 10.1557/mrs.2011.236.

De, S., Higgins, T. M., Lyons, P. E., Doherty, E. M., Nirmalraj, P. N., Blau, W. J., Boland, J. J. & Coleman, J. N. (2009). Silver Nanowire Networks as Flexible, Transparent, Conducting Films: Extremely High DC to Optical Conductivity Ratios. *ACS Nano*, 3(7), 1767–1774.

De, S., King, P. J., Lyons, P. E., Khan, U. & Coleman, J. N. (2010). Size Effects and the Problem with Percolation in Nanostructured Transparent Conductors. *ACS Nano*, 4(12), 7064–7072.

Delahoy, A. E. & Guo, S. (2010). Transparent Conducting Oxides for Photovoltaics. In *Handbook of Photovoltaic Science and Engineering* (ch. 17, pp. 716–796). doi: 10.1002/9780470974704.ch17.

Dembele, K. T., Selopal, G. S., Soldano, C., Nechache, R., Rimada, J. C., Concina, I., Sberveglieri, G., Rosei, F. & Vomiero, A. (2013). Hybrid Carbon Nanotubes–TiO2 Photoanodes for High Efficiency Dye-Sensitized Solar Cells. *The Journal of Physical Chemistry C*, 117(28), 14510–14517.

Deng, D., Xia, J., Cao, J., Qu, L., Tian, J., Qian, Z., Gu, Y. & Gu, Z. (2012). Forming Highly Fluorescent Near-Infrared Emitting PbS Quantum Dots in Water Using Glutathione as Surface-Modifying Molecule. *Journal of Colloid and Interface Science*, 367(1), 234–240. doi: 10.1016/j.jcis.2011.09.043.

Dexter, M., Bhandari, R., Chang, C.-H. & Malhotra, R. (2017). Controlling Processing Temperatures and Self-Limiting Behaviour in Intense Pulsed Sintering by Tailoring Nanomaterial Shape Distribution. *RSC Advances*, 7(89), 56395–56405. doi: 10.1039/C7RA11013H.

Dexter, M., Gao, Z., Bansal, S., Chang, C.-H. & Malhotra, R. (2018). Temperature, Crystalline Phase and Influence of Substrate Properties in Intense Pulsed Light Sintering of Copper Sulfide Nanoparticle Thin Films. *Scientific Reports*, 8(1), 1–14.

Dharmadasa, R., Lavery, B., Dharmadasa, I. M. & Druffel, T. (2014). Intense Pulsed Light Treatment of Cadmium Telluride Nanoparticle-Based Thin Films. *ACS Applied Materials & Interfaces*, 6(7), 5034–5040. doi: 10.1021/am500124t.

Di Giacomo, F., Zardetto, V., D'Epifanio, A., Pescetelli, S., Matteocci, F., Razza, S., Di Carlo, A., Licoccia, S., Kessels, W. M. M., Creatore, M. & Brown, T. M. (2015). Flexible Perovskite Photovoltaic Modules and Solar Cells Based on Atomic Layer Deposited Compact Layers and UV-Irradiated TiO2 Scaffolds on Plastic Substrates. *Advanced Energy Materials*, 5(8), 1401808. doi: 10.1002/aenm.201401808.

Diebold, U. (2003). The Surface Science of Titanium Dioxide. *Surface Science Reports*, 48(5), 53–229.

Ding, B., Gao, T., Wang, Y., Waldeck, D. H., Leu, P. W. & Lee, J.-K. (2014). Synergistic Effect of Surface Plasmonic Particles in PbS/TiO2 Heterojunction Solar Cells. *Solar Energy Materials and Solar Cells*, 128, 386–393. doi: 10.1016/j.solmat.2014.06.001.

Ding, S., Jiu, J., Gao, Y., Tian, Y., Araki, T., Sugahara, T., Nagao, S., Nogi, M., Koga, H., Suganuma, K. & Uchida, H. (2016). One-Step Fabrication of Stretchable Copper Nanowire Conductors by a Fast Photonic Sintering Technique and Its Application in Wearable Devices. *ACS Applied Materials & Interfaces*, 8(9), 6190–6199. doi: 10.1021/acsami.5b10802.

Dissanayake, M. A. K. L., Jaseetharan, T., Senadeera, G. K. R. & Thotawatthage, C. A. (2018). A Novel, PbS:Hg Quantum Dot-Sensitized, Highly Efficient Solar Cell Structure with Triple Layered TiO2 Photoanode. *Electrochimica Acta*, 269, 172–179.

Duraisamy, N., Muhammad, N. M., Kim, H.-C., Jo, J.-D. & Choi, K.-H. (2012). Fabrication of TiO2 Thin Film Memristor Device Using Electrohydrodynamic Inkjet Printing. *Thin Solid Films*, 520(15), 5070–5074.

Etgar, L., Lee, H. J., Seok, S. I., Nazeeruddin, M. K. & Grätzel, M. (2013). Semiconductor Quantum Dot Sensitized TiO2 Mesoporous Solar Cells. In Sargent, E. H. & Konstantatos, G. (Eds.), *Colloidal Quantum Dot Optoelectronics and Photovoltaics* (pp. 292–309). Cambridge University Press.

Feleki, B., Bex, G., Andriessen, R., Galagan, Y. & Di Giacomo, F. (2017). Rapid and Low Temperature Processing of Mesoporous TiO2 for Perovskite Solar Cells on Flexible and Rigid Substrates. *Materials Today Communications*, 13, 232–240. doi: 10.1016/j.mtcomm.2017.09.007.

Fernée, M. J., Thomsen, E., Jensen, P. & Rubinsztein-Dunlop, H. (2006). Highly Efficient Luminescence from a Hybrid State Found in Strongly Quantum Confined PbS Nanocrystals. *Nanotechnology*, 17(4), 956. doi: 10.1088/0957-4484/17/4/020.

Ferrari, A. C., Meyer, J. C., Scardaci, V., Casiraghi, C., Lazzeri, M., Mauri, F., Piscanec, S., Jiang, D., Novoselov, K. S., Roth, S. & Geim, A. K. (2006). The Raman Fingerprint of Graphene. *Physical Review Letters*, 97(18), 187401. doi: 10.1103/PhysRevLett.97.187401.

Ferrari, A. C. (2007). Raman Spectroscopy of Graphene and Graphite: Disorder, Electron–Phonon Coupling, Doping and Nonadiabatic Effects. *Solid State Communications*, 143(1), 47–57. doi: 10.1016/j.ssc.2007.03.052.

Fortunato, E., Ginley, D., Hosono, H. & Paine, D. C. (2007). Transparent Conducting Oxides for Photovoltaics. *MRS Bulletin*, 32(3), 242–247. doi: 10.1557/mrs2007.29.

Fourmont, P. & G. Cloutier, S. (2022). Screen-Printed p–n BiOCl/BiFeO 3 Heterojunctions for Efficient Photocatalytic Degradation of Rhodamine B. *RSC Advances*, 12(38), 24868–24875. doi: 10.1039/D2RA03308A.

Fourmont, P., Gerlein, L. F., Fortier, F.-X., Cloutier, S. G. & Nechache, R. (2018). Highly Efficient Thermoelectric Microgenerators Using Nearly Room Temperature Pulsed Laser Deposition. *ACS Applied Materials & Interfaces*, 10(12), 10194–10201. doi: 10.1021 /acsami.7b18852.

Fujishima, A. & Honda, K. (1972). Electrochemical Photolysis of Water at a Semiconductor Electrode. *Nature*, 238(5358), 37.

Garnett, E. C., Cai, W., Cha, J. J., Mahmood, F., Connor, S. T., Greyson Christoforo, M., Cui, Y., McGehee, M. D. & Brongersma, M. L. (2012). Self-Limited Plasmonic Welding of Silver Nanowire Junctions. *Nature Materials*, 11(3), 241–249. doi: 10.1038/nmat3238.

Garzella, C., Comini, E., Tempesti, E., Frigeri, C. & Sberveglieri, G. (2000). TiO2 Thin Films by a Novel Sol–Gel Processing for Gas Sensor Applications. *Sensors and Actuators B: Chemical*, 68(1), 189–196. doi: 10.1016/S0925-4005(00)00428-7.

Geim, A. K. & Novoselov, K. S. (2007). The Rise of Graphene. *Nature Materials*, 6(3), 183–191. doi: 10.1038/nmat1849.

Gerlein, L. F., Benavides-Guerrero, J. A. & Cloutier, S. G. (2019). Laser-Assisted, Large-Area Selective Crystallization and Patterning of Titanium Dioxide Polymorphs. *Advanced Engineering Materials*, 22(2), 1901014. doi: 10.1002/adem.201901014.

Gerlein, L. F., Benavides-Guerrero, J. A. & Cloutier, S. G. (2021). High-Performance Silver Nanowires Transparent Conductive Electrodes Fabricated Using Manufacturing-Ready High-Speed Photonic Sinterization Solutions. *Scientific Reports*, 11(1), 24156. doi: 10.1038/s41598-021-03528-w.

Gerlein, L. F., Benavides, J. A. & Cloutier, S. G. (2023). *Photonic Sintering of a Multi-Material Transparent Conductive Electrode Architecture for Optoelectronic Device Integration*. Submitted for Revision.

Ghobadi, N. (2013). Band Gap Determination Using Absorption Spectrum Fitting Procedure. *International Nano Letters*, 3(1), 2.

Giansante, C., Infante, I., Fabiano, E., Grisorio, R., Suranna, G. P. & Gigli, G. (2015). "Darker-than-Black" PbS Quantum Dots: Enhancing Optical Absorption of Colloidal Semiconductor Nanocrystals via Short Conjugated Ligands. *Journal of the American Chemical Society*, 137(5), 1875–1886.

Gilshtein, E., Tacneng, J., Bolat, S., Torres Sevilla, G. & Romanyuk, Y. E. (2021). Invisible and Flexible Printed Sensors Based on ITO Nanoparticle Ink for Security Applications. *Frontiers in Nanotechnology*, 3, 7. doi: 10.3389/fnano.2021.700539.

Guisbiers, G. (2012). Review on the analytical models describing melting at the nanoscale. *Journal of Nanoscience Letters*, 2(8), 10.

H. Rebelo, S. L., Guedes, A., E. Szefczyk, M., M. Pereira, A., P. Araújo, J. & Freire, C. (2016). Progress in the Raman Spectra Analysis of Covalently Functionalized Multiwalled Carbon Nanotubes: Unraveling Disorder in Graphitic Materials. *Physical Chemistry Chemical Physics*, 18(18), 12784–12796.

Haacke, G. (1976). New Figure of Merit for Transparent Conductors. *Journal of Applied Physics*, 47(9), 4086–4089.

Han, C. J., Park, B.-G., Oh, M. S., Jung, S.-B. & Kim, J.-W. (2017). Photo-Induced Fabrication of Ag Nanowire Circuitry for Invisible, Ultrathin, Conformable Pressure Sensors. *Journal of Materials Chemistry C*, 5(38), 9986–9994. doi: 10.1039/C7TC01423F.

Hanaor, D. A. H. & Sorrell, C. C. (2011). Review of the Anatase to Rutile Phase Transformation. *Journal of Materials Science*, 46(4), 855–874.

Hao, Y., Wang, Y., Wang, L., Ni, Z., Wang, Z., Wang, R., Koo, C. K., Shen, Z. & Thong, J. T. L. (2010). Probing Layer Number and Stacking Order of Few-Layer Graphene by Raman Spectroscopy. *Small*, 6(2), 195–200. doi: 10.1002/smll.200901173.

Hauger, T. C., Al-Rafia, S. M. I. & Buriak, J. M. (2013). Rolling Silver Nanowire Electrodes: Simultaneously Addressing Adhesion, Roughness, and Conductivity. *ACS Applied Materials & Interfaces*, 5(23), 12663–12671.

Hench, L. L. & West, J. K. (1990). The Sol-Gel Process. *Chemical Reviews*, 90(1), 33–72. doi: 10.1021/cr00099a003.

Hernandez, Y., Lotya, M., Rickard, D., Bergin, S. D. & Coleman, J. N. (2010). Measurement of Multicomponent Solubility Parameters for Graphene Facilitates Solvent Discovery. *Langmuir*, 26(5), 3208–3213. doi: 10.1021/la903188a.

Hinds, S., Myrskog, S., Levina, L., Koleilat, G., Yang, J., Kelley, S. O. & Sargent, E. H. (2007). NIR-Emitting Colloidal Quantum Dots Having 26% Luminescence Quantum Yield in Buffer Solution. *Journal of the American Chemical Society*, 129(23), 7218–7219. doi: 10.1021/ja070525s.

Hines, M. & Scholes, G. (2003). Colloidal PbS Nanocrystals with Size-Tunable Near-Infrared Emission: Observation of Post-Synthesis Self-Narrowing of the Particle Size Distribution. *Advanced Materials*, 15(21), 1844–1849.

Hirotani, J. & Ohno, Y. (2019). Carbon Nanotube Thin Films for High-Performance Flexible Electronics Applications. *Topics in Current Chemistry*, 377(1), 3. doi: 10.1007/s41061-018-0227-y.

Hong, J., Hou, B., Lim, J., Pak, S., Kim, B.-S., Cho, Y., Lee, J., Lee, Y.-W., Giraud, P., Lee, S., Park, J. B., Morris, S. M., Snaith, H. J., Sohn, J. I., Cha, S. & Kim, J. M. (2016). Enhanced Charge Carrier Transport Properties in Colloidal Quantum Dot Solar Cells via Organic and Inorganic Hybrid Surface Passivation. *Journal of Materials Chemistry A*, 4(48), 18769–18775.

Hosseinzadeh Khaligh, H. & Goldthorpe, I. A. (2014). Hot-Rolling Nanowire Transparent Electrodes for Surface Roughness Minimization. *Nanoscale Research Letters*, 9(1), 310.

Hsu, J. W. (2021). Low-Temperature, High-Speed Processing of Oxide Dielectric Thin Films. 14 slides. doi: 10.2172/1764309. MRS invited talk.

Hu, L., Wang, W., Liu, H., Peng, J., Cao, H., Shao, G., Xia, Z., Ma, W. & Tang, J. (2014). PbS Colloidal Quantum Dots as an Effective Hole Transporter for Planar Heterojunction Perovskite Solar Cells. 3(2), 515–518.

Hu, L., Li, D.-B., Gao, L., Tan, H., Chen, C., Li, K., Li, M., Han, J.-B., Song, H., Liu, H. & Tang, J. (2016). Graphene Doping Improved Device Performance of ZnMgO/PbS Colloidal Quantum Dot Photovoltaics. *Advanced Functional Materials*, 26(12), 1899–1907. doi: 10.1002/adfm.201505043.

Huang, J.-J., Cheng, T.-F., Ho, Y.-R. & Huang, D.-P. (2021a). Performance Improvement of Dye-Sensitized Solar Cells by Using TiO2 Compact Layer and Silver Nanowire Scattering Layer. *Thin Solid Films*, 736, 138903. doi: 10.1016/j.tsf.2021.138903.

Huang, X., Zhang, R., Gao, X., Yu, B., Gao, Y. & Han, Z.-g. (2021b). TiO2-rutile/Anatase Homojunction with Enhanced Charge Separation for Photoelectrochemical Water Splitting. *International Journal of Hydrogen Energy*, 46(52), 26358–26366. doi: 10.1016/j.ijhydene.2021.05.118.

Hughes, B. K., Ruddy, D. A., Blackburn, J. L., Smith, D. K., Bergren, M. R., Nozik, A. J., Johnson, J. C. & Beard, M. C. (2012). Control of PbSe Quantum Dot Surface Chemistry and Photophysics Using an Alkylselenide Ligand. 6(6), 5498–5506.

Hwang, H.-J. & Kim, H.-S. (2015). Ultra-High Speed Fabrication of TiO2 Photoanode by Flash Light for Dye-Sensitized Solar Cell. *Journal of Nanoscience and Nanotechnology*, 15(7), 5028–5034. doi: 10.1166/jnn.2015.9868.

Hwang, H.-J., Devaraj, H., Yang, C., Gao, Z., Chang, C.-h., Lee, H. & Malhotra, R. (2018). Rapid Pulsed Light Sintering of Silver Nanowires on Woven Polyester for Personal Thermal Management with Enhanced Performance, Durability and Cost-Effectiveness. *Scientific Reports*, 8(1), 1–12.

Hwang, H.-J., Zeng, C., Pan, C., Dexter, M., Malhotra, R. & Chang, C.-h. (2020). Tuning Electronic and Photocatalytic Properties in Pulsed Light Synthesis of Cu2ZnSnS4 Films from CuS-ZnS-SnS Nanoparticles. *Materials Research Bulletin*, 122, 110645.

Hwang, J., Lee, K., Jeong, Y., Lee, Y. U., Pearson, C., Petty, M. C. & Kim, H. (2014). UV-Assisted Low Temperature Oxide Dielectric Films for TFT Applications. *Advanced Materials Interfaces*, 1(8), 1400206. doi: 10.1002/admi.201400206.

Iijima, S. & Ichihashi, T. (1993). Single-Shell Carbon Nanotubes of 1-Nm Diameter. *Nature*, 363(6430), 603–605. doi: 10.1038/363603a0.

Im, J.-H., Lee, C.-R., Lee, J.-W., Park, S.-W. & Park, N.-G. (2011). 6.5% Efficient Perovskite Quantum-Dot-Sensitized Solar Cell. *Nanoscale*, 3(10), 4088–4093. doi: 10.1039/C1NR10867K.

Im, T. H., Lee, J. H., Wang, H. S., Sung, S. H., Kim, Y. B., Rho, Y., Grigoropoulos, C. P., Park, J. H. & Lee, K. J. (2021). Flashlight-Material Interaction for Wearable and Flexible Electronics. *Materials Today*, 51, 525–551. doi: 10.1016/j.mattod.2021.07.027.

Ip, A. H., Thon, S. M., Hoogland, S., Voznyy, O., Zhitomirsky, D., Debnath, R., Levina, L., Rollny, L. R., Carey, G. H., Fischer, A., Kemp, K. W., Kramer, I. J., Ning, Z., Labelle, A. J., Chou, K. W., Amassian, A. & Sargent, E. H. (2012). Hybrid Passivated Colloidal Quantum Dot Solids. *Nature Nanotechnology*, 7(9), 577–582.

Jang, Y.-R., Joo, S.-J., Chu, J.-H., Uhm, H.-J., Park, J.-W., Ryu, C.-H., Yu, M.-H. & Kim, H.-S. (2020). A Review on Intense Pulsed Light Sintering Technologies for Conductive Electrodes in Printed Electronics. *International Journal of Precision Engineering and Manufacturing-Green Technology*, 8, 327–363. doi: 10.1007/s40684-020-00193-8.

Jeong, I., Jung, H., Park, M., Park, J. S., Son, H. J., Joo, J., Lee, J. & Ko, M. J. (2016). A Tailored TiO2 Electron Selective Layer for High-Performance Flexible Perovskite Solar Cells via Low Temperature UV Process. *Nano Energy*, 28, 380–389. doi: 10.1016/j.nanoen.2016.09.004.

Ji, S., He, W., Wang, K., Ran, Y. & Ye, C. (2014). Thermal Response of Transparent Silver Nanowire/PEDOT:PSS Film Heaters. *Small*, 10(23), 4951–4960. doi: 10.1002/smll.201401690.

Jia, Y., Chen, C., Jia, D., Li, S., Ji, S. & Ye, C. (2016). Silver Nanowire Transparent Conductive Films with High Uniformity Fabricated via a Dynamic Heating Method. *ACS Applied Materials & Interfaces*, 8(15), 9865–9871. doi: 10.1021/acsami.6b00500.

Jiang, F., Yu, Y., Feng, A. & Song, L. (2018). Effects of Ammonia on Graphene Preparation via Microwave Assisted Intercalation Exfoliation Method. *Ceramics International*, 44(11), 12763–12766. doi: 10.1016/j.ceramint.2018.04.081.

Jiao, J., Zhou, Z.-J., Zhou, W.-H. & Wu, S.-X. (2013). CdS and PbS Quantum Dots Co-Sensitized TiO2 Nanorod Arrays with Improved Performance for Solar Cells Application. *Materials Science in Semiconductor Processing*, 16(2), 435–440.

Jiu, J., Nogi, M., Sugahara, T., Tokuno, T., Araki, T., Komoda, N., Suganuma, K., Uchida, H. & Shinozaki, K. (2012). Strongly Adhesive and Flexible Transparent Silver Nanowire Conductive Films Fabricated with a High-Intensity Pulsed Light Technique. *Journal of Materials Chemistry*, 22(44), 23561–23567.

Joo, J., Na, H. B., Yu, T., Yu, J. H., Kim, Y. W., Wu, F., Zhang, J. Z. & Hyeon, T. (2003). Generalized and Facile Synthesis of Semiconducting Metal Sulfide Nanocrystals. *Journal of the American Chemical Society*, 125(36), 11100–11105. doi: 10.1021/ja0357902.

Joo, J., Kwon, S. G., Yu, T., Cho, M., Lee, J., Yoon, J. & Hyeon, T. (2005). Large-Scale Synthesis of TiO2 Nanorods via Nonhydrolytic Sol-Gel Ester Elimination Reaction and Their Application to Photocatalytic Inactivation of E. Coli. *The Journal of Physical Chemistry B*, 109(32), 15297–15302.

Ju, T., Graham, R. L., Zhai, G., Rodriguez, Y. W., Breeze, A. J., Yang, L., Alers, G. B. & Carter, S. A. (2010). High Efficiency Mesoporous Titanium Oxide PbS Quantum Dot Solar Cells at Low Temperature. *Applied Physics Letters*, 97(4), 043106.

Jumabekov, A. N., Deschler, F., Böhm, D., Peter, L. M., Feldmann, J. & Bein, T. (2014). Quantum-Dot-Sensitized Solar Cells with Water-Soluble and Air-Stable PbS Quantum Dots. *The Journal of Physical Chemistry C*, 118(10), 5142–5149. doi: 10.1021/jp4110773.

Ka, I., Gerlein, L. F., Nechache, R. & Cloutier, S. G. (2017). High-Performance Nanotube-Enhanced Perovskite Photodetectors. *Scientific Reports*, 7, 45543. doi: 10.1038/srep45543.

Ka, I., Gerlein, L. F., M. Asuo, I., Nechache, R. & Cloutier, S. G. (2018). An Ultra-Broadband Perovskite-PbS Quantum Dot Sensitized Carbon Nanotube Photodetector. *Nanoscale*, 10(19), 9044–9052. doi: 10.1039/C7NR08608C.

Ka, I., Gerlein, L. F., Asuo, I. M., Bouzidi, S., Gedamu, D. M., Pignolet, A., Rosei, F., Nechache, R. & Cloutier, S. G. (2020). Solution-Processed p-Type Copper Thiocyanate (CuSCN) Enhanced Sensitivity of PbS-Quantum-Dots-Based Photodiode. *ACS Photonics*, 7(7), 1628–1635. doi: 10.1021/acsphotonics.0c00491.

Kamat, P. V. (2013). Quantum Dot Solar Cells. The Next Big Thing in Photovoltaics. *The Journal of Physical Chemistry Letters*, 4(6), 908–918.

Kamyshny, A., Steinke, J. & Magdassi, S. (2011). Metal-Based Inkjet Inks for Printed Electronics. *The Open Applied Physics Journal*, 4(1), 19-36. doi: 10.2174/1874183501104010019.

Kaptay, G. (2012). The Gibbs Equation versus the Kelvin and the Gibbs-Thomson Equations to Describe Nucleation and Equilibrium of Nano-Materials. *Journal of Nanoscience and Nanotechnology*, 12(3), 2625–2633.

Kastner, J., Pichler, T., Kuzmany, H., Curran, S., Blau, W., Weldon, D. N., Delamesiere, M., Draper, S. & Zandbergen, H. (1994). Resonance Raman and Infrared Spectroscopy of Carbon Nanotubes. *Chemical Physics Letters*, 221(1), 53–58. doi: 10.1016/0009-2614(94)87015-2.

Khaligh, H. H. (2016). *Silver Nanowire Transparent Electrodes for Device Applications*. (Ph.D. thesis, University of Waterloo, Ontario, Canada). Retrieved from: https://uwspace.uwaterloo.ca/handle/10012/10973.

Khan, U., May, P., O'Neill, A. & Coleman, J. N. (2010a). Development of Stiff, Strong, yet Tough Composites by the Addition of Solvent Exfoliated Graphene to Polyurethane. *Carbon*, 48(14), 4035–4041. doi: 10.1016/j.carbon.2010.07.008.

Khan, U., O'Neill, A., Lotya, M., De, S. & Coleman, J. N. (2010b). High-Concentration Solvent Exfoliation of Graphene. *Small*, 6(7), 864–871. doi: 10.1002/smll.200902066.

Kim, B.-S., Neo, D. C. J., Hou, B., Park, J. B., Cho, Y., Zhang, N., Hong, J., Pak, S., Lee, S., Sohn, J. I., Assender, H. E., Watt, A. A. R., Cha, S. & Kim, J. M. (2016). High Performance PbS Quantum Dot/Graphene Hybrid Solar Cell with Efficient Charge Extraction. 8(22), 13902–13908.

Kim, H.-S., Dhage, S. R., Shim, D.-E. & Hahn, H. T. (2009). Intense Pulsed Light Sintering of Copper Nanoink for Printed Electronics. *Applied Physics A*, 97(4), 791.

Kim, Y., Chikamatsu, M., Azumi, R., Saito, T. & Minami, N. (2013). Industrially Feasible Approach to Transparent, Flexible, and Conductive Carbon Nanotube Films: Cellulose-Assisted Film Deposition Followed by Solution and Photonic Processing. *Applied Physics Express*, 6(2), 025101. doi: 10.7567/APEX.6.025101.

Kinney, L. C. & Tompkins, E. H. (1969). Method of Making Printed Circuits. Patent No. US3451813A, USA.

Klem, E. J. D., Shukla, H., Hinds, S., MacNeil, D. D., Levina, L. & Sargent, E. H. (2008). Impact of Dithiol Treatment and Air Annealing on the Conductivity, Mobility, and Hole Density in PbS Colloidal Quantum Dot Solids. 92(21), 212105.

Klimov, V. I., Mikhailovsky, A. A., Xu, S., Malko, A., Hollingsworth, J. A., Leatherdale, C. A., Eisler, H.-J. & Bawendi, M. G. (2000). Optical Gain and Stimulated Emission in Nanocrystal Quantum Dots. *Science*, 290(5490), 314–317. doi: 10.1126/science.290.5490.314.

Kojima, A., Teshima, K., Shirai, Y. & Miyasaka, T. (2009). Organometal Halide Perovskites as Visible-Light Sensitizers for Photovoltaic Cells. *Journal of the American Chemical Society*, 131(17), 6050–6051. doi: 10.1021/ja809598r.

Kontos, A. G., Likodimos, V., Vassalou, E., Kapogianni, I., Raptis, Y. S., Raptis, C. & Falaras, P. (2011). Nanostructured Titania Films Sensitized by Quantum Dot Chalcogenides. *Nanoscale Research Letters*, 6(1), 266.

Kou, P., Yang, L., Chang, C. & He, S. (2017). Improved Flexible Transparent Conductive Electrodes Based on Silver Nanowire Networks by a Simple Sunlight Illumination Approach. *Scientific Reports*, 7(1), 42052.

Kramer, I. J., Zhitomirsky, D., Bass, J. D., Rice, P. M., Topuria, T., Krupp, L., Thon, S. M., Ip, A. H., Debnath, R., Kim, H.-C. & Sargent, E. H. (2012). Ordered Nanopillar Structured Electrodes for Depleted Bulk Heterojunction Colloidal Quantum Dot Solar Cells. *Advanced Materials*, 24(17), 2315–2319.

Krylova, G. & Na, C. (2015). Photoinduced Crystallization and Activation of Amorphous Titanium Dioxide. *The Journal of Physical Chemistry C*, 119(22), 12400–12407. doi: 10.1021/acs.jpcc.5b02048.

Kubo, R., Kawabata, A. & Kobayashi, S.-I. (1984). Electronic Properties of Small Particles. *Annual Review of Materials Science*, 14(1), 49–66.

Kumar, R., Mehta, B. R., Bhatnagar, M., S, R., Mahapatra, S., Salkalachen, S. & Jhawar, P. (2014). Graphene as a Transparent Conducting and Surface Field Layer in Planar Si Solar Cells. *Nanoscale Research Letters*, 9(1), 349. doi: 10.1186/1556-276X-9-349.

Kwan, Y. C. G., Le, Q. L. & Huan, C. H. A. (2016). Time to Failure Modeling of Silver Nanowire Transparent Conducting Electrodes and Effects of a Reduced Graphene Oxide over Layer. *Solar Energy Materials and Solar Cells*, 144, 102–108.

Kwon, J., Suh, Y. D., Lee, J., Lee, P., Han, S., Hong, S., Yeo, J., Lee, H. & Ko, S. H. (2018). Recent Progress in Silver Nanowire Based Flexible/Wearable Optoelectronics. *Journal of Materials Chemistry C*, 6(28), 7445–7461.

Langley, D. P., Lagrange, M., Giusti, G., Jiménez, C., Bréchet, Y., Nguyen, N. D. & Bellet, D. (2014). Metallic Nanowire Networks: Effects of Thermal Annealing on Electrical Resistance. *Nanoscale*, 6(22), 13535–13543.

Latif, H., Ashraf, S., Shahid Rafique, M., Imtiaz, A., Sattar, A., Zaheer, S., Ammara Shabbir, S. & Usman, A. (2020). A Novel, PbS Quantum Dot-Sensitized Solar Cell Structure with TiO2-fMWCNTS Nano-Composite Filled Meso-Porous Anatase TiO2 Photoanode. *Solar Energy*, 204, 617–623.

Lee, C.-J., Han, J.-I., Choi, D.-K. & Moon, D.-G. (2010). Transparent Organic Light-Emitting Devices with CsCl Capping Layers on Semitransparent Ca/Ag Cathodes. *Materials Science and Engineering: B*, 172(1), 76–79.

Lee, D.-H., Chang, Y.-J., Herman, G. S. & Chang, C.-H. (2007). A General Route to Printable High-Mobility Transparent Amorphous Oxide Semiconductors. *Advanced Materials*, 19(6), 843–847. doi: 10.1002/adma.200600961.

Lee, D. G., Lee, D., Yoo, J. S., Lee, S. & Jung, H. S. (2016). Effective Passivation of Ag Nanowire-Based Flexible Transparent Conducting Electrode by TiO2 Nanoshell. *Nano Convergence*, 3(1), 20. doi: 10.1186/s40580-016-0080-z.

Lee, D. J., Park, S. H., Jang, S., Kim, H. S., Oh, J. H. & Song, Y. W. (2011). Pulsed Light Sintering Characteristics of Inkjet-Printed Nanosilver Films on a Polymer Substrate. *Journal of Micromechanics and Microengineering*, 21(12), 125023. doi: 10.1088/0960-1317/21/12/125023.

Lee, S.-Y. & Park, S.-J. (2013). TiO2 Photocatalyst for Water Treatment Applications. *Journal of Industrial and Engineering Chemistry*, 19(6), 1761–1769.

Lee, W., Ryu, I., Lee, H. & Yim, S. (2018). Enhanced Interfacial Contact between PbS and TiO2 Layers in Quantum Dot Solar Cells Using 2D-Arrayed TiO2 Hemisphere Nanostructures. *Applied Surface Science*, 432, 255–261.

Leitsmann, R. & Bechstedt, F. (2009). Characteristic Energies and Shifts in Optical Spectra of Colloidal IV-VI Semiconductor Nanocrystals. *ACS Nano*, 3(11), 3505–3512. doi: 10.1021/nn900987j.

Lermusiaux, L., Mazel, A., Carretero-Genevrier, A., Sanchez, C. & Drisko, G. L. (2022). Metal-Induced Crystallization in Metal Oxides. *Accounts of Chemical Research*, 55(2), 171–185. doi: 10.1021/acs.accounts.1c00592.

Lettieri, S., Pallotti, D. K., Gesuele, F. & Maddalena, P. (2016). Unconventional Ratiometric-Enhanced Optical Sensing of Oxygen by Mixed-Phase TiO2. *Applied Physics Letters*, 109(3), 031905. doi: 10.1063/1.4959263.

Li, H., Huang, J., Zheng, Q. & Zheng, Y. (2020). Flexible Ultraviolet Photodetector Based ZnO Film Sputtered on Paper. *Vacuum*, 172, 109089. doi: 10.1016/j.vacuum.2019.109089.

Li, J., Ye, F., Vaziri, S., Muhammed, M., Lemme, M. C. & Östling, M. (2013). Efficient Inkjet Printing of Graphene. *Advanced Materials*, 25(29), 3985–3992. doi: 10.1002/adma.201300361.

Li, N., Wang, Z., Zhao, K., Shi, Z., Gu, Z. & Xu, S. (2010). Large Scale Synthesis of N-doped Multi-Layered Graphene Sheets by Simple Arc-Discharge Method. *Carbon*, 48(1), 255–259. doi: 10.1016/j.carbon.2009.09.013.

Li, X., Wang, L. & Yan, G. (2011). Review: Recent Research Progress on Preparation of Silver Nanowires by Soft Solution Method and Their Applications. *Crystal Research and Technology*, 46(5), 427–438. doi: 10.1002/crat.201100023.

Li, X., Cai, W., An, J., Kim, S., Nah, J., Yang, D., Piner, R., Velamakanni, A., Jung, I., Tutuc, E., Banerjee, S. K., Colombo, L. & Ruoff, R. S. (2009a). Large-Area Synthesis of High-Quality and Uniform Graphene Films on Copper Foils. *Science*, 324(5932), 1312–1314. doi: 10.1126/science.1171245.

Li, Y., Fang, X., Koshizaki, N., Sasaki, T., Li, L., Gao, S., Shimizu, Y., Bando, Y. & Golberg, D. (2009b). Periodic TiO2 Nanorod Arrays with Hexagonal Nonclose-Packed Arrangements: Excellent Field Emitters by Parameter Optimization. *Advanced Functional Materials*, 19(15), 2467–2473. doi: 10.1002/adfm.200801857.

Lim, S. P., Pandikumar, A., Lim, H. N. & Huang, N. M. (2016). Essential Role of N and Au on TiO2 as Photoanode for Efficient Dye-Sensitized Solar Cells. *Solar Energy*, 125, 135–145.

Lingley, Z., Lu, S. & Madhukar, A. (2014). The Dynamics of Energy and Charge Transfer in Lead Sulfide Quantum Dot Solids. *Journal of Applied Physics*, 115(8), 084302.

Linnet, J., Walther, A. R., Wolff, C., Albrektsen, O., Mortensen, N. A. & Kjelstrup-Hansen, J. (2018). Transparent and Conductive Electrodes by Large-Scale Nano-Structuring of Noble Metal Thin-Films. *Optical Materials Express*, 8(7), 1733–1746.

Linsebigler, A. L., Lu, G. & Yates, J. T. (1995). Photocatalysis on TiO2 Surfaces: Principles, Mechanisms, and Selected Results. *Chemical Reviews*, 95(3), 735–758.

Lira-Cantu, M. & Krebs, F. C. (2006). Hybrid Solar Cells Based on MEH-PPV and Thin Film Semiconductor Oxides (TiO2, Nb2O5, ZnO, CeO2 and CeO2–TiO2): Performance Improvement during Long-Time Irradiation. *Solar Energy Materials and Solar Cells*, 90(14), 2076–2086. doi: 10.1016/j.solmat.2006.02.007.

Liu, K., Cao, M., Fujishima, A. & Jiang, L. (2014). Bio-Inspired Titanium Dioxide Materials with Special Wettability and Their Applications. *Chemical Reviews*, 114(19), 10044–10094.

Liu, R., Tan, M., Zhang, X., Xu, L., Chen, J., Chen, Y., Tang, X. & Wan, L. (2018). Solution-Processed Composite Electrodes Composed of Silver Nanowires and Aluminum-Doped Zinc Oxide Nanoparticles for Thin-Film Solar Cells Applications. *Solar Energy Materials and Solar Cells*, 174, 584–592. doi: 10.1016/j.solmat.2017.09.042.

Luo, S., Zhang, S., Bourgeois, B. B., Riggs, B. C., Schroder, K. A., Zhang, Y., He, J., Adireddy, S., Sun, K., Shipman, J. T., Oguntoye, M. M., Puli, V., Liu, W., Tu, R., Zhang, L., Farnsworth, S. & Chrisey, D. B. (2017). Instantaneous Photoinitiated Synthesis and Rapid Pulsed Photothermal Treatment of Three-Dimensional Nanostructured TiO2 Thin Films through Pulsed Light Irradiation. *Journal of Materials Research*, 32(9), 1701–1709. doi: 10.1557/jmr.2017.139.

Ma, J., Wu, L., Hou, Z., Song, Y., Wang, L. & Jiang, W. (2014). Visualizing the Endocytosis of Phenylephrine in Living Cells by Quantum Dot-Based Tracking. *Biomaterials*, 35(25), 7042–7049. doi: 10.1016/j.biomaterials.2014.04.081.

Ma, X., Xu, F., Benavides, J. & Cloutier, S. G. (2012). High Performance Hybrid Near-Infrared LEDs Using Benzenedithiol Cross-Linked PbS Colloidal Nanocrystals. 13(3), 525–531. doi: 10.1016/j.orgel.2011.12.012.

Maarisetty, D. & Sundar Baral, S. (2020). Defect Engineering in Photocatalysis: Formation, Chemistry, Optoelectronics, and Interface Studies. *Journal of Materials Chemistry A*, 8(36), 18560–18604. doi: 10.1039/D0TA04297H.

Madeira, A. (2018). *Enhancing the Performance of Transparent Electrodes through the Design of New Silver Nanostructures*. (Ph.D. thesis, University of Waterloo, Ontario, Canada). Retrieved from: https://uwspace.uwaterloo.ca/handle/10012/13760.

Majee, S., Song, M., Zhang, S.-L. & Zhang, Z.-B. (2016). Scalable Inkjet Printing of Shear-Exfoliated Graphene Transparent Conductive Films. *Carbon*, 102, 51–57. doi: 10.1016/j.carbon.2016.02.013.

Malard, L. M., Guimarães, M. H. D., Mafra, D. L., Mazzoni, M. S. C. & Jorio, A. (2009). Group-Theory Analysis of Electrons and Phonons in N-Layer Graphene Systems. *Physical Review B*, 79(12), 125426. doi: 10.1103/PhysRevB.79.125426.

Malesevic, A., Vitchev, R., Schouteden, K., Volodin, A., Zhang, L., Tendeloo, G. V., Vanhulsel, A. & Haesendonck, C. V. (2008). Synthesis of Few-Layer Graphene via Microwave Plasma-Enhanced Chemical Vapour Deposition. *Nanotechnology*, 19(30), 305604. doi: 10.1088/0957-4484/19/30/305604.

Mali, S. S. & Hong, C. K. (2016). P-i-n/n-i-p Type Planar Hybrid Structure of Highly Efficient Perovskite Solar Cells towards Improved Air Stability: Synthetic Strategies and the Role of p-Type Hole Transport Layer (HTL) and n-Type Electron Transport Layer (ETL) Metal Oxides. *Nanoscale*, 8(20), 10528–10540. doi: 10.1039/C6NR02276F.

Mali, S. S., Betty, C. A., Bhosale, P. N. & Patil, P. S. (2012). Synthesis, Characterization of Hydrothermally Grown MWCNT–TiO2 Photoelectrodes and Their Visible Light Absorption Properties. *ECS Journal of Solid State Science and Technology*, 1(2), M15-M23.

Mandelis, A., Hu, L. & Wang, J. (2016). Quantitative Measurements of Charge Carrier Hopping Transport Properties in Depleted-Heterojunction PbS Colloidal Quantum Dot Solar Cells from Temperature Dependent Current–Voltage Characteristics. *RSC Advances*, 6(95), 93180–93194.

Market Stats News. (2021). Printed Electronics Market To Garner $44.4 Bn By 2030. Market Stats News. Retrieved from: http://www.marketstatsnews.com/printed-electronics-market/.

Markets and Markets. (2020). Optoelectronic Components Market by Component (Sensor, LED, Laser Diode, and Infrared Components), Application (Measurement, Lighting, Communications, and Security & Surveillance), Material, Vertical, and Region - Global Forecast to 2025. Markets and Markets. Retrieved from: https://www.marketsandmarkets.com/Market-Reports/optoelectronics-market-450.html.

Markets and Markets. (2021). Printed Electronics Market Size, Share and Global Trends Report 2030. Markets and Markets. Online; accessed on 26-Feb-2023, Retrieved from: https://www.marketsandmarkets.com/Market-Reports/printed-electronics-market-197.html.

Marra, F., Minutillo, S., Tamburrano, A. & Sarto, M. S. (2021). Production and Characterization of Graphene Nanoplatelet-based Ink for Smart Textile Strain Sensors via Screen Printing Technique. *Materials & Design*, 198, 109306. doi: 10.1016/j.matdes.2020.109306.

Menamparambath, M. M., Yang, K., Kim, H. H., Bae, O. S., Jeong, M. S., Choi, J.-Y. & Baik, S. (2016). Reduced Haze of Transparent Conductive Films by Smaller Diameter Silver Nanowires. *Nanotechnology*, 27(46), 465706.

Meng, Z.-y., Huang, S.-l., Liu, Z., Zeng, C.-h. & Bu, Y.-k. (2012). Design and Fabrication of a Novel High Damage Threshold HfO2/TiO2/SiO2 Multilayer Laser Mirror. *Optoelectronics Letters*, 8(3), 190–192. doi: 10.1007/s11801-012-1149-5.

Min, K., Umar, M., Seo, H., Hyuk Yim, J., Gun Kam, D., Jeon, H., Lee, S. & Kim, S. (2017). Biocompatible, Optically Transparent, Patterned, and Flexible Electrodes and Radio-Frequency Antennas Prepared from Silk Protein and Silver Nanowire Networks. *RSC Advances*, 7(1), 574–580. doi: 10.1039/C6RA25580A.

Miyoshi, A., Nishioka, S. & Maeda, K. (2018). Water Splitting on Rutile TiO2-Based Photocatalysts. *Chemistry – A European Journal*, 24(69), 18204–18219.

Moreels, I., Lambert, K., Smeets, D., De Muynck, D., Nollet, T., Martins, J. C., Vanhaecke, F., Vantomme, A., Delerue, C., Allan, G. & Hens, Z. (2009). Size-Dependent Optical Properties of Colloidal PbS Quantum Dots. *ACS Nano*, 3(10), 3023–3030. doi: 10.1021/nn900863a.

Moreels, I., Justo, Y., De Geyter, B., Haustraete, K., Martins, J. C. & Hens, Z. (2011). Size-Tunable, Bright, and Stable PbS Quantum Dots: A Surface Chemistry Study. *ACS nano*, 5(3), 2004–2012. doi: 10.1021/nn103050w.

Murray, C. B., Norris, D. J. & Bawendi, M. G. (1993). Synthesis and Characterization of Nearly Monodisperse CdE (E = Sulfur, Selenium, Tellurium) Semiconductor Nanocrystallites. *Journal of the American Chemical Society*, 115(19), 8706–8715.

Murray, C. B., Kagan, C. R. & Bawendi, M. G. (2000). Synthesis and Characterization of Monodisperse Nanocrystals and Close-Packed Nanocrystal Assemblies. *Annual Review of Materials Science*, 30(1), 545–610. doi: 10.1146/annurev.matsci.30.1.545.

Nakajima, T., Shinoda, K. & Tsuchiya, T. (2014). UV-assisted Nucleation and Growth of Oxide Films from Chemical Solutions. *Chemical Society Reviews*, 43(7), 2027–2041. doi: 10.1039/C3CS60222B.

Nanda, K. K., Kruis, F. E., Fissan, H. & Behera, S. N. (2004). Effective Mass Approximation for Two Extreme Semiconductors: Band Gap of PbS and CuBr Nanoparticles. *Journal of Applied Physics*, 95(9), 5035–5041. doi: 10.1063/1.1691184.

Nardes, A. M., Kemerink, M., de Kok, M. M., Vinken, E., Maturova, K. & Janssen, R. A. J. (2008). Conductivity, Work Function, and Environmental Stability of PEDOT:PSS Thin Films Treated with Sorbitol. *Organic Electronics*, 9(5), 727–734.

Ni, M., Leung, M. K. H., Leung, D. Y. C. & Sumathy, K. (2007). A Review and Recent Developments in Photocatalytic Water-Splitting Using TiO2 for Hydrogen Production. *Renewable and Sustainable Energy Reviews*, 11(3), 401–425.

Niittynen, J., Sowade, E., Kang, H., Baumann, R. R. & Mäntysalo, M. (2015). Comparison of Laser and Intense Pulsed Light Sintering (IPL) for Inkjet-Printed Copper Nanoparticle Layers. *Scientific Reports*, 5(1), 8832. doi: 10.1038/srep08832.

Ning, Z., Gong, X., Comin, R., Walters, G., Fan, F., Voznyy, O., Yassitepe, E., Buin, A., Hoogland, S. & Sargent, E. H. (2015). Quantum-Dot-in-Perovskite Solids. *Nature*, 523(7560), 324–328. doi: 10.1038/nature14563.

Noh, Y., Kim, G. Y., Lee, H., Shin, J., An, K., Kumar, M. & Lee, D. (2022). A Review on Intense Pulsed Light Process as Post-Treatment for Metal Oxide Thin Films and Nanostructures for Device Application. *Nanotechnology*, 33(27), 272001. doi: 10.1088/1361-6528/ac6314.

Novacentrix. (2018). Inkjet Roll to Roll System.

Novoselov, K. S., Geim, A. K., Morozov, S. V., Jiang, D., Zhang, Y., Dubonos, S. V., Grigorieva, I. V. & Firsov, A. A. (2004). Electric Field Effect in Atomically Thin Carbon Films. *Science*, 306(5696), 666–669. doi: 10.1126/science.1102896.

Novoselov, K. S., Jiang, D., Schedin, F., Booth, T. J., Khotkevich, V. V., Morozov, S. V. & Geim, A. K. (2005). Two-Dimensional Atomic Crystals. *Proceedings of the National Academy of Sciences*, 102(30), 10451–10453. doi: 10.1073/pnas.0502848102.

Novoselov, K. S., Fal′ko, V. I., Colombo, L., Gellert, P. R., Schwab, M. G. & Kim, K. (2012). A Roadmap for Graphene. *Nature*, 490(7419), 192–200. doi: 10.1038/nature11458.

Oliver, J. & Barnes, F. (1969). A Comparison of Rare-Gas Flashlamps. *IEEE Journal of Quantum Electronics*, 5(5), 232–237. doi: 10.1109/JQE.1969.1075765.

Oluwafemi, O. S., Sakho, E. H. M., Parani, S. & Lebepe, T. C. (2021). Chapter Seven - Bioimaging and Therapeutic Applications of Ternary Quantum Dots. In Oluwafemi, O. S., Sakho, E. H. M., Parani, S. & Lebepe, T. C. (Eds.), *Ternary Quantum Dots* (pp. 155–206). doi: 10.1016/B978-0-12-818303-8.00006-X.

O'Regan, B. & Grätzel, M. (1991). A Low-Cost, High-Efficiency Solar Cell Based on Dye-Sensitized Colloidal TiO2 Films. *Nature*, 353, 737.

Owen, J. & Brus, L. (2017). Chemical Synthesis and Luminescence Applications of Colloidal Semiconductor Quantum Dots. *J. Am. Chem. Soc.*, 139(32), 10939–10943. doi: 10.1021/jacs.7b05267.

Padrón-Hernández, W. Y., Ceballos-Chuc, M. C., Pourjafari, D., Oskam, G., Tinoco, J. C., Martínez-López, A. G. & Rodríguez-Gattorno, G. (2018). Stable Inks for Inkjet Printing of TiO2 Thin Films. *Materials Science in Semiconductor Processing*, 81, 75–81. doi: 10.1016/j.mssp.2018.03.015.

Palneedi, H., Park, J. H., Maurya, D., Peddigari, M., Hwang, G.-T., Annapureddy, V., Kim, J.-W., Choi, J.-J., Hahn, B.-D., Priya, S., Lee, K. J. & Ryu, J. (2018). Laser Irradiation of Metal Oxide Films and Nanostructures: Applications and Advances. *Advanced Materials*, 30(14), 1705148. doi: 10.1002/adma.201705148.

Pan, X., Yang, M.-Q., Fu, X., Zhang, N. & Xu, Y.-J. (2013). Defective TiO2 with Oxygen Vacancies: Synthesis, Properties and Photocatalytic Applications. *Nanoscale*, 5(9), 3601–3614. doi: 10.1039/C3NR00476G.

Pandey, R., Khanna, A., Singh, K., Patel, S. K., Singh, H. & Madan, J. (2020). Device Simulations: Toward the Design of >13% Efficient PbS Colloidal Quantum Dot Solar Cell. *Solar Energy*, 207, 893–902. doi: 10.1016/j.solener.2020.06.099.

Park, J., Dvoracek, C., Lee, K. H., Galloway, J. F., Bhang, H.-e. C., Pomper, M. G. & Searson, P. C. (2011). CuInSe/ZnS Core/Shell NIR Quantum Dots for Biomedical Imaging. *Small*, 7(22), 3148–3152. doi: 10.1002/smll.201101558.

Park, J. H., Hwang, G.-T., Kim, S., Seo, J., Park, H.-J., Yu, K., Kim, T.-S. & Lee, K. J. (2017). Flash-Induced Self-Limited Plasmonic Welding of Silver Nanowire Network for Transparent Flexible Energy Harvester. *Advanced Materials*, 29(5), 1603473. doi: 10.1002/adma.201603473.

Park, S. & Ruoff, R. S. (2009). Chemical Methods for the Production of Graphenes. *Nature Nanotechnology*, 4(4), 217–224. doi: 10.1038/nnano.2009.58.

Parvez, K., Li, R., Puniredd, S. R., Hernandez, Y., Hinkel, F., Wang, S., Feng, X. & Müllen, K. (2013). Electrochemically Exfoliated Graphene as Solution-Processable, Highly Conductive Electrodes for Organic Electronics. *ACS Nano*, 7(4), 3598–3606. doi: 10.1021/nn400576v.

Parvez, K., Wu, Z.-S., Li, R., Liu, X., Graf, R., Feng, X. & Müllen, K. (2014). Exfoliation of Graphite into Graphene in Aqueous Solutions of Inorganic Salts. *Journal of the American Chemical Society*, 136(16), 6083–6091. doi: 10.1021/ja5017156.

Paton, K. R., Varrla, E., Backes, C., Smith, R. J., Khan, U., O'Neill, A., Boland, C., Lotya, M., Istrate, O. M., King, P., Higgins, T., Barwich, S., May, P., Puczkarski, P., Ahmed, I., Moebius, M., Pettersson, H., Long, E., Coelho, J., O'Brien, S. E., McGuire, E. K., Sanchez, B. M., Duesberg, G. S., McEvoy, N., Pennycook, T. J., Downing, C., Crossley, A., Nicolosi, V. & Coleman, J. N. (2014). Scalable Production of Large Quantities of Defect-Free Few-Layer Graphene by Shear Exfoliation in Liquids. *Nature Materials*, 13(6), 624–630. doi: 10.1038/nmat3944.

Pattantyus-Abraham, A. G., Kramer, I. J., Barkhouse, A. R., Wang, X., Konstantatos, G., Debnath, R., Levina, L., Raabe, I., Nazeeruddin, M. K., Grätzel, M. & Sargent, E. H. (2010). Depleted-Heterojunction Colloidal Quantum Dot Solar Cells. *ACS Nano*, 4(6), 3374–3380.

Pavan, M., Rühle, S., Ginsburg, A., Keller, D. A., Barad, H.-N., Sberna, P. M., Nunes, D., Martins, R., Anderson, A. Y., Zaban, A. & Fortunato, E. (2015). TiO2/Cu2O All-Oxide Heterojunction Solar Cells Produced by Spray Pyrolysis. *Solar Energy Materials and Solar Cells*, 132, 549–556. doi: 10.1016/j.solmat.2014.10.005.

Pereira, H. J. & Hatton, R. A. (2019). High Figure-of-Merit Transparent Copper–Zinc Oxide Window Electrodes for Organic Photovoltaics. *Frontiers in Materials*, 6(228), 228.

Peterson, J. J. & Krauss, T. D. (2006). Fluorescence Spectroscopy of Single Lead Sulfide Quantum Dots. 6(3), 510–514. doi: 10.1021/nl0525756.

Pham, H. H. & Wang, L.-W. (2014). Oxygen Vacancy and Hole Conduction in Amorphous TiO2. *Physical Chemistry Chemical Physics*, 17(1), 541–550. doi: 10.1039/C4CP04209C.

Piper, R. T., Daunis, T. B., Xu, W., Schroder, K. A. & Hsu, J. W. P. (2021). Photonic Curing of Nickel Oxide Transport Layer and Perovskite Active Layer for Flexible Perovskite Solar Cells: A Path Towards High-Throughput Manufacturing. *Frontiers in Energy Research*, 9, 12. doi: 10.3389/fenrg.2021.640960.

Preston, C., Xu, Y., Han, X., Munday, J. N. & Hu, L. (2013). Optical Haze of Transparent and Conductive Silver Nanowire Films. *Nano Research*, 6(7), 461–468. doi: 10.1007/s12274-013-0323-9.

Proppe, A. H., Sun, B., Rossouw, D., Sargent, E. H., de-Arquer, F. P. G., Botton, G. A., Walters, G., Fan, J. Z., Liu, M., Voznyy, O., Quintero-Bermudez, R., Kelley, S. O., Hoogland, S., Lan, X. & Yang, Z. (2017). Mixed-Quantum-Dot Solar Cells. *Nature Communications*, 8(1), 1325. doi: 10.1038/s41467-017-01362-1.

Qian, B. & Shen, Z. (2013). Laser Sintering of Ceramics. *Journal of Asian Ceramic Societies*, 1(4), 315–321. doi: 10.1016/j.jascer.2013.08.004.

Rajaraman, T., Parikh, S. P. & Gandhi, V. G. (2020). Black TiO2: A Review of Its Properties and Conflicting Trends. *Chemical Engineering Journal*, 389, 123918. doi: 10.1016/j.cej.2019.123918.

Rajbongshi, B. M. & Verma, A. (2018). Plasmonic Noble Metal Coupled Biphasic TiO2 Electrode for Dye-Sensitized Solar Cell. *Materials Letters*, 232, 220–223.

Ramasamy, P., Seo, D.-M., Kim, S.-H. & Kim, J. (2012). Effects of TiO 2 Shells on Optical and Thermal Properties of Silver Nanowires. *Journal of Materials Chemistry*, 22(23), 11651–11657. doi: 10.1039/C2JM00010E.

Ramsden, J. J. & Grätzel, M. (1984). Photoluminescence of Small Cadmium Sulphide Particles. *Journal of the Chemical Society, Faraday Transactions 1: Physical Chemistry in Condensed Phases*, 80(4), 919–933.

Rao, C. N. R., Kulkarni, G. U., Thomas, P. J. & Edwards, P. P. (2000). Metal Nanoparticles and Their Assemblies. *Chemical Society Reviews*, 29(1), 27–35.

Rekemeyer, P. H., Chuang, C.-H. M., Bawendi, M. G. & Gradečak, S. (2017). Minority Carrier Transport in Lead Sulfide Quantum Dot Photovoltaics. *Nano Letters*, 17(10), 6221–6227.

Ren, Z., Yang, J., Qi, D., Sonar, P., Liu, L., Lou, Z., Shen, G. & Wei, Z. (2021). Flexible Sensors Based on Organic–Inorganic Hybrid Materials. *Advanced Materials Technologies*, 6(4), 2000889. doi: 10.1002/admt.202000889.

Resende, J., Sekkat, A., Nguyen, V. H., Chatin, T., Jiménez, C., Burriel, M., Bellet, D. & Muñoz-Rojas, D. (2021). Planar and Transparent Memristive Devices Based on Titanium Oxide Coated Silver Nanowire Networks with Tunable Switching Voltage. *Small*, 17(21), 2007344. doi: 10.1002/smll.202007344.

Ricci, P. C., Casu, A., Salis, M., Corpino, R. & Anedda, A. (2010). Optically Controlled Phase Variation of TiO2 Nanoparticles. *The Journal of Physical Chemistry C*, 114(34), 14441–14445.

Ricci, P. C., Carbonaro, C. M., Stagi, L., Salis, M., Casu, A., Enzo, S. & Delogu, F. (2013). Anatase-to-Rutile Phase Transition in TiO2 Nanoparticles Irradiated by Visible Light. *The Journal of Physical Chemistry C*, 117(15), 7850–7857.

Rogach, A. L., Eychmüller, A., Hickey, S. G. & Kershaw, S. V. (2007). Infrared-Emitting Colloidal Nanocrystals: Synthesis, Assembly, Spectroscopy, and Applications. *Small*, 3(4), 536–557. doi: 10.1002/smll.200600625.

Roose, B., Pathak, S. & Steiner, U. (2015). Doping of TiO2 for Sensitized Solar Cells. *Chem. Soc. Rev.*, 44(22), 8326–8349.

Rossetti, R. & Brus, L. (1982). Electron-Hole Recombination Emission as a Probe of Surface Chemistry in Aqueous Cadmium Sulfide Colloids. *The Journal of Physical Chemistry*, 86(23), 4470–4472.

Rossetti, R., Nakahara, S. & Brus, L. E. (1983). Quantum Size Effects in the Redox Potentials, Resonance Raman Spectra, and Electronic Spectra of CdS Crystallites in Aqueous Solution. *The Journal of Chemical Physics*, 79(2), 1086–1088.

Rühle, S., Anderson, A. Y., Barad, H.-N., Kupfer, B., Bouhadana, Y., Rosh-Hodesh, E. & Zaban, A. (2012). All-Oxide Photovoltaics. *The Journal of Physical Chemistry Letters*, 3(24), 3755–3764. doi: 10.1021/jz3017039.

Russo, P., Liang, R., Xiu He, R. & Norman Zhou, Y. (2017). Phase Transformation of TiO 2 Nanoparticles by Femtosecond Laser Ablation in Aqueous Solutions and Deposition on Conductive Substrates. *Nanoscale*, 9(18), 6167–6177.

Sahu, D. R., Lin, S.-Y. & Huang, J.-L. (2006). ZnO/Ag/ZnO Multilayer Films for the Application of a Very Low Resistance Transparent Electrode. *Applied Surface Science*, 252(20), 7509–7514. doi: 10.1016/j.apsusc.2005.09.021.

Sannicolo, T., Lagrange, M., Cabos, A., Celle, C., Simonato, J.-P. & Bellet, D. (2016). Metallic Nanowire-Based Transparent Electrodes for Next Generation Flexible Devices: A Review. *Small*, 12(44), 6052–6075.

Saran, R. & Curry, R. J. (2016). Lead Sulphide Nanocrystal Photodetector Technologies. *Nature Photonics*, 10(2), 81–92. doi: 10.1038/nphoton.2015.280.

Sargent, E. H. (2012). Colloidal Quantum Dot Solar Cells. *Nature Photonics*, 6(3), 133–135.

Sarkar, A. & Khan, G. G. (2019). The Formation and Detection Techniques of Oxygen Vacancies in Titanium Oxide-Based Nanostructures. *Nanoscale*, 11(8), 3414–3444. doi: 10.1039/C8NR09666J.

Sarkar, S. K., Gupta, H. & Gupta, D. (2017). Flash Light Sintering of Silver Nanoink for Inkjet-Printed Thin-Film Transistor on Flexible Substrate. *IEEE Transactions on Nanotechnology*, 16(3), 375–382.

Sawatsuk, T., Chindaduang, A., Sae-kung, C., Pratontep, S. & Tumcharern, G. (2009). Dye-Sensitized Solar Cells Based on TiO2–MWCNTs Composite Electrodes: Performance Improvement and Their Mechanisms. *Diamond and Related Materials*, 18(2), 524–527.

Scheideler, W. & Subramanian, V. (2019). Printed Flexible and Transparent Electronics: Enhancing Low-Temperature Processed Metal Oxides with 0D and 1D Nanomaterials. *Nanotechnology*, 30(27), 272001. doi: 10.1088/1361-6528/ab1167.

Schniepp, H. C., Kudin, K. N., Li, J.-L., Prud'homme, R. K., Car, R., Saville, D. A. & Aksay, I. A. (2008). Bending Properties of Single Functionalized Graphene Sheets Probed by Atomic Force Microscopy. *ACS Nano*, 2(12), 2577–2584. doi: 10.1021/nn800457s.

Schroder, K. A., Rawson, I. M., Pope, D. S. & Farnsworth, S. (2011). Photonic Curing Explanation and Application to Printing Copper Traces on Low Temperature Substrates. *International Symposium on Microelectronics*, 2011(1), 001040–001046. doi: 10.4071/isom-2011-THA4-Paper6.

Schroder, K. (2011). Mechanisms of Photonic Curing™: Processing High Temperature Films on Low Temperature Substrates. *TechConnect Briefs*, 2(2011), 220–223.

Schroder, K., McCool, S. & Furlan, W. (2006). Broadcast Photonic Curing of Metallic Nanoparticle Films. *TechConnect Briefs*, 3(2006), 198–201.

Selman, A. M. & Hassan, Z. (2015). Highly Sensitive Fast-Response UV Photodiode Fabricated from Rutile TiO2 Nanorod Array on Silicon Substrate. *Sensors and Actuators A: Physical*, 221, 15–21. doi: 10.1016/j.sna.2014.10.041.

Semonin, O. E., Luther, J. M. & Beard, M. C. (2012). Quantum Dots for Next-Generation Photovoltaics. *Materials Today*, 15(11), 508–515.

Sepulveda-Mora, S. B. & Cloutier, S. G. (2012). Figures of Merit for High-Performance Transparent Electrodes Using Dip-Coated Silver Nanowire Networks. *Journal of Nanomaterials*, 2012(286164), 7.

Serpelloni, M., Cantù, E., Borghetti, M. & Sardini, E. (2020). Printed Smart Devices on Cellulose-Based Materials by Means of Aerosol-Jet Printing and Photonic Curing. *Sensors*, 20(3), 841. doi: 10.3390/s20030841.

Silva, D. L., Campos, J. L. E., Fernandes, T. F. D., Rocha, J. N., Machado, L. R. P., Soares, E. M., Miquita, D. R., Miranda, H., Rabelo, C., Vilela Neto, O. P., Jorio, A. & Cançado, L. G. (2020). Raman Spectroscopy Analysis of Number of Layers in Mass-Produced Graphene Flakes. *Carbon*, 161, 181–189. doi: 10.1016/j.carbon.2020.01.050.

Siuzdak, K., Haryński, Ł., Wawrzyniak, J. & Grochowska, K. (2020). Review on Robust Laser Light Interaction with Titania – Patterning, Crystallisation and Ablation Processes. *Progress in Solid State Chemistry*, 67, 100297. doi: 10.1016/j.progsolidstchem.2020.100297.

Siwal, S. S., Saini, A. K., Rarotra, S., Zhang, Q. & Thakur, V. K. (2021). Recent Advancements in Transparent Carbon Nanotube Films: Chemistry and Imminent Challenges. *Journal of Nanostructure in Chemistry*, 11(1), 93–130. doi: 10.1007/s40097-020-00378-2.

Song, C.-H., Ok, K.-H., Lee, C.-J., Kim, Y., Kwak, M.-G., Han, C. J., Kim, N., Ju, B.-K. & Kim, J.-W. (2015a). Intense-Pulsed-Light Irradiation of Ag Nanowire-Based Transparent Electrodes for Use in Flexible Organic Light Emitting Diodes. *Organic Electronics*, 17, 208–215. doi: 10.1016/j.orgel.2014.12.015.

Song, T.-B., Rim, Y. S., Liu, F., Bob, B., Ye, S., Hsieh, Y.-T. & Yang, Y. (2015b). Highly Robust Silver Nanowire Network for Transparent Electrode. *ACS Applied Materials & Interfaces*, 7(44), 24601–24607. doi: 10.1021/acsami.5b06540.

Soni, A. K., Joshi, R. & Ningthoujam, R. S. (2021). Hot Injection Method for Nanoparticle Synthesis: Basic Concepts, Examples and Applications. In Tyagi, A. K. & Ningthoujam, R. S. (Eds.), *Handbook on Synthesis Strategies for Advanced Materials : Volume-I: Techniques and Fundamentals* (pp. 383–434). Singapore: Springer. doi: 10.1007/978-981-16-1807-9_13.

Stathopoulos, S., Khiat, A., Trapatseli, M., Cortese, S., Serb, A., Valov, I. & Prodromakis, T. (2017). Multibit Memory Operation of Metal-Oxide Bi-Layer Memristors. *Scientific Reports*, 7(1), 17532.

Steigerwald, M. L., Alivisatos, A. P., Gibson, J. M., Harris, T. D., Kortan, R., Muller, A. J., Thayer, A. M., Duncan, T. M., Douglass, D. C. & Brus, L. E. (1988). Surface Derivatization and Isolation of Semiconductor Cluster Molecules. *Journal of the American Chemical Society*, 110(10), 3046–3050.

Steigerwald, M. L. & Brus, L. E. (1990). Semiconductor Crystallites: A Class of Large Molecules. *Accounts of Chemical Research*, 23(6), 183–188.

Sun, Y., Egawa, T., Zhang, L. & Yao, X. (2002a). High Anatase-Rutile Transformation Temperature of Anatase Titania Nanoparticles Prepared by Metalorganic Chemical Vapor Deposition. *Japanese Journal of Applied Physics*, 41(8B), L945.

Sun, Y., Du, C., Wu, M., Zhao, L., Yu, S., Gong, B. & Ding, Q. (2020). Synchronously Improved Reliability, Figure of Merit and Adhesion of Flexible Copper Nanowire Networks by Chitosan Transition. *Nanotechnology*, 31(37), 375303.

Sun, Y., Gates, B., Mayers, B. & Xia, Y. (2002b). Crystalline Silver Nanowires by Soft Solution Processing. *Nano Letters*, 2(2), 165–168. doi: 10.1021/nl010093y.

Sun, Y., Yin, Y., Mayers, B. T., Herricks, T. & Xia, Y. (2002c). Uniform Silver Nanowires Synthesis by Reducing AgNO3 with Ethylene Glycol in the Presence of Seeds and Poly(Vinyl Pyrrolidone). *Chemistry of Materials*, 14(11), 4736–4745. doi: 10.1021/cm020587b.

Taleshi, F. (2015). The Effect of Carbon Nanotube on Band Gap Energy of TiO2 Nanoparticles. *Journal of Applied Spectroscopy*, 82(2), 303–306.

Tan, C., Chen, J., Wu, X.-J. & Zhang, H. (2018). Epitaxial Growth of Hybrid Nanostructures. *Nature Reviews Materials*, 3(2), 1–13. doi: 10.1038/natrevmats.2017.89.

Tang, J., Kemp, K. W., Hoogland, S., Jeong, K. S., Liu, H., Levina, L., Furukawa, M., Wang, X., Debnath, R., Cha, D., Chou, K. W., Fischer, A., Amassian, A., Asbury, J. B. & Sargent, E. H. (2011). Colloidal-Quantum-Dot Photovoltaics Using Atomic-Ligand Passivation. 10(10), 765.

Tang, Y., Ruan, H., Huang, Z., Shi, D., Liu, H., Chen, S. & Zhang, J. (2018). Fabrication of High-Quality Copper Nanowires Flexible Transparent Conductive Electrodes with Enhanced Mechanical and Chemical Stability. *Nanotechnology*, 29(45), 455706.

Thamaphat, K., Limsuwan, P. & Ngotawornchai, B. (2008). Phase Characterization of TiO2 Powder by XRD and TEM. *Kasetsart Journal: Natural Science*, 42(5), 357–361.

Therese Dembele, K., Singh Selopal, G., Milan, R., Trudeau, C., Benetti, D., Soudi, A., Maria Natile, M., Sberveglieri, G., Cloutier, S., Concina, I., Rosei, F. & Vomiero, A. (2015). Graphene below the Percolation Threshold in TiO2 for Dye-Sensitized Solar Cells. *Journal of Materials Chemistry A*, 3(6), 2580–2588.

Tokuno, T., Nogi, M., Karakawa, M., Jiu, J., Nge, T. T., Aso, Y. & Suganuma, K. (2011). Fabrication of Silver Nanowire Transparent Electrodes at Room Temperature. *Nano Research*, 4(12), 1215–1222.

Tong, L., Qiu, F., Zeng, T., Long, J., Yang, J., Wang, R., Zhang, J., Wang, C., Sun, T. & Yang, Y. (2017). Recent Progress in the Preparation and Application of Quantum Dots/Graphene Composite Materials. *RSC Advances*, 7(76), 47999–48018. doi: 10.1039/C7RA08755A.

Ullattil, S. G., Narendranath, S. B., Pillai, S. C. & Periyat, P. (2018). Black TiO2 Nanomaterials: A Review of Recent Advances. *Chemical Engineering Journal*, 343, 708–736.

Vaenas, N., Konios, D., Stergiopoulos, T. & Kymakis, E. (2015). Slow Photocharging and Reduced Hysteresis in Low-Temperature Processed Planar Perovskite Solar Cells. *RSC Advances*, 5(130), 107771–107776. doi: 10.1039/C5RA23845E.

Vásquez, G. C., Peche-Herrero, M. A., Maestre, D., Gianoncelli, A., Ramírez-Castellanos, J., Cremades, A., González-Calbet, J. M. & Piqueras, J. (2015). Laser-Induced Anatase-to-Rutile Transition in TiO2 Nanoparticles: Promotion and Inhibition Effects by Fe and Al Doping and Achievement of Micropatterning. *The Journal of Physical Chemistry C*, 119(21), 11965–11974.

Vaussenat, F., Bhattacharya, A., Payette, J., Benavides-Guerrero, J. A., Perrotton, A., Gerlein, L. F. & Cloutier, S. G. (2023). Continuous Critical Respiratory Parameter Measurements Using a Single Low-Cost Relative Humidity Sensor: Evaluation Study. *JMIR Biomedical Engineering*, 8(1), e47146. doi: 10.2196/47146.

Vitoratos, E., Sakkopoulos, S., Dalas, E., Paliatsas, N., Karageorgopoulos, D., Petraki, F., Kennou, S. & Choulis, S. A. (2009). Thermal Degradation Mechanisms of PEDOT:PSS. *Organic Electronics*, 10(1), 61–66.

Wajid, A. S., Das, S., Irin, F., Ahmed, H. S. T., Shelburne, J. L., Parviz, D., Fullerton, R. J., Jankowski, A. F., Hedden, R. C. & Green, M. J. (2012). Polymer-Stabilized Graphene Dispersions at High Concentrations in Organic Solvents for Composite Production. *Carbon*, 50(2), 526–534. doi: 10.1016/j.carbon.2011.09.008.

Walker, S. B. & Lewis, J. A. (2012). Reactive Silver Inks for Patterning High-Conductivity Features at Mild Temperatures. *Journal of the American Chemical Society*, 134(3), 1419–1421. doi: 10.1021/ja209267c.

Wall, M. (2011). *The Raman Spectroscopy of Graphene and the Determination of Layer Thickness* (Report n°AN52252). Retrieved on 2021-03-08 from: https://assets.thermofisher.com/TFS-Assets/MSD/Application-Notes/raman-spectroscopy-graphene-determination-layer-thickness-an52252.pdf.

Wang, D., Zhang, X., Sun, P., Lu, S., Wang, L., Wang, C. & Liu, Y. (2014). Photoelectrochemical Water Splitting with Rutile TiO2 Nanowires Array: Synergistic Effect of Hydrogen Treatment and Surface Modification with Anatase Nanoparticles. *Electrochimica Acta*, 130, 290–295.

Wang, G., Wang, H., Ling, Y., Tang, Y., Yang, X., Fitzmorris, R. C., Wang, C., Zhang, J. Z. & Li, Y. (2011). Hydrogen-Treated TiO2 Nanowire Arrays for Photoelectrochemical Water Splitting. *Nano Letters*, 11(7), 3026–3033.

Wang, H., Wang, Y., Cao, X., Feng, M. & Lan, G. (2009). Vibrational Properties of Graphene and Graphene Layers. *Journal of Raman Spectroscopy*, 40(12), 1791–1796. doi: 10.1002/jrs.2321.

Wang, R., Hashimoto, K., Fujishima, A., Chikuni, M., Kojima, E., Kitamura, A., Shimohigoshi, M. & Watanabe, T. (1997). Light-Induced Amphiphilic Surfaces. *Nature*, 388(6641), 431.

Wang, R., Hashimoto, K., Fujishima, A., Chikuni, M., Kojima, E., Kitamura, A., Shimohigoshi, M. & Watanabe, T. (1998). Photogeneration of Highly Amphiphilic TiO2 Surfaces. *Advanced Materials*, 10(2), 135–138.

Wang, R., Shang, Y., Kanjanaboos, P., Zhou, W., Ning, Z. & H. Sargent, E. (2016). Colloidal Quantum Dot Ligand Engineering for High Performance Solar Cells. *Energy & Environmental Science*, 9(4), 1130–1143. doi: 10.1039/C5EE03887A.

Wang, Y., Yang, X., Zhao, Y. & Zhang, X. (2019). New Insights into Flexible Transparent Conductive Silver Nanowires Films. *International journal of molecular sciences*, 20(11), 2803-2815.

Weber, J. W., Calado, V. E. & van de Sanden, M. C. M. (2010). Optical Constants of Graphene Measured by Spectroscopic Ellipsometry. *Applied Physics Letters*, 97(9), 091904. doi: 10.1063/1.3475393.

Weerasinghe, H. C., Sirimanne, P. M., Franks, G. V., Simon, G. P. & Cheng, Y. B. (2010). Low Temperature Chemically Sintered Nano-Crystalline TiO2 Electrodes for Flexible Dye-Sensitized Solar Cells. *Journal of Photochemistry and Photobiology A: Chemistry*, 213(1), 30–36. doi: 10.1016/j.jphotochem.2010.04.016.

Weidling, A. M., Turkani, V. S., Luo, B., Schroder, K. A. & Swisher, S. L. (2021). Photonic Curing of Solution-Processed Oxide Semiconductors with Efficient Gate Absorbers and Minimal Substrate Heating for High-Performance Thin-Film Transistors. *ACS Omega*, 6(27), 17323–17334. doi: 10.1021/acsomega.1c01421.

Wikipedia. (2021). Thermal Diffusivity. Online; accessed on 24-May-2022, Retrieved from: https://en.wikipedia.org/w/index.php?title=Thermal_diffusivity&oldid=1062007291.

Wikipedia. (2022). Laser Flash Analysis. Online; accessed on 24-May-2022, Retrieved from: https://en.wikipedia.org/w/index.php?title=Laser_flash_analysis&oldid=1085243704.

Wilder, J. W. G., Venema, L. C., Rinzler, A. G., Smalley, R. E. & Dekker, C. (1998). Electronic Structure of Atomically Resolved Carbon Nanotubes. *Nature*, 391(6662), 59–62.

Wise, F. W. (2000). Lead Salt Quantum Dots: The Limit of Strong Quantum Confinement. *Accounts of Chemical Research*, 33(11), 773–780. doi: 10.1021/ar970220q.

Wong, D., Abuzalat, O., Mostafa, S., Kim, S. & Park, S. S. (2019). Intense Pulsed Light Conversion of Anatase to Rutile TiO2 for Hybrid TiO2-SnO2/MWCNTs/PVB Room Temperature VOCs Sensor. *IEEE Sensors Journal*, 19(20), 9113–9121. doi: 10.1109/JSEN.2019.2924108.

Wu, H. & Ning, Z. (2023). Tutorial: Lead Sulfide Colloidal Quantum Dot Infrared Photodetector. *Journal of Applied Physics*, 133(4), 041101. doi: 10.1063/5.0133809.

Wu, J.-B., Lin, M.-L., Cong, X., Liu, H.-N. & Tan, P.-H. (2018). Raman Spectroscopy of Graphene-Based Materials and Its Applications in Related Devices. *Chemical Society Reviews*, 47(5), 1822–1873. doi: 10.1039/C6CS00915H.

Wu, J. & McCreery, R. L. (2009). Solid-State Electrochemistry in Molecule/ TiO2 Molecular Heterojunctions as the Basis of the TiO2 “Memristor”. *Journal of The Electrochemical Society*, 156(1), P29-P37.

Wu, J.-M., Shih, H. C. & Wu, W.-T. (2005). Electron Field Emission from Single Crystalline TiO2 Nanowires Prepared by Thermal Evaporation. *Chemical Physics Letters*, 413(4), 490–494. doi: 10.1016/j.cplett.2005.07.113.

Xiao, X., Yang, S., E, T. & Li, Y. (2023). Maximizing the Synergistic Effect on Accelerated Photoelectron Transfer of TiO2 by Double Z-scheme Heterojunctions and Specific Oxygen Vacancies. *Materials Today Chemistry*, 27, 101281. doi: 10.1016/j.mtchem.2022.101281.

Xu, F., Ma, X., Haughn, C. R., Benavides, J., Doty, M. F. & Cloutier, S. G. (2011). Efficient Exciton Funneling in Cascaded PbS Quantum Dot Superstructures. *ACS Nano*, 5(12), 9950–9957. doi: 10.1021/nn203728t.

Xu, F., Benavides, J., Ma, X. & Cloutier, S. G. (2012). Interconnected TiO2 Nanowire Networks for PbS Quantum Dot Solar Cell Applications. *Journal of Nanotechnology*, 2012, 1–6.

Xu, F., Gerlein, L. F., Ma, X., Haughn, C. R., Doty, M. F. & Cloutier, S. G. (2015). Impact of Different Surface Ligands on the Optical Properties of PbS Quantum Dot Solids. *Materials*, 8(4), 1858–1870.

Xu, W., Piper, R. T., Daunis, T. B., Schroder, K. A. & Hsu, J. W. P. (2020). Photonic Curing Enabling High-Speed Processing for Perovskite Solar Cells. *2020 47th IEEE Photovoltaic Specialists Conference (PVSC)*, pp. 0079–0081. doi: 10.1109/PVSC45281.2020.9300927.

Yahaya, M. Z., Azam, M. A., Mat Teridi, M. A., Singh, P. K. & Mohamad, A. A. (2017). Recent Characterisation of Sol-Gel Synthesised TiO2 Nanoparticles. In *Recent Applications in Sol-Gel Synthesis*.

Yamuna, A., Sundaresan, P. & Chen, S.-M. (2019). Ethylcellulose Assisted Exfoliation of Graphite by the Ultrasound Emulsification: An Application in Electrochemical Acebutolol Sensor. *Ultrasonics Sonochemistry*, 59, 104720. doi: 10.1016/j.ultsonch.2019.104720.

Yang, C., Hirose, Y., Nakao, S., Hoang, N. L. H. & Hasegawa, T. (2012). Metal-Induced Solid-Phase Crystallization of Amorphous TiO2 Thin Films. *Applied Physics Letters*, 101(5), 052101. doi: 10.1063/1.4739934.

Yang, Y., Ding, S., Araki, T., Jiu, J., Sugahara, T., Wang, J., Vanfleteren, J., Sekitani, T. & Suganuma, K. (2016). Facile Fabrication of Stretchable Ag Nanowire/Polyurethane Electrodes Using High Intensity Pulsed Light. *Nano Research*, 9(2), 401–414.

Yeh, M.-H., Chen, P.-H., Yang, Y.-C., Chen, G.-H. & Chen, H.-S. (2017). Investigation of Ag-TiO2 Interfacial Reaction of Highly Stable Ag Nanowire Transparent Conductive Film with Conformal TiO2 Coating by Atomic Layer Deposition. *ACS Applied Materials & Interfaces*, 9(12), 10788–10797. doi: 10.1021/acsami.6b13070.

Yeo, J., Kim, G., Hong, S., Kim, M. S., Kim, D., Lee, J., Lee, H. B., Kwon, J., Suh, Y. D., Kang, H. W., Sung, H. J., Choi, J.-H., Hong, W.-H., Ko, J. M., Lee, S.-H., Choa, S.-H. & Ko, S. H. (2014). Flexible Supercapacitor Fabrication by Room Temperature Rapid Laser Processing of Roll-to-Roll Printed Metal Nanoparticle Ink for Wearable Electronics Application. *Journal of Power Sources*, 246, 562–568.

Yi, P., Zhu, Y. & Deng, Y. (2018). Fabrication and Applications of Flexible Transparent Electrodes Based on Silver Nanowires. *Flexible Electronics*, 21–45. doi: 10.5772/intechopen.77506.

Yin, D., Chen, Z.-Y., Jiang, N.-R., Liu, Y.-F., Bi, Y.-G., Zhang, X.-L., Han, W., Feng, J. & Sun, H.-B. (2020). Highly Transparent and Flexible Fabric-Based Organic Light Emitting Devices for Unnoticeable Wearable Displays. *Organic Electronics*, 76, 105494.

Yu, H. L., Hsiao, C. C. & Liu, W. C. (2006a). New Apparatus for Haze Measurement for Transparent Media. *Measurement Science and Technology*, 17(8), N29–N36. doi: 10.1088/0957-0233/17/8/N01.

Yu, H., Li, S., Peng, S., Yu, Z., Chen, F., Liu, X., Guo, J., Zhu, B., Huang, W. & Zhang, S. (2023). Construction of Rutile/Anatase TiO2 Homojunction and Metal-Support Interaction in Au/TiO2 for Visible Photocatalytic Water Splitting and Degradation of Methylene Blue. *International Journal of Hydrogen Energy*, 48(3), 975–990. doi: 10.1016/j.ijhydene.2022.10.010.

Yu, P., Zhu, K., Norman, A. G., Ferrere, S., Frank, A. J. & Nozik, A. J. (2006b). Nanocrystalline TiO2 Solar Cells Sensitized with InAs Quantum Dots. *J. Phys. Chem. B*, 110(50), 25451–25454.

Yu, S.-Y., Schrodj, G., Mougin, K., Dentzer, J., Malval, J.-P., Zan, H.-W., Soppera, O. & Spangenberg, A. (2018). Direct Laser Writing of Crystallized TiO2 and TiO2/Carbon Microstructures with Tunable Conductive Properties. *Advanced Materials*, 30(51), 1805093.

Yuhas, B. D. & Yang, P. (2009). Nanowire-Based All-Oxide Solar Cells. *Journal of the American Chemical Society*, 131(10), 3756–3761. doi: 10.1021/ja8095575.

Zamanpour, F., Behrouznejad, F., Ghavaminia, E., Khosroshahi, R., Zhan, Y. & Taghavinia, N. (2021). Fast Light-Cured TiO2 Layers for Low-Cost Carbon-Based Perovskite Solar Cells. *ACS Applied Energy Materials*, 4(8), 7800–7810. doi: 10.1021/acsaem.1c01168.

Zhai, G., Bezryadina, A., Breeze, A. J., Zhang, D., Alers, G. B. & Carter, S. A. (2011a). Air Stability of TiO2/PbS Colloidal Nanoparticle Solar Cells and Its Impact on Power Efficiency. *Applied Physics Letters*, 99(6), 063512.

Zhai, T., Li, L., Ma, Y., Liao, M., Wang, X., Fang, X., Yao, J., Bando, Y. & Golberg, D. (2011b). One-Dimensional Inorganic Nanostructures : Synthesis, Field-Emission and Photodetection. *Chemical Society Reviews*, 40(5), 2986–3004. doi: 10.1039/C0CS00126K.

Zhang, D. R., Jin, X. Z. & Li, J. H. (2016). Effects of Sc and V Dopants on the Anatase-to-Rutile Phase Transition and Crystallite Size of TiO2 Nanoparticles. *Materials Chemistry and Physics*, 176, 68–74.

Zhang, J., Gao, J., Miller, E. M., Luther, J. M. & Beard, M. C. (2014). Diffusion-Controlled Synthesis of PbS and PbSe Quantum Dots with in Situ Halide Passivation for Quantum Dot Solar Cells. 8(1), 614–622.

Zhang, J., Crisp, R. W., Gao, J., Kroupa, D. M., Beard, M. C. & Luther, J. M. (2015). Synthetic Conditions for High-Accuracy Size Control of PbS Quantum Dots. *The Journal of Physical Chemistry Letters*, 6(10), 1830–1833.

Zhang, M., Chen, T. & Wang, Y. (2017). Insights into TiO 2 Polymorphs: Highly Selective Synthesis, Phase Transition, and Their Polymorph-Dependent Properties. *RSC Advances*, 7(83), 52755–52761.

zhang, Q., Liu, C., Gan, G. & Cui, X. (2017). Visible Perfect Reflectors Realized with All-Dielectric Metasurface. *Optics Communications*, 402, 226–230. doi: 10.1016/j.optcom.2017.05.053.

Zhang, R. & Engholm, M. (2018). Recent Progress on the Fabrication and Properties of Silver Nanowire-Based Transparent Electrodes. *Nanomaterials*, 8(8), 628.

Zhang, Z., Shi, C., Lv, K., Ma, C., Xiao, G. & Ni, L. (2018). 200-Nm Long TiO2 Nanorod Arrays for Efficient Solid-State PbS Quantum Dot-Sensitized Solar Cells. *Journal of Energy Chemistry*, 27(4), 1214–1218.

Zhu, M., Liu, W., Ke, W., Clark, S., B. Secor, E., Song, T.-B., G. Kanatzidis, M., Li, X. & C. Hersam, M. (2017). Millisecond-Pulsed Photonically-Annealed Tin Oxide Electron Transport Layers for Efficient Perovskite Solar Cells. *Journal of Materials Chemistry A*, 5(46), 24110–24115. doi: 10.1039/C7TA07969A.

Zocca, A., Colombo, P., Gomes, C. M. & Günster, J. (2015). Additive Manufacturing of Ceramics: Issues, Potentialities, and Opportunities. *Journal of the American Ceramic Society*, 98(7), 1983–2001. doi: 10.1111/jace.13700.

Zou, J., Zhang, Q., Huang, K. & Marzari, N. (2010). Ultraviolet Photodetectors Based on Anodic TiO2 Nanotube Arrays. *The Journal of Physical Chemistry C*, 114(24), 10725–10729. doi: 10.1021/jp1011236.